2.1.3.2 Study on buffer(KH_2PO_4)concentration.
The KH_2PO_4 buffer(pH6) for mobile phase system was prepared as 20 ,30, 40,50,60 and 70 mM and mixed with ethanol at the optimized ratio from 2.1.3.1.Those system was used to separated the MDA-TBA derivertised products in HPLC system in 2.1.2.

2.1.3.3Study on pH buffer(KH_2PO_4.) The KH_2PO_4 buffer was prepared by variation of pH as 5.4,5.8,6.0,6.8 and 7.0. and mixed with ethanol at the optimized ratio from 2.1.3.1.-2.1.3.2. Those system was used to separated the MDA-TBA derivertised products in HPLC system in 2.1.2.

2.1.3.4 Study on flow rate of mobile phase system.
The mobile phase between K_2HPO_4 buffer at best condition from 2.1.3.1-2.1.3.3 and mixed with best ratio from 2.1.3.1-2.1.3.3 was used to apply in this section by varied flow rate as 0.5 to 1.0 ml/min. Those system was used to separated the MDA-TBA derivertised products in HPLC system in 2.1.2.

2.1.4.Method validation.
The MDA standard solutions were prepared as 0.5 ,1.0,2.0 ,3.0 and 5.0 µM and derivertised with standard TBA to form adduct products and separated with the best condition from 2.1.3. to evaluate LOD and LOQ.

2.2 *Analysis of MDA in soybean and soymilk products*.
Preparation samples. Soybean was purchased from Food land supermarket. Soymilk products were purchased as fresh drinking soymilk for 3 samples from fresh market in Bangkok, commercial UHT milk as pure soymilk samples for 4 samples and UHT milk of soymilk samples mixed with another products such corn milk, black seasame, *Coix lacryma-jobi*, chocolate, green tea, barley ,malt and wheat germ for 13 samples. All those samples were treated with 5% of trichloroacetic acid and filtered through membrane syringe filter (polytetra-fluoroethylene) 0.45 micron.
Those clarified soymilk samples were injected to C18 column and treated as in 2.1 by choosing the optimization condition from 2.1.3.1-2.1.3.3.The area peak of MDA in sample were recored and calculated the MDA content by compared with the standard calibration curve of standard MDA.

3. Results and Discussion

From part 2.1, the optimized condition from 2.1.3.1 showed that the ratio of buffer : ethanol should be 60:40.From the study of phosphate buffer concentration ,the appropriate buffer concentration should be used 50 mM as shown in figure 1.

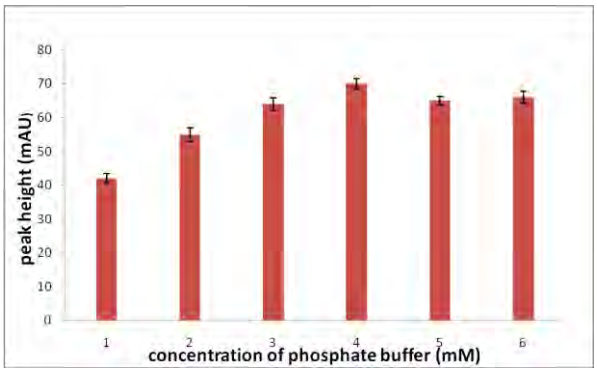

Figure 1 Effect of phosphate buffer concentration
Note: 1= 20mM 2= 30mM 3 = 40mM
4= 50mM 5= 60mM 6= 70mM
Note: number of replication of each experiment = 3

From figure 1. the peak height of MDA standard solution showed the maximum signal at 50 mM of phosphate buffer,so this condition should be the optimum concentration of buffer. The result from 2.1.3.3 showed in figure 2.

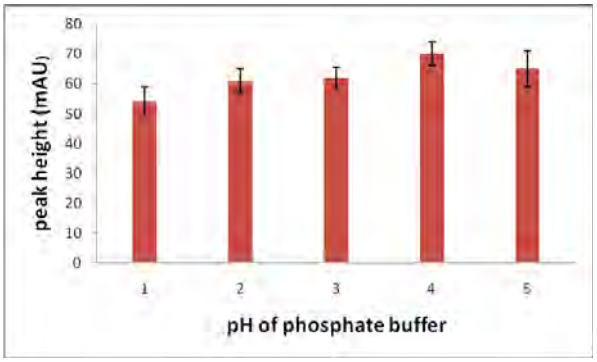

Figure 2 Effect of pH buffer
Note: 1= pH 5.4 2= pH 5.8 3 = pH 6.0
4= pH 6.8 5= pH 7.0
Note: number of replication of each experiment = 3

As in fig.2 , the peak height of MDA showed the maximum value at pH 6.8,so the buffer should prepared at this pH.The result from flow rate study in 2.1.3.4 showed the maximum peak height at 0.7 ml/min as in figure 3

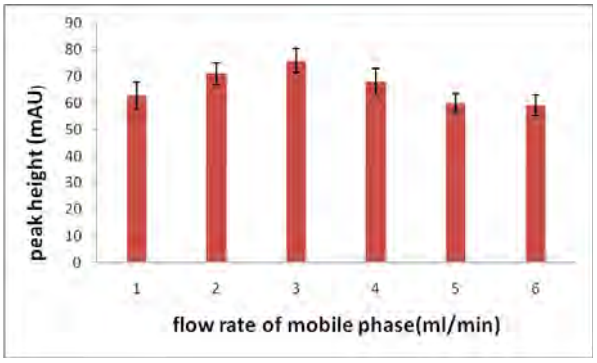

Figure 3. Effect of flow rate of mobile phase

Note:1= flow rate 0.5 ml/min, 2= flow rate 0.6 ml/min

3= flow rate 0.7 ml/min, 4= flow rate 0.8 ml/min
5= flow rate 0.9 ml/min, 6= flow rate 1.0 ml/min
Note: number of replication of each experiment = 3

After optimized condition ,the standard calibration curves were prepared and calculated LOD and LOQ.by standard MDA (0.1µM) spiked in blank (n=10).This showed LOD = 0.01 µM and LOQ = 0.04 µM.The method for analysis of MDA that used in this work showed the high sensivity with low LOD and LOQ.(LOD = limit of detection ,LOQ = limit of quantitation)

The standard chromatogram of MDA-TBA adduct which was operated with the best condition from part 2.1.3.1-2,1.3.4 showed ,the analysed peak at7.45 minute as an example in figure 4 after prepared calibration curve as in figure 5.

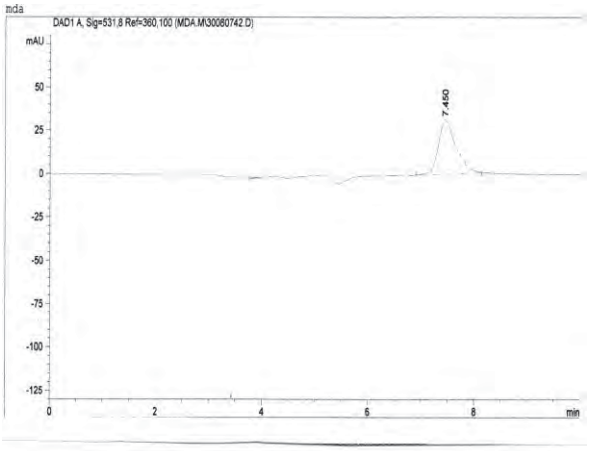

Figure 4. Chromatogram of 0.5 micromolar of standard MDA solution.

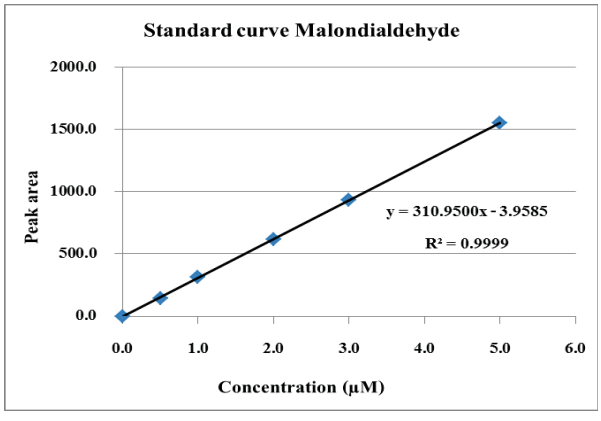

Figure 5. Standard Calibration curve of standard MDA solution.

The chromatogram of each sample was recorded as showed an example in figure 6.

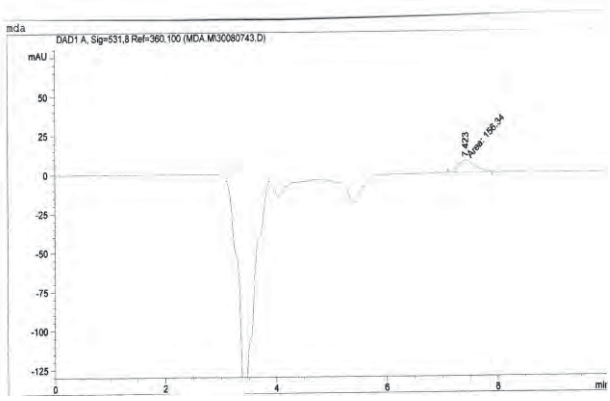

Figure 6. Chromatogram of MDA in soy milk sample

The results for analysis of MDA in soybean and soymilk products were presented in figure5

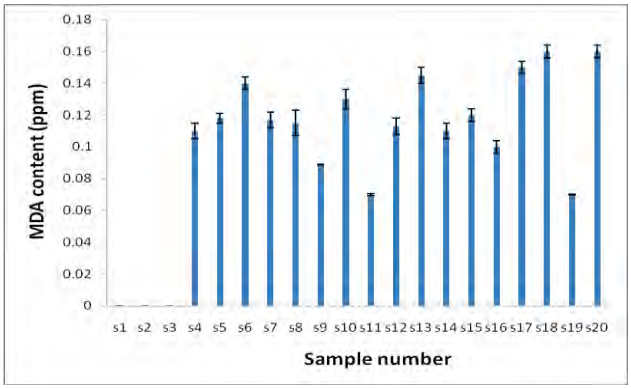

Figure 7 MDA contents in soybean and soymilk samples
Note: S1-S3 = soybean samples
S4-S5 =pasteurised pure soymilk samples
S6- S7= UHT pure soymilk samples
S8-S9 = UHT pure soymilk samples, low sugar
S10-S20= UHT soymilk mixed with others Samples
Note: number of replication of each sample = 3

From the above figure 7,it showed that soybean has the lowest MDA content about 0.0005-0.0006 ppm.
The S19 which was the soymilk mixed with wheatgerm contained lower MDA content than found MDA in soymilk mixed with other.This may the reason that wheatgerm could contain vitamin E with has the effect to protect the occurrence of lipid peroxidation in food[13]. However,the processing method such as pasteurised or UHT did not effect the MDA content in soy milk samples ,this may from the effect of the other component in soymilk.

4. Conclusions

From the above study about the optimum condition showed in table 1

Table 1 Optimum condition for High performance liquid chromatography.

Parameter	condition
Column	Reverse phase C18
Mobile phase	
K_2HPO_4, Conc.	50mM
K_2HPO_4 ,pH	6.8
Ratio buffer:ethanol	60:40
Flow rate	0.7 ml/min

The method that use in this analysis is very sensitive method with low LOD in nanomolar unit.

The soy bean contained the lowest MDA content about $5x10^{-4}$ – $6x\ 10^{-4}$ ppm.The processing soybean to soymilk trend to increase MDA content.The soymilk with wheat germ contained the lowest MDA content compare with all soymilk products.However, all soy milk showed the MDA content between 0.07 – 0.16 ppm. The MDA found in soymilk showed the occurrence of lipid peroxidation in soybean between processing to soymilk.

Acknowledgements

The authors wish to thank the Faculty of Science Srinakharinwirot University for funding this research..

References

[1] E. Middelton, *Int. J. Pharmacol*. **34** (1996) 344-350.
[2] A. Mora, M. Paya, J.L. Rios, M.J. Alcaraz, *Biochem. Pharmacol*. **40**(1990) 793-801.
[3] J.P. Kehrer, *Crit. Rev. Toxicol*. **23** (1993) 21-26.
[4] H.C. Yeo, H.J. Helbock, D.W. Chyu and B.N. Ames, *Anal. Biochem*.**220** (1994) 391..
[5] J. Pilz, I. Meineke and C.H. Gleiter, *J. Chromatogr. B* **742** (2000) 315-322.
[6] J. Suttnar, J. Cermak and E. Dyr, *Anal. Biochem*. **249** (1997) 20-26.
[7] J. Suttnar, L. Masova, and E. Dyr, *J. Chromatogr. B*. 751 (2001) 193.
[8] R.P. Bird and H.H. Draper, Methods *Enzymol*. 105 (1984) 299-302.
[9] D.R. Janero, Free Radic. *Biol. Med***. 9 (**1990) 515-520;
[10] W.Zuojun .W, Li.Xinghua, T. Dilantha and, L.Yingxin .*J of Food Eng*.**107**(2011).379-384
[11] M.Roğrio ,C. Carlos C and P.Carla .*Food Chemistry* **112** (2009) 1038–1045.
[12] Fenaille, F., Mottier, P., Turesky, R.J., Ali, S., and P.A.Guy, *Journal of Chromatography A* **921**, (2001)237-245.
[13] G. Setiowaty and Y.B. Che Man.Food Chemistry **81** (2003) 147–154
[14] M.Raquel ,G.Luis and B. Laura. Journal of Chromatography B, **805** (2004) 33–39

SOPHOROLIPID PRODUCTION BY *PICHIA ANOMALA* MUE24 IN A 5-L BATCH BIOREACTOR GROWN IN GLUCOSE AND SOYBEAN OIL

Tiwaporn Punrat[1*], Suchada Napathorn[1], Jirarat Tattiyakul[2], Suthep Thaniyavarn[1], Jiraporn Thaniyavarn[1]

[1] Department of Microbiology, Faculty of Science, Chulalongkorn University, PhyaThai Rd, Bangkok 10330, Thailand
.[2] Department of Food Technology, Faculty of Science, Chulalongkorn University, PhyaThai Rd, Bangkok 10330, Thailand

[*] Author for correspondence; E-Mail: sina_up@hotmail.com, Tel. +66 834933331

Abstract: Sophorolipid is one type of glycolipid biosurfactant, produced by *Pichia anomala* MUE24. In this work, sophorolipid was produced in modified medium containing 0.02 % (w/v) KH_2PO_4, 0.02 % (w/v) $MgSO_4 \cdot 7H_2O$, 0.64 % (w/v) yeast extract, 0.11% (w/v) $NaNO_3$, adjusted to an initial pH of 4.5. The mixed carbon sources (S) were 13.34 % (w/v) soybean oil and 6.66 % (w/v) glucose. The shaken flask cultivation was performed with 10% (v/v) inoculum controlled at 30 °C and 200 rpm. After 168 h of cultivation, the surface tension of the culture broth reduced to 36 mN/m. The final concentrations of cells (X) and biosurfactant (P) were 16.4 and 0.55 g/L, respectively. This resulted in biosurfactant yield (YP/S) and productivity (QP) of 0.0038 g-P/g-S and 0.003 g-P/L/h, respectively. To improve process yield and productivity, batch cultivations in 5 liters bioreactor was performed at 30 °C, 168 h, without pH control. After 72 h of cultivation, cell (X) and biosurfactant (P) concentrations were 45.78 and 19.40 g/L, respectively. In which the yield ($Y_{P/S}$) value of 0.1351 g-P/g-S, and the productivity (Q_P) value of 0.2695 g-P/L/h were obtained. The specific productivity of biosurfactant in the shake flask culture and in the batch bioreactor was 0.199 and 5.887 (mg-P/g-X/h), respectively. The results of cells stained with Nile Red at 72h of cultivation showed accumulation glycolipid in the cells. The biosurfactant obtained was isolated and purified by thin layer chromatography.

1. Introduction

Surfactants can be divided into 2 major types those are chemical surfactants and biosurfactant. The advantages of biosurfactant over chemical surfactants are low toxicity, high biodegradability, ecological safety and high specific activity at extreme conditions such as temperatures, pH levels and salinity. Whereas most chemical surfactants are toxic, hardly biodegradable and manufacturing processes and by products can be hazardous to environmental. Furthermore, biosurfactant can be used in several industries such as food, cosmetic and pharmaeutical industries (Najafi et al, 2010). Biosurfactant can be categorized into four groups those are lipopeptides or lipoproteins, phospholipids, polymeric surfactants and glycolipids. Glycolipid surfactants are composed of a carbohydrate head and a lipid tail. They are a class of nonionic surfactants that has significantly increased its market share during the last 10 years. Sophorolipid is one type of glycolipid biosurfactant, produced by several yeast such as *Candida* sp and *Pichia anomala*, etc.

Thaniyavarn et al, 2008 reported that sophorolipid was produced by *Pichia anomala* PY1. *Pichia anomala* MUE24, the mutant strain of PY1 selected by UV and ethylmethane sulfonate (EMS) mutation, can produce biosurfactant higher than the wild type. *P.anomala* MUE24 would produce sophorolipid in modified medium containing glucose and soybean oil as a carbon sources (Punrat et al, 2010). So this paper focuses on scale up of sophorolipid production in 5-L batch bioreactor for increasing high yield of sophorolipid. Finally, kinetics parameters were calculated and compared with those of flask scale and the crude biosurfactant was analysed by thin layer chromatography.

2. Materials and Methods

2.1 Microorganism and seed medium

For seed culture preparation, *P. anomala* MUE24 was cultured in YM medium containing 0.3% yeast extract, 0.3% malt extract, 0.5% bacto peptone and 1% glucose (v/v) for 18 hours.

2.2 Modified production medium

The modified medium is contained of 0.02% KH_2PO_4, 0.02% $MgSO_4 \cdot 7H_2O$, 0.64 %yeast extract, 0.11% $NaNO_3$, 6.66% glucose and 13.34% soy bean oil (v/v) with an initial pH 4.5.

2.3 Culture conditions

2.3.1 Shake flask scale: *P. anomala* MUE24 was cultured in modified medium: production volume of 250mL in 500mL flask. Shaken flask cultivation was performed in incubator shaker at 30ºC, 200rpm for 168 h.

2.3.2 5-L batch bioreactor was operated with pH control at 4.5: *P. anomala* MUE24 was inoculated at cell density of 1 at 600 nm (10%v/v) into the modified medium production volume was 2L in 5L batch bioreactor (FS01-5L Double Jacket, Winpact Bench-Top Fermentor) and controlled culture condition at 30ºC, 400rpm, 2vvm for 168 h adjusted with an initial pH 4.5 and controlled pH at 4.5 throughout the experiment.

2.3.3 5-L batch bioreactor (similar medium and condition as 2.3.2) was operated without pH control and controlled air flow rate at 1vvm for 168h.

According to these conditions the samples were collected every 24 hours for analysis.

2.4 Analytical methods

Culture samples were centrifuged at 8,000 rpm for 25 min for cell removal and the cell free broth was obtained to measure biosurfactant activity. Surface tensions were determined with a Krüss Tensiometer (model K6, Hamburg, Germany) using du Nouy ring method at room temperature and oil displacement area as described by Morikawa *et al*. (1993). Growth was measured in terms of dry cell mass. Reducing sugar was determined by the use of dinitrosalicylic acid reagent. The soybean oil concentrations in the samples were determined via partition-gravimetric method using dichloromethane as solvent (APHA *et al*., 1992).

2.5 Extraction of biosurfactant

Sample of fermentation broth was centrifuged to remove the yeast cells. The obtained supernatant was extracted with hexane to remove fatty acids. The crude extract was obtained by extraction with an equal volume of ethyl acetate.

2.6 Kinetics calculations

In this study, kinetics of production yield was calculated by the following equation:

X = Biomass (g/l)

P = Sophorolipid product (g/l)

$Y_{P/S}$ = Sophorolipid per used substrates (g-P/g-S)

Q_P = Productivity (g-P/l/h)

Specific productivity = Q_P(mg-P/l/h)/ g-X

Specific growth rate =

$$\mu = \frac{\ln (X_2 - X_1)}{t_2 - t_1}, \; t_2 > t_1 \quad (1)$$

X_2 = final biomass concentration

X_1 = initial biomass concentration

t_2 = final time and t_1 = initial time

2.7 Staining yeast cells by Nile red dye

1 mL of sample was collected in eppendorf and then centrifuged at 8,000 rpm, 20 minutes for collecting cell pellet. The cells pellet was washed at least 3 times with normal saline solution (NSS). Cells were suspended in NSS and added nile red at a final conc. 0.1 μg/ml. Then, cells were incubated at 37ºC for 5 minutes. Finally, stained cell was rinsed with NSS at least 3 times and observation with fluorescence microscopy (Morita *et al*, 2008).

2.8 Thin layer chromatography (TLC)

The crude biosurfactant was dissolved at final concentration 20 mg/mL in ethyl acetate and spotted 20 μL of sample on TLC plate. Then Chloroform: Methanol: Water (65:25:4 vol/vol) was used as solvent system (Robert *et al*., 1989).

3. Results and Discussion

3.1 Shake flask scale

In shake flask scale, the surface tension of culture broth was reduced to minimum of 36 mN/m at 168 hours of cultivation time. Furthermore, the culture broth at 168h also gave the highest biomass and oil dispersion value (Fig1).

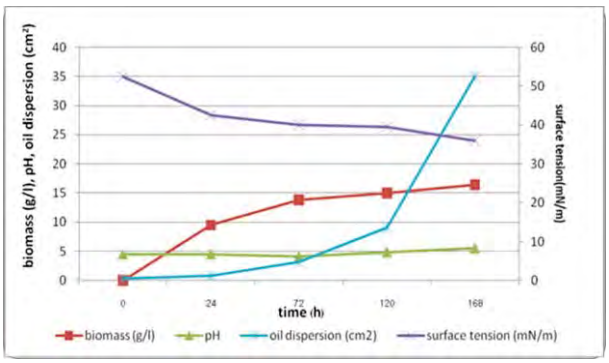

Figure 1. Time course of SL production, in shake flasks scale.

3.2 Batch culture in 5-L fermenter with pH controlled at 4.5

P. Anomala MUE24 was cultured in 5-L batch bioreactor with pH control at 4.5 throughout diauxic growth curve was observed because cells utilized 2 carbon sources consequently (glucose and soybean oil). As the results, yeast cells utilized glucose as a primary carbon source and soybean oil as a secondary carbon source. The surface tension of culture broth was reduced to minimum of 36 mN/m and gave the highest oil dispersion value of 28.274 at 168 hours of cultivation time (Fig2).

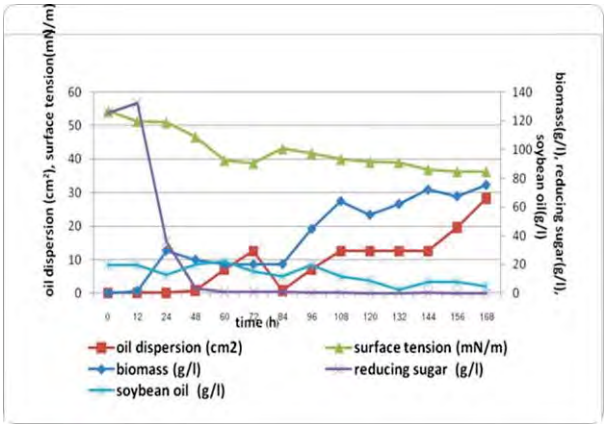

Figure 2 Time course of SL production in batch culture in a 5-L fermenter with pH control

3.3 Batch culture in 5-L fermenter without pH controlled

The results showed that pH value was increased rapidly from 4.5 to pH7during the 48th and 72nd hours of cultivation time and the activity of biosurfactant production was the highest at 72 hours of cultivation time: minimum surface tension of 29.33 mN/m and highest oil dispersion of 153.94 (all of area test). Fig3 shows the ooptimal sophorolipid production because the yeast cells could produce sophorolipid faster than the products obtained in shake flask scale and in bioreactor with pH control at 4.5. These results

indicated that pH about 7 was suitable for sopphorolipid production.

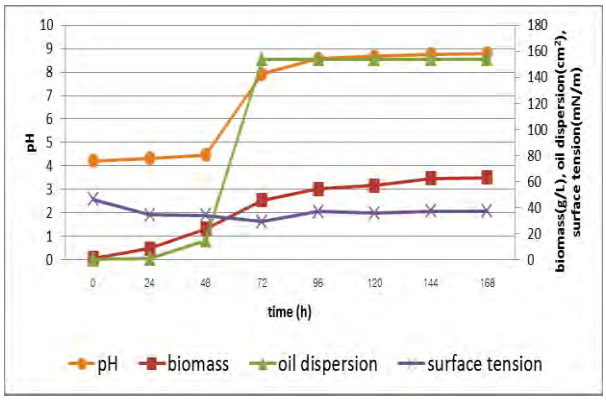

Figure 3. Time course of SL production in batch culture in a 5-L fermenter without pH control

3.4 Kinetics calculations

Comparative study of kinetic calculation showed that optimal under the cultivation of sophorolipid production was obtained in 5-L bioreactor without pH control at 72 hours: highest sophorolipid (P), sophorolipid per used substrates ($Y_{P/S}$), productivity (Q_P), specific productivity (Q_P) and specific growth rate (μ) once shown in table 1.

Table 1: Kinetic values of biosurfactants production under difference conditions.

Para-meters	Shake flask 168h	Biore-actor 168h pH control	Bioreact or 168h without pH control	Bioreac-tor 72h without pH control
X (g/L)	16.4000	75.4600	63.1840	45.7760
P (g/L)	0.5500	1.9500	4.2080	19.4057
$Y_{P/S}$ (g-P/g-S)	0.0038	0.0135	0.0292	0.2352
Q_P (g-P/L/h)	0.0030	0.0116	0.0250	0.2695
μ	0.0087	0.7970	0.3693	0.6200
Specific productivity (mg-P/g-X/h)	0.1990	0.1540	0.3957	5.8874

3.4 Staining yeast cells by Nile red dye

Yeast cells obtained from culture broth at 72h was stained with nile red reagent and observed by Fluorescence microscope. The result shows an accumulation of lipids inside the cells (Fig4). It was supported that *P. anomala* MUE24 can utilized soybean oil as a carbon source. Furthermore, the result of nile red staining showed accumulation of glycolipid in the cells in accord with Morita *et al*, 2008 at shown in figure 4. (including with TEM observation).

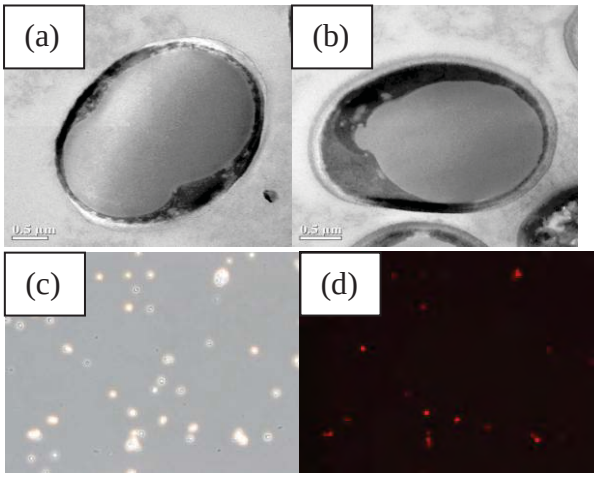

Figure 4. TEM observation (a)cell culture for 72h (b) cell culture for 168h and Fluorescence microscopy observation by nile red staining (c,d) of lipids accumulation in *P. anomala* MUE24. Cells were cutured in modified medium in bioreactor without pH control for 72h.

3.5 Thin layer chromatography (TLC)

The crude biosurfactant, extracted from supernatant of culture broth after 72 h, was analysed by TLC. The result shows 3 fractions of R_f 0.90, 0.79 and 0.69 (Fig5). The result was similar with the crude biosurfactant obtained in shake flask scale (data not shown).

Figure 5. Fractions of crude biosurfactant as analysed by TLC.

4. Conclusions

P. anomala MUE24 was found capable of producing sophorolipid in the modified medium at initial pH of 4.5. The mixed carbon sources (S) were soybean oil and glucose. To improve the yield and productivity, the batch cultivations in a 5-L bioreactor were performed at 30°C, 168 h either with or without pH controlled at 4.5. As a result, we found that the batch cultivations in a 5-l bioreactor at 72 h of cultivation without pH controlled, gave high biosurfactant. Both cell (X) and biosurfactant (P) concentration increased to 45.78 and 19.40 g/l, respectively, in which the yield ($Y_{P/S}$) of 0.2352 g-P/g-S, and the productivity (Q_P) of 0.2695 g-P/l/h were

obtained. The specific productivity of biosurfactant in shake flask culture and batch bioreactor without pH controlled was 0.1990 and 5.8870 (mg-P/g-X/h), respectively. The results of staining yeast cells with nile red after 72h of cultivation showed accumulation of glycolipid inside the cells. Furthermore, 3 fractions of crude biosurfactant were observed via Thin-Layer Chromatography analysis.

Acknowledgements

This work was supported by the H.M. the king's 72nd Birthday Scholarship, Chulalongkorn University and the Higher Education Research Promotion and National Research University Project of Thailand, Office of the Higher Education Commission (FW 653A). Special thanks for kindly suggestion of Prof. Yoshikazu Ohya on the lipid accumulation in yeast cell. (Prof. of Laboratory of signal transduction, Department of integrated biosciences, Graduate school of frontier sciences, University of Tokyo)

References

[1] APHA, AWWA and WEF. *American public health and association* (1992)

[2] A.R. Najafi, M.R. Rahimpour, A.H. Jahanmiri, R. Roostaazad, D. Arabian, M. Soleimani and Z. Jamshidnejad, *Colloids and Surfaces B: Biointerfaces*. **82** (2011) 33–39.

[3] J. Thaniyavarn, T. Chianguthai, P. Sangvanich, N. Roongsawang, K. Washio, M. Morikawa and S. Thaniyavarn. *Biosci Biotechnol Biochem*. **72** (2008) 2061-2068.

[4] M. Morikawa, H. Daido, T. Takao, S. Murata, Y. Shimonishi and T. Imanaka. *Bacteriol*. **175** (1993) 6459-6466.

[5] T. Morita, M. Konishi, T. Fukuoka, T. Imura and D. Kitamoto. *Bioscience and Bioengineering*. **105** (2008) 493-50.

[6] T. Punrat, P. Sangwanich and J. Thaniyavarn. *Senior Project* (2010) 1-53.

PRODUCTION OF BIOSURFACTANT FROM *Pichia anomala* PY189 USING SOYBEAN OIL

Wanwisa Sudsamai[1*], Jirarat Anantagool[2], Suthep Thaniyavarn[1] and Jiraporn Thaniyavarn[1]

[1]Department of Microbioloy, Faculty of Science, Chulalongkorn University, Pathumwan, Bangkok, 10330 Thailand
[2]Department of Food Technology, Faculty of Science, Chulalongkorn University, Pathumwan, Bangkok, 10330 Thailand

[*] Author for correspondence; E-mail: nin_gsm@hotmail.com, Tel. +66 8960756293

Abstract: In recent years, the interest in microbial produced biosurfactants has been increasing due to many advantages over chemical surfactants including the employ of renewable resources for their production, low toxicity and environmentally friendly. Owing to these advantages, biosurfactants found their application in various fields, including food, cosmetic, pharmaceutics, petroleum and environment. The aim of this study was to investigate effect of soybean oil:glucose ratio, carbon:nitrogen sources ratio and $NaNO_3$:yeast extract ratio on the production of biosurfactant by yeast *Pichia anomala* PY189. Type and ratio of carbon and nitrogen sources influence on their characterization (e.g. surface activity) and yield. The best result was obtained when using 3% (v/v) of soybean oil, 1% (w/v) of glucose, 0.35% (w/v) of yeast extract, 0.35% (w/v) of $NaNO_3$, 0.02% (w/v) of KH_2PO_4, 0.02% (w/v) of $MgSO_4 \cdot 7H_2O$ and pH 5.5 in a shaking incubator at 30°C, 200 rpm for 7 days. The surface tension of the culture broth was reduced from 54.33 to 41.44 mN/m and the oil displacement was measured at 6.32 cm^2. The supernatant was extracted with ethyl acetate giving 0.57 g/L of crude biosurfactant. The crude biosurfactant in water exhibited hydrophilic lipophilic balance (HLB) value of 10-13.

1. Introduction

Surfactants are amphiphilic molecules containing both hydrophilic and hydrophobic moieties in its molecules can be divided into two types: chemical surfactants and biosurfactants [7]. Although most of surfactants in the market are chemical surfactants the use of face with environment and health impact. Nowadays industry and research organizations are in search for new methods for the production of surfactants from renewable resources (vegetable oil, whey, sugarcane molasses, etc.), low toxicity and environment friendly. For these reasons, biosurfactans therefore gained considerable interest and found their applications in a wide variety of usages, including food, cosmetic, pharmaceutics, petroleum and environment [3, 9]. Biosurfactants are synthesized by a variety of microorganisms, including bacteria, yeast and filamentous fungi secreted into medium or localized on the cell surface [6]. When comparing with chemical surfactants, biosurfactants are still costly thus ways to compete with chemical surfactants are to increase its productivity or else new applicational values (antibacterial, antifungal, antiviral, insecticide, etc.) [3].

Type and ratio of carbon and nitrogen sources influence on their characterization (e.g. surface activity) and yield [4]. In this study, effect of variation of soybean oil:glucose ratio, carbon:nitrogen ratio and $NaNO_3$:yeast extract ratio on biosurfactant production and growth of *P. anomala* PY189 were investigated. Sophorolipid glycolipid biosufactant producer *P. anomala* PY 189, is an ethyl methanesulfonate (EMS) induced mutant of wild type P1 which was isolated from Khao Mhak; a kind of Thai fermented food [5]. *P. anomala*, a non-pathogenic yeast and biosurfactant producer was selected for its use in food industry [11]. The obtained crude biosurfactant will be used to produce oil-in-water emulsion with application of lemongrass oil incorporated film for sausage wrapping.

2. Materials and Methods

2.1 Inoculum preparation

P. anomala PY189 a mutant of *P. anomala* PY1 was inoculated into 250-mL Erlenmeyer flask containing 50 mL of YM broth (per liter, 3 g of yeast extract, 3 g of malt extract, 5 g of peptone and 10 g of glucose, pH 4.5) and incubated in a shaking incubator at 30°C, 200 rpm for 18 hours. Inoculum size was at 10% (v/v).

2.2 Medium optimization

To study effect of soybean oil:glucose ratio, carbon:nitrogen ratio and $NaNO_3$:yeast extract ratio on biosurfactant production and growth of *P. anomala* PY189. Soybean oil:glucose ratio in the employed medium was varied from 4:0 to 0:4 while concentrations of yeast extract, $NaNO_3$, KH_2PO_4 and $MgSO_4 \cdot 7H_2O$ were kept constant at 0.1, 0.4, 0.02 and 0.02% (w/v). In case of carbon:nitrogen sources, a varied ratio of 4:0.25 to 4:2 were employed while fix $NaNO_3$:yeast extract ratio at 1:1, and 0.02% (w/v) of KH_2PO_4 and 0.02% (w/v) of $MgSO_4 \cdot 7H_2O$. Finally, effect of $NaNO_3$:yeast extract ratio was varied between 0.15:0.55 to 0.55:0.15 while fix concentration of other constituents of medium as follow: carbon source (4%), KH_2PO_4 (0.02 % (w/v)) and $MgSO_4.7H_2O$ (0.02 % (w/v)). All experiments were carried out in 250 mL Erlenmeyer flasks containing 50 mL of the media at pH 5.5 and incubated in shaking incubator at 200 rpm, 30°C, for 7 days. Culture broth obtained were

analyzed for their biosurfactant activities along with their respective growth.

2.3 Production and extraction of crude biosurfactant

Biosurfactant was produced by inoculating inoculums into a 500 mL Erlenmeyer flasks containing 200 mL of production medium (with total volume of 2 L) followed by incubated in shaking incubator at 30°C, 200 rpm for 7 days. After which culture broth was centrifuged at 4°C, 8000 rpm for 20 minutes for cell removal. Supernatant obtained was extracted once with hexane to remove residual soybean oil. The supernatant was extracted three times with an equal volume of ethyl acetate. The solvent phase (containing biosurfactant) was evaporated on rotary evaporator and weighted.

2.4 Biomass and pH measurement

The culture broth was centrifuged at 4°C, 8000 rpm for 20 minutes. Then the obtained cell pellet, which was washed once with hexane in order to remove residual soybean oil, was dried overnight at 85°C and weighted for determining yeast biomass concentration. For the pH of culture supernatant was measured with a digital pH meter.

2.5 Biosurfactant activity measurement

The surface tension of the culture broth was measured with a du Nöuy ring-type tensiometer. For oil displacement test, this was done by adding 40 mL of distilled to a petri dish (150 mm in diameter), 15 µL of crude oil was dropped onto the surface of water followed by 10 µL of sample onto the surface of crude oil. The clear zone appears was measured and calculated [2].

2.6 Substrates measurement

Reducing sugar was determined by dinitrosalicylic acid (DNS) method [1]. The residual soybean oil was extracted with hexane then evaporated by a rotary vacuum evaporator and weighted [8].

2.7 Hydrophilic-Lipophilic Balance (HLB)

The crude biosurfactant (1 mg/mL) was mixed into water, and thereafter the mixture was shaken vigorously in a vortex mixer for 2 minutes and allowed to sit for 10 minutes before observing the appearance. The appearance of biosurfactant in water is indicative of its likely HLB value.

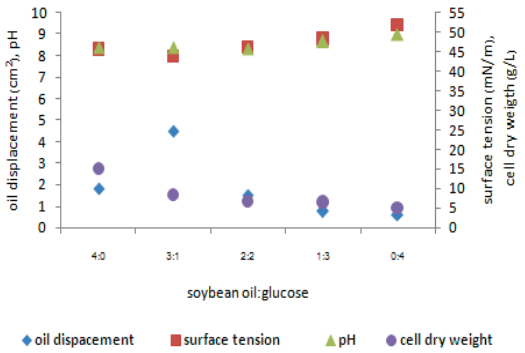

Figure 1. Effect of soybean oil:glucose ratio on biosurfactant activity and growth of *P. anomala* PY189.

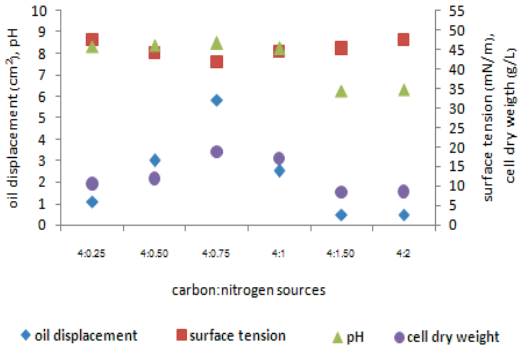

Figure 2. Effect of carbon:nitrogen sources ratio on biosurfactant activity and growth of *P. anomala* PY189.

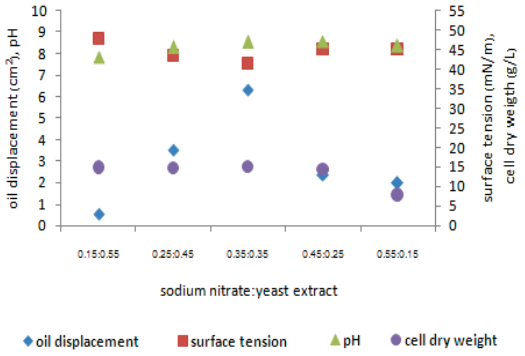

Figure 3. Effect of $NaNO_3$:yeast extract ratio on biosurfactant activity and growth of *P. anomala* PY189.

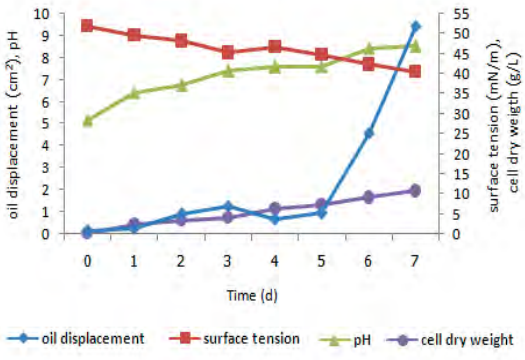

Figure 4. Biosurfactant activity and growth profile of *P. anomala* PY189 in the optimized medium.

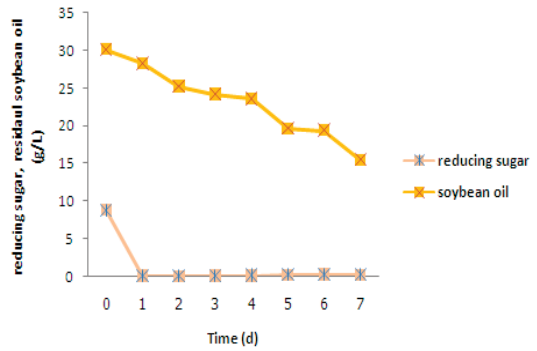

Figure 5. Carbon sources remained profile of *P. anomala* PY189 in the optimized medium.

3. Results and Discussion

Figure 1 shows biosurfactant activity and growth of yeast *P. anomala* PY189 at various concentrations of soybean oil and glucose. Biosurfactant production was determined in term of surface tension and its oil displacement activities. It was observed that the combination of 3% (v/v) of soybean oil and 1% (w/v) of glucose was most effective for the biosurfactant production. While 4% (w/v) of glucose was used as sole source of carbon poor growth and low biosurfactant production was observed. Effects of carbon and nitrogen sources are shown in Figure 2. At 4% of carbon sources, the optimum concentration of nitrogen sources in the study was found to be 0.75%. Effects of $NaNO_3$ and yeast extract are shown in Figure 3. The results suggesting that at 0.35% (w/v) of $NaNO_3$ and 0.35% (w/v) of yeast extract is the best ratio for biosurfactant production in which at day 7th the surface tension and the oil displacement of the culture broth were 41.44 mN/m and 6.32 cm^2, respectively. Thus, the optimum medium composition for biosurfactant production is: 3% (v/v) of soybean oil, 1% (w/v) of glucose, 0.35% (w/v) of yeast extract, 0.35% (w/v) of $NaNO_3$, 0.02% (w/v) of KH_2PO_4 and 0.02% (w/v) of $MgSO_4 \cdot 7H_2O$. Biosurfactant activity, growth and utilization of carbon sources pattern of *P. anomala* PY189 in this optimized medium while shaken at 30°C, 200 rpm for 7 days are depicted in figure 4 and 5. Glucose content in culture medium was almost completely utilized within 24 hours followed by further used of soybean oil. After 7 days of cultivation, a 0.57 g/L of crude biosurfactant was obtained. When compared to others, the present organism gave higher biosurfactant yield than *P. anomala* PY1 which gave 0.06-0.2 g/L yield, comparable to *Rhodotorula bogoriensis* with 0.5-1.0 g/L yield and lower than that of *Candida bombicola*. [5, 10]. The obtained biosurfactant possessed a HLB value of 10-13, the value of which enable it to form an oil-in-water emulsion.

4. Conclusions

A newly optimized medium is presented, when *P. anomala* PY189 grown in this medium gave 0.56 g/L of crude biosurfactant was obtained. The surface tension and the oil displacement of the culture broth were found to be 41.44 mN/m and 6.32 cm^2, respectively and exhibited HLB value of 10-13. This characteristic of oil-in-water emulsion may render its use as film for sausage wrapping.

References

[1] G. L. Miller *Analytical Chemistry* **31** (1959) 426-428.
[2] M. Morikawa, H. Daido, T. Takao, S. Murata, Y. Shimonishi and T. Imanaka *Journal of Bacteriology* **175** (1993) 6459-6466.
[3] M. Deleu and M. Paquot *Comptes Rendus Chimie* **7** (2004) 641-646.
[4] R. R. Fonseca, A. J. R. Silva, F. P. De França, V. L. Cardoso and E. F. C. Sérvulo *Applied Biochemistry and Biotechnology* **471** (2007) 136-140.
[5] J. Thaniyavarn, T. Chianguthai, P. Singvanich, N. Roongsawang, K. Washio, M. Morikawa and S. Thaniyavarn *Bioscience Biotechnology and Biochemistry* **72** (9) (2008) 2061-2068.
[6] K. Muthusamy, S. Gopalakrishnan, T. K. Ravi and P. Sivachidambaram *Current Science* **94** (6) (2008) 736-747.
[7] O. Pornsunthorntawee, P. Wongpanit, S. Chavadej, M. Abe and R. Rujiravanit *Bioresource Technology* **99** (2008) 1589-1595.
[8] Y. B. Kim, H. S. Yun and E. K. Kim *Bioresource Technology* **100** (2009) 6028-6032.
[9] E. Gharaei-Fathabad *American Journal of Drug Discovery and Development* **1** (1) (2011) 58-69.
[10] I. N. A. Van Bogaert, J. Zhang and W. Soetaert *Process Biochemistry* **46** (2011) 821–833.
[11] G. M. Walker *Antonie van Leeuwenhoek* **99** (2011) 25-34.

EFFECTS OF O_2 DURING VARIOUS PROCESSING STEPS ON FREE RADICAL CONCENTRATIONS IN HOT AQUEOUS EXTRACTS OF ROAST & GROUND COFFEE AND THEIR CHANGES DURING STORAGE

Chahan Yeretzian[1], Ederlinda C. Pascual[2] and Bernard A. Goodman[3*]

[1] Zurich University of Applied Sciences, Institute of Chemistry and Biological Chemistry, Einsiedlerstrasse 31, CH-8820 Wädenswil, Switzerland

[2] Scottish Crop Research Institute, Invergowrie, Dundee, DD2 5DA, United Kingdom

[3]State Key Laboratory for Conservation and Utilization of Subtropical Agro-Bioresources, Guangxi University, Nanning, 530004 Guangxi, Peoples' Republic of China

[*] Author for correspondence; E-Mail: bernard_a_goodman@yahoo.com Tel. +86 771 3234439

Abstract: As part of the development of a strategy for improving the shelf-life of liquid coffee concentrates, we report variations in concentrations of free radicals and paramagnetic metal ions in aqueous extracts of roast and ground (R&G) coffee as a function of the presence of O_2 during the cooling/grinding, extraction, and retorting/processing stages. Free radical concentrations in all samples decreased on storage for one month, in contrast to previous observations with extracts of whole roasted coffee beans where increases were observed. This decrease was in the range 10-50%, the smallest changes being observed for samples that had been extracted with deoxygenated water. The oxygen content of the water used in the extraction also had an appreciable effect on the intensity of the paramagnetic Fe(III) signal, although this was unaffected by the atmosphere during retorting.

1. Introduction

The development of the ready-to-drink and concentrates segments of the coffee business is hampered by problems of flavor and physical stability. These result in unacceptably short shelf-lives for the beverage, and have thus presented a major obstacle in the development of liquid coffee products. The changes which limit the shelf-life of liquid coffee extracts are (i) loss of flavor intensity and quality, (ii) an increase in perceived acidity, and (iii) the formation of sediments. In whitened liquid coffee products, flocculation may be an additional issue. Although several processes, such as the presence of O_2, or chemical reactions of macromolecular compounds in the extracts, can be considered to contribute to coffee instability, liquid coffee seems to be intrinsically unstable, even in the absence of O_2 or light. Hence, a liquid coffee extract, especially in a concentrated form, may require specific physical or chemical interventions, and/or specialised extraction procedures, in order to optimise its shelf life at ambient temperature. Possible strategies are (i) addition of antioxidants or O_2-scavenging agents to limit oxidative damage, (ii) separation of the extract into different molecular size fractions that are individually stable, or (iii) immobilisation of reactive species on functionalised surfaces. Currently, stability problems are addressed by the addition of buffers, stabilisers, antioxidants and commercial flavours, but there is a definite consumer interest in the availability of high quality products without additives (clean label). Furthermore, retailers, under pressure to reduce the costs of logistics and warehousing, and to limit the complexity of distribution channels, seek products that are stable at ambient temperatures with shelf-lives of several months.

Oxidation processes are widely believed to be responsible for changes that occur during storage of roasted coffee beans and their aqueous extracts; one property of such reactions is that they involve free radicals. Molecular species containing unpaired electrons, such as free radicals and paramagnetic transition metal ions and complexes, can be investigated by the technique of electron paramagnetic resonance (EPR) spectroscopy, which determines the energies of transitions between electron spin states. This, in principle quantitative, technique is specific for molecules with unpaired electrons and it is able to determine their presence and often their chemical identities with great sensitivity. In addition to identifying the presence of free radicals in roasted coffee beans (e.g. [1-3]), EPR spectroscopy has also been used to investigate free radical dynamics, including their generation during roasting [4], changes during storage under various conditions [5-7], and in solutions of soluble coffee [8]. In the last of these papers, signals from the paramagnetic ions Mn(II) and Fe(III) were also characterised in fluid and frozen solutions, respectively.

We have recently investigated changes in the free radical EPR signals during the storage of aqueous extracts of whole roasted beans [9]. As with our previous measurements on roasted whole and ground coffee beans [7], the free radical concentrations of the samples increased during storage. With the solid samples, the rate of free radical increase was much greater with half beans and ground samples than with intact beans, and in the whole bean extracts the free radical increase during storage under N_2 was related to the O_2 content of the extracting water and the temperature of storage. In both sets of experiments, it was concluded that exposure to O_2 was the main factor governing these free radical increases. Thus these former works demonstrated that the free radical signal, analysed via EPR spectroscopy, is a very sensitive and precise probe for oxidative processes in coffee.

In the present paper we have built on the work of Pascual et al [9], and designed experiments to investigate the effects of O_2 during various processing steps on the changes in free radical concentrations of the resulting liquid coffee extracts during storage. We have specifically considered the effect of O_2 during the cooling (at the end of roasting) and grinding, extraction, and retorting stages. EPR measurements were then performed to determine variations in the intensities of the free radical, Mn(II) and Fe(III) signals in this series of samples, and a discussion is presented of their implications for understanding the processes that are important in the degradation of liquid coffee concentrates.

2. Materials and Methods

2.1 Samples

Samples were prepared from a blend of Arabica and Robusta beans made from a total of 6 varieties, and roasted under air to a medium roast level. The parameter that was varied was the atmosphere, either N_2 or air, under which the subsequent processing steps were conducted. These were:

(i) Cooling/grinding: These two processing steps were combined, such that coffee cooled under N_2 was always ground under N_2, whilst coffee cooled under air was ground under air.

(ii) Extraction: Extraction of the ground roasted coffee beans was performed either under air without de-oxygenating the water or under N_2 in de-oxygenated water. In both cases extraction was performed in a closed vessel using water at 110 °C for 5 minutes.

(*iii) Retorting/storage:* The extracted coffee samples were retorted for 6 minutes at 121 °C in closed glass bottles with either air or N_2 in the headspace.

Thus a total of eight samples were produced, and their details are summarised in Table 1. After retorting, the samples were immediately frozen to -40 °C and stored at that temperature until being transferred to a refrigerator at 4 °C 1 day before commencing the EPR measurements. Finally, EPR spectra of the samples were recorded in triplicate at the beginning and end of one month storage at laboratory temperature (~21 °C).

Table 1: Schematic description of the experimental plan showing the atmosphere during three processing stages along with the total solid content of the eight concentrated liquid coffee samples.

Cooling/ grinding	**Extraction**	**Retorting/ storage**	Tc(%)[1]
Air	Air	Air	7.12
Air	Air	N_2	7.12
Air	N_2	Air	7.27
Air	N_2	N_2	7.27
N_2	Air	Air	7.26
N_2	Air	N_2	7.26
N_2	N_2	Air	7.29
N_2	N_2	N_2	7.29

[1] Concentrations of the samples (**T**otal solid **c**ontent) based on % weight.

2.2 EPR spectroscopy

EPR measurements were made at both room temperature and 77K at X-band frequencies (~9.5 GHz) using a Bruker ESP300E computer-controlled spectrometer incorporating an ER4103TM cylindrical microwave cavity. Fluid solution measurements were made in a quartz flat cell, whereas the low temperature measurements used 3 mm i.d. quartz tubes, which were immersed in liquid nitrogen in a quartz "finger dewar" in the microwave cavity. It was necessary to use low temperature measurements to observe the Fe(III) signal, the relaxation properties for which are such that low temperatures are required for its observation.

All spectra were acquired in 1024 data points using a modulation frequency of 100 kHz. Sweep widths of 5, 200 and 500 mT were used to optimize the spectra of the free radical, Mn(II) and Fe(III) components, respectively. Microwave powers of 1, 5 and 10 mW were used for measurement of the signals from the free radical at room temperature, Mn(II) at room temperature, and Fe(III) at 77K, respectively. The modulation amplitude for Mn(II) and Fe(III) measurements was set to 1 mT (10 gauss = 1 mT), that for free radical measurements was 0.5 mT. Other parameters such as receiver gain were adjusted as necessary to obtain good signal-to-noise ratios. As is conventional in EPR spectroscopy, all spectra were recorded as 1st derivatives of the microwave absorption and displayed as functions of absorption versus magnetic field at a constant microwave frequency.

2.3 Analysis of EPR data

Because all samples contained the same sets of signals, the peak-to-peak distances between inflection points of the 1st derivative spectra were used to measure the EPR absorption intensities; these are proportional to the concentrations of the individual EPR components, but cannot be used to determine the concentrations of different components. This approach was preferred to the double integration method for determination of absorption areas, because of difficulties in separating the individual contributions from overlapping components with greatly different line widths. In addition, there are considerable difficulties in calculating accurately the absolute concentrations of paramagnetic components in EPR spectra, especially when working with aqueous solutions. However, relative concentrations of components can be measured with much higher accuracy provided the spectra for each component are recorded under non-saturating conditions. Since there

was little, if any, significant change in the Mn(II) EPR signal in coffee extracts as a result of processing conditions (E.C. Pascual, unpublished results), the present paper reports the ratios of the intensities of the free radical and Fe(III) signals to that of the Mn(II) signal.

3. Results and Discussion

The ratios of the free radical : Mn(II) EPR signal intensities at Day1 and after one month of storage at room temperature are shown in Figure 1; similar results (not shown) were obtained from spectra recorded at 77K. In the fresh samples, the free radical signal intensity was around 25% higher in the samples extracted from beans that had been cooled and ground under N_2 than for the equivalent samples from beans cooled and ground under air. In the latter samples, there was little effect of the atmosphere during either extraction or retorting. However, with the former set of samples, the free radical signal intensities were higher when the extraction was performed under N_2 than for the corresponding samples extracted under air, whereas the retorting atmosphere produced the opposite trend.

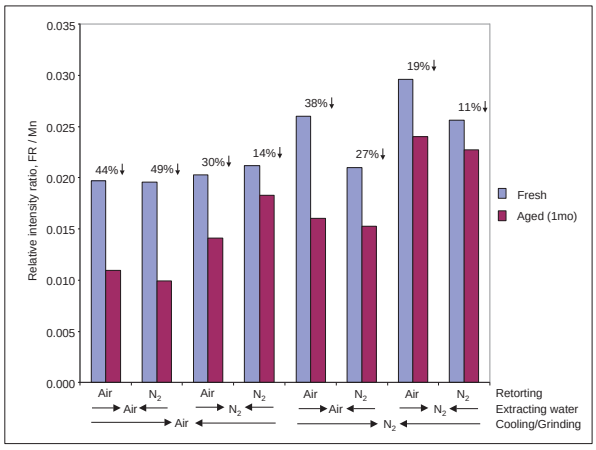

Figure 1: Relative intensity ratios (free radical : manganese) in the EPR spectra of concentrated coffee extracts at room temperature at Day1 (fresh) and after aging in air for 1 month.

For every sample, the free radical signal intensity decreased during storage, which is in contrast to the observation with extracts of whole roasted coffee beans [9], where the free radical signal intensity increased. There were, however, appreciable differences in the relative magnitudes of this decrease for different samples. The most important parameter influencing these changes was the composition of the extraction water; for samples with equivalent cooling/grinding and retorting conditions, the reductions corresponding to the presence or absence of O_2 in the extraction water were 44%-30%, 49%-14%, 38%-19%, and 27%-11%. The atmosphere used for retorting was less important, but not insignificant, and the smallest changes were observed for those samples in which both extraction and retorting were performed in the absence of O_2. Also, except for the samples that were cooled/ground and extracted under air, there was a smaller percentage decrease in the free radical signal intensity during storage for the samples retorted under N_2 than with the corresponding samples retorted under air.

The intensities of the Fe(III) (g = 4.3) signal for the various samples on Day 1 are shown in Figure 2; there were no significant changes during storage, a result which is similar to that observed for the same signal in extracts of whole roasted coffee beans during storage [9]. The presence or absence of O_2 during the extraction process was the largest single factor which affected the Fe(III) (g = 4.3) signal intensity. Furthermore, the samples with the largest Fe(III) (g = 4.3) signal exhibited the largest percentage changes in the free radical signal on storage. Also, although there were no significant differences in the Fe(III) (g = 4.3) signal intensity as a result of the atmosphere used for cooling/grinding when extractions were performed in air, there was an effect when the extraction was performed under N_2; the lowest signal intensity was seen when both the cooling/grinding and extraction operations were performed in the absence of O_2. The atmosphere used during the retorting process had no significant effect on the Fe(III) (g = 4.3) signal in any of the sets of samples.

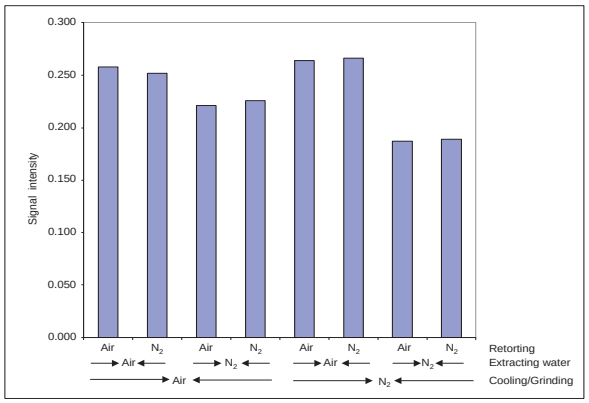

Figure 2: Fe(III)(g = 4.3) signal intensities in the EPR spectra at 77K of concentrated coffee extracts at room temperature on Day1.

The relationship between the intensity of the Fe(III) (g = 4.3) signal and the percentage change in the intensity of the free radical signal during subsequent storage suggests that the iron speciation could be relevant to the free radical reactions that occur during storage of the beverage. If this is the case, then it seems possible that the mononuclear Fe(III) complexes which produce this signal could have a direct influence on the subsequent keeping properties of the product. Since antioxidants (such as chlorogenic acids) and H_2O_2 are normal components of coffee, Fenton reaction chemistry (to produce hydroxyl radicals) should occur if these Fe complexes can be redox cycled; this hypothesis will be tested in future experiments. However, if the relationship between the

mononuclear complexes in the coffee brew and subsequent free radical reactions during storage can be established, then it might eventually be possible to develop a simple EPR assay that can be used at the time of preparation to provide an accurate shelf life prediction for individual coffee extracts.

4. Conclusions

The aim of the study was to determine whether EPR spectroscopy could function as a simple probe that would provide information on the stability during ambient temperature storage of aqueous coffee concentrates. The results show the extent to which the free radical and Fe(III) spectra change as a result of various processing steps of coffee preparation (cooling/grinding, extraction, retorting) and on the storage of the concentrated extract. The presence or absence of O_2 in the water used for extraction of the roast and ground coffee beans was the most important parameter for determining both the intensity of the Fe(III) (g = 4.3) EPR signal and the stability of the free radical EPR signal during storage. The presence of O_2 during the cooling/grinding step also had a significant effect, whereas the atmosphere used for the retorting process had the lowest effect of the three processes investigated. The intensity of the Fe(III) (g = 4.3) EPR signal and the percentage change in the free radical EPR signal during storage were directly related, and this observation could form the basis for the development of an assay for early prediction of shelf-life.

Acknowledgements

The Scottish Office Agriculture Environment and Fisheries Department (SOAEFD) (now Agriculture Environment and Fisheries Department Scottish Executive) is acknowledged for the provision of the EPR facilities.

References

[1] J.P. O'Meara, F.K. Truby and T.M. Shaw. *Food Res.* **22** (1957) 96-101.
[2] G.J. Troup, J.R. Pilbrow, D.R. Hutton, C.R. Hunter and G.L. Wilson. *Int. J. Radiat. Appl. Instr. A. Appl.Radiat. Isotop.* **40** (1989) 1223-1226.
[3] P.P. Levêque, Q. Godechal and B. Gallez, *Israel J. Chem.* **48** (2008) 19-26.
[4] B.A. Goodman, E.C. Pascual and C. Yeretzian *Food Chem.* **125** (2011) 248-254.
[5] M.L. Baesso, E.C. Da Silva, H. Vargas, J.G. Cortez, J. Pelzl. *Z. Lebesm. Unters. Forsch.* **191** (1990) 24-27.
[6] E. Nebesny and G. Budryn. *Deutsche Lebensm. Rundsch.* **102** (2006) 526-530.
[7] C. Yeretzian, E. C. Pascual and B. A. Goodman *Food Chemistry* **131** (2012) 811-816.
[8] E.C. Pascual, B.A. Goodman and C. Yeretzian *J. Agric. Food Chem.* **50** (2002) 6114-6122.
[9] E.C. Pascual, C. Yeretzian and B.A. Goodman (2013). *J. Agric. Food Chem.* under review.

GROWTHS, ANTIBACTERIAL AND ANTIFUNGAL ACTIVITIES OF KEFIR GROWN IN DIFFERENT CULTURE MEDIA

Sathika Jariyatamkitti, Somrutai Kitchalao, Pattarawan Wuttisan, Rachnarin Nitisoravut*, Issara Poljungreedand and Siwarutt Boonyarattanakalin

School of Bio-Chemical Engineering and Technology (BCET), Sirindhorn International Institute of Technology, Thammasat University, Rangsit, Pathum Thani, 12121, Thailand

* Author for correspondence; E-Mail: snitisor@siit.tu.ac.th, Tel. +66 29869009 ext. 2304

Abstract: The purposes of this study were to observe kefir culture in different culture media such as milk, coconut milk and coconut water (coconut juice), and determine the antibacterial and antifungal activities of the three kefir types including coconut milk-kefir, coconut water-kefir and cow milk-kefir. All kefir types were cultured in different media at room temperature. Growth of all three kefir cultures was recorded daily, and the data obtained showed that milk-kefir grew at an exponential rate, while the growths of coconut milk-kefir and coconut water-kefir were observed to be fluctuated. Disc diffusion method was used to test antibacterial and antifungal activities of all three kefir types, in comparison with antibacterial reagents as positive controls against certain microorganisms. All kefirs show significant antibiotic activities. Coconut milk kefir and coconut water kefir showed higher activities against microorganisms than milk kefir. The preliminary antibiotic activity of the kefir cultures scientifically reinstates the important benefit, from the consumption of fermented kefir culture, of suppressing the growth of other pathogenic bacteria.

1. Introduction

Kefir is a milk-based beverage that is normally made by fermenting milk with kefir grains and kefir culture. It is a natural probiotic which is rich in both enzymes and beneficial live bacteria. Kefir has long been popularly used as live microbial food supplement. It improves the microbial balance of the host animals. Kefir grains are normally used in the fermenting of dairy product. Kefir is made in the culture which is known as grains which are prepared in goat hide bag filling with pasteurized milk inoculated with sheep intestinal flora. Kefir grains usually compose of lactic acid bacteria, yeasts and polysaccharides. They are known as kefir starters or kefir cultures. They are white cauliflowers shaped like. An examination of kefir under a microscope shows many bacteria and yeasts containing inside the grains that are health beneficial.

Kefir grains are small clusters of microorganisms held together by a polysaccharide matrix (kefiran), they are soft and white biological mass which consist of proteins, lipids and soluble-polysaccharides. The yeast and bacteria species in kefir were found to be different under different conditions for culturing such as cultivating media, temperature or cultivation time. The survived species must fit to the nutrient source and be able to utilize biological products generated by other survive species as an energy source. This is a result of a symbiotic relationship between bacteria and yeasts in kefir.

Kefir provides several biological activities that are health benefits to human body such as antimicrobial, antifungal, antitumor, antimutagenic and antioxidant, anti-inflammatory, and reduce cholesterol and blood pressure. Nowadays, kefir is often used in daily diet food. This is because it is easily digested. It can also clean the intestines and provides beneficial bacteria and yeasts, proteins, vitamins and minerals. If kefir is consumed regularly, it can relieve intestinal disorders, promotes bowel movement and maintain a healthy digest system [1-5].

Normally, sources of kefir supplement or culture media are milk and sugar. However, the symbiotic relationship in kefir may allow flexible carbon sources. We are interested in whether the milk kefir may be cultured in media other than milk and more importantly whether kefirs cultured in these alternative media still possess important health benefits.

Thailand is located in tropical region where coconut trees are grown abundantly throughout the country. The readily available products from coconut tree - coconut milk and coconut water (coconut juice) which are rich in carbon source and proteins [10-11] may constitute essential media for the kefir cultivation. Thus, the main focus of this research is to investigate the growth of kefir culture in coconut milk and coconut water. The important benefits of antibacterial property were also examined by using the disc diffusion method. Isolation and cultivation method were used to identify the types of bacteria and yeasts in kefir grains which are a prerequisite for any in depth study of kefir functional properties and other characteristics [3].

2. Materials and Methods

2.1 Kefir grains

Kefir grains from the central part of Thailand were grown in laboratory at Sirindhorn International Institute of Technology, Thailand. They were cultured in three different media which are cow milk, coconut milk and coconut water at room temperature. The culturing media were changed daily to maximize growth of kefir grains.

2.2 Isolation and cultivation of lactic acid bacteria, acetic acid bacteria and yeast from kefir grains and kefir products

Kefir grains were obtained from the cultures after 24 h fermentation. Ten grams of each kefir grains were suspended in 90 g of phosphate buffer and homogenized with a mortar. Serial dilutions of the suspended samples were used for microbial enumerations and isolation by MRS agar, DECA agar and YM agar. The plates were incubated at 35 ºC for 24 h and the resulted colonies from different cultures kefir were counted and observed by microscope.

2.3 Antibacterial and antifungal testing

Escherichia coli, *Staphylococcus aureus*, *Salmonella typhi*, *Candida albican*, and *Bacillus subtilis* were used as the test microorganisms. Their isolated colonies were selected and transferred into a test tube containing 8 mL of nutrient broth medium before being incubated at 35 ºC for 24 h. The turbidity was adjusted compared to the 0.5 McFarland standards. The absorbance at 625 nm was from 0.08 to 0.1 ($1.5x10^8$ cells mL^{-1}).

The antibacterial and antifungal activities of kefir grown in different cultures were evaluated using the disk diffusion method described by Indian Association of Medical Microbiologists [6]. Antibiotics- ampicillin V, penicillin, chloramphenicol and flucozole were used to compare antibacterial and antifungal activities. Watchman filter paper disks with 5 mm in diameter soaked with fermented solutions and antibiotic agents were applied to agar surface previously inoculated with bacterial and fungal suspensions and then incubated at 35 ºC for 24 h. The diameter of clear zones of completed inhibition was measured. Experiments were performed in duplicates and mean values were reported [3, 6-8].

3. Results and Discussion

3.1 Growth rate of kefir grown in three different cultures

Kefir grown in different cultures demonstrated different growth patterns as seen in Figure 1. For kefir grown in milk, it took almost 3 days before the grains started their exponential growth. However, for kefir grown in coconut milk and coconut water, the growth rates were relatively slower and fluctuated. The growth rate of coconut water kefir was more stable as compared to coconut milk kefir after 2 weeks. It is generally known that the growth rate of kefir depend upon the availability of macro nutrients in media particularly carbon and nitrogen sources. Higher amount of nutrients in cultivating mediums led to the faster growth rate of kefir. Due to the highest amount of sugar level in cow milk which is 4.7g/100g, kefir grew faster in milk in comparison to coconut milk and coconut water of which their sugar levels are 2.8g/100g and 2.61g/100g, respectively [9, 10]. Since coconut milk and coconut water had almost same composition of sugar, growth rate of kefir grown in these media showed similar pattern with the similar rate [11].

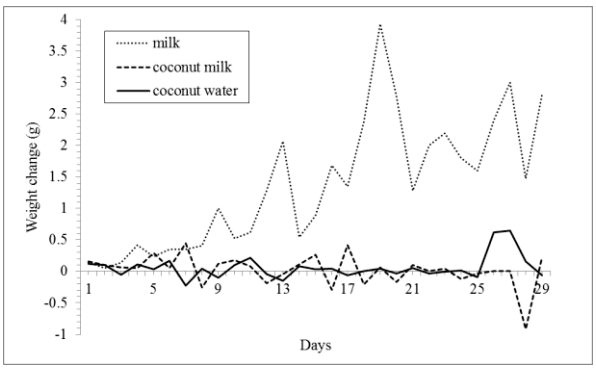

Figure 1: Growth data for kefir grains grown in three different culturre media (50 mL) at 25ºC. Kefir grains were initiated at 0.5 g and weight changes of grains were obtained daily.

3.2 Lactic acid bacteria, acetic acid bacteria and yeast isolation

In order to find out 3 main types of microorganisms in milk, coconut milk and coconut water kefir products and grains, 3 different selective media which are MRS, GECA and YM were used for isolation and observation of number of colonies in milk, coconut milk and coconut water kefir products and grains. Results indicated that the selectivity of the media used to isolate lactic acid, acetic acid bacteria and yeast was found to be non-specific. Bacillus grew on all three media (Table 1), whereas yeast can only be isolated by MRS agar.

Table 1 shows microscopic examination of colonies after culturing in three selective media. There were three morphologies found on each selective plate which were bacillus, coccus, and yeast. For bacteria presence, only milk kefir showed both bacillus and coccus while others showed only bacillus and there was no yeast presented in MRS agar. The results showed that bacillus was presented in all kind of kefir products.

There is a need of development for microorganism profiles of coconut milk and coconut water kefir products and grains using advanced identification techniques such as Denaturing Gradient Gel Electrophoresis (DGGE). A preliminary results found in this study suggests that kefir grown in coconut milk and coconut water may contain different types of bacteria and yeasts compared to milk kefir.

Table 1**: Microscopic examinations of kefir and kefir grains in three different culturing media

Selective plates	GECA			MRS			YM		
Shape of microorganisms	**Bacillus**	**Coccus**	**Yeast**	**Bacillus**	**Coccus**	**Yeast**	**Bacillus**	**Coccus**	**Yeast**
Milk kefir	+	+	-	+	+	-	+	+	-
Milk kefir grain	+	+	+	+	-	-	+	-	+
Coconut milk kefir	+	-	+	+	-	-	+	-	+
Coconut milk kefir grain	+	-	+	+	-	-	+	-	+
Coconut water kefir	+	-	+	+	-	-	+	-	+
Coconut water kefir grain	+	-	+	+	-	-	+	-	+

** + indicate the presence of the microbial where – indicates the absence of the microbials.

3.3 Antibacterial and antifungal testing

Inhibitions of kefir grown in three different cultures against the pathogenic strains were determined using the disk diffusion method. Table 2 shows inhibition zone diameters by kefir grown in milk, coconut milk and coconut water and the antimicrobial agents at 24 h. The results showed the different level of growth inhibitions by kefir cultures in all pathogens. For fungi, only milk kefir can inhibit the growth of fungi strains which was equal to 11 mm in diameter.

The non-fermented media which are milk, coconut milk and coconut water were also subjected to the antibiotic activity testing side by side with the fermented kefir cultures, none of the non-fermented media show inhibition zone (data not shown). These results indicated that the kefirs cultured in alternative media including coconut milk and coconut water have the kefir unique property of antibacterial.

In another experiment, to be sure that this antibiotic activity do not arise from the low pH of the cultures, the pH of non-fermented media were adjusted to be the same level as the fermented media and subjected to the disk diffusion method. The results show no inhibition zone (data not shown). This experiment suggests that the antibacterial properties of the fermented kefir culture may not arise from their low pH.

Although antimicrobial activity by several isolated strains from milk kefir had been reported, antimicrobial activity by coconut milk and coconut water kefir had not been previously described. This work had shown antimicrobial activity by kefir fermented coconut milk and coconut water kefir.

Milk kefir was able to inhibit the growth of the four bacteria, namely, *E. coli*, *S. typhi*, *S. aureus*, and *B. subtilis* and the fungus - *C. albican*, while coconut milk and coconut water were able to inhibit only the growth of the four bacteria. Both coconut milk and coconut water kefir were capable of inhibiting Gram-positive and Gram–negative bacterial strains with the mean values diameter of inhibition zone of 13.0 and 11.6 mm, respectively. When compared with the positive controls used, kefir grown in all cultures had lower inhibition activities than typical antibiotic drugs.

There is a need for details investigation on the mechanisms of antibacterial activity exerted kefir fermented milk, coconut milk and coconut water for further utilizations of these kefir cultures. The data presented in this work suggest that kefir grown media other than milk have their antibacterial activities.

Table 2***: Antibacterial and antifungal activities using disk diffusion method* of 24 h kefir fermentation in various culturing media.

Strain	Antibiotic Agents				Kefir Products		
	Flucozole	**Ampicillin**	**Chloramphenicol**	**Penicillin**	**Milk**	**Coconut milk**	**Coconut water**
E. coli	0.0±0.0	15.5±4.9	25.0±4.2	0.0±0.0	8.9±0.1	11.5±0.7	11.0±1.4
S. typhi	0.0±0.0	27.0±0.0	35.5±2.1	8.5±0.7	11.5±3.5	15.5±3.5	11.0±2.8
S. aureus	8.0±1.4	29.5±2.1	25.5±0.7	33.5±0.7	12.5±2.1	12.0±0.0	10.0±0.0
B. subtilis	10.5±3.5	51.5±2.1	34.5±4.9	53.5±4.9	11.5±0.7	13.0±0.0	14.5±0.7
C. albican	18.5±2.1	0.0±0.0	20.5±2.1	0.0±0.0	11.0±1.4	0.0±0.0	0.0±0.0

*** The results represent the mean of clear zone diameters (in mm). The non fermented media (milk, coconut milk and coconut water) show no inhibition zone (data not shown).

4. Conclusions

This study demonstrated that kefir can grow not only in milk, but also in coconut water and coconut milk. Nevertheless, the growth rates are slower for coconut water and coconut milk. This may be due to the facts that milk contains more macronutrients required for growth than coconut water and coconut milk. The microbial species, presence in the kefir cultured in coconut water and coconut milk, were observed during the isolation of lactic acid, acetic acid bacteria and yeast were found to be bacillus, coccus, and yeast. The selectivity of the selective media was non-specific to types of bacteria and yeast. Bacillus and yeast were found in all kefir fermented products, but coccus presented only in milk kefir. Using disk diffusion method for antibacterial and antifungal tests, the antibiotic activity of all kefirs cultured in cow milk, coconut milk and coconut water against *E. coli*, *S. typhi*, *S. aureus*, and *B. subtilis* were observed. Only kefir culture in cow milk was able to inhibit the growth of the fungus - *C. albican*. The antibiotic activity of the kefir cultures scientifically highlights the important benefit of probiotic from the consumption of fermented kefir culture.

As coconut milk and coconut water were proved to be used as the alternative to milk as culture media and possessed antibacterial activity, knowing these results would lead to more detailed study of the identification of bacteria and yeast in different media. This may be useful in order to develop kefir fermented products as parts of antibiotic drugs against bacteria and fungus.

Acknowledgements

This research was financially supported Sirindhorn International Institute of Technology, Thailand as a part of senior project for the degree of Bachelor of Engineering in Bio-Chemical Engineering and Technology.

References

[1] Semih Otes , a. O. C., *Pakistan Journal of Nutrition*, (2003) **2**, 54.

[2] Fernando Lopitz-Otsoa, A. R., Natalia Elguezabal and Javier Garaizar, *Rev Lbaroam Micol*, (2006) **23**, 67.

[3] Hsi-Chia Chen, S.-Y. W., Ming-Ju Chen, *Food Microbiology*, (2008) **25**, 492.

[4] Zhou Jianzhonga, L. X., Jiang Hanhub, Dong Mingshengb, *Food Microbiology*, (2009) **26**, 770.

[5] Chujian Chen, McGill University Montreal, (2005), p 222.

[6] Prof.Dr.Lalitha Kameswaran, Manual on Antimicrobial Susceptibility Testing, In (2004).

[7] Mueller, J. H.; Hinton, J., A protein-free medium for primary isolation of the gonococcus and meningococcus, In *Proceedings of the Society for Experimental Biology and Medicine. Society for Experimental Biology and Medicine (New York, NY)*, Royal Society of Medicine: (1941); Vol. 48, pp 330.

[8] Kamila Leite Rodrigues, L. R. G. C., Jose Carlos Tavares Carvalho, Joao Evangelista and Jose Mauricil Schneedorf, *International Journal of Antimicrobial Agents*, (2005) **25**, 404.

[9] Michel Andre Wattiaux, Milk Composition and Nutritional Value, In *Dairy Essentials - Lactation and Milking*.

[10] Muhammad Majeed, P. D., Lakshmi Prakash, Ph.D., Cococin^{TM}: The Nourishment Factor^{TM} Freeze-Dried Coconut Water Solids, In (2007).

[11] Fineli, The Fineli Food Composition Database: Coconut milk, In (2011).

Industrial Chemistry and Innovation

VARIABILITY ASSESSMENT OF *PONGAMIA PINNATA* OIL FROM VARIOUS SOURCES IN SOUTHERN REGION OF THAILAND FOR BIODIESEL QUALITY

Chutarat Khamchum[1], Rayakorn Nokkaew[2] , Vittaya Punsuvon[1,2,3]*

[1] Department of Chemistry, Faculty of Science, Kasetsart University, Chatuchak, Bangkok,10900 Thailand
[2] Center of Excellence-Oil Palm, Kasetsart University, Chatuchak, Bangkok, 10900 Thailand
[3] Center for advanced Studied in Tropical Natural Resource, NRU-KU, Kasetsart University, Chatuchak, Bangkok, 10900 Thailand

* Author for correspondence; E-Mail: fscivit@ku.ac.th, Tel. +66 5625555 Ext.2120, Fax. +66 56 25555 Ext.2119

Abstract: The present study was undertaken to assess the existence of variability for some of the important biodiesel quality as a prelude in selection of more efficient biodiesel yield. With this objective the survey, collection and characterization of *Pongamia pinnata* which was the native plant grown in the Southern part of Thailand had been undertaken to assess the variability existing for various economically important parameters for development as a profitable crop for biodiesel production in the future of Thailand. The variability of oil content was observed in 45 tree accessions of *Pongmia pinnata* collected from three provinces in the Southern region of Thailand. Out of these, fatty acid profiles of 20 accessions with varying seed oil content were examined. Large variation in fatty acid content (%wt) were observed in stearic (C_{18}), oleic ($C_{18:1}$) and linoleic ($C_{18:2}$) acid with the value 3.88-13.84% (wt), 37.15-47.42% (wt) and 16.61-22.23% (wt), respectively. While less variation in fatty acid content (%wt) with the value 12.82-17.63% (wt), 0.00-5.88% (wt) and 6.30-12.87% (wt) were found with palmitic (C_{16}), linolenic ($C_{18:3}$) and behenic (C_{20}) acid. Saponification number (SN), Iodine value (IV) and Cetane number (CN) of fatty acid methyl esters or biodiesel of oils varied from 196.81-207.69, 61.66-90.07 and 52.72-59.41, respectively. Fatty acid composition, IV and CN are used to predict the quality of fatty acid methyl esters of oil for using as biodiesel fuel. Fatty acid methyl esters of oil of *Pongamia pinnata* accessions RB3, RS11, RS15 (from Rayong), PK2 (from Phungnga) and KB1 (from Krabi) were found most suitable (CN more than 52.72) oil for using as biodiesel and they met the major specification of commercial biodiesel standard.

1. Introduction

Biodiesel is renewable, non-toxic, environmental friendly and biological origin alternative fuel for diesel engines. Many studies have shown that the fuel properties of biodiesel are very close to diesel fuel. Biodiesel has many advantages compared to diesel fuel and it plays an important role in meeting future fuel requirements. It has higher cetane number than diesel fuel, and contains no aromatics, almost no sulfur, and 10-12% oxygen by weight. Biodiesel fuelled engines produces less CO, HC, and particulate emissions than petroleum diesel fuelled engines [1]. The first generation biodiesel which was usually produced from the edible oils such as palm, soybean, and rapeseed oils would be more expensive compared to petroleum diesel. In addition, the use of edible oils for biodiesel production may be contrary to current social movement and energy policies. Non-edible vegetable oils, which were mostly produced by seed-bearing trees and shrubs, could be an alternative oil source. Non-edible oil crops, which can be grown on a large scale on non-cropped marginal lands and wastelands, are considered to be the best feed stock for biodiesel that does not affect the edible-oil market. Thus the availability and sustainability of non-edible feed stocks will be the crucial determinations in the popularization of biodiesel.

Pongamia pinnata belongs to the family Leguminaceae. It is a medium sized glabrous tree that generally attains a height of about 18 m and a trunk diameter>50 cm. It can grow under a wide range of agroclimatic condition and it is a common sight around coastal areas, riverbanks, tidal forests and roadsides. It can grow on soil types ranging from stony to sandy to clay, including verticals. It is highly tolerant of salinity and can be propagated either by seeds or by root suckers [2].

After 5-7 years of growth, it bears fruits containing one to two kidney-shaped brownish-red kernels [3]: *Pongamia pinnata* oil is eco-friendly, biodegradable and has been identified as one of the best alternatives to petrochemical [4]. The seed kernels containing 27-40% oil contain mainly oleic acid ($C_{18:1}$; 44.5-71.3%) and linoleic acid ($C_{18:2}$; 10.8-18.3%) along with minor quantity of palmitic acid ($C_{16:0}$; 3.7-7.8%), stearic acid ($C_{18:0}$; 5.5-6.0%) [5]. *Pongamia pinnata* oil consists of karanjin, Karanjone, diketone pongamol [6]. Karanjin is a four angular furanoflavone present in the seeds which is used in several industries inclusing medicine [7]. Freshly extracted oil is yellowish orange to brown in color having a disagreeable odor and a bitter taste. The presence of toxic karanjin make *Pongamia pinnata* oil as inedible oil [8].

Pongamia pinnata oil is regarded as a potential fuel substitute that it contains 16-22 carbon atoms per molecule. Attempts have been made for the conversion of *Pongamia pinnata* oil to methyl esters by Meher et. al[2], Naik et. al. [4]. With the growing interest in the seed oil of *Pongamia pinnata*, the need for raising of plantation has been realized. In this context, the present study was undertaken to assess the existence of variability for some of the important biodiesel quality as a prelude in selection of more efficient biodiesel

yield. With this objective, the survey, collection and characterization of *Pongamia pinnata* that is the native plant in the Southern part of Thailand has been undertaken to assess the variability existing for various economically important parameters for development as a profitable crop for biodiesel production in the near future of Thailand.

2. Materials and Methods

Exploration trips were conducted during the months of January to May, 2011 to various districts of Ranong, Phungnga, Krabi provinces and 45 accessions were collected. Representative samples consisting of 2-3 kg pods covering all sides of the selected tree were collected. Pods were stored at room temperature. For seed oil content and fatty acid composition analysis, one kg pod was randomly picked from this lot, threshed and the final sample was randomly drawn from this material. Seed oil content was determined by soxhlet extraction with hexane for 45 accessions. The accessions code RB and RS represented the samples from Rayong province. The code PK and KB represented the sample from Phungnga and Krabi provinces. Among these, 20 accessions covering all the ranges of oil content were examined for fatty acid composition of the oil using gas chromatography (GC). Briefly explained, seed oil was methylated with boron trifluoride in methanol followed with NaOH/methanol treatment to from methyl esters. These fatty acid methyl esters were subjected to GC analysis. An Agilent Technologies GC fitted with a DB-WAX 127-2012 column (30 m, 0.32 mm, 0.25 μm) and FID for detection of fatty acid composition. The temperature of oven, injector and detector block were maintained at 210°C, 250°C and 250°C, respectively. The column temperature program, initial temperature at 80°C and hold 1 min, increased temperature to 250°C with 10°C/min and hold 2 min. Helium was used as carrier gas. Peaks were identified by comparison with retention time of mixed fatty acid methyl esters standard (FAME: Mixed C8-C24) and quantification was performed by internal normalization method.

Saponification number (SN) and iodine value (IV) were determined as described in ASTM D5558 and AOCS official method 1c-85. Cetane number (CN) of FAMEs was estimated from the following equation [9].

$$CN = 46.3 + \frac{5458}{SN} - 0.225 \times IV$$

The CN is the dimensionless descriptor of the ignition quality of a diesel fuel. It is a prime indicator of biodiesel quality. The higher the CN, the shorter is the ignition time. CN increase with the length of the branch carbon of the FAMEs component [10]. Standards for CN have been established worldwide. American Society for Testing and Materials (ASTM D6751) for biodiesel fuel requires a minimum CN of 47. In the European standard (EN 14214) requires a minimum CN of 51. [11]

3. Results and Discussion

3.1 Oil content

Oil yield forms the most important quality which will affect the overall commercial success of the efforts for *Pongamia pinnata* cultivation and its use as an energy crop. Frequency distribution of 45 tree accessions of *Pongamia pinnata* for seed oil content is present in Table1.

Table 1: Frequency distribution of 45 tree accessions of *Pongamia pinnata* for seed oil content

Characteristic	Range (%wt)	Number of accessions
Seed oil	25.0-30.0	33
	30.1-35.0	12

From the Table1, it shows that seventy three percent of the accessions have exhibited oil content ranging from 25 to 30% by weight. While 27% exhibited higher oil content in the range of 30.1 to 35% by weight.

The 20 P*ongamia pinnata* accessions selected for fatty acid analysis covered the whole range of oil content from minimum of 25.67% in KB4 (from Krabi) to maximum of 33.12% in PK2 (from Phungnga). The variability in oil content might be the variation in species or different ecological condition or different in the maturation stage of seeds. The five accessions with very high oil content (>30%) as the code no RB3, RS11, RS15 (from Rayong), PK2 (from Phungnga) and KB1 (from Krabi) will be valuable for selection in development as a high oil crop for biodiesel production.

3.2 Fatty acid composition

The quality of oil is a function of its fatty acid composition fatty acid; palmitic, stearic, oleic, linoleic, linolenic and behenic fatty acid composition varied widely in the 20 accessions selected for this study (Table2).

Table 2: Variability for oil content, fatty acid composition and biodiesel quality in 20 accessions on *Pongamia pinnata* oil

Code no	Seed oil content (%)	Fatty acid composition [a]						SN	IV	CN	O/L [b]
		Palmitic	Stearic	Oleic	Linoleic	Linolenic	Behenic				
RB1	26.65	13.01	5.32	47.42	14.99	4.49	9.12	207.65	83.75	53.74	3.16
RB2	26.83	13.31	13.28	37.15	18.14	4.23	6.30	205.99	83.45	54.02	2.05
RB3	30.48	14.09	8.71	44.36	16.27	3.36	7.25	198.56	71.95	57.60	2.73
RB4	27.97	15.39	13.84	40.86	12.21	1.91	7.42	202.27	61.66	59.41	3.35
RB5	26.89	16.67	51.16	48.15	12.47	2.17	8.27	213.69	71.89	55.67	3.86
RS11	30.51	12.95	5.61	42.04	20.98	3.69	8.65	206.85	88.41	52.79	2.00
RS12	27.35	13.34	5.06	42.97	20.43	4.07	8.48	203.35	87.72	53.40	2.10
RS13	27.81	15.35	4.89	43.64	16.43	2.29	10.24	198.95	81.02	55.50	2.66
RS14	30.09	13.45	5.87	47.34	18.18	2.50	7.64	207.69	78.41	54.94	2.60
RS15	31.31	12.82	6.32	46.22	18.89	2.83	8.55	199.29	83.40	54.92	2.45
PK1	30.07	13.59	4.67	40.84	21.52	3.26	9.89	195.40	83.62	55.42	1.89
PK2	33.12	12.59	4.71	40.19	19.84	3.90	11.56	204.69	85.71	53.68	2.03
PK3	28.75	14.06	6.34	41.41	19.67	2.42	9.98	201.82	81.96	54.90	2.11
PK4	32.53	13.70	3.88	38.33	22.23	3.66	11.32	195.04	84.77	55.21	1.72
PK5	29.19	17.63	6.18	44.20	10.61	-	12.87	202.04	67.73	58.08	4.17
KB1	30.70	13.75	5.28	43.39	18.56	4.71	10.70	204.52	90.07	52.72	2.34
KB2	29.28	13.37	5.03	45.40	17.54	4.24	10.80	206.23	79.96	54.77	2.59
KB3	30.29	13.93	4.88	44.53	21.24	4.27	7.92	196.81	85.12	54.88	2.09
KB4	26.67	15.69	4.99	45.26	15.56	2.82	11.58	203.58	80.24	55.06	2.91
KB5	28.40	15.62	4.49	42.24	16.19	5.88	11.03	201.15	76.52	56.22	2.61
Mean	29.24	14.22	8.53	43.30	17.60	3.69	9.48	202.78	80.37	55.15	2.57
SD	1.93	1.38	10.39	2.97	3.26	1.03	1.77	4.66	7.25	1.70	0.64
Range	26.65-33.12	12.82-17.63	3.88-13.84	37.15-47.42	10.61-22.23	0-5.88	6.30-12.87	196.81-207.69	61.66-90.07	52.72-59.41	1.72-4.17

[a] percentage may not add to 100% due to the noninclusion of other constituents. [b] Oleic/linoleic acid

The major fatty acid was oleic acid ($C_{18:1}$) in a concentration range of 37.15-47.42%, followed by linoleic acid ($C_{18:2}$) at 10.61-22.23%, palmitic acid ($C_{16:0}$) at 12.82-17.63%, stearic acid ($C_{18:0}$) at 3.88-13.84%, behenic acid ($C_{20:0}$) at 6.30-12.87% and linolenic acid ($C_{18:3}$) at 0-5.88%. The results of large difference in fatty acid concentration was determined at 9.96%, 10.27%, 11.62% of stearic, oleic and linoleic acid, respectively. In adding, the results of less difference in fatty acid concentration were found at 4.81%, 5.88%, 6.57% of palmitic, linolenic and behenic acid, respectively.

Comparison of the fatty acid composition in our work with Mukta et. al. [12] who studied the variability assessment of Indian *Pongamia pinnata* oil, the result showed Indian *Pongamia pinnata* had higher range in oleic acid (46.66-13.25%) and linoleic acid (12.02-32.58) than our study. The reason was Indian *Pongamia pinnata* oil contained only four major fatty acids (palmitic, stearic, oleic and linoleic acid) but Thai *Pongamia pinnata* oil contained six major fatty acids (palmitic, stearic, oleic, linoleic , linolenic and behenic acid). The percentage of all fatty acid in concentration may add to 100% on both oil. When they were compared on oleic and linoleic concentration.

Oleic/linoleic acid (O/L) ratio and iodine value indicated the stability and shelf life. When O/L ratio and iodine value compared with Indian *Pongamia pinnata* oil [12], the O/L of both oils were nearly the same that it indicated Thai and Indian oil had the same stability. For iodine value, Indian oil was higher value than Thai oil that it indicated Thai oil had longer shelf life than Indian oil. O/L ratio among the various *Pongamia pinnata* accessions varied from 1.72-4.17. Accession PK5 exhibited high O/L ratio and low iodine value (Table 2), which indicated higher stability and longer shelf life.

Saponification number (SN) is an indicator of molecular weight of the fatty acid or chain length of fatty acid in the oil. Our Thai *Pongamia pinnata* oil had higher SN value (196.81-207.69) than Indian oil that had 183.30-200.91 of SN value (Mukta al. al., 2009). The result supported Thai oil consisted of long chain fatty acids such as linolenic ($C_{18:2}$), behenic ($C_{22:0}$) acids but Indian oil lacked of both acids as we mentioned earlier in fatty acid composition analysis.

3.3 Biodiesel quality

SN and IV were determined followed ASTM D5558 and AOCS 1c-85. CN of fatty acid methyl esters of oil was empirically determined. The result of SN, IV and CN varied from 196.81-207.69, 61.66-90.07 and 52.72-59.41, respectively (Table 2). CN is the ability of fuel to ignite quickly after being injected and a higher value indicates better ignition quality of fuel. Biodiesel standards of USA and European organization have set this value as 47 and 51, respectively. IV is the degree of unsaturation. With increase of CN, IV decrease which means degree of unsaturation decreases. This saturation will lead to the solidification of fatty acid methyl esters at higher temperature. In addition, European organization set IV less than 120. In the present investigation, values for the two standards (IV and CN) fell within these limits in the case of 20 accessions studied. Among the FAMEs of *Pongamia pinnata*, all accessions had CN had than 51 that indicated all the accessions study satisfied this limit with respect to CN. The IV of 20 accessions (Table 2) ranged from 61.66-90.07 also met the specification of IV. Besides these parameters, the concentration of linolenic acid containing three bonds in FAMEs should not exceed the limit of 12% in accordance with European standard organization. *Pongamia pinnata* oil could produced fatty acid methyl esters with most suitable for using as biodiesel since it met the major specification of biodiesel standards of USA and European organization [13].

4. Conclusions

The present study documents the variation in oil content, fatty acid composition, saponification number, iodine value and cetane number of Thai *Pongamia pinnata* oil from Southern region of Thailand. The present investigation, code number RB3, RS11, RS15 from Rayong, PK2 from Phungnga and KB1 from Krabi provice were selected with oil content > 30% (wt), CN>51 and IV<120 that meet the specific requirement of biodiesel standard.

Acknowledgements

The authors acknowledge the financial support from National Research Council of Thailand (NRCT). We also would like to thank the Center of Excellence – oil Palm, Kasetsart university for partial support of this research.

References

[1] E. Alptekin and M. Canakci, *Fuel.* **89** (2010) 4035-4039.

[2] L.C. Maher, S.N. Naik and L.M. Das, *J. Sci.of Indus, Res.* **63** (2004) 913–918.

[3] M. Bala, Y.N. Nug, M. Kumar, A. Vyas and N.S. Bhogal, *J. Am. Oil. Soc.* **88** (2011) 559-562.

[4] M. Naik, L.C. Meher, S.N. Naik and L.M. Das, *Biomass and Bioenergy*. **32** (2008) 354-357.

[5] S. Birajdur, S. Ramesh, V. and C.S. Patil, *Int. J. Biotec. appl.* **3**:1(2011) 52-54

[6] S. Kumar and A. Chadha, *Bioresource technology*. **96** (2005) 1425-1429.

[7] D. Majumdur, *Nat. Prod. Rediance.* **7:1** (2008) 58-67.

[7] W. Vismaya, S. Eipeson, J.R. Manjunatha, P. Srinivas and T.C. Sindhu Kanya, *Indus. Crop. And Prod.* **32** (2010) 118-122.

[9] K.A. Krisnankura, *J. Am. Oil. Soc.* **63**(1986) 552-553.

[10] G.H Knothe, *Fuel process technol.* **86** (2005) 1059-1070.

[11] E.C Francisco, D.B. Neves, E. Jacob-Lopes, and T.T. Franco, *J. Chem. Techol. Biotechnol.* **85** (2010) 395-403.

[12] N. Mukta, I.Y.L.N. Murthy, and P. Sripal, *Indus. Crops and Prod.* **29** (2009) 536-540.

[13] M.M. Azam, A. Waris and N.M. Nahar, *Biomass Bioenergy.* **29** (2005) 293-302.

PREDICTION OF NITROGEN OXIDE GENERATED FROM GAS TURBINE ENGINE

Natchanon Chaiprasert, Amornchai Arpornwichanop*

Department of Chemical Engineering, Faculty of Engineering, Chulalongkorn University, Bangkok 10330, Thailand

* Author for correspondence; E-Mail: Amornchai.a@chula.ac.th, Tel. +66 2218 6878, Fax. +66 2218 6877

Abstract: Presently, emission control of pollutants has become an important issue due to more strict regulation. A gas turbine engine, which is generally used as a mechanical drive in most of power generation plants, is among the sources that can generate air pollutants, such as nitrogen oxide, from the burning of fuels in a combustion chamber. In this study, a simulation model of the combustion chamber in an aero-derivative type gas turbine engine is developed with the aim to predict an amount of generated nitrogen oxide. Modeling of the combustion chamber is divided into two steps. First, a process simulator is employed to generate stream data and boundary conditions around the combustion chamber and secondly, based on this information and combustion kinetics (including thermal NO_x, prompt NO_x and N_2O intermediate pathways), fluid dynamic software is used to predict gaseous composition profiles in the combustor. The simulation results have indicated that engine load, engine performance and ambient temperatures are the most important parameters, which highly affect the generation of nitrogen oxide. The results obtained from this model-based analysis are beneficial for an understanding of the combustor, leading to an efficient operation of the gas turbine engine in terms of minimizing pollutant generation.

1. Introduction

In a cogeneration power generation plant, a gas turbine engine is normally used as a mechanical driver. Although the cogeneration power plant is accepted in terms of its efficiency, it is also an emission source causing air pollution problems. Currently, the environmental regulation is strict and control of air pollutant emissions becomes an important issue.

A gas separation plant is the upstream industry of a petrochemical complex. In general, natural gas is employed to produce electricity and heat source for the gas separation processes. In a particular power and heat generation, two types of gas turbine generators are employed. The first one is the latest technology gas turbine, Rolls Royce RB-211 DLE, in which a pre-mixed combustor is applied, resulting in a low emission of air pollutants. The second one is the smaller-model gas turbine, Rolls Royce Avon A200. Regarding the latest-revision environmental law, the Avon A200 gas turbine has been normally operated under the conditions that release nitrogen oxide (NOx) at a limitedly allowable range. However, there were many evident that the continuous emission monitoring system (CEMS) indicates the excess amount of NOx generated. Presently, the release of NOx is still unpredictable and the management of NOx generation takes the issue as priority while concerning a production capacity. In general, operators of a gas turbine power plant have many available experimental data concerning about the thermodynamic quantities of streams flowing within the turbine engine to check plant operation and to monitor main performance indexes. These data, however, may not be sufficient to set up policies that provide maximum revenues and minimum pollutant generation and that fulfil the technological constraints. Simulation models describing thermodynamic processes are therefore required to obtain reliable and accurate performance predictions of the gas turbine from available experimental data. This information may be useful for operators to response to load variations and a large range of load settings offered by gas turbines [1].

In the last few years, a computational fluid dynamic (CFD) has become popular and represents a useful approach for providing preliminary information and facilitating economical combustion system design. However, the phenomena occurring in burners are highly complex with hot flue gas recirculation, energy transfer and strong turbulence chemistry effects, especially in case of swirled combustors. For this reason, the CFD analysis of swirling confined reacting flows is one of the most important and challenging areas of modern CFD [2]. To find a reasonable solution, basic knowledge in many related topics is required. In addition to a detailed analysis of the combustion system, the performance of a gas turbine engine system should be investigated with respect to operating and design parameters as they have effects on NOx generation. At present, two approximate combustion models are sufficient to describe chemical kinetic mechanisms: flamelet model and reactor model [3].

2. Modelling and Theory

2.1 Gas Turbine Engine

A power generator system driven by gas turbine engine is first simulated. The power system consists of compressor, splitter, combustor, gas turbine, mixer and power turbine as shown in Figure 1. Plant data, such as air inlet temperature, compressor discharge pressure, fuel mass flow rate, gas turbine exhaust temperature and generator output power, are employed for simulation and unknown stream data obtained is used as boundary conditions to model a combustion chamber.

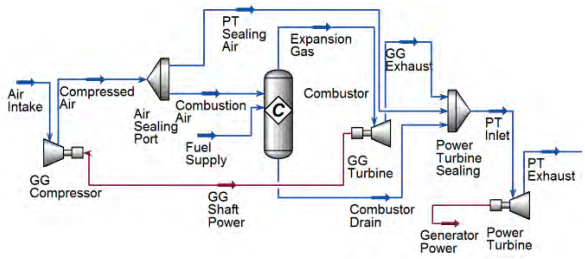

Figure 1. Flow diagram of a power generator system.

The result indicates the mass flow rate across each boundary surfaces of combustion chamber. By varying trending data with significant set, the interpolating performance of each unit operation becomes available as a function of non-dimensional speed, which is determined by the gas turbine rotating speed divided by square root of ambient temperature. This data is employed to predict other operating conditions within a certain operational range.

2.2 Kinetic of NOx formation

Thermal NOx, prompt NOx, fuel NOx and intermediate N_2O path formation are currently the category of NOx formation considered in the present study. The CFD software used in this study applies the rate model developed at the Department of Fuel and Energy, University of Leed. To predict NOx emission, the software solves transport equations for nitric oxide and intermediate species (only when fuel NOx source and NOx from intermediate N_2O are present) concentration. Because fuel NOx is generated by the combustion process of the nitrogen containing in organic compounds present in liquid or solid fossil fuel. The gas turbine engine uses natural gas, which methane is the majority. Hence fuel NOx can be neglected. The mass transport equation is described by:

$$\frac{\partial}{\partial t}(\rho Y_{NO}) + \nabla\cdot(\rho \vec{v} Y_{NO}) = \nabla\cdot(\rho D \nabla Y_{NO}) + S_{NO} \quad (1)$$

$$\frac{\partial}{\partial t}(\rho Y_{N2O}) + \nabla\cdot(\rho \vec{v} Y_{N2O}) = \nabla\cdot(\rho D \nabla Y_{N2O}) + S_{N2} \quad (2)$$

An analysis of the reaction paths responsible for NO formation showed that 67% of NO contribution is derived from the thermal reaction path and 33% of NO is come from the prompt path [4]

2.2.1 Thermal NOx formation

The formation of thermal NOx is determined by a set of highly temperature-dependent chemical reactions known as the extended Zeldovich mechanism. The principal reactions governing the formation of thermal NOx from molecular nitrogen are as follows:

$$O + N_2 \leftrightarrow N + NO \quad (3)$$
$$N + O_2 \leftrightarrow O + NO \quad (4)$$

The third reaction contributes to the formation of thermal NOx, particularly at near-stoichiometric conditions and in fuel-rich mixtures:

$$N + OH \leftrightarrow H + NO \quad (5)$$

The rate constants for these reactions are obtained from numerous experimental studies and the data obtained from these studies have been critically evaluated. The expressions for the rate coefficients for Equations (3)-(5) used in the NOx model are given below.

$k_{f,1} = 1.8 \times 108e{-}38370/T$ $k_{r,1} = 3.8 \times 107e{-}425/T$
$k_{f,2} = 1.8 \times 104Te{-}4680/T$ $k_{r,2} = 3.81 \times 103Te{-}20820/T$
$k_{f,3} = 7.1 \times 107e{-}450/T$ $k_{r,3} = 1.7 \times 108e{-}24560/T$

The net rate of formation of NO via Reactions (3)-(5) is given by:

$$\frac{d[NO]}{dt} = k_{f,1}[O][N_2] + k_{f,2}[N][O_2] + k_{f,3}[N][OH] - k_{r,1}[NO][N] - k_{r,2}[NO][O] - k_{r,3}[NO][H] \quad (6)$$

where all concentrations have units of gmol/m3.

The rate of NO formation will increase with increasing oxygen concentration. The thermal NO formation should be highly dependent on temperature but independent of fuel type. In fact, the thermal NOx production rate doubles for every 90 K temperature increase beyond 2200 K. The NO source term due to the thermal NOx mechanisms is as:

$$S_{thermal,NO} = M_{w,NO} \frac{d[NO]}{dt} \quad (7)$$

2.2.2 Prompt NOx formation

The presence of a second mechanism leading to NOx formation was first identified by Fenimore and was termed “prompt NOx”. There is good evidence that prompt NOx can be formed in a significant quantity in some combustion environments, such as low temperature, fuel-rich conditions and short residence time. Surface burners, staged combustion systems and gas turbines can create such conditions. At present, the prompt NOx contribution to total NOx from stationary combustors is small. However, as NOx emissions are reduced to very low levels by employing new strategies (burner design or furnace geometry modification), the relative importance of the prompt NOx can be expected to increase.

Presently, there have been many developed prompt NOx prediction. The predicted results indicated that the model performance declines significantly under fuel-rich conditions and for higher hydrocarbon fuels. To reduce this error and predict the prompt NOx adequately in all conditions, the Department of Fuel and Energy, University of Leeds developed the correction factor, derived from experimental data. The rate of prompt NOx formation can be determined from:

$$\frac{d[\mathrm{NO}]}{dt} = f\ k_{\mathrm{pr}}[\mathrm{O_2}]^{a}[\mathrm{N_2}] + [\mathrm{FUEL}]e^{-Ea/RT} \quad (8)$$

where

$f = 4.75 + 0.0819n - 23.2ø + 32ø^2 - 12.2\ ø^3$

$k_{pr} = 6.4 \times 10^6\ (RT / p)^{a+1}$

$E_a = 303474.125$ J/gmol

Thus, the source term due to the prompt NOx mechanism is as:

$$S_{\mathrm{prompt,NO}} = M_{\mathrm{w,NO}}\ \frac{d[\mathrm{NO}]}{dt} \quad (9)$$

2.2.3 NOx formation from intermediate N_2O

Under desired conditions, which are elevated pressures and oxygen-rich conditions, this intermediate mechanism can contribute as much as 90% of the NOx formed during combustion. This makes it particularly important in equipment such as gas turbines and compression-ignition engines. Because these devices are operated at increasingly low temperatures to prevent NOx formation via the thermal NOx mechanism, the relative importance of the N2O intermediate mechanism is increasing. It has been observed that about 30% of the NOx formed in these systems can be attributed to the N_2O-intermediate mechanism. According to the kinetic rate laws, the rate of NOx formation via the N_2O-intermediate mechanism is

$$\frac{d[\mathrm{NO}]}{dt} = 2(k_{f,2}\ [\mathrm{N_2O}][\mathrm{O}] - k_{f,2}\ [\mathrm{NO}]^2) \quad (10)$$

3. Results and Discussion

First, the model of the combustion chamber developed in the previous section is validated. Simulations are performed over the operating range of the cogeneration power plant and the results show that the average error of the model prediction is in range of 5–20%. The model can reasonably predict the NOx generation, especially at high load operation, which the thermal NOx is highly involved. For example, at 81% plant load, the formation of NOx from various sources is as follows:

- Thermal NOx rate = 6.90e-05 (kgmol/m3-s) (59% of total NOx formation)
- Prompt NOx rate = 1.88e-06 (kgmol/m3-s) (16% of total NOx formation)
- N_2O Path NOx rate = 2.90e-06 (kgmol/m3-s) (25% of total NOx formation)

Figure 2 shows each NOx path location within the combustion chamber.

Next, effect of key operating parameters on NOx generation is studied. The generator power (or engine load), ambient temperature, fuel gas heating value and engine performance are considered as these parameters can be changed periodically by electricity demand, process requirement and surrounding environment.

Figure 2. Reaction rate contour of thermal NOx, prompt NOx and N_2O path (from left to right).

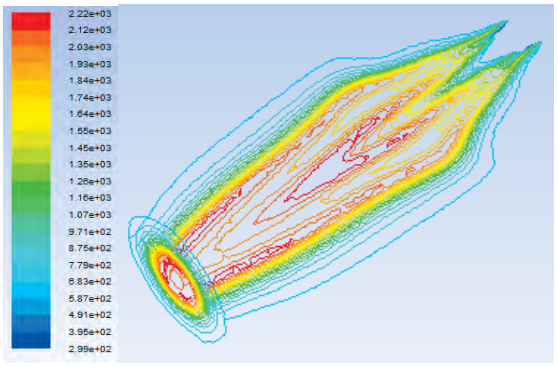

Figure 3. Temperature contour in the combustor at 10.68 MW power generation.

Effect of power generation: The engine load is directly proportional to flame temperature. It shall have greatly affect to NOx level at high load which the maximum flame temperature is higher than 2200 K. At above 89% load (10.68 MW), as shown in Figure 3, the maximum temperature of 2200 K is estimated. This causes an increase in the amount of NOx resulting from the thermal NOx effect.

Effect of air intake temperature: Because the ambient temperature is periodically changed by time and season. In fact, air density is also changed by temperature. Hence, it affects air mass flow rate that can increase the engine power without increasing of fuel gas supply. Less amount of NOx can be indicated from a lower flame temperature. The combined effect of engine load and air intake temperature on NOx generation is shown in Figure 4.

Effect of fuel gas heating value: Similar to a load change, the engine power is transformed from chemical energy in fuel gas. Changing the component composition, such as carbon dioxide in fuel gas, causes the heating value to be changed. In order to compensate the lower heating value fuel, more fuel flow is required to maintain the same amount of energy supplied to the engine. This affects the velocity of fuel gas in the injector. The higher fuel velocity supplied to the system reduces the resident time in the combustor. Better mixing effect from the turbulent flow of fuel has a slightly positive result. Note that lean pre-mixed combustion flame temperature is always lower than diffusion flame temperature.

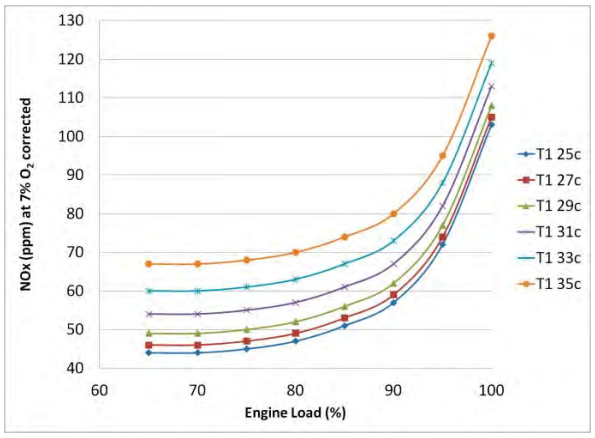

Figure 4. Effect of the engine load on NOx generation at different air intake temperature.

Effect of engine performance: Normally the engine performance is related to the axial compressor efficiency. Downgrading the compressor efficiency causes the reduction of a total air mass flow. In some case, the compressor discharge pressure decrease due to the fouling effect. Intermediate N2O path reduces while thermal NOx increases from bad cooling in the combustion chamber.

From the sensitivity analysis of key parameters on the generation of NOx, the future work will be focused on an optimization of the overall power generation process. The aim is to find a suitable operational range to maximize engine power while satisfying NOx emission constraints. The result can also be used as a scheduling proper maintenance program such as compressor cleaning in order to recovery the compressor efficiency.

4. Conclusions

In this study, a computational fluid dynamic model of the combustion chamber in a gas turbine-driven power generator was developed to predict the amount of NOx generated. A flowsheet simulation of the power generator was performed to generate a boundary stream data used for modeling the combustion chamber. The developed model can accurately predict the content of NOx; the prediction error is in an acceptable range. From sensitivity analysis, it was found that engine load, air intake temperature, fuel gas and compressor condition are key operating parameters affecting NOx generation. The result of the study can be used as a operational guideline of the combustion chamber for achieving local environmental regulation and production capacity.

Acknowledgements

Support from the Computational Process Engineering Research Group, Special Task Force for Activating Research (STAR), Chulalongkorn University Centenary Academic Development Project is also gratefully acknowledged.

Nomenclature

ρ gas density (kg/m^3)
Y mass faction of a component in gas phase
D effective diffusion coeficient
$\vec{v}$ gas velocity (m/s)
S source term of mechanism (kg/m^{3}s)
M_w molecular weight (kg/gmol)
k_f forward reaction rate (m^3/gmol-s)
k_r reverse reaction rate (m^3/gmol-s)
T reaction tempearature (K)
f a coefficient which incorporates the effect of fuel type and air-to-fuel ratio
k_{pr} prompt reaction rate
E_a activation energy (J/gmol)
a oxigen reaction order
n number of carbon atom per molecule
ø equivalent ratio

References

[1] A. Lazzaretto, A. Toffolo. *Prediction of performance and emissions of a two-shaft gas turbine from experimental data*, Department of Mechanical Engineering, University of Padova, Via Venezia 1, 35131 Padova, Italy (2008).

[2] A. Frassoldatia, S. Frigerioa, E. Colombob, F. Inzolib, T. Faravellia, *Determination ofNO x emissions from strong swirling confined flames with an integrated CFD-based procedure*. aCMIC Dipartimento di Chimica, Materiali e Ingegneria Chimica, Politecnico di Milano, Piazza Leonardo da Vinci 32, 20133 Milano, Italy bDipartimento di Energetica, Politecnico di Milano, Piazza Leonardo da Vinci 32, 20133 Milano, Italy (2004).

[3] A.B. Lebedev, A.N. Secundov, A.M. Starik *, N.S. Titova, A.M. Schepin, *Modeling study of gas-turbine combustor emission*. Central Institute of Aviation Motors (CIAM), Department of Physical and Chemical Kinetics, Aviamotornaya Street 2, Moscow 111116, Russian Federation (2009).

[4] H. Barths, N. Peters, N. Brehm, A. Mack, M. Pfitzner and V. Smiljanovski, *Simulation of pollutant formation in a gas-turbine combustor using unsteady flamelets*. 1Institut fu¨r Technische Mechanik RWTH Aachen, Germany 2BMW Rolls-Royce GmbH D-15827 Dahlewitz, Germany22 (1998).

RAPID PROPERTIES ANALYSIS OF *PONGAMIA PINNATA* SEED OIL BY NEAR-INFRARED SPECTROSCOPY, A POTENTIAL BIOFUEL CROP

Chutarat Khamchum[1*], Vittaya Punsuvon[1,2,3], Potjanart Suwanruji[1], Sumaporn Kasemsumran[4] and Nattaporn Suttiwijitpukdee[4]

[1]Department of Chemistry, Faculty of Science, Kasetsart University, Bangkok 10900, Thailand
[2]Center of Excellence-Oil Palm, Kasetsart University, Bangkok 10900, Thailand
[3]Center of Advanced studied in Tropical Natural Resource, NRU-KU, Kasetsart University, Bangkok 10900, Thailand
[4]Kasetsart Agricultural and Agro-Industrial Product Improvement Institute (KAPI), Kasetsart University, Bangkok 10900, Thailand

*E-mail: diy704@hotmail.com Tel. +66 891306906

Abstract: The objective of this research is to investigate the fatty acid compositions and the free fatty acid (FFA) content in *Pongamia Pinnata* seed oil by using Near Infrared Spectroscopy (NIR). This technique is a rapid analysis method which is used to replace a conventional method that spends a lot of time, cost, destroys the samples and uses hazardous chemicals. Applications of NIR include pharmaceutical, agricultural, polymer, and clinical analysis. A total 120 spectra of seed oils were recorded in the region of 1100-2500 nm and the spectrum were pretreated by combination techniques for comparing and obtaining the optimal calibration models. Partial least squares (PLS) analysis method was introduced to develop the calibration model for individual fatty acid content (palmitic C16:0, stearic C18:0, oleic C18:1, linoleic C18:2, behenic C22:0) and FFA content. The results of experiment showed that the calibration of FFA content provided the highest accuracy model as presented in the high correlation coefficient value (R =0.977). For fatty acid compositions, oleic acid gave the highest correlation coefficient of calibration (R=0.859), followed by stearic acid (R=0.841), behenic acid (R=0.774), linoleic acid (R=0.792), and palmitic acid gave the poorest correlation coefficient (R=0.693). The calibration models of all fatty acids were reliable, accurate to estimate the fatty acid content in oil. The results strikingly indicated that the reflectance NIR spectroscopy is a non-destructive and rapid technique which has the ability for estimating the fatty acid compositions and the FFA content in *P. Pinnata* seed oil.

1. Introduction

Pongamia Pinnata is commonly found in alluvial and coastal situations. In the south of Thailand, we can found this plant on Andaman coast such as Ranong, Krabi, Phuket provinces. *P. Pinnata* is one of non-edible oil plants as same as Jatropha curcus that this plant contains about 17-28% oil content [1]. The advantages of *P. pinnata* are dominantly powerful. All parts of the plant possibly used as a herb for the treatment of tumors, piles, skin diseases, itches, abscess, painful rheumatic joints wounds, ulcers and diarrhea [2]. Normally, it is used as ingredients or raw materials in soap, leather tanning and pharmaceutically industries. *P. Pinnata* oil is one of non-edible oil because in the freshly extracted oil also contain the toxicity of flavonoids such as karanjin, pongapin and pongaglubin [3]. *P. Pinnata* oil is regarded as a potential fuel substitute that contains 16-22 carbon atoms per molecule. Therefore, *P. Pinnata* oil has potential to be a raw material for the conversion to methyl esters [4] that can use for biofuel industries specifically for biodiesel production.

Near-Infrared Spectroscopy (NIR) is the measurement of the wavelength and intensity of absorption in near-infrared light of a sample. Near-infrared light spans the 800 nm – 2500 nm (12,500 - 4000 cm^{-1}) range and is energetic enough to excite overtones and combinations of molecular vibrations to higher energy levels. NIR spectroscopy is typically used for quantitative measurement of organic functional groups, especially O-H, N-H, and C=O. Detection limits are typically 0.1% and applications include pharmaceutical, agricultural, polymer, and clinical analysis. In the previous reports, NIRS has been applied to fatty acid profiling in oil seeds including rapeseed [5], peanut [6], sesame [7], sheanut [8], and jatropha curcas [9]. It has also been used to study oil content in cotton seed [10].

Absorption of radiation in the regions 1100 nm-2500 nm is used to develop calibration curves, which can be related to sample properties. After calibration, the regression equations developed allows accurate analysis of many other samples by prediction of data based on the spectra [11].

The objective of this study is to investigate the feasibility of predicting fatty acid composition and free fatty acid content in *P. Pinnata* seed oil by using Near Infrared Spectroscopy (NIR). In this study, the partial least squares (PLS) analysis was introduced to develop statistical models in terms of calibration equation for each value.

2. Materials and Methods

2.1 Samples preparation

Pongamia Pinnata seeds (60 samples) were collected from the southern part of Thailand. Then we

air dried them to protect moisture and fungi. The hull's pods were manually removed to obtain seed kernels after that the kernel were ground by a grinder and sized with sieve (40-60 mesh) to make ground kernels (meals or seed powder). The final sample was randomly drawn from this powder for the experiment.

2.2 Oil extraction

Pongamia Pinnata powders were extracted by hexane in an automatic soxhlet extractor at 70 °C for 4 h. After 4 h, the solvent was evaporated using a rotary evaporator. Then oil sample were kept in brown bottle and all of samples were duplicated.

2.3 Free fatty acid content

Free fatty acid content was determined according to AOCS Official Method Ca 5a-40. Oil samples were dissolved in ethanol, added 1 ml. of phenolphthalein indicator and titrated with 0.25N NaOH. Finally, the volume of tritrant wes recorded and calculated the free fatty acid content.

2.4 Fatty acid compositions analysis

The methylation of oils was performed by reacting with boron trifluoride/ methanol, and then the solution was treated with KOH/methanol as described by AOAC 969.3 official method. These fatty acid methyl esters were identified and separated by gas chromatrography (GC) using an Agilent 6890 Gas Chromatograph (Agilent Technologies) equipped with a flame ionization detector and a 30 m x 0.32 mm (i.d.) fused siloxane capillary column (DB-WAX 127-7012, 0.25 µm film thickness). The oven temperature was maintained at 110˚C for 5 min, and then increased to 200˚C at 5˚C/min. The injector and detector temperature were 210˚C and 250˚C, respectively. Helium was the carrier gas at a split ratio of 30:1 and a constant flow rate of 1.0 ml/min. Fatty acid peaks were identified by comparing retention times with known fatty acid methyl ester standards (Sigma-Aldrich Chemie). The quantification of each fatty acid was performed by internal normalization method.

2.5 NIRS analysis

NIRS technique was used to analyze the properties of *P. Pinnata* seed oil. The transmitted-reflectance mode was applied to all measurements. Seed oil samples were placed in liquid cell with a gold cover to optimize the best spectral condition that used with a multi-cup adapter. NIRS spectra were collected in the region of 1100 to 2500 nm by near- infrared spectrophotometer (Unity, Spectrastar). Seed oils were scanned twice and the reflectance spectra (log 1/R) were recorded at 1 nm intervals. All spectra and calibrations were conducted with the Unscrambler 9.8 (Camo) software.

2.6 NIR spectral pretreatment and calibration

NIR calibration equations were developed for free fatty acid content, oleic acid (C18:1), linoleic acid (C18:2), palmitic acid (C16:0), stearic acid (C18:0) and behenic acid (C22:0). Savitzky-Golay first derivative (1De) was combined with other techniques such as smoothing (SM), normalize (NM) to transform spectra, in order to overcome distortions.

Calibration equations were developed based on the treated spectral data by partial least squares (PLS) regression with Unscrambler 9.8 software (Camo). The correlation coefficient of determination (R), the standard error of calibration (SECV), the standard error of prediction (SEP) of external validation, and bias served as indicators of prediction quality. Optimum calibration equations were obtained based on the highest R and the lowest SECV or SEP values. The standard deviation over standard error of prediction (SD/SEP) ratio which referred as relative predictive determination (RPD_p) in prediction set was used to evaluate the accuracy of calibration equation.

3. Results and Discussion

3.1 Fatty acid composition

The chromatogram showed each acid occurred at different retention times (RT) when compared with fatty acid standard. The RT of palmitic acid (C16:0), stearic acid (C18:0), oleic acid (C18:1), linoleic acid (C18:2), and behenic acid (C22:0) were at 12.82, 14.60, 14.78, 15.17, and 17.78 min, respectively. The chromatogram of fatty acid compositions of oil extracted from seed presented in Figure 1.

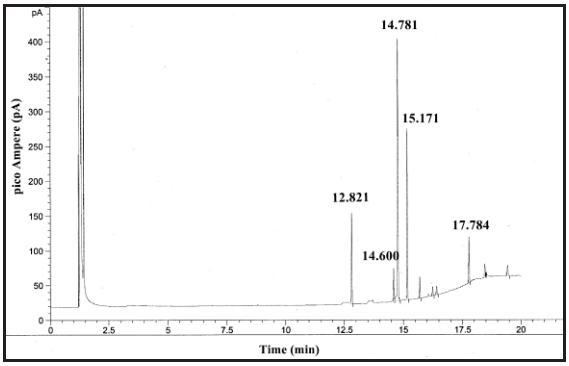

Figure 1, Chromatogram of fatty acid composition in *P. Pinnata* seed oil samples

The results in the range of free fatty acid content and individual fatty acid composition in the calibration set (45 samples) and prediction set (15 samples) were determined to follow these results. The range value of each component in calibration and prediction set is shown in Table 1.

Table 1: The range value of each composition in calibration and prediction sets

Contents	Calibration set		Prediction set	
	% w/w	SD	% w/w	SD
FFA	1.03-35.40	4.076	1.05-35.27	4.281
C18:1	35.01-50.65	3.677	35.01-50.47	3.780
C18:2	10.03-26.87	3.972	10.21-26.86	4.004
C16:0	10.36-15.69	1.283	10.92-15.62	1.331
C18:0	2.66-13.84	1.802	2.99-8.71	1.160
C22:0	4.15-12.87	1.800	5.38-12.87	1.785

3.2 NIRS analysis

The original NIRS spectra of oils in 1100-2500 nm are shown in Figure 2. The average spectra of oil samples had maximum absorption bands at 1210, 1388, 1720, 1760, 2140, 2306, and 2348 nm.

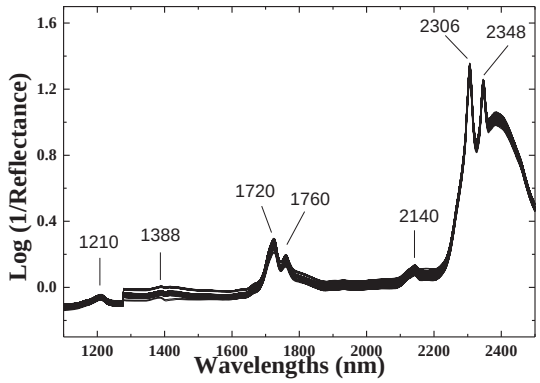

Figure 2, The original NIRS spectra of 90 *P. Pinnata* seed oil samples

Figure 2 shows broad spectra, so they need to use mathematic pretreatment to obtain the narrow band. In our work, the pretreatment with first derivatives (1De) was used to pretreat the original spectra of oil samples. The pretreated spectra were presented in Figure 3. The overall narrow absorption bands in first derivatives spectra were used to determine free fatty acid contents and fatty acid compositions.

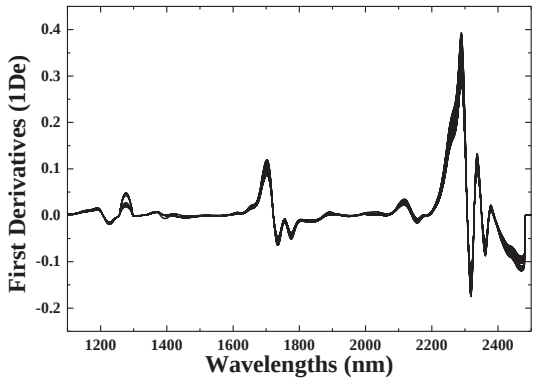

Figure 3, The pretreated spectra with first derivatives (1De) of 90 *P. Pinnata* seed oil samples

3.3 Calibration model

In developing NIRS model for free fatty acid content and fatty acid composition analysis, different pretreatment techniques combined with first derivative spectra and partial least square analysis were applied to get the accurate model. The best NIRS calibration was characterized by small value of SECV and Bias and large R and RPD value. The summary of selected pretreatment techniques for each composition analysis was shown in Table 2 and Table 3.

Table 2: Summary of the pretreatment techniques, monitoring statistics in the calibration model in the wavelength 1100-2500 nm of seed oil samples.

Contents	Pretreatment	F	Calibration		
			R	SECV	Bias
FFA	SM + 1De(21)	4	0.977	0.873	-0.022
C18:1	SM	12	0.859	1.893	0.033
C18:2	NM + 1De (21)	12	0.792	2.461	-0.026
C16:0	NM + 1De (25)	10	0.693	0.928	-0.004
C18:0	NM + 1De (21)	13	0.841	1.019	0.000
C22:0	SM + 1De (23)	12	0.774	1.169	-0.023

Table 3: Summary of the pretreatment techniques, monitoring statistics in the external prediction in the wavelength 1100-2500 nm of seed oil samples.

Contents	Pretreatment	F	Prediction	
			SEP	RPD_p
FFA	SM + 1De(21)	4	0.830	5.158
C18:1	SM	12	2.007	1.883
C18:2	NM + 1De (21)	12	2.236	1.791
C16:0	NM + 1De (25)	10	0.899	1.480
C18:0	NM + 1De (21)	13	0.927	1.251
C22:0	SM + 1De (23)	12	1.073	1.664

** SM: smoothing, 1De: first derivatives Savitsky–Golay, NM: normalize, F: number of factor, R: coefficient of correlation; SECV: standard error of calibration, Bias: the average of differences between reference value and NIR value, SEP: standard error of prediction, and RPD_p: relative of predictive determinant of calibration (SD/SEP).

The optimum calibration model was selected based on the low standard error of calibration (SECV), low bias value, high correlation coefficient (R) and high relative predictive determination (RPD). Table 2 shows that the calibration of free fatty acid content had the highest correlation coefficient of calibration (R = 0.977). For fatty acid compositions, oleic acid gave the highest correlation coefficient of calibration (R=0.859), followed by stearic acid (R = 0.841), linoleic acid (R = 0.792), behenic acid (R=0.774), and palmitic acid gave the lowest correlation coefficient (R = 0.693).

3.4 External prediction

The prediction statistics included coefficient of correlation (R), standard error of prediction (SEP), relative of the predictive determinant of calibration (RPD_p) or SD/SEP values, which were factors used to evaluate the reliability of the calibration model. The

RPD_p values of palmitic acid, stearic acid (1.480 and 1.251, respectively), indicating a poor correlation between reference values and NIRS estimated values. The prediction for free fatty acid content, oleic acid, linoleic acid, and behenic acid were confirmed by RPD_p (5.158, 1.883, 1.791, and 1.664, respectively). The RPD_p value as the cut off point for evaluating the accuracy of equations was above 1.5 for this study, which was recommended for reliable prediction [12].

The correlation plots between the predicted values and the actual values of prediction set are shown in Figure 4(a-f). The broad ranges of these compositions were the reasons that made all of these models had accurate prediction. The FFA had the most broad ranges that made the prediction models the highest accurate. Since palmitic acid and stearic acid had narrow range, so the prediction models were less accurate. The less accuracy of palmitic acid and stearic acid could be sufficiently used by increasing the number and broader range of reference samples.

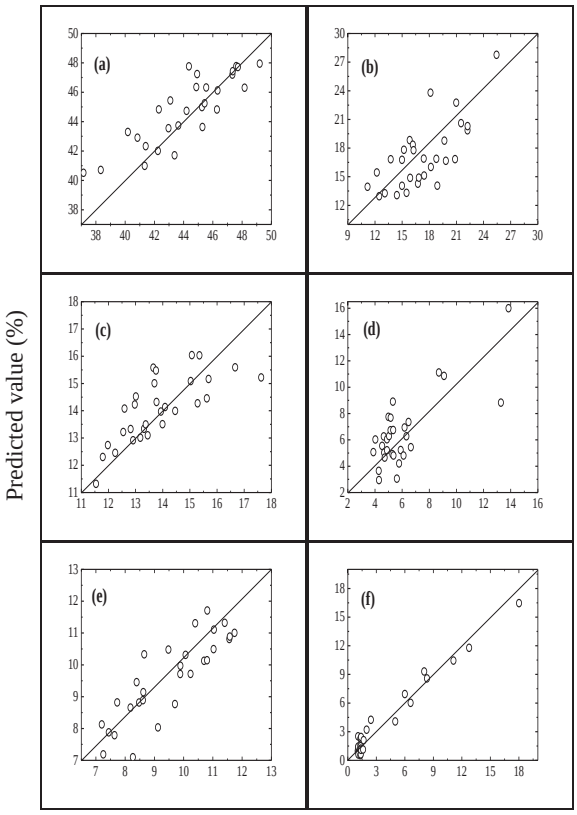

Figure 4, Correlation plots between the predicted value and actual value; (a): %Oleic acid, (b): %Linoleic acid, (c): %Palmitic acid, (d): %Stearic acid, (e): %Behenic acid, and (f): %FFA

4. Conclusions

The analyzed technique of the free fatty acid content and fatty acid compositions: oleic acid, linoleic acid, palmitic acid, stearic acid, and behenic acid of *Pongamia Pinnata* oil are developed by the NIR technique which is a simple, rapid, and non-destructive method. Finally, the NIR can be successfully applied for the selection of *Pongamia Pinnata* seed that has suitable properties for tree breeding and plantation in the biofuel industry.

Acknowledgements

This study was supported by the Graduate School, Kasetsart University. We also would like to thank the Higher Education Research Promotion and National Research University Project of Thailand, office of the Higher Education Commission, National Research council of Thailand and Center of Excellence-Oil palm Kasetsart University for partial supporting of this study.

References

[1] M. Bala, T. Nag, S. Kumar, M. Vyas, A. Kumar and N. Bhogal, *Journal of the American Oil Chemists' Society*. **88** (2011) 559-562.

[2] V. Kesari, A. Das and L. Rangan, *Biomass and Bioenergy*. **34** (2010) 108-115.

[3] Vismaya, W.S. Eipeson, J.R. Manjunatha, P. Srinivas and T.C. Sindhu, *Industrial Crops and Products*. **32** (2010) 118-122.

[4] L.C. Meher, S.N. Naik and L.M. Das, *Journal of Scientific & Industrail Research*. **63** (2004) 913-918.

[5] J.G. Wu, C.H. Shi and H.Z Zhang, *Spectroscopy and Spectral Analysis*. **26** (2006) 259-262.

[6] B.L. Tilman, D.W. Gorbet and G. Person, *Crop Science*. **46** (2006) 2121-2126.

[7] T. Sato, A. Maw and M. Katsuta, *Journal of the American Oil Chemists' Society*. **80** (2003) 1157-1161.

[8] F. Davrieux, F. Allal, G. Piombo, B. Kelly, J.B Okulo, M. Thaim, O.B. Diallo and J.M. Bouvet, *Journal of Agricultural and Food Chemistry*. **57** (2010) 7811-7819.

[9] Y. Vaknin, M. Ghanim, S. Samra, L. Dvash, E. Hendelsman, D. Eisikowitch and Y. Samocha, *Industrial Crops and Products*. **34** (2011) 1029-1034.

[10] R.J. Kohel, *Journal of Cotton Science*. **2** (1998) 23-26.

[11] R. Font, M. del Río-Celestino and A. de Haro-Bailón, *Industrial Crops and Products*. **24** (2006) 307-313.

[12] A. Quampah, Z.R. Huang, J.G. Wu, H.Y. Liu, J.R. Li, S.J. Zhu and C.H. Shi, *Journal of the American Oil Chemists' Society*. **89** (2012) 567-575.

HYDRODYNAMICS AND MASS TRANSFER BEHAVIOR IN NATURAL-INDUCED FLOW FLAT PANEL AIRLIFT REACTORS

Praewpakun Sintharm, Prasert Pavasant*

Chemical Engineering Research Unit for Value Adding of Bioresources, Department of Chemical Engineering, Faculty of Engineering, Chulalongkorn University, Phayathai Road, Patumwan, Bangkok 10330, Thailand

* Author for correspondence; E-Mail: prasert.p@chula.ac.th, Tel. +66 2186870, Fax. +66 2186877

Abstract: Natural-induced flow flat panel airlift reactors were examined for their hydrodynamic and mass transfer performances. The reactors of various widths, i.e. at 20, 30, 40, and 50 cm, were examined. The hydrodynamics were investigated in terms of gas hold-up and liquid velocity whilst the gas-liquid mass transfer coefficient was used to indicate the level of mass transfer. Each reactor was operated at three air flow rate, 0.1, 0.2, and 0.3 vvm. The behavior of the natural induced flow reactor was compared with the draft tube induced flow reactor. The riser to downcomer cross-section area was determined by the color tracer method with the image analyzing technique whereas the liquid velocity was measured also with the color tracer injection method [Gopal and Sharma, 1982]. The overall gas hold-up was determined by the volume expansion method whereas the gas-liquid mass transfer coefficient was determined by the dynamic method. The effect of unaerated liquid height will also be investigated.

1. Introduction

Airlift reactors are one type of pneumatic reactors which have several advantages over other types of pneumatic reactors such as simple construction, low energy requirement, low shear, good recirculation and uniform flow pattern. These make airlift reactors widely applied in many industries e.g. chemical, water treatment, pharmaceuticals, fermentation particularly in biotechnologies for cell culture cultivation.

Airlift reactors are developed in many shapes, depending on usability such as cylindrical, concentric tube and rectangular. Airlift reactors are classified into two types based on their structure (1) internal loop and (2) external loop. An airlift reactor comprises of three sections, each section has different flow pattern. The first is: the section in which liquid rises up is called a riser. The gas is separated from liquid by a second section called a gas-liquid separator. The last section, namely, the downcomer, is where the liquid flows downwards. The behaviour in airlift system can be explained by hydrodynamics (gas holdup and liquid velocity) and mass transfer which are significant parameters for designing the airlift reactor systems.

Typical airlift reactors employ either draft tube or separation plate installed inside the column to physically separate the riser from the downcomer. This extra partitioning component has generated some drawbacks such as the installation, cleaning, maintenance, not to mention the higher cost of construction. Due to these problems, a novel airlift system "Natural induced-flow airlift reactors" has been developed at the Department of Chemical Engineering, Faculty of Engineering, Chulalongkorn University. This novel system was designed such that a pattern cyclic movement of fluid can be induced without having to install the draft tube or separating plate. Preliminary examination indicates that this configuration works quite well as an airlift system. This work aimed to study the hydrodynamics and mass transfer of this novel reactor to generate necessary design information for such system.

2. Materials and Methods

2.1 Reactors and systems

The large scale internal-loop airlift reactor was used in this work. The airlift system was operated as a two phase system (liquid and gas), where the liquid phase was water supply and the gas phase was ambient air. The liquid was filled in the airlift reactors and the gas was supplied by air pump. The shape of airlift reactors in this work was flat panels that were made of fiber with the dimension of: length 100 cm, height 80 cm and varied widths (20, 30, 40 and 50 cm) as shown in Figures 1 and 2. For all experiments, air was dispersed by porous spargers installed along the length of flat panel. Gas flow rate was controlled in range 0.1 to 0.3 vvm (gas volume flow per unit of liquid volume per minute) and regulated by rotameters.

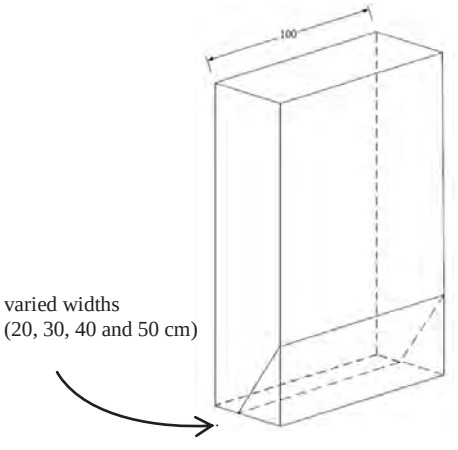

Figure 1 Schematic of natural induced-flow flat panel airlift reactor

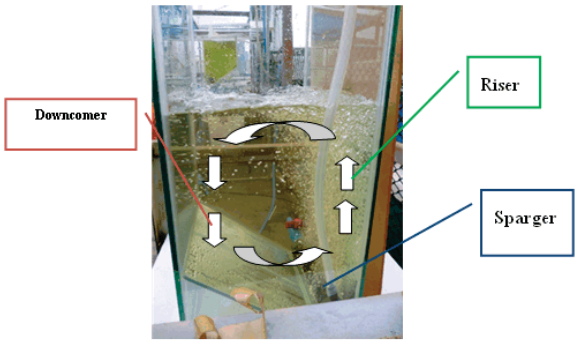

Figure 2 Sections and flow regions in airlift reactor

2.2 Measurements

2.2.1 Determination of virtual riser and downcomer cross-sectional area

As the novel airlift reactor has no solid partition to indicate the riser and downcomer area, the sizes of the riser and the downcomer are variable. It was the purpose of this section to propose a method to determine the 'virtual' cross sectional area of riser. Color tracer injection was used in this experiment. The shape of the riser was assumed to be rectangular cylinder. From experiment, the width of riser was known, so that the riser cross sectional area was:

$$A_r = W_r \times L$$

and downcomer cross sectional area was:

$$A_d = W_d \times L$$

where : A is cross section area (cm^2), W is width of riser(r) or downcomer(d) and L is length of reactor (cm).

2.2.2 Gas holdup

The riser and downcomer gas holdups are volumetric gas fraction in each section. The U-tube water manometer was used to measure the pressure differences between the two measuring ports at the side of the reactor. The riser and downcomer gas holdups from the height of defined liquid level in the reactor (ΔH) and the height of the liquid level in the U-tube manometer (ΔZ) can be calculated by:

$$\varepsilon_r = 1 - \frac{\Delta Z}{\Delta H}$$

$$\varepsilon_d = 1 - \frac{\Delta Z}{\Delta H}$$

2.2.3 Liquid velocity

The liquid velocity of the downcomer in the airlift system was measured by the color tracer injection method [Gopal and Sharma, 1982]. Time for the tracer to move between two fixed vertical distances was measured and calculated liquid velocity by:

$$v_d = \frac{L_d}{t_d}$$

where: V_d is the downcomer liquid velocity (cm/s), L_d is a fixed vertical distance (cm) and t_d is time that the tracer was taken to be in motion (s).

2.2.4 Mass transfer

Mass transfer in this experiment was obtained in term of the overall volumetric gas-liquid mass transfer coefficient (k_La). The k_La was determined using the dynamic method. In this method, the solution was freed of oxygen by nitrogen purge, and as the aeration was supplied, the time profile of dissolved oxygen concentration in the system was measured and recorded. The k_La can be calculated from:

$$ln\frac{(c^* - c_0)}{(c^* - c_L)} = k_L at$$

where: c* is the final oxygen concentration (mg/L), c_0 is the initial oxygen concentration (mg/L), c_L is the oxygen concentration in the liquid phase (mg/L) and t is the time to reach the final oxygen concentration(s).

k_La can be determined from the slope of the linear plot of $\ln[(c^*-c_0)/(c^*-c_L)]$ against t.

2.2.5 Effect of liquid height

Liquid height poses the hydrostatic pressure in the system which could affect both hydrodynamic and mass transfer behaviors in a contactor. This work aimed to investigate such relationships where the unaerated liquid height was varied from 40, 50, 60 cm and height at 100 L water (fill 100 L of water in the reactor and measure the water height from bottom of the reactor). The fixed reactor width of 40 cm was used in this study.

3. Results and Discussion

3.1 Riser and downcomer cross-sectional area

Figure 3 shows the riser cross section area ratio at different widths of reactor and air flow rate. It indicates the riser cross section area increased with the increase in the reactor width at the same air flow rate. At the same reactor width, the riser cross sectional areas slightly increased with air flow rate.

The downcomer to riser cross section area ratios (A_d/A_r) at different widths of reactor and air flow rate are shown in Figure 4. The A_d/A_r decreased with increasing air flow rate.

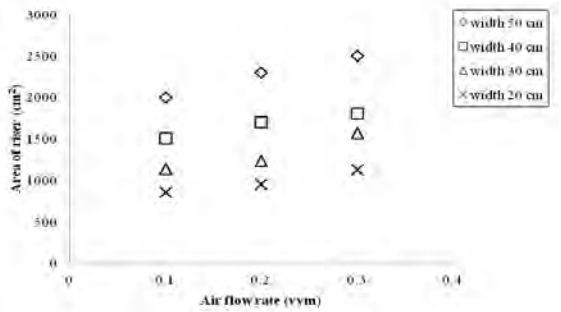

Figure 3 Riser cross sectional areas for different reactor widths

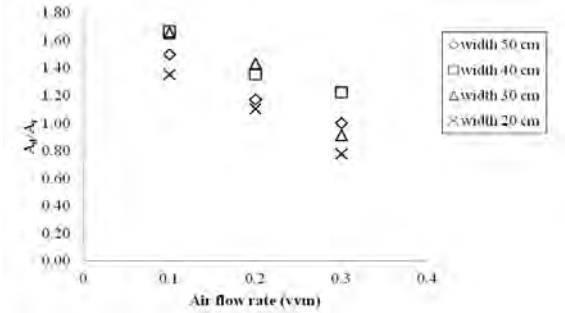

Figure 4 Downcomer to riser cross sectional area ratios for different reactor widths

3.2 Gas holdup

Air flow rate used in this experiment was 0.1, 0.2 and 0.3 vvm (10, 20 and 30 l/min). These were quite low such that the pressure differences between the two measuring ports of reactor were insufficient to allow visual observation.

3.3 Downcomer liquid velocity

Figure 5 shows the liquid velocities in downcomer evaluated for various air flow rates. For all reactor widths, the dowmcommer liquid velocity slightly increased with air flow rate. Similar results were also reported by Kochbeck [1], Freitas [2] and Simcik et al. [3].

On the other hand, the downcomer liquid velocity was also affected by the width of reactor. Figure 5 indicates that the downcomer liquid velocity at the width of reactor 50, 40 and 30 cm were nearly the same at the same air flow rate whilst downcomer liquid velocity of width 20 cm was the smallest. Chisti [4] and Wongsuchoto [5] reported that, at the same superficial gas velocity, the riser liquid velocity increased with an increase in the riser cross sectional area. This was because a smaller riser area normally induced a faster liquid velocity in the riser and decreased the mean residence time of bubbles in the riser resulting in an increase in bubbles being dragged from the gas separator down into the downcomer so that downcomer liquid velocity decreased. This indicated that the downcomer liquid velocity of the reactor with the width of 20 cm took the lower value because the riser cross section area of the 20 cm width reactor was the smallest (Figure 3).

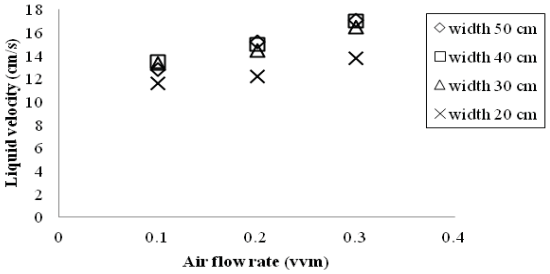

Figure 5 Liquid velocity in downcomer for reactors with different widths

3.4 Mass transfer

Experimental data of the overall volumetric gas-liquid mass transfer coefficient (k_La) for different widths of the reactor are shown in Figure 6. It is clear that k_La increased with an increase in air flow rate for all widths of the reactor. The lowest k_La was obtained with width of 20 cm because small riser cross sectional area led to faster liquid velocity. This resulted in a smaller difference between bubble and liquid velocities which then lowered the mass transfer coefficient between gas bubbles and liquid [7-8].

3.5 Effect of liquid height

The effect of liquid height was investigated only at the reactor width of 40 cm. The unaerated liquid height (h_u) changed according to the liquid volume within the reactor, i.e. at h_u = 37 cm, the total volume is equal to 100 L, at h_u = 40 cm, the volume is 120 L, at h_u = 50 cm, the volume is 160 L and at h_u = 60 cm, the volume is 200 L. The effect of unaerated liquid height on the downcomer liquid velocity is shown in Figure 7. This indicates that the downcomer liquid velocity increased linearly with the air flow rate and unaerated liquid height. When the unaerated liquid height increased, an increase in the liquid velocity was observed as the gas bubbles stayed longer in the reactor and a greater energy transfer between gas bubbles and liquid occurred [6]. This resulted in a faster liquid movement.

The unaerated liquid height had a small effect on k_La as can be seen in Figure 8. Increasing liquid height although resulted in a faster liquid velocity which should decrease k_La, however, it posed a stronger hydrostatic pressure which prevented the bubbles from coalescing with each other. This maintained the large contact area between bubbles and liquid which rendered a higher k_La in such systems.

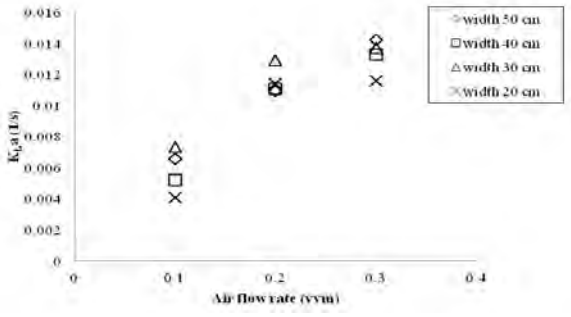

Figure 6 k_La in airlift reactors with different widths

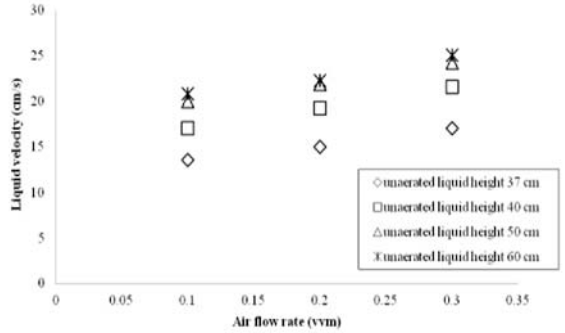

Figure 7 Downcomer liquid velocity in airlift reactors with different unaerated liquid heights

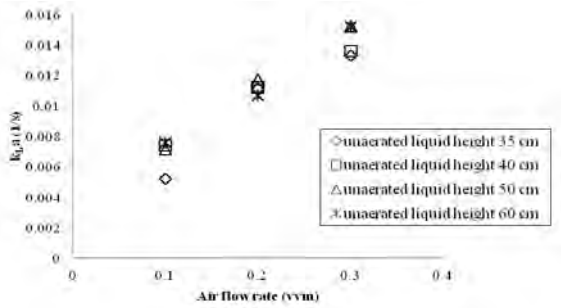

Figure 8 k_La in airlift reactors with different unaerated liquid heights

3.6 Performances of draft tube and non-draft tube airlift reactors

The downcomer liquid velocity and k_La were compared between natural induced flow (non-draft tube) and draft tube airlift reactors with the width of 20 cm. Figure 9 indicates that the downcomer liquid velocity of non-draft tube was lower than that in the draft tube system. This was because the virtual circulating loop induced in the non-draft tube system was not as rigid as that in the draft tube airlift. This resulted in a slower liquid movement in the non-draft tube, which naturally raised the mass transfer rate as the differences between liquid and bubble velocities became larger. These results are illustrated in Figure 10.

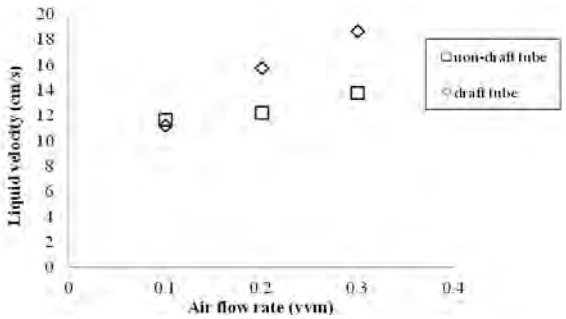

Figure 9 Downcomer liquid velocity in non-draft tube and draft tube airlift reactors

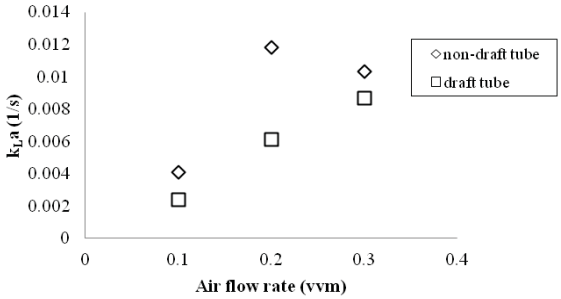

Figure 10 k_La between non-draft tube and draft tube airlift reactors

4. Conclusions

This work provides the design fundamentals of the two types of airlift systems, i.e. typical draft tube airlift and the novel non draft tube, so call "Natural induced-flow plat panel airlift reactors". Not only that, the flat panel airlift of various widths, i.e. 20, 30, 40, and 50 cm, were investigated for their different performances. The examination revealed that the downcomer liquid velocity and k_La of width of reactor at 20 cm was the lowest, whilst the performances of the other reactors did not vary significantly from each other. The unaerated liquid velocity has a large effect on the downcomer liquid velocity but not significantly affect k_La. The mass transfer of natural induced flow airlift reactor was higher than the draft tube reactor but the opposite was found for the liquid velocity.

Acknowledgements

The authors would like to acknowledge the financial supports from Engineering Research Unit for Value Adding of Bioresources, Department of Chemical Engineering, Faculty of Engineering, Chulalongkorn University.

References

[1] B. Kochbeck, *Chemical Engineering Technology.* **17** (1994) 401–405.
[2] C. Freitas, *Chemical Engineering Technology.* **54** (1999) 5253-5258.
[3] M. Simcik, A. Mota, M.C. Ruzicka, A. Vicente and J. Teixeira, *Chemical Engineering Technology.* **66** (2011) 3268-3279.
[4] M.Y.Chiti, *Airlift Bioreactors*, Elsevier, London and New York (1989).
[5] P. Wongsuchoto and P. Pavasant, *Chemical Engineering Journal.* **100** (2004) 1-9.
[6] C. Bentifraouine, C. Xuereb and J.P. Riba, *Chemical Engineering Journal.* **64** (2009) 91-95.
[7] WT.Wu, JY.Wu and JZ.Jong, *Biotechnology Progress.* **8** (1992) 465-468.
[8] J.V.Littlejohns, A.J.Daugulis, *Chemical Engineering Journal.* **66** (1997) 4171-4177

CONVERT OF BAGASSE FLY ASH TO SODIUM SILICATE

Titimat Suksawatsak[1],Tawan Sooknoi[2], Prasert Pavasant[1*]

[1]*Chemical Engineering Research Unit for Value Adding of Bioresources, Department of Chemical Engineering, Faculty of Engineering, Chulalongkorn University, Phayathai Rd., Patumwan, Bangkok 10330*
[2]*Department of Chemistry, Faculty of Science,King Mongkut's Institute of Technology Ladkrabang, Chalongkrung Road, Ladkrabang, Bangkok 10520*
[*] Author for correspondence: E-mail: prasert.p@chula.ac.th

Abstract: Bagasse has been used as a raw material substitution for fossil fuel as it is renewable with relatively high heat capacity. The burning of bagasse, although is considered carbon neutral, ends up with the generation of a large amount of fly ash. Depending on the nature of bagasse, the composition of fly ash varies significantly, but mostly with a high composition of Si. This work intends to find the suitable conditions for the conversion of bagasse fly ash (BFA) to sodium silicate which can find its use in various applications such as zeolite, nutrient substitute, detergent and cleaning compound etc. Such conversion is subjected to parameters, i.e. temperature (650-950^{o}C), time of reaction (30-120 min) and amount of alkali source. The alkali source employed in this work is sodium carbonate (Na_2CO_3). High yield of sodium silicate from BFA is obtained at the conversion temperature of 850°C, 60 min with SiO_2:Na_2CO_3 molar ratio of 1:1.25. Properties of sodium silicate are analyzed by X-ray fluorescence spectrometry (XRF) and Inductive Coupled Plasma Optical Emission Spectroscopy (ICP-OES) for chemical composition, FT-Raman (Fourier Transform Raman Spectrophotometer) for chemical framework, and solid crystal structure determined by X-ray diffraction (XRD).

1. Introduction

Bagasse has been used as a raw material substitution for fossil fuel as it is renewable with relatively high heat capacity. The burning of bagasse, although is considered carbon neutral, ends up with the generation of a large amount of fly ash that needs to be dealt with. Typically BFA is disposal which generates transportation and landfill costs. It is estimated that landfill of BFA would cost around 800-1,500 THB/ton depending on the locations of the plant and the landfill site, and for a 10 ton coal fire boiler, about 10 tons of BFA is generated daily.

Electricity in Thailand is mostly produced from fossil fuel power plants. Among the several fuel types, coal fire power plants are among the largest. Smaller electricity generators use more of biomass fuel as this will help reduce the CO_2 emission and is considered carbon neutral. However, due to the existing of noncombustible components in bagasse, the burning of bagasse generally ends up with large amount of ash both bottom and fly ashes.

Fly ash can be utilized in several applications. It can either be used as precursor for the production of jardiniere, ceramics. A more typical use is to mix fly ash in concrete and use as construction material.

As fly ash contains mostly silica (SiO_2), this can be applied as raw material for some chemical compounds such as Sodium silicate (Na_2SiO_3). Sodium silicate can be used in several industrial utilization, the demand of sodium silicate increases as it can be used in washing powder or detergent, industrial ceramics and petrochemical etc.

Sodium silicate from bagasse fly ash was by this work of attend chemical compound process. This chemical compound can be substrate for many processes such as zeolites synthesis, catalyst synthesis, wastewater treatment, geopolymer and moreover use for industrial washing. Effect to large usability be can high demand and suitable reduce emission of industrial.

Typically, if silica source was fly ash (FA), the setting reaction temperature must be at above 500 °C and ratio of FA:NaOH with 1:1.2 by weight [1,2], but when silica analytical reagent is used, this will be fused at temperature higher than 1400°C [3-5]. Alkali sources can be either sodium hydroxide or sodium carbonate where sodium hydroxide often creates mixing problem as it tends to pile up in the reactor. Sodium carbonate is in a powder form and allows an easier mixing. One precaution is that the sodium silicate product can undergo phase change which normally takes place at very high temperature [3].

Sample was ground about 1 day by ball mill, after that sample was period dissolve about 1 day with 1:5 with weight ratio of sample:water [2,6] and that sample was separated solid and solution by centrifuge[3]

2. Materials and Methods

2.1 Raw Materials

Bagasse fly ash (BFA) from only one local factory in Ratchaburi province was obtained in the year 2012. Commercial sodium carbonate anhydrous (molecular weight 105.98 grams/mol, Na_2CO_3, CARLO ERBA, Purity ≥ 99.5%, white powder) and distilled water.

2.2 Methods

The pathway to produce sodium silicate from fly ash is illustrated Eq. (1) where SiO_2 reacts with Na_2CO_3 and is converted to Na_2SiO_3 and carbon dioxide.

$$SiO_2(s) + Na_2CO_3(s) \longrightarrow Na_2SiO_3(s) + CO_2(g) \quad (1)$$

Steps in synthesizing sodium silicate by hydrothermal method are shown as followed

2.2.1 Mix BFA and sodium carbonate at molar ratio of SiO_2:Na_2CO_3 with 1:(0.75 to 3.25)

2.2.2 Transfer the mix powder to crucible

2.2.3 Determine the weight of mixed powder

2.2.4 Fuse the mix powder at setting reaction temperature of 650°C-850°C and setting time about 30-120 minutes

2.2.5 Cool the samples down at 60°C with air reducing temperature

2.2.6 Determine the weight loss of sample

2.2.7 Grind the sample to powder

2.2.8 Dissolve the sample with distilled water

2.2.9 Separate the precipitate and the solution by filtration

2.2.10 Analyze the components using ICP

2.3 Analytical Instrument

2.3.1 XRF by X–Ray Fluorescence Spectrometer (XRF), Wavelength Dispersive, Model Philips PW2400

XRF is used to analyze the amount of each chemical composition, sample can be solid, liquid and colloid. This technique does detect the X-ray fluorescence discharged by each element which has specific fluorescent wavelength. Therefore this shows chemical composition and its quantity in the sample.

2.3.2 ICP-OES by Inductively Coupled Plasma Optical Emission Spectrometer (ICP-OES), Model Agilent Technology ICP-Plasma-710

Element analysis is measured with atomic spectroscopy by heating up the liquid sample until the atom is ionized, atomic plasma or ions are activated and release light at specific wavelength which are measured by detector. Intensity by wavelength depends on the amount of elements in sample.

2.3.3 XRD by X–Ray Diffractometer (XRD) with Super Speed Detector, Model Bruker D8-Discover

Morphology of material is analyzed with X-ray diffraction at 5°- 60° for its crystalline structure. This will reflect the sample chemical composition and chemical structure.

2.3.4 FT-Raman by Fourier Transform Raman Spectrometer (FT-Raman), Model Perkin Elmer Spectrum GX

FT-Raman can detect both organic and inorganic materials with spectroscopy in frequency range of 400-3500 cm^{-1}. Structure is analyzed by the adsorption of light at difference frequency as the frequency is specific to the particular structure.

3. Results and Discussion

Table 1 presents the composition bagasse fly ash analysted by XRF. BFA is mostly constituted of silicon dioxide (SiO_2) as a major component, aluminium oxide (Al_2O_3), calcium oxide (CaO), magnesium oxide (MgO), and iron oxide (Fe_2O_3) as main components, and some heavy metal compounds such as arsenic (As), barium (Ba), beryllium (Be), borom (B), cadmium (Cd), chromium (Cr), Cobalt (Co), copper (Cu), fluorime (F), lead (Pb), manganese (Mn), nikel (Ni), vanadium (V) and zinc (Zn) etc. as minor components.

ICP-OES silica results of soluble sodium silicate synthesized at each condition are shown in Figure 1. Optimum setting temperature of reaction was 830°C-850°C, that had activation energy for reaction of sodium silicate between bagasse fly ash and sodium carbonate. From Eq. 1, sodium silicate synthesized with SiO_2:Na_2CO_3 ratio of 1:1.25 by molar showed the high amount of silica. 30% silica element in soluble sodium silicate were detected.

Figure 2, XRD patterns of sodium silicate synthesized with suitable reactant, bagasse fly ash and sodium carbonate reactant were presented. Conversion of sodium silicate was achieved by increasing the setting temperature of reaction. Suitable condition for sodium silicate synthesis from bagasse fly ash was in setting temperature range of 830°C-850°C and SiO_2:Na_2CO_3 ratio of 1:1.25 by mole. Setting time was studied between 30-120 minutes. At 30 minutes, synthesis was incomplete remaining the sodium carbonate in product. So sodium silicate synthesis had completed at setting reaction time of 60 minutes.

Table 1 Composition of bagasse fly ash with XRF analysis

Compound	Concentration (%) weight	Compound	Concentration (%) weight
Na_2O	0.349	TiO_2	0.251
MgO	1.667	Cr_2O_3	0.026
Al_2O_3	3.668	MnO_2	0.158
SiO_2	61.81	Fe_2O_3	1.791
P_2O_5	2.146	NiO	0.007
SO_3	2.959	ZnO	0.01
Cl	0.991	SrO	0.005
K_2O	3.193	ZeO_2	0.014
CaO	1.913	BaO	0.043

Raman spectra (Figure 3) show an absorption band at 1060-1200 cm^{-1} with appearance of Si-O band stretching. Sodium silicate synthesis with SiO_2:Na_2CO_3 with 1:1.25, setting reaction at 850°C and 60 minutes showed the Si-O stretching at 1060 cm^{-1}.

In addition, the intensity of Si-O-Si planes (rocking mode) in the three-dimensional network is symmetric oxygen stretching vibration of 440 cm^{-1}, and Si-O-Si (bending mode) stretching peak appears at 800 cm^{-1} approximately. For weak peak at 600 cm^{-1}, it is explained by SiO_4 tetrahedral structure.

The intensity shows with Na_2O absorption band at near 950 cm^{-1}

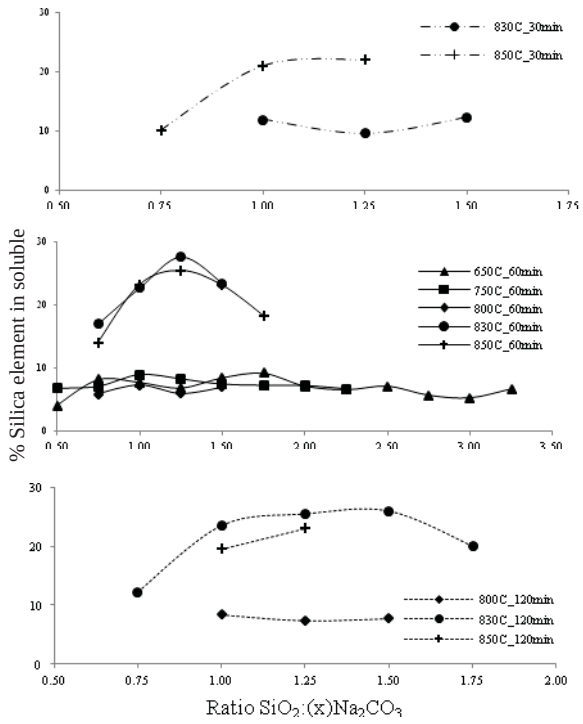

Figure 1 ICP-OES of soluble sodium silicate synthesized with setting time of 30, 60 and 120 min

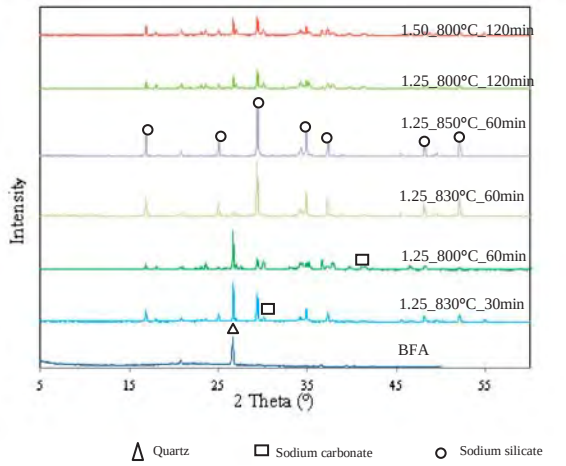

Figure 2 XRD diffraction patterns of sodium silicate synthesized with setting time 30, 60 and 120 min

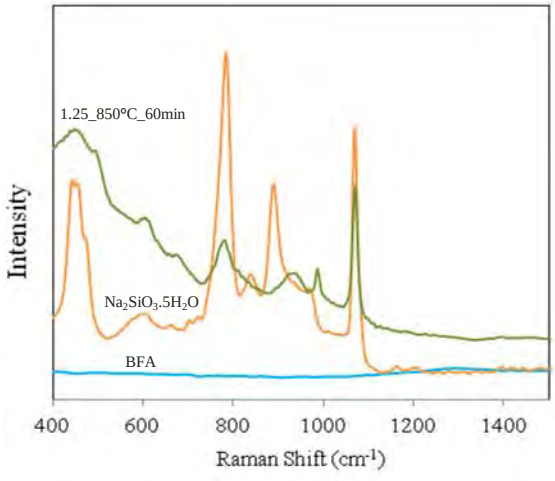

Figure 3 Raman spectra of sodium silicate synthesized at SiO_2:Na_2CO_3 ratio of 1:1.25 by mole, 850°C and 60 min

4. Conclusions

This work intends to find the suitable and optimum conditions for the conversion of bagasse fly ash (BFA) to sodium silicate. Content of soluble silicon represents the yield of sodium silicate synthesised from BFA. Optimum condition for synthesis is setting reaction temperature of 850°C, setting reaction time of 60 minutes and molar ratio SiO_2:Na_2CO_3 of 1:1.25.

Acknowledgements

This work is supported by Chemical Engineering Research Unit for Value Adding of Bioresources, Department of Chemical Engineering, Faculty of Engineering, Chulalongkorn University.

References

[1] Claudia Belviso, Francesco Cavalcante, Antonio Lettino, Saverio Fiore, *Ultrasonics Sonochemistry* **18** (2011) 661-668.

[2] Nicholas M. Musyoka, Leslie F. Petrika, Eric Hums, Hasan Baser, Wilhelm Schwieger, *Catalyst Today* **190** (2012) 38-46.

[3] Mei-rong Yuan, Jin-tang Lu, Gang Kong, Chun-shan Che, *Surface & Coatings Technllogy* **205** (4466-4470).

[4] Shigeru Yamashita, Harald Behrens, Burkhard C. Schmidt, Ray Dupree, *Chemical Geology* **256** (2008) 231–241.

[5] Yi Ding, Guangfu Yin, Xiaoming Liao, Zhongbin Huang, Xianchun Chen, Yadong Yao, *Materials Letters* **75** (2012) 45-47.

[6] Chandra Wahyu Purnomo, Chris Salim, Hirofumi Hinode, *Microporous and Mesoporous Materials* **162** (2012) 6-13 .

PRODUCT DISTRIBUTION OF ELECTROCHEMICAL CONVERSION OF GLYCEROL VIA Pt ELECTRODE

Payia Saila[1], Mali Hunsom*

[1]*Department of Chemical Technology, Faculty of Science, Chulalongkorn University, Bangkok, 10330 Thailand*
[*]*Center of Excellence on Petrochemical and Materials Technology (PETRO-MAT), Chulalongkorn University, Bangkok 10330, Thailand*
**E-mail:payiakiss@hotmail.com*

Abstract: The product distribution of the electrochemical conversion of glycerol to valuable compounds was evaluated with platinum (Pt) electrode under galvanostatic conditions. Effects of initial pH of glycerol and electrolysis time were investigated. The preliminary results demonstrated that either initial pH of glycerol or electrolysis time affected the glycerol conversion as well as types of product and product yield. Greater than 80% of glycerol was converted within 10, 17 and 15 hr at pH 1, 7 and 11, respectively by using current intensity of 4.5 A, and various compounds such as acetol, 1,2-propanediol, 1,3-propanediol, glycidol, etc were generated.

1. Introduction

Glycerol is an important feedstock for industrial application including food products, solvent, pharmaceutical industries and others application. Since glycerol forms the backbone of triglycerides, it can be produced by soap production industry and also as a by-product from transesterification reaction of biodiesel production [1]. Many processes have been developed to make value-added glycerol-based products. For example, the biological production of 1,3-propanediol from glycerol has been demonstrated for several bacterial strains; most prominently in *Klebsiella*, *Clostridium* species and heterologously in *Escherichia coli* by metabolic engineering [2-5]. In heterogeneous catalysis, several monometallic (Pt, Pd, Au) [6-7] and bimetallic catalysts (Pt-Bi, Au-Pt) [6,8-11] have been investigated and revealed that the Pt-Bi bimetallic system showed a promising conversion and selectivity toward DHA at low pH and mild operating conditions [10]. Also homogeneous catalysts have been reported for the selective glycerol oxidation to DHA [12]. The electrochemical technique is an alternative method to reform glycerol due to its unique features such as simplicity and robustness in structure and operation [13]. The selective conversion of glycerol to DHA may be achieved by electro-catalytic oxidation on a carbon-supported platinum (Pt/C) electrode in a bismuth saturated acidic solution [14-15,16].

In this paper, the electrochemical technique has the potential to develop a cost-effective technology for glycerol reforming to 1,2-propanediol, 1,3-propanediol, glycidol and many others products.

2. Materials and Methods

2.1 Chemical substances

The aqueous glycerol solution was prepared from a commercial glycerol stock (99.5%, Fisher) at constant concentration of 0.3 M. The pH of glycerol solution was adjusted by analytical grade H_2SO_4 (98%, Qrec) or NaOH (1 M, Qrec).

2.2 Polarization curve

The possibility of electrochemical conversion of glycerol at different pH (1, 7 and 11) was performed using a Potentiostat/Galvanostat (Auto Lab, model PG stato). Two Pt grids in cylindrical structure were used as working and counter electrodes, while Ag/AgCl was used as reference electrode. The scan potential was varied in the range from +1.75 to -0.50 V with a scan rate of 5 mV/s. In each set, the system was agitated by a magnetic stirrer at a constant rate of 650 rpm.

2.3 Electrochemical conversion of glycerol

The electrochemical system was performed in a laboratory scale at ambient temperature and pressure. The electrochemical reactor was made from Pyrex glass having a total capacity of 0.6 L. Two Pt grids in a cylinder shape were used as the anode and cathode, respectively. The temperature of electrolytic cell was controlled by a cooling system, a magnetic bar was used to stir the electrolyte in the electrolytic cell at 650 rpm. A regulated DC power supply (ZS 3205-2X type) was employed to supply the external electricity at a galvanostatic mode (4.5A).

2.4 Analytical methods

The chemical compounds generated in the electrochemical reactor were analyzed by gas chromatography equipped with flame ionization detector (Hewlett Packard/HP 5890 Series II). The conversion of glycerol was analyzed by High Performance Liquid Chromatography (HPLC: Agilent 1100) with a RID-10A refractive index detector. The stationary phase was a Pinnacle II C18 column (240 × 4.6 mm) and the mobile phase was a 99.9:0.1 (v/v) ratio of 10 mM H_2SO_4: pure CH_3OH, passed through the column at 0.5 ml/min.

3. Results and Discussion

3.1 Polarization curve

Fig. 1 shows the polarization curve of glycerol solution at pH 1, 7 and 11. At pH 1, the oxidation of glycerol was observed at the potential of +0.3477 V (peak B) and the reduction of glycerol was observed at the potential of -0.2962 V (peak A), which gave the maximum current intensity of 1.891 mA and 0.356 mA, respectively. At the potential greater than 0 V, the significant increase of current was observed as the

region D, causing by the reduction of H^+ to H_2. Also, at the potential greater than -0.76 V, significant change of current intensity was observed due to the oxidation of H_2O to O_2 (region E). At neutral pH, the oxidation--reduction of glycerol was not clearly observed during the investigated potential range. It was appeared a wide shoulder as demonstrated as the insert of Fig.1. At the potential lower than -0.1 V and greater than +0.75 V, it had the formation of H_2O reduction to H_2 and H_2O oxidation to O_2, respectively. For the polarization curve of glycerol solution at pH 11, the forward scan did not represent the oxidation-reduction peaks obviously, except the reduction of H_2O to H_2 at potential greater than 0 V. For the backward scan, the oxidation peak of glycerol was observed at the

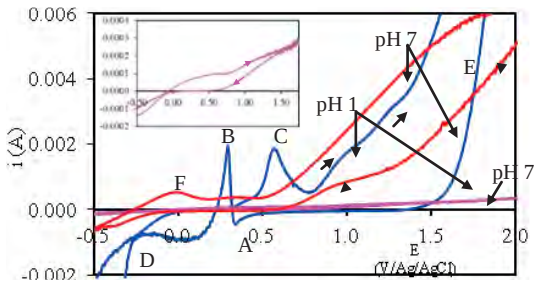

Fig.1 Polarization curved of 0.3 M glycerol at different pH via Pt electrode.

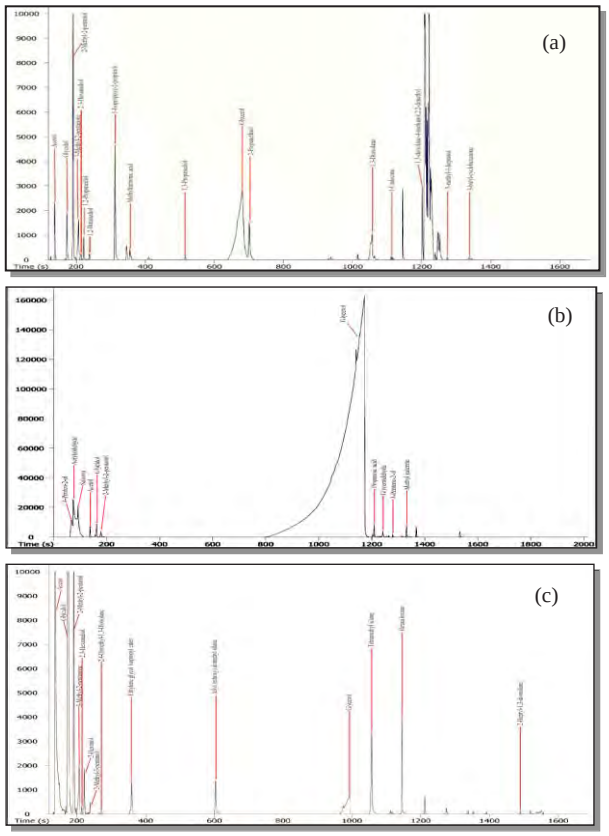

Fig.2 Representative GC/MS spectra of glycerol solution at pH (a) 1, (b) 7 and (c) 11 by using Pt electrode.

potential of -0.0331 V (peak F), providing the maximum current intensity of 0.548 mA. According to the polarization curve, it can be said that glycerol can be oxidized or reduced under strong acid and basic conditions [17].

Fig. 2 demonstrates the product analysis generated from the electrochemical conversion of glycerol different pH values. For example, acetol, glycidol and 2-methyl-2-pentanol were generated by electrochemical conversion of glycerol at all investigated pH values. Other compounds such as 1,2-propanediol, 1,3-propanediol, 1,2-butanediol, 5-methyl-1-heptanol were produced in acid condition; whilst acrolein and glyceraldehyde were produced under basic condition. Various generated compounds have a higher market value and also have a high market capacity and application in industries, as listed in Table 1.

3.2 Glycerol conversion and product distribution

Fig.3 exhibits the conversion of glycerol solution (0.3 M) by electrochemical technique at current intensity of 4.5 A during 0-24 hr electrolysis time. It was clear that the conversion of glycerol increase as the increase of electrolysis time. High conversion was observed under strong acid condition compared with that of neutral and basic conditions. The conversion of glycerol was greater than 99.5 at 18 hr electrolysis time, while those of pH 7 and 11 were around 91.0 and 87.1, respectively. This is because the dehydration reaction can proceed effectively under strong acid condition [1], resulting to high conversion of glycerol.

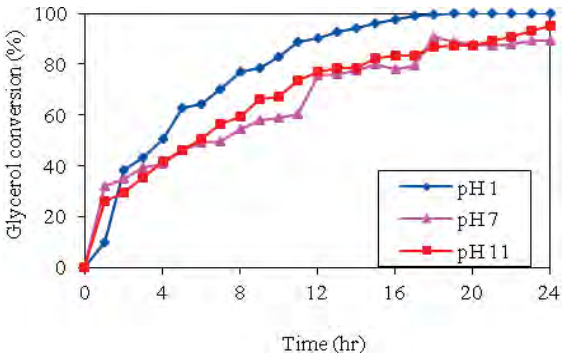

Fig.3 Glycerol conversion by electrochemical technique at different pH values and current intensity of 4.5 A. by using Pt electrode.

Fig. 4 reveals the product distribution of electrochemical conversion of glycerol at different pH values and current intensity of 4.5 A by using Pt electrode. The generated products which can be detected and measured at pH 1 were ethylene glycol, acetol, glycidol, acrolein, ethanol, 1,2-propanediol and 1,3-propanediol at electrolysis time of 8,1, 1, 6, 14, 10 and 15 hr, respectively (Fig. 4(a)). Some of them increased as a function of time and remained constants such as acetol, glycidol, 1,2-propanediol, 1,3-propanediol and ethanol. The rest of them including ethylene glycol and acrolein increased as a function of time during early

Table 1. Listed of compounds generated from elctrochemcial conversion of glycerol.

Chemical substances	pH 1	pH 7	pH 11	USD (purity, %) [CAS no.]
Acetol/ hydroxyacetone	✓	✓	✓	55.63/100g(90%)[a] [116-09-6]
Glycidol	✓	✓	✓	61.13/100g(96%)[b] [556-52-5]
2-methyl-2-pentanol / Dimethyl propyl carbinol	✓	✓	✓	79.23/10g(99%)[c] [590-36-3]
3-methyl-2-pentanone	✓		✓	381.84/25g(99%) [565-61-7]
2,3-hexanediol	✓		✓	80.96/1mL(99%)[c] [617-30-1]
1,2-propanediol	✓			95.05/500mL(>99.5%)[c] [57-55-6]
1,2-butanediol	✓			174.94/1L(>98.0%)[d] [584-03-2]
1-isopropoxy-2-propanol	✓			213.45/1g(98%)[c] [3944-36-3]
1,3-propanediol	✓			48.18/100g(98%)[c] [504-63-2]
1,3-dioxolane	✓			165.51/1L(99%)[c] [646-06-0]
1,3-dioxolane-4-methanol,2,2-dimethyl	✓			49.23/100g(98%)[c] [100-79-8]
5-methyl-1-heptanol	✓			894.0/1mL(96%)[c] [57803-73-3]
2,4-dimethyl-1,3-dioxane			✓	105.04/10g[c] [766-20-1]
Ethylene glycol isopropyl ether			✓	65.04/1L(99%)[c] [109-59-1]
2-hexanol			✓	262.96/100g(>98%)[c] [626-93-7]
Tetramethylsilane			✓	57.99/25g (>99.9%)c [75-76-3]
4-methyl-1-hexanol			✓	104/1mL(>98%)[c] [1767-46-0]
Acrolein/acryraldehyde		✓		150/1kg(97%)[c] [107-02-8]
4-Pentene-2-ol		✓		111.72/5g (99%)[c] [625-31-0]
Propanoic acid/ Propionic acid		✓		67.35/100mL (>99.5%)[c][79-09-4]
3-Pentene-2-ol		✓		815.19/25g (96%)[c] [3899-34-1]
Glyceraldehyde		✓		1866.1/25g (>90%)[c] [56-82-6]
Methyl valerate		✓		109.71/1kg (>99%)[C] [624-24-8]

[a]Technical grade; [b]Natural grade; [c]Reagent grade; [d]Purum grade

period of experiment and then decreased. This demonstrated that ethylene glycol and acrolein are the intermediate substances that can be further converted to other products under strong acid condition. Among the generated products, maximum product yield was observed for acetol and the 1,3-propanediol at 20% and 19%, respectively.

Under neutral condition, the detected products were ethylene glycol, acetol, glycidol, acrolein and ethanol at electrolysis time of 9, 1, 1, 9 and 1 hr, respectively (Fig.4 (b)). The yield of ethylene glycol, glycidol, ethanol and acrolein increased as the increase of electrolysis time, whereas the yield of acetol increased as a function of electrolysis time up to 15 hr and it decreased afterward. This implies that acetol can convert to other substance under neutral condition. According to the obtained results, the maximum yield of glycidol was observed at 29.6% at 20hr electrolysis time.

Under strong basic condition, various products including ethylene glycerol, acetol, acrolein, ethanol were detected at 7, 2, 1, 12 and 9 hr electrolysis time, respectively (Fig.4(c)). The product yield of glycidol, ethylene glycerol, ethanol and acrolein increased as the increase of electrolysis time, whilst the acetol increased to 12% at 4 hr and decreased afterward. Under this condition, the maximum product yield was observed for glycidol at 31.9% at electrolysis time of 20 hr.

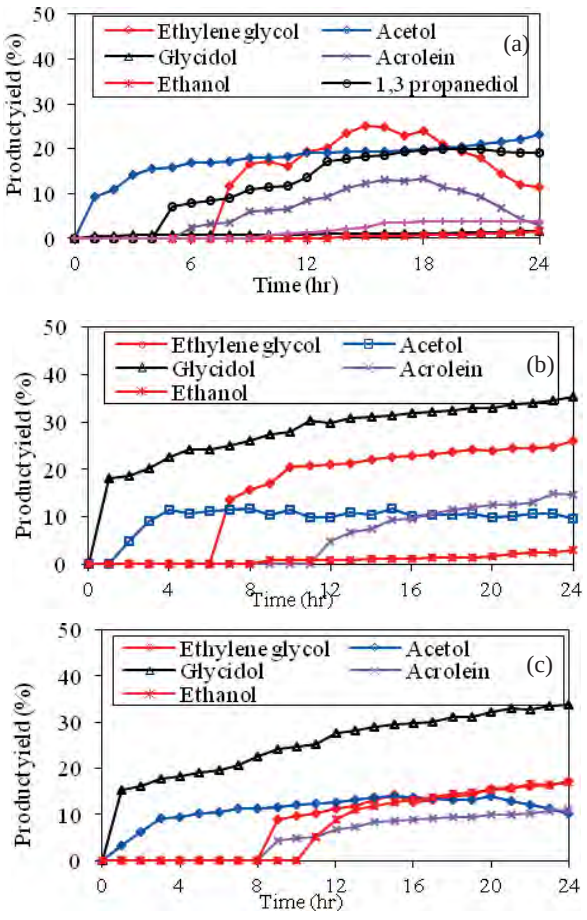

Fig.4 Product distribution of electrochemical conversion of glycerol at different pH values and current intensity of 4.5 A by using Pt electrode.

4. Conclusions

The generated products at different pH values were ethylene glycol, acetol, glycidol, acrolein, ethanol, 1,2-propanediol and 1,3-propanediol. The electrochemical conversion of glycerol under strong acid was higher than 99.5% at 18 hr electrolysis time because the dehydration reaction can proceed effectively in this condition, resulting to high conversion of glycerol. Under neutral and basic conditions were around 91.0 and 87.1%,, respectively. The maximum product yield of strong acid was observed for acetol and the 1,3-propanediol at 20% and 19% while under neutral condition the maximum yield of glycidol was observed at 29.6% and at strong basic condition, glycidol was observed for the maximum yield at 31.9%. Some of these products are the intermediate substances that can be further converted to other products but some of them increased as a function of time. However, to achieve a higher yield of each desired compound, the specific electrochemical conditions, such as concentration of glycerol and applied current density, etc., need to be resolved.

References

[1] D.T. Johnson, K.A.Taconi, *Environ. Prog* **26** (2007) **338- 348.**

[2] I.T. Tong, et al, *Appl. Environ. Microbiol* **57** (1991) 3541–3546.

[3] M. Gonza´lez-Pajuelo, et al, *Appl. Environ. Microbio* **72** (2006) 96–101.

[4] Z.L. Xiu, A.P. Zeng, *Appl. Microbiol. Biotechnol* **78** (2008) 917–926.

[5] X. Tang, et al, *Appl. Environ. Microbiol* **75** (2009) 1628–1634.

[6] S. Demirel, K. Lehnert, M. Lucas, P. Claus, *Appl. Catal. B* **70** (2007) 637−643.

[7] S. Carretin, P. McMorn, P. Johnston, K. Griffin, C. Kiely, G. J. Hutchings, *Phys. Chem. Chem. Phys* **5** (2003) 1329−1336.

[8] H. Kimura, K. Tsuto, T. Wasisaka, Y. Kazumi, Y. Inaya, *Appl.Catal.* **96** (1993) 217−228.

[9] H. Kimura, *Appl. Catal.* **105** (1993) 147−158.

[10] W. Hu, D. Knight, B. Lowry, A. Varma, *Ind. Eng. Chem. Res*. **49** (2010) 10876−10882.

[11] N. Wörz, A. Brandner, P. J. Claus, *Phys. Chem.* **114** (2010) 1164−1172.

[12] R. M. Painter, D. M. Pearson, R. M. Waymouth, *Angew. Chem. Int. Ed.* **49** (2010) 9456−9459.

[13] N.A. Grace, K. Pandian, *Electrochemistry Communications* **8** (2006) 1340–1348.

[14] R. Ciriminna, G. Palmisano, D.C. Pina, Rossi, M. Pagliaro, *Tetrahedron Letters*. **47** (2006) 6993–6995.

[15] M. El. M. Chbihi, D. Takky, F. Hahn, H. Huser, J.M. Le´ger, C. Lamy, *Electroanalytical Chemistry* **463** (1999) 63–71.

[16] Y. Kwon, Y. Birdja, I. Spanos, P. Rodriguez, T. M. Koper, *ACS Catalysis* **2** (2012) 759-764.

[17] S. Kongjoa, S. Damrongleard and M. Hunsom, *J. Appl. Electrochem.* **41** (2011) 215-222.

PERFORMANCE EVALUATION OF MEMBRANE REACTOR WITH NON-UNIFORM MEMBRANE ALLOCATION AND CATALYST DENSITY DISTRIUTION

Akkarapon Cheevataranakorn[1], Pakorn Piroonlerkgul[1], Suwimol Wongsakulphasatch[2], Supawat Vivanpatarakij[3], Worapon Kiatkittipong[2], Suttichai Assabumrungrat[1,*]

[1] Center of Excellence in Catalysis and Catalytic Reaction Engineering, Department of Chemical Engineering, Faculty of Engineering, Chulalongkorn University, Bangkok, 10330, Thailand
[2] Department of Chemical Engineering, Faculty of Engineering and Industrial Technology, Silpakorn University, Nakhon Pathom 73000, Thailand
[3] Energy Research Institute, Chulalongkorn University, Phyathai Road, Wang Mai, Phatumwan, Bangkok 10330, Thailand

*E-mail: Suttichai.A@chula.ac.th

Abstract: Membrane reactor is an attractive hydrogen production unit due to its lower energy consumption and operating cost, higher hydrogen purity in gas product compared to those of a conventional unit. Inside this reactor, steam reforming and water gas shift (WGS) reactions take place to generate hydrogen which is simultaneously separated from reaction chamber in order to thermodynamically enhance hydrogen yield. Pd-based membrane is equipped in the membrane reactor as a hydrogen separator owing to its high hydrogen selectivity. By the fact that the rate of reaction should not be too fast at the initial zone of the reactor to prevent cold-spot problem, the use of high catalyst packing density and installation of Pd-membrane into this reactor zone might not be useful. Therefore, the uniform distribution membrane reactor should not be the best reactor configuration. Varying distribution of membrane area and catalyst in a membrane reactor is a potential approach to improve its performance. In this work, mathematical model taking into account mass and energy balances was used as a tool to evaluate the performance of methane steam reforming in a shell-and-tube membrane reactor with different reactor configurations. Tubes inside the reactor were made from two materials, i.e. Pd-base membrane and stainless steel tube, while catalyst and inert were packed in the annulus. The reactor was divided into two sections containing different amount of membrane area and catalyst weight; however, total amount of membrane area and catalyst were kept constant for all scenarios. The results showed that, for a 2-section reactor, the membrane reactor equipped with lower density of catalyst and membrane area in the first section could offer higher hydrogen yield and methane conversion than those equipped with higher density of catalyst and membrane area in the first section. There were some ranges in which the operation under non-uniform distribution outperforms that of uniform distribution.

1. Introduction

Steam methane reforming was widely-used in hydrogen production. Because of its thermodynamic limitation, severe operating conditions were required to achieve complete methane conversion. The use of Pd-based membrane reactor for steam methane reforming reaction could offer complete methane conversion under mild operating conditions [1].

Generally, membrane reactor configuration is shell-and–tube type. Pd-membranes are equipped as tubes inside the shell. Catalyst is packed in annulus side. Using this configuration, membrane and catalyst are not effectively utilized. The catalyst is not fully utilized due to the limitation of chemical reaction equilibrium, while the superior hydrogen partial pressure at permeate side to retentate side inhibits the utilization of Pd-membrane [2].

In this study, Pd-membrane membrane reactor with non-uniform catalyst density and Pd-membrane allocation was proposed and investigated. Distributions of catalyst density and Pd-membrane allocation along the membrane reactor were varied to achieve optimum performance of Pd-membrane reactor. Hydrogen yield and methane conversion were considered as the performance indicators.

2. Mathematical Models

2.1 Reactor configuration

A shell–and-tube membrane reactor was investigated in this study. Catalyst was packed in the annulus side where the reactants were fed as shown in Fig. 1, while the membrane was equipped as a tube. The inert particle was also packed with catalyst at the annulus side to control the catalyst density, while the stainless-steel was also equipped as the tube to control Pd-membrane allocating distribution.

In this study, the Pd-membrane reactor was divided into two same-sized sections containing different catalyst density and Pd-membrane area. However, the total amounts of catalyst and membrane area were controlled to be similar for every scenarios. The total reactor length was 50 cm, and the inner tube diameter and shell diameter were set to be 1.2 and 6.4 cm, respectively. For the Pd-membrane dimension, the membrane thickness and total area were set to be 20 μm and 0.189 m^2, respectively. Total weight of catalyst was kept at 0.151 kg.

2.2 Governing equations

One-dimensional pseudo-homogenous model taking into account the thermal effect was used in this work. The effects of concentration polarizations and pressure drop along the reactor were assumed negligible. The mass balance equations of each component were given in Eqs. (1) and (2) for the retentate and permeation sides, respectively.

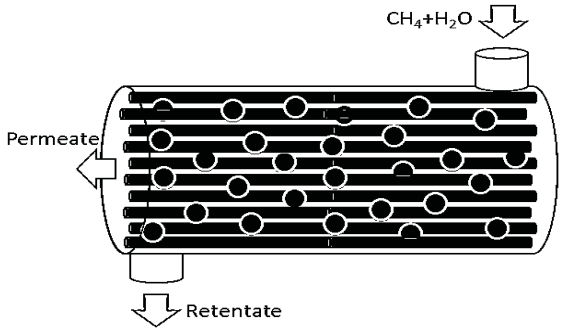

Figure 1. Pd-membrane reactor configuration

Mole balance of the retentate side:

$$\frac{dF_i}{dz} = \rho_{cat} \times A_x \sum_{j=1}^{3} \upsilon_{ij} \eta_j R_j - \pi D_{\text{int}} \sum_{k=1}^{NM} J_{i,k} \qquad (1)$$

Mole balance of the permeation side:

$$\frac{dF^{perm}_{H_2,k}}{dz} = \pi D_{\text{int}} J_{H_2,k} \qquad (2),$$

where F_i and F_i^{perm} are the axial molar flow rate of the specie i inside the retentate and permeation sides, respectively. R_j is the reaction rate for reaction j. It should be noted that the reaction kinetic equations used in this study were derived from Xu and Froment's work [3]. J_i is the permeation flux of specie i which is calculated using Sievert's law [4]. For the conventional steam methane reformer, J_i is set to be 0 for all species. It was assumed in this study that the permeation flux for all components excluding hydrogen was equal to 0. The energy balance equations for the retentate and permeation sides are expressed in Eqs (3) and (4), respectively.

Energy balance of the retentate side:

$$\left(\sum_{i=1}^{5} F_i Cp_i\right)\frac{dT}{dz} = \pi D_{ext} U \left(T_w - T\right) - \pi D_{\text{int}} \left[\sum_{k=1}^{NM} U_{m,k}\left(T - T_k^{perm}\right)\right] + \rho_{cat} A_x \sum_{j=1}^{3} \eta_j R_j \left(-\Delta H_j\right) \qquad (3)$$

Energy balance around permeation side:

$$\left(F^{perm}_{H_2,k} Cp_{H_2}\right)\frac{dT_k^{perm}}{dz} = \pi D_{\text{int}} \left[U_{m,k}\left(T - T_k^{perm}\right)\right] - \pi D_{\text{int}} J_{H_2,k} \int_{T}^{T_k^{perm}} Cp_{H_2} dT \qquad (4),$$

where T and T^{perm} represent temperatures at the retentate side and the permeation side, respectively. The overall heat transfer coefficients, U (reactor wall and reaction side) and U_m (reaction side and permeation side), were calculated using the expressions given in Media et al.'s work [5]. For conventional steam methane reformer, U_m is equal to 0.

The model was solved using backward finite difference method. All material and energy balance equations were included in the simulation model written in the platform of Visual Basic for MS Excel. The performance of membrane reactor was defined in term of hydrogen yield and methane conversion as expressed in Eqs. (5) and (6), respectively.

$$X_{CH_4} = \frac{\left(F_{CH_4,initial} - F_{CH_4}\right)}{F_{CH_4,initial}} \times 100\% \qquad (5)$$

$$Y_{H_2} = \frac{F^{perm}_{H_2}}{4F_{CH_4,initial}} \times 100\% \qquad (6)$$

3. Results and Discussion

3.1 Model validation

As shown in Fig. 2, the results of mathematical model and experiment [4] were compared. All information and experimental data used in the model verification are from F. Gallucci et al.'s work [4]. The results showed that the solid lines representing simulation results fitted well with the experimental results for both conventional steam methane reformer and Pd-membrane reactor. Therefore, this developed mathematical model could well predict the phenomena of both conventional steam methane reformer and Pd-membrane reactor.

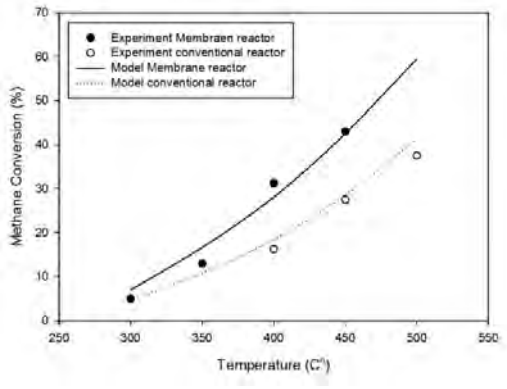

Figure 2. Comparison of the results from simulation works and experimental works

3.2 Catalyst and membrane distribution

In this work, the operating conditions for simulation were: methane feed rate = 120 mol/h, steam to methane ratio = 3, inlet reactant temperature = 650 ^{o}C, and pressure at retentate side = 200 kPa. Permeation side was operated under vacuum operation. The catalyst fraction in each reactor section was defined as the ratio of catalyst weight in that section to the total catalyst weight in the reactor, while membrane fraction in each reactor section was defined as the ratio of membrane area in that section to the total membrane area. The abbreviation which was used in this work was C*i*-A-M*i*-B, where C*i* represented the packing of the catalyst at section *i*, A represented the catalyst fraction at section *i*, M*i* represented the allocation of membrane at section *i*, and B represented the membrane fraction at section *i*.

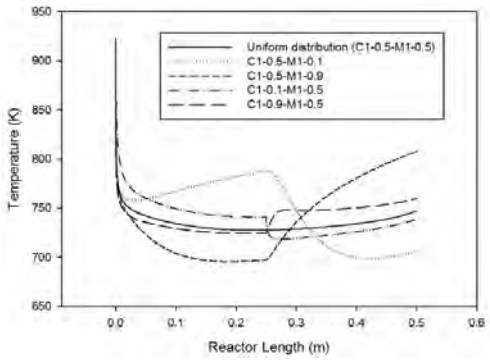

Figure 3. Distribution of temperature along the reactor

Temperature profile of membrane reactor in case of uniform distribution and non-uniform distribution of membrane allocation and catalyst density were illustrated in Fig. 3. In this figure, C1-0.5-M1-0.5 represented uniform distribution, while C1-0.5-M1-0.1 and C1-0.5-M1-0.9 showed the effect of non-uniform distribution of membrane allocation and C1-0.1-M1-0.5 and C1-0.9-M1-0.5 showed the effect of non-uniform distribution of catalyst packing density.

Since steam methane reforming was a highly endothermic reaction, temperature of gas stream extremely decreased as the reaction occurred. As shown in Fig. 3, if the catalyst fraction in the 1st section was lower than that in the 2nd section (C1-0.1-M1-0.5), temperature of gas stream became higher than that of uniform distribution case in the 1st section and lower in the 2nd section due to the lower and higher reaction rate at the 1st and 2nd sections, respectively, while the opposite trend was observed for the case of C1-0.9-M1-0.5. C1-0.5-M1-0.1, which contained lower membrane area in the 1st section compared to uniform distribution case, offered the similar trend of temperature distribution to C1-0.1-M1-0.5 because of lower reaction rate than uniform distribution in the 1st section. Its behavior would be almost similar to the conventional reactor in the first section due to low membrane area fraction (0.1).

Fig. 4 illustrates the distribution of hydrogen partial pressure for uniform and non-uniform distribution cases. The results showed that the values of hydrogen partial pressure of C1-0.5-M1-0.1 and C1-0.9-M1-0.5 were higher than uniform distribution case in the first section and became lower in the second section. For C1-0.9-M1-0.5, higher catalyst density in the first section caused the higher reaction rate and also higher hydrogen partial pressure, while the opposite trend was observed in the 2nd section. For C1-0.5-M1-0.1, lower membrane area at the first section caused lower hydrogen permeation and also higher hydrogen partial pressure in the retentate side at the first section, while the opposite trend was found in the second section. For C1-0.1-M1-0.5 and C1-0.5-M1-0.9, the opposite trends of hydrogen partial pressure distribution in the retentate side to C1-0.9-M1-0.5 and C1-0.5-M1-0.1 was found.

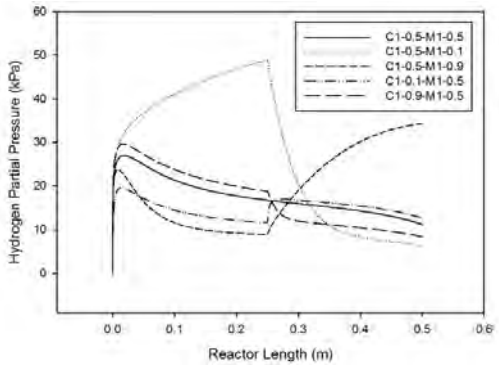

Figure 4. Distribution of hydrogen partial pressure along the reactor

The profiles of hydrogen yield for uniform and non-uniform reactor cases were envisioned as illustrated in Fig. 5. The results show that C1-0.5-M1-0.1 and C1-0.1-M1-0.5 cases offered lower hydrogen yield compared to the uniform distribution case in the 1st section due to their lower reaction rate and hydrogen permeation in the 1st section and the opposite trend was found in the 2nd section. With the same reason, C1-0.5-M1-0.9 and C1-0.9-M1-0.5, which were the cases that contained high membrane area and high catalyst density in the 1st section, respectively, offered higher hydrogen yield in the 1st section compared to the uniform distribution case.

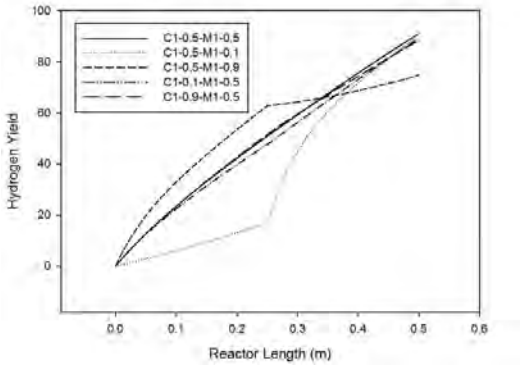

Figure 5. Profile of hydrogen yield along the reactor

Figs. 6 and 7 visualized the performance indicators, hydrogen yield and methane conversion, at the reactor exit as the function of the catalyst and membrane fractions in the 1st section of the reactor. The term "Fraction(1)" represented the fractions of catalyst and membrane in the 1st section of reactor. The solid line in Figs. 6 and 7 represented the variation of the performance indicators on the change in membrane distribution as the catalyst density distribution was uniform; while the dash line represented the variation of the performance indicators on the change in catalyst density distribution as the membrane distribution was uniform. The results showed that membrane reactor with non-uniform distributions of membrane allocation and catalyst density could offer superior methane conversion and hydrogen yield to that with uniform distribution configuration (Fraction(1)=0.5). The configuration which the membrane area and catalyst density in the 1st section were lower than those in the 2nd section offered higher performance than the cases that the membrane area and catalyst density in the 1st section were higher than those in the 2nd section. The catalyst density distribution strongly affected methane conversion since the catalyst density directly controlled the reaction rate and also methane conversion, while the membrane allocation strongly affected hydrogen yield due to the direct dependence of hydrogen permeation on the presence of Pd-membrane. Conclusively, in case of the membrane reactor with non-uniform catalyst distribution, the optimum hydrogen yield and methane conversion could be achieved as the catalyst packing fractions in the 1st section were 0.45 and 0.4, respectively. For the membrane reactor with non-uniform membrane allocation, membrane fractions in the 1st section of 0.35 and 0.4 were required to achieve optimum hydrogen yield and methane conversion, respectively.

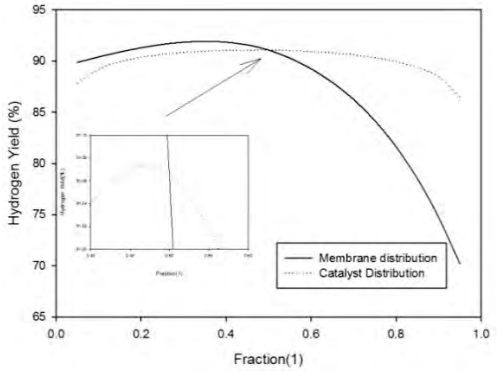

Figure 6. Hydrogen yield at reactor exit

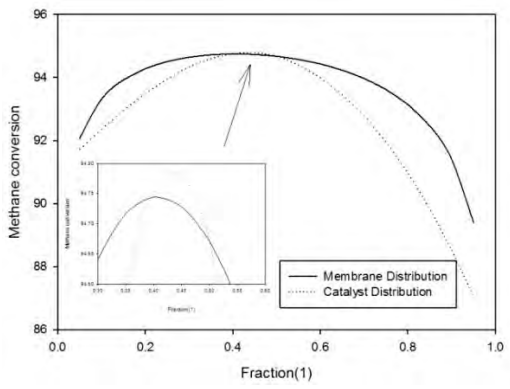

Figure 7. Methane conversion at reactor exit

4. Conclusion

It could be concluded from this study that the variation on the distributions of catalyst density and membrane allocation along the membrane reactor with non-uniform catalyst density distribution or membrane allocation strongly affected the distributions of temperature, reaction rate and hydrogen permeation. With well tuning of catalyst density distribution and membrane allocation, the membrane reactor with non-uniform catalyst density distribution or membrane allocation could offer superior performance to the membrane reactor with uniform catalyst density distribution and membrane allocation. As concluded in this study, the performance of the membrane reactor was favored as the catalyst density and membrane area in the 1st section were lower than those in the 2nd section.

Acknowledgement

The authors would like to acknowledge the support from The Thailand Research Fund.

Notation

A_x	cross-sectional area in the annulus side (m^2)
Cp	Heat capacity (J/(mol.K))
D_{ert}	Outside diameter (m)
D_{int}	Inside diameter (m)
ΔH	Heat of reaction (J/mol)
NM	Number of membrane in each section
z	abscissa (m)

Greek symbols

η	Effectiveness factor
ρ	Catalyst density (kg/m^3)
ν	Stoichiometry coefficient

Subscribes

Cat	Catalyst bed

Superscripts

perm	Permeation side

References

[1] P. Bernardo, G. Barbieri, E. Drioli, *Chem. Eng. Sci.* **2010**, *65*, 1159-1166

[2] A. Caravella, F. P. Di Maio, A. Di Renzo, *J. Membr. Sci.* **2008**, *321*, 209-221

[3] J. Xu, G. F. Froment, *AIChE J.* **1989**, *35*, 88-96

[4] F. Gallucci, L. Paturzo, A. Famà, A. Basile, *Ind. Eng. Chem. Res.* **2004**, *43*, 928-933

[5] G. S. Madia, G. Barbieri, E. Drioli, *Can. J. Chem. Eng.* **1999**, *77*, 698-706

PERFORMANCE IMPROVEMENT OF WASTE PLASTIC GASIFICATION WITH CO_2 SORBENT: SIMULATION STUDY

Makapat Pakhathirathien, Suttichai Assabumrungrat, Amornchai Arpornwichanop*

Department of Chemical Engineering, Faculty of Engineering, Chulalongkorn University, Bangkok 10330 Thailand

* Author for correspondence; E-Mail: Amornchai.a@chula.ac.th, Tel. +66 2218 6878, Fax. +66 2218 6877

Abstract: A waste-to-energy conversion through a gasification process is an alternative technology handling huge waste management problem along with resolving a long degradation cycle of massive waste plastic, which is generated from household sectors each year. Through the gasification process, waste plastic or in some case biomass has been thermochemically converted to synthesis gas that can be used among various applications. In this study, the performance of the waste plastic gasification is investigated via a simulation study. A model of the gasification process consisting of devolatilization, oxidation and reduction stages, is developed using a flowsheet simulator and then used to investigate effect of key operating parameters on hydrogen content in the synthesis gas. Calcium oxide (CaO) as a CO_2 sorbent is used to improve the quality of a synthesis gas obtained from the gasification process by removing CO_2.

1. Introduction

Increasing energy demand has long become a focal concern of energy resources, thus projection of substituting traditional fossil fuel with a sustainable alternative appears to have grown constantly. Plastic waste is regarded as one of the largest proportion of municipal solid waste (MSW) and can be used as a valuable energy source for a thermochemical conversion process to generate gaseous fuel.

Gasification has been widely known as a promising solution to achieve todays environmental concern and stands among significant modern technologies. An energy conversion within gasification process is devided into four stages: drying, devolatilization, oxidation and reduction. [1] Gasified products are presented in forms of gas, tar and char. In present, gasification technology has continuously been developed over time; however, the availability of biomass feedstock and its rising price have largely affected many gasification-based power plants. Likewise, plastic has been described as a material of which the proximate and ultimate carbonaceous properties are similar to biomass. Thus, it is considered to be an alternative feed material for gasification process.

Conventionally, biomass gasification have been extensively studied on lab scale. To scale up the lab scale experiment to pilot scale or commercial scale is a demanding and time consuming task. Simulation study has come to interest and has been a focal point in trending and pointing necessity of testing parameters through commissioning. It is an important tool for process analysis and design. Thus, the aim of this study is to model and simulate a gasification process using waste plastic as feedstock. Use of calcium oxide to remove CO_2 from the synthesis gas obtained from the waste plastic gasification process is considered. Modeling of such the process is performed using a process simulator (ASPEN PLUS). Simulation is carried out to investigate the effect of key operating parameters on performance of the gasification and adsorption integrated process.

Table 1: Waste plastic properties [2]

Moisture content (wt. %)	0.6
Proximate analysis (wt.%, dry basis)	
Volatile matter	94.2
Fixed carbon	0.4
Ash	4.8
Ultimate analysis (wt.%, dry basis)	
Carbon	79.9
Hydrogen	12.6
Oxygen	5.1
Chlorine	1.13
Nitrogen	1.27
Sulfur	0

2. Gasification of Waste Plastic

2.1 Waste Plastic

Waste plastic used as a feedstock for the gasification process consists of polyethylene (PE), polypropylene (PE), polystyrene (PS), polyvinyl-chloride (PVC), small contents of polymethyl methacrylate (PMMA) and polyethylene terephthalate (PET) [2]. Its properties are shown in Table 1.

2.2 Modeling of gasification process

Gasification is a quite complicated system and requires several parameters to accomplish its extensive simulations [3,4]. A producer gas (also known as a synthesis gas) consists of mostly hydrogen (H_2), carbon monoxide (CO) and carbon dioxide (CO_2), which is a convinient form of fuel for handling and transportation [5]. The reactions occurred within a gasifer involve combustion, methanation, water-gas shift reaction and char gasification, as summarized in Table 2. In this study, simulation of the gasification process is based on a thermodynamic approach. The complex kinetics are neglected by assuming that the

gasification reactions occur fast enough to reach equilibrium at the reactor outlet [6].

Modeling of the gasifier is divided into two major parts (Figure 1 (a)): (1) devolatilization (or decomposition) and (2) oxidation and reduction. The first part is represented by RYield module and the other is modeled by RGibbs module [7]. Figure 2 shows a detail flowsheet of the gasification process.

Regarding the gasifier agent, it is more reasonable to use air as the gasifying agent instead of pure oxygen, which is more expensive utility as it requires prior preparation by air separation unit (ASU) [8].

Table 2: Reactions occurred within gasification and gas cleaning processes

Drying Reaction		**Units**
Moist feed → Dry feed + $H_2O_{(g)}$		
Devolatilization Reaction		
Dry feed → Volatiles +Char		RYield
Gasification Reactions		
$C_{(s)} + H_2O_{(g)} \rightarrow H_{2(g)} + CO_{(g)}$	(1)	RGibb
$C_{(s)} + 2H_2O_{(g)} \rightarrow 2H_{2(g)} + CO_{2(g)}$	(2)	
$C_{(s)} + CO_{2(g)} \rightarrow 2CO_{(g)}$	(3)	
$C_{(s)} + 2H_{2(g)} \rightarrow CH_{4(g)}$	(4)	
$C_{(s)} + 3H_{2(g)} \rightarrow CH_{4(g)} + H_2O_{(g)}$	(5)	
$CO_{(g)} + H_2O_{(g)} \leftrightarrow CO_{2(g)} + H_{2(g)}$	(6)	
Combustion Reactions		
$C_{(s)} + 0.5O_{2(g)} \rightarrow CO_{(g)}$	(7)	RGibb
$C_{(s)} + O_{2(g)} \rightarrow CO_{2(g)}$	(8)	
$H_{2(g)} + 0.5O_{2(g)} \leftrightarrow H_2O_{(g)}$	(9)	
Char → Slag		
Carbonation Reactions		
$CaO_{(s)} + H_2O_{(g)} \leftrightarrow Ca(OH)_{2(s)}$	(10)	RGibb
$Ca(OH)_{2(s)} + CO_{2(g)} \leftrightarrow CaCO_{3(s)} + H_2O_{(g)}$	(11)	
$CaO_{(s)} + CO_{2(g)} \leftrightarrow CaCO_{3(s)}$		
Sulfuration Reactions		
$CaO_{(s)} + H_2S_{(g)} \rightarrow CaS_{(s)} + H_2O_{(g)}$	(12)	
$CaS_{(s)} + 2O_{2(g)} \rightarrow CaSO_{4(s)}$	(13)	
$CaO_{(s)} + SO_{2(g)} + 0.5O_{2(g)} \rightarrow CaSO_{4(s)} + CO_{2(g)}$	(14)	

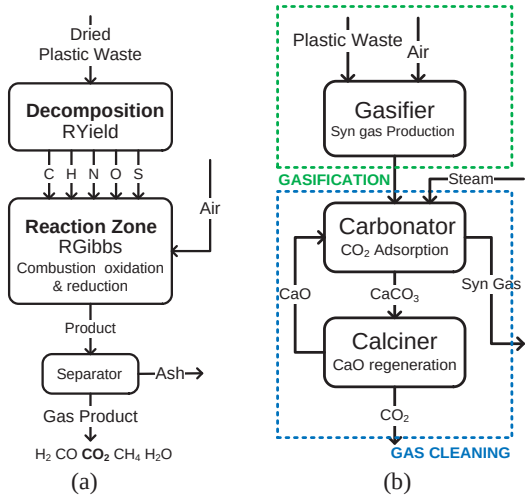

Figure 1. Schematic diagram of (a) gasification process and (b) gasification process integrated with gas cleaning step.

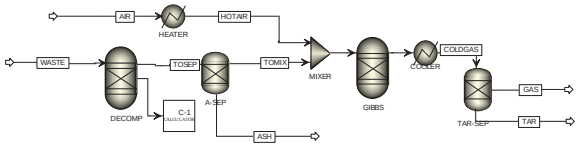

Figure 2. Flowsheet of the gasification process

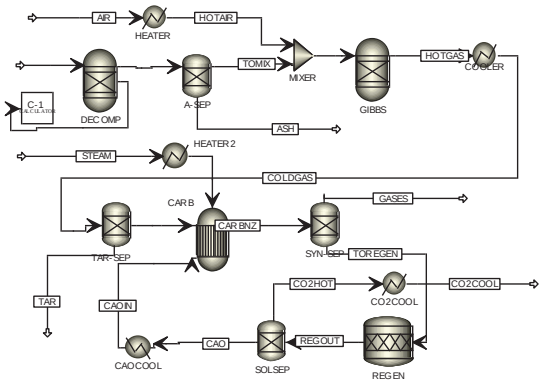

Figure 3. Flowsheet of the gasification and CO_2 sorption integrated process

However, the synthesis gas produced from an air-gasification process have a low heating value due to the dilution effect of nitrogen. Moreover, steam, as another gasifying agent, is sometimes added to the gasifier to improve its performance, providing a higher gas product with less tar. Tar is corrosive and could cause slagging in the gasifier that a plant shutdown will be nescessary to remove slag and coke formation. By using different household wastes, the composition of gasification gaseous product, including an amount of tar, varies with operating conditions and proximate and ultimate properties of feedstock [9].

2.3 Gas cleaning section: CO_2 sorbent

Since the synthesis gas obtained from gasification process contains CO_2, a gas cleaning section is combined with the gasification process to purify the synthesis gas, improving its quality (post-gasified cleaning stage). In this study, an adsorption process using calcium oxide (CaO) as an adsorbent is applied to remove CO_2.

CaO, the most commercially used natural-mineral sorbent, is widely employed for a hydrogen production process through steam gasification and steam reforming of coal. It can improve the hydrogen yield and system efficiency [10,11]. CaO is also used in reformer and water gas shift reactors to improve fuel conversion, leading to a low temperature operation [12-13].

Figure 1 (b) shows the schematic diagram of the gasificaion process integrated with gas cleaning section. CO_2 in the synthesis gas is removed by CaO sorbent via a carbonation reaction. $CaCO_3$ obtained is regenerated; CaO is reclycled to the carbonator and CO_2 is separated and sent to a storage tank. The flowsheet of the integrated system is shown in Figure 3 while operating conditions are shown in Table 3.

(a)

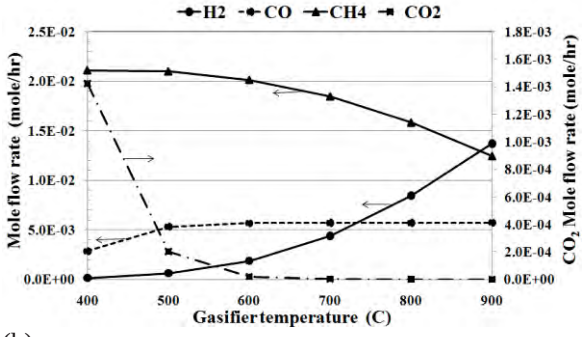

(b)

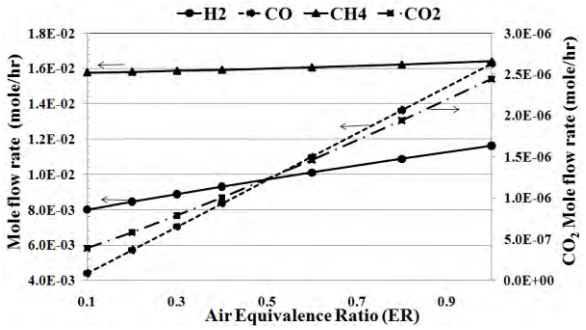

(c)

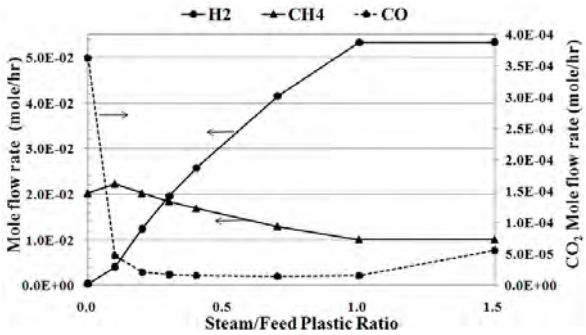

(d)

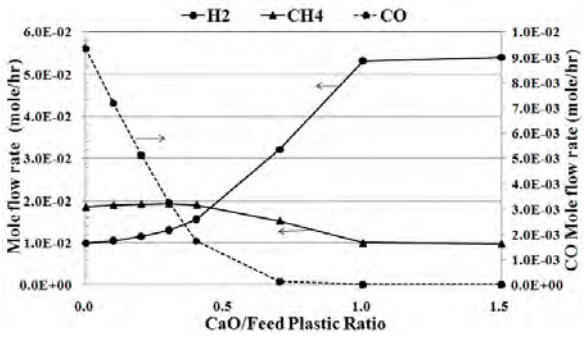

Figure 4. Effects of (a) gasifier pressure, (b) air equivalence ratio, (c) steam/plastic feed ratio and (d) calcium oxide/plastic feed ratio, on the gas product flow rate.

3. Results and Discussion

Simulation has been conducted to analyze the performance of the gasification and CO_2 sorption integrated process. The following components are considered: H_2, CO, CO_2, CH_4, C_2H_6, C_2H_4, C_3H_8, C_4H_{10}, C_5H_{12} and small yields of benzene, toluene and tar, which is presented by aromatic ring hydrocarbons

Table 3: Operating conditions

Gasifier conditions [2]	
Temperature (°C)	400 - 900
Pressure (atm)	1
Plastic feed (kg/hr)	1
ER (kg/kg)	0.1 – 1.0
Gas cleaning conditions	
Carbonator temperature (°C)	600
Cabonator pressure (atm)	21
S/F (kg/kg)	0.0 – 1.5
CaO/F (kg/kg)	0.0 – 1.5
Calciner temperature (°C)	850
$CaCO_3$ conversion	1.0

(e.g., naphthalene, fluorine, anthracene) [2]. These gaseous products are affected by several operating parameters.

Gasifier Temperature. Figure 4(a) shows the molar flow rates of gaseous product from the gasifier as a function of operating temperature ranged from 400-900 °C when the air equivalence ratio (ER), defined as the ratio of air fed into the gasifier to the stoichiometric amount of air required for a complete combustion, equals to 0.2. The amount of hydrogen product increases with increased temperature due to the endothermic nature of the gasification reactions.

Air Equivalent Ratio (ER). Effect of ER (0.1-1) on the gasification process is shown in Figure 4(b). It is found that when more oxygen is fed to the gasifier, the oxidation reactions are highly pronounced. This causes increases in the amount of hydrogen, carbon monoxide and carbon dioxide.

Steam/Plastic Feed Ratio (S/F). In the carbonator, calcium oxide is firstly reacted with steam, resulting in calcium hydroxide ($Ca(OH)_2$) as an intermediate. $Ca(OH)_2$ further reactes with carbon dioxide and yields calcium carbonate and steam as product (Equations (10) and (11)). Thus, an amount of steam is quite important parameters. Figure 4(c) shows the effect of S/F on the treated systhesis gas product. The steam/plastic feed ratio is varied from 0.1 to 1.5. It is found the a higher ratio of S/F has not only promoted char oxidation but also created a tendency toward water gas shift reaction (Equations (1), (2) and (6)). Thus, increased hydrogen product is mainly observed. However, the addition of excess steam (S/F > 1.0) has slight effect on the composition of the produced gas.

Calcium oxide/Plastic Feed Ratio (CaO/F). Figure 4 shows effect of CaO/F on the treated synthesis gas (0-1.5). An increased amount of calcium oxide to the carbonator affects $Ca(OH)_2$ reactivity and gas product composition. More hydrogen is generated from a water gas shift reaction (Equation (6)). However, adding more calcium oxide has no effect on an amount of hydrogen produced since steam in the carbonator is limited. It is noted that in practical operation, a fresh calcium oxide needs to be fed in constantly due to sorbent deactivation.

Since the aim of this study is mainly focused on using calcium oxide as a sorbent to remove carbon dioxide, thereby obtaining a high quality of synthesis gas in terms of hydrogen content and heating value, a

cold gas efficiency (*CGE*) of the synthesis gas produced is evaluated (Equation (15)).

$$CGE = \frac{\dot{m}_{\text{syngas}} LHV_{\text{syngas}}}{\dot{m}_{\text{fuel}} LHV_{\text{fuel}}} \quad (15)$$

It is found that the treated synthesis gas has a heating value of 57.1 MJ/kg, compared with 51.6 MJ/kg of the synthesis gas obtained from the gasification process. When considering the overall process performance, the CGE is 1.38, which is based on waste plastic feedstock with a heating value of 41.5 MJ/kg.

4. Conclusions

A gasification of waste plastic integrated with gas cleaning process is investigated in this study. Modeling of the integrated system based on a thermodynamic approach is performing using a process simulator. Calcium oxide is used to adsorb carbon dioxide in a synthesis gas obtained from the gasification process. This enhances a quality of the synthesis gas in terms of hydrogen purity and gas heating value. The simulation result indicates that the gasification and calcium oxide-based adsorption process should be operated at gasifier temperature of 800 ºC, ER 0.2, steam/plastic feed ratio of 1.0 and CaO/plastic feed ratio of 1.0.

Acknowledgements

Support from the Thailand Research Fund and the Computational Process Engineering Research Group, Special Task Force for Activating Research (STAR), Chulalongkorn University Centenary Academic Development Project is also gratefully acknowledged.

Nomenclature

S/F	Steam to feed plastic flow rate ratio
CaO/F	Calcium oxide sorbent to feed plastic flow rate ratio
ER	Equivalence ratio

References

[1] N. Ramzan, A. Ashraf, S. Naveed, A. Malik, *Biomass and Bioenergy*. **35** (2011) 3962-3969.

[2] J.W. Kim, T.Y. Mun, J.O. Kim, J.S.Kim, *Fuel*. **90** (2011) 2266-2272.

[3] M.Puig-Arnavat, J. C. Bruno, A. Coronas, *Renewable and Sustainable Energy Reviews*. **14** (2010) 2841-2851.

[4] P. Basu, *Biomass Gasification and Pyrolysis: Practical Design and Theory*, Academic Press, USA (2010).

[5] A. Franco, N. Giannini , *International Journal of Thermal Sciences*. **44** (2005) 163–177.

[6] I. Hannula, E. Kurkela, *Biomass and Bioenergy*. **38** (2012) 58-67.

[7] S.M. Atnaw Sulaiman, S.A. Sulaiman, *Prediction of Calorific Value of Syngas Produced from Oil-Palm Fronds Gasification* Proceedings of ICEE 2009 3rd International Conference on Energy and Environment, 7-8 December 2009, Malacca, Malaysia.

[8] R.Xiao, B. Jin, H. Zhou, Z. Zhong, M. Zhang, *Energy Conversion and Management*. **48** (2007) 778–786.

[9] J.C. Schmid, U. Wolfesberger, S. Koppatz, C. Pfeifer, H. Hofbauer, *Environmental Progress & Sustainable Energy* **31** (2012) 206-215.

[10] N. Striugas, K. Zakarauskas, G.S. Striugas, *Comparison of steam reforming of biomass gasification tars over lithuanian dolomite and waste tires char* Selected paper of Environmental Engoneering The 8th International Conference 19–20 May 2011, Vilnius, Lithuania.

[11] J. Blamey, E.J. Anthony, J. Wang, P.S. Fennell, *Progress in Energy and Combustion Science*. **36** (2010) 260–279.

[12] J. Corella, J.M. Toledo, G. Molina, *Ind. Eng. Chem. Res*. **46** (2007) 6831−6839.

[13] M.R. Mahishi, D. Goswami, *Int. J. Hydrogen Energy*. **32** (2007) 2803–2808.

[14] T.Y. Mun, B.S. Kang, J.S. Kim, *Energy Fuel*. **23** (2009) 3268–76.

[15] C. Chen, Y. Jin, J. Yan, Y. Chi, *Appl Phys & Eng*. **11** (2010) 619-628.

ANALYSIS OF FLUID FLOW PATTERN IN A SPRAY DRYER

Artitaya Patniboon, Apinan Soottitantawat, Amornchai Arpornwichanop*

Department of Chemical Engineering, Faculty of Engineering, Chulalongkorn University, Bangkok 10330, Thailand

* E-Mail: Amornchai.a@chula.ac.th, Tel. +66 2218 6878, Fax. +66 2218 6877

Abstract: Spray drying is widely used in many industrial drying processes for food, healthcare and pharmaceutical products. In spray dryers, some particles do contact the metal surface of a dryer chamber, causing a corrosion. This phenomenon is known as a wall deposition problem, which lowers a final product quality. To find a solution of this operational problem, this study aims to investigate a fluid flow pattern of droplet particles in the spray dryer. The drying process of an anthocyanin, an antioxidant substance extracted from red grape skin, is considered a case study. A two-dimensional, computational fluid dynamic model of the dryer is developed taking into account the co-current, turbulent flows of anthocyanin droplets and hot air, and solved by a finite element method. Fluid flow characteristics such as velocity, spray dryer configuration and particle impact position within the dryer are focused as these factors affect the spray drying performance and the wall deposition problem.

1. Introduction

Drying is a process to remove liquid (usually water) from solids. It helps reduce transportation weight and prolongs product lifetime. Different drying techniques have been developed for performance improvement of the drying process. Presently, a spray drying is among the various techniques that can be applied to obtain a final solid powder product from liquid feed. In the spray dryer, the liquid feed is atomized by an atomizer and contacted with hot air. The way, type and position of the atomizer have an effect on the evaporation and the particle size of final powder products.

There are two steps in the evaporation process [1]. Firstly, the liquid at the surface of an droplet is evaporated at a constant rate when the temperature of the droplet surface equals the wet-bulb temperature of hot air and usually, more than 95% of the total moisture in the liquid feed is removed at this step. Secondly, moisture in the internal wet core of the droplet is diffused through the droplet surface. The final powder product with desired particle size and moisture content is obtained. However, operation of the spray dryer may cause some difficulties as some particles having high moisture content (stickiness) do contact the metal surface of a dryer chamber, leading to a wall deposition problem. This problem causes a product contamination and affects a quality of the final product [2].

In this study, the fluid flow characteristics of droplet particles, such as velocity, residence time and impact position, within a co-current spray dryer is investigated via a simulation study. A two-imensional, computational fluid dynamic model of the spray dryer is developed and solved by a finite element method. The drying process of an anthocyanin, an antioxidant substance extracted from red grape skin, is chosen as a case study.

2. Modelling of a Spray Dryer

Atomization is a crucial technology area that has been developed and nozzles atomizers are commercially used in spray drying. In this study, the flow pattern of droplet particles and a wall deposition problem will be focused without considering a change in the product size distribution. An anthocyanin solution feed at 50 wt.% and nominal inflow velocity of 80 m/s is considered.

In a co-current spray dryer, feed solution and hot air enter the chamber in the same direction. As a result, the hot air contacts a droplet of feed solution at its maximum moisture content. As the rate of water evaporation is rapid, the air temperature is reduced. Therefore, a final product does not suffer from heat degradation. Figure 1 shows the schematic diagram of the spray dryer used in this study.

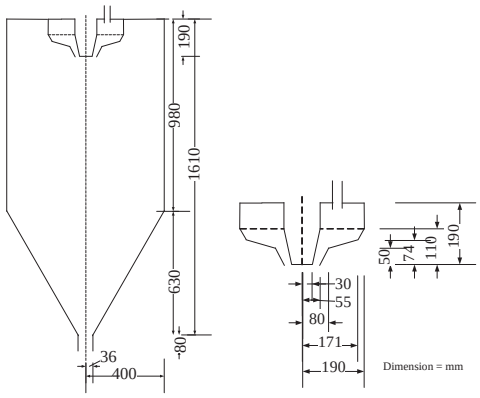

Figure 1. Schematic diagram of the spray dryer [3].

In this study, an incompressible and newtonian fluid is assumed. A drying step within droplet particles is assumed to be occurred under an isothermal condition. The turbulence model is employed to describe fluid flow in the spray dryer as shown below [4]:

$$\rho(u\cdot\nabla)k=\nabla\cdot\left[(u+\frac{u_T}{\sigma_k})\nabla k\right]+p_k-\rho\varepsilon \qquad (1)$$

$$\rho(u\cdot\nabla)\varepsilon=\nabla\cdot\left[(u+\frac{u_T}{\sigma_e})\nabla\varepsilon\right]+C_{e1}\frac{\varepsilon}{k}p_k-C_{e2}\rho\frac{\varepsilon^2}{k} \quad (2)$$

$$\varepsilon = ep$$

$$\mu_T=\rho C_\mu\frac{k^2}{\varepsilon} \quad (3)$$

$$p_k=\mu_T\left[\nabla u:(\nabla\mu+(\nabla\mu)^T)\right] \quad (4)$$

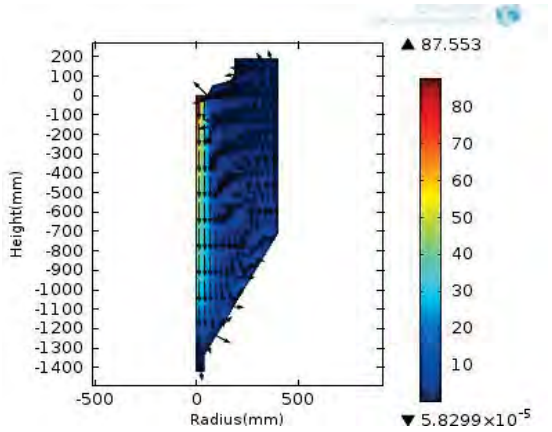

Figure 2. Velocity (m/s) of droplets in the spray dryer.

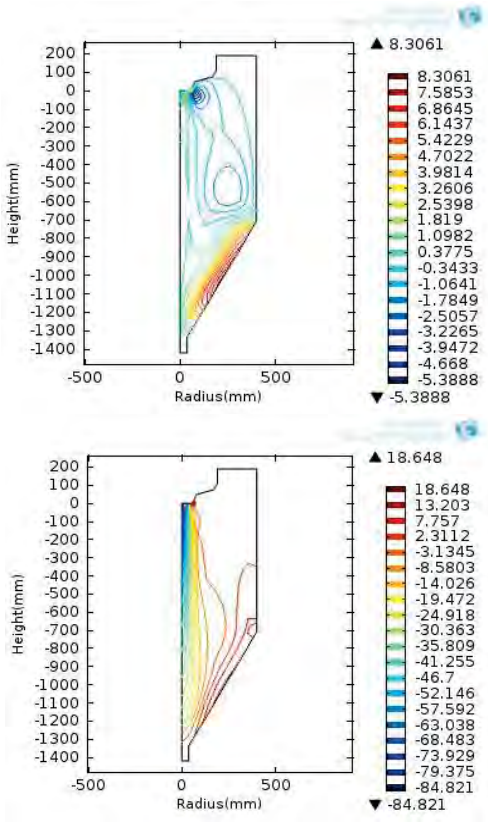

Figure 3. Contour plot of the velocity field (m/s) in the radial (top) and axial (bottom) directions.

where p_k is the generation of kinetic energy due to the mean velocity gradients, σ_k and σ_e are the turbulent Prandtl numbers for the turbulence kinetic energy and turbulence dissipation rate, respectively, C_{e1} (= 1.44) and C_{e2} (= 1.92) are constant.

The Reynolds-averaged Navier-Stokes and continuity equations are given as follows:

$$\rho(u\cdot\nabla)u=\nabla\cdot\left[-pI+(u+u_T)(\nabla u+(\nabla u)^T)-\frac{2}{3}\rho kI\right]+F \quad (5)$$

$$\rho\nabla\cdot u=0 \quad (6)$$

The boundary conditions for fluid velocities involve a no-penetration condition and a shear stress condition as:

$$u\cdot n=0 \quad (7)$$

$$\left[(\mu+\mu_T)\left(\nabla u+(\nabla u)^T\right)-\frac{2}{3}\rho kI\right]n=-\rho\frac{u_\tau}{\delta_W^+}u_{\tan g} \quad (8)$$

$$u_{\tan g}=u-(u\cdot n)n \quad (9)$$

$$\nabla k\cdot n=0 \quad (10)$$

$$\varepsilon=-\rho\frac{C_\mu k^2}{k_v\delta_W^+\mu} \quad (11)$$

$$u_\tau=\frac{|u|}{\frac{1}{k_v}\ln\delta_W+B} \quad (12)$$

where k_v is the von karman constant (=0.41).

The initial values and the inlet boundary conditions for a steady-state simulation are as follows:

$$u=0 \quad (13)$$

$$p=0 \quad (14)$$

$$u=-u_0 n \quad (15)$$

$$k=\frac{3}{2}(u_0 l_T)^2,\ \varepsilon=C_\mu^{3/4}\frac{k^{3/2}}{L_T} \quad (16)$$

3. Results and Discussion

The feed solution consists of anthocyanin spherical particles and water with density of 1,240 kg/m^3 and dynamic viscosity of 3.588×10^{-4} mPa·s. The predicted velocity of droplets is shown in Figure 2. It is found that the droplet particle has its maximum velocity near the atomizer region. The particle velocity slightly decreases along the center of the drying chamber. Figure 2 also shows the flowing direction of the particle. Three patterns of the droplet flow direction are observed: (1) the particle falls down along the center and goes out the chamber at the outlet with high velocity because of its high moisture content, (2) some

particles hit the conical wall and then fall down along the slope-sided surface at the medium velocity and (3) moisture-containing droplets hit the side wall and flow upward to the top of the chamber and then recirculate downward to the bottom with low velocity. The recirculation results in a longer residence time of the droplets with high moisture content. This factor may degrade a quality of the final product if some important nutrient in the producet is sensitive to heat.

Figure 3 shows the region of velocity field in the radial and axial directions. The results indicate that most droplets with high moisture content hit the conical wall of the chamber with radial and axial-direction forces, resulting from a viscous stress of the droplets. Figure 4 shows that the viscous stress in the axial and radial directions. It is found that the viscous stress is dominated by the force in the axial direction. So the droplets are possibly attached at the maximum viscous stress region. In general, dry particles absorb moisture from wet and hot particles. As the result, the rebond of these particles tends to be stick. The first layer of sticky particles attaches to the chamber wall with the adhesion of particles to top layer of the wall. The second layer of sticky particles attaches to the first layer of the sticky particles with the cohesion of layer particles and the pattern for the next layers is similar. In order to understand the effect of a wall deposition problem, the friction velocity at the chamber wall is studied. Figure 5 indicates that the maximum friction velocity region is at the conical wall, which is the same region as the viscous stress in the axial direction (Figure 4).

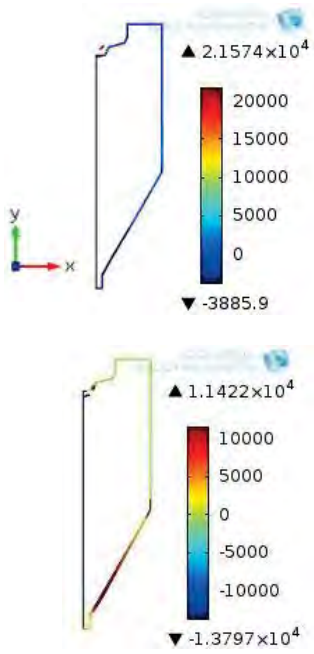

Figure 4. Viscous stress (N/m^2) in the radial (top) and axial (bottom) directions.

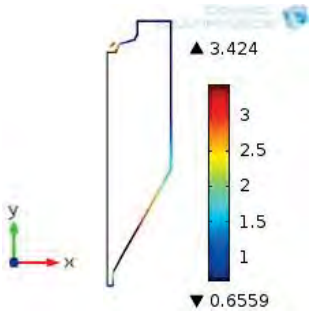

Figure 5. Friction velocity (m/s) at the wall chamber.

The flow pattern of droplets within the spray dryer with different conical wall angles is studied. Figures 6 and 7 show effect of the conical wall angle on the viscous stress along the axial direction. When the height of side wall and diameter of chamber increase, they decrease the angle of the conical wall. The maximum viscous stress in the axial direction increases as the angle of the conical wall is less than its nominal value. It is found that the droplets hit a conical wall and then move upward to the top or downward to the bottom of the chamber with slow velocity and high tangential viscous stress. Thus, the droplets build up on the wall.

Effect of inlet fluid velocity on the wall depoition problem is studied. Figure 8 shows the viscous stress in the axial direction when the inlet velocity is 80 m/s (nominal flowrate). When the inlet velocity is changed from 60 to 100 m/s, a similar trend is observed.

In addition, the flow fields obtained show a similar trend The maximum viscous stresses at the inlet velocity of 60, 80 and 100 m/s are 6,420, 11,422 and 17,858 N/m^2, respectively. The results show a linear relationship of the inlet velocity of feed droplets and the maximum viscous stresses. The viscous stress increases with increased inlet velocity. Thus, at a higher inlet fluid velocity, the trendency of the droplet to be attached to the wall increases due to high adhesive force.

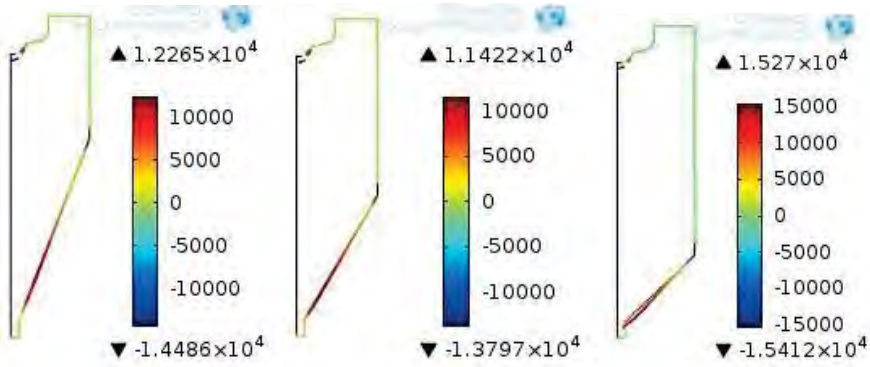

< 40% normal normal > 40% normal

Figure 6. Comparison of the viscous stress (N/m^2) in the axial direction at different heights of the side wall.

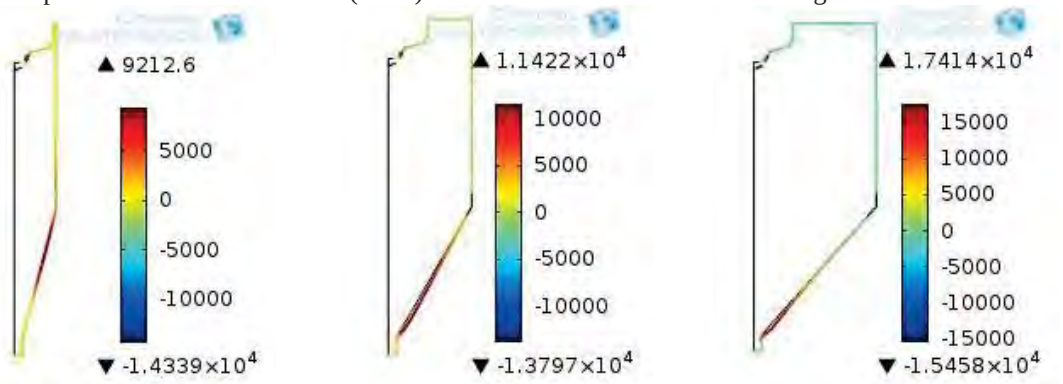

< 25% normal normal > 25% normal

Figure 7. Comparison of the viscous stress (N/m^2) in the axial direction at different chamber diameters.

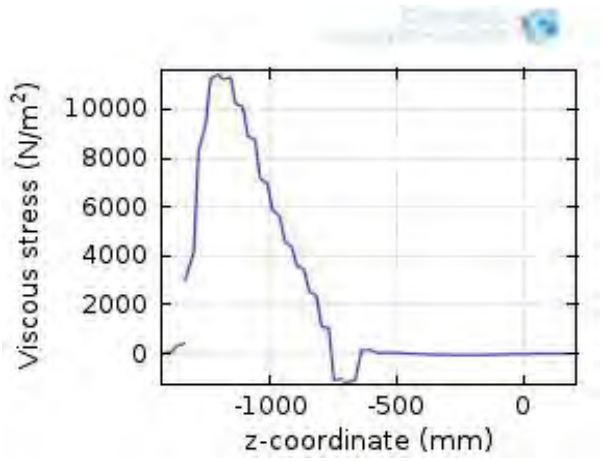

Figure 8. Viscous stress (m/s) in the axial direction at the wall chamber (inlet fluid velocity = 80 m/s).

4. Conclusions

This study investigated a turbulent flow behavior within a co-current spray dryer for anthocyanin droplets. The simulation results indicated three flow patterns; (1) droplets fall down and go out the dryer, (2) droplets hit the conical wall and then fall down along the wall of the chamber and (3) droplets hit and move upward to the top of the chamber at the side wall and then recirculate downward to the bottom.

The viscous stress and friction velocity in the axial direction are key factors to explain a wall deposition problem. Droplets are possibly attached to the wall at the position that the viscous stress and friction velocity show their maximum values. The influences of design parameters of the spray dryer and inlet fluid velocity were also studied. When the angle of the conical wall decreases, the maximum viscous stress in the axial direction increases. The viscous stress region at the wall chamber shows a linear relation with the inlet fluid velocity.

Acknowledgement

Support from the Computational Process Engineering Research Group, Special Task Force for Activating Research (STAR), Chulalongkorn University Centenary Academic Development Project is also gratefully acknowledged.

References

[1] M. Mezhericher, A. Levy and I. Borde, *Chemical Engineering and Processing.* **49** (2010) 1205-1213.
[2] B. Guo, T.A.G. Langrish and D.F. Fletcher, *Trans IchemE.* **3** (2003) 263-8762.
[3] D.F. Fletcher and T.A.G. Langrish, *Chemical Engineering Research and Design.* **87** (2009) 1371-1378.
[4] R. Kuriakose and C. Anandharamakrishnan, *Trends in food Science & Technology.* **21** (2010) 383-398.

PREPARATION AND CHARACTERIZATION OF ISOTACTIC-POLYPROPYLENE/SYNTHESIZED MICRO CELLULOSE TRAYS FOR MICROWAVABLE PACKAGING

Pongpat Sukhavattanakul[1] , Lerpong Jarupan[1, 2] and Chiravoot Pechyen[1, 2*]

[1]Department of Packaging and Materials Technology, Faculty of Agro-Industry, Kasetsart University ,Bangkok 10900, Thailand
[2]Center for Advanced Studies in Agriculture and Food ,KU Institute for Advanced Studies, Kasetsart University, Bangkok 10900 ,Thailand (CASAF ,NUR-KU, Thailand)

*E-mail: chiravoot.p@ku.ac.th, Tel. +66 836166332, Fax. +66 25625045

Abstract: Microcellulose was synthesized from cotton fabric waste. Composite of isotactic-polypropylene (i-PP) and microcellulose fibers (MC) were prepared by melting and mixing process, and 10%wt/wt of maleic anhydride grafted polypropylene (MA-g-PP) as compatibilizer. The MC at different ratios 5, 10 and 20 phr was blended with i-PP using corotating twin-screw compounder and tray forming using injection molding. The effects of microwave heating and microcellulose loading on the structures and properties of i-PP/MC and i-PP/MA-g-PP/MC composite trays were studied. Changes in mechanical and morphological properties with different MC loading were discussed. The composite trays were subjected to compression tests immediately after microwave heating at 340, 650 and 1300 watt for 2.5, 5 and 10 min. After the composite trays were heated in the microwave oven, an increase in compressive strength and modulus of the composite trays were observed. Especially, i-PP/MA-g-PP/MC-20phr composites showed higher compressive strength and modulus than the i-PP/MC-20 phr without MA-g-PP due to increased interfacial interaction between MC and i-PP matrix. A power and time of microwave heating and microcellulose loading also significantly affected to the mechanical properties of the tray. Microwave power at 340 and 650 watt, time spent using a microwave heating did not affected change in mechanical properties. However, at 1300 watt for 2.30 min, i-PP/MA-g-PP/MC-20 phr composite trays showed the highest compressive strength and modulus as 5.86 MPa and 1.72 GPa, respectively. Thermal properties of i-PP/MC composites with and without MA-g-PP were not significantly different from pure i-PP. In conclusion, MC synthesized from cotton fabric waste could be used as a reinforcing agent for thermoplastic manufacturing, moreover the mechanical properties increased after microwave heating as the percentage of crystallinity of the composite trays increased.

1. Introduction

Isotactic polypropylene (iPP) is a semicrystalline thermoplastic polymeric material that has been universally used due to its attractive integration of good processability, good chemical resistance and good mechanical properties [1]. Nowadays, plastic/fiber composites are widely used in many industries such as automobile, electronic, medical industries and packaging. The use of natural fibers in plastic/fiber composite are currently receiving the great attention, due to the global warming and growing environmental awareness [2]. Among other fillers used for such polymeric products, cellulose fibers became an interesting choice of the reinforcing materials because they display many advantages such as low density, little requirements on processing equipment, good thermal degradation, relatively low price and the most abundant natural polymer on Earth [3, 4]. Furthermore, polymeric packaging materials are well created in the microwave market and are now the most popular materials used for microwave packaging because of the ease of processing and forming, good transparency, safety and attraction to consumers. Among all properties of microwavable polymeric packaging, mechanical properties are often the most significant because they affect shelf-life and the majority of end-use applications [5]. As the result, the aim of this present work was to investigate effects of microwave heating and characterization on structures and properties of i-PP composites with the synthesized micro cellulose extracted from cotton fabric waste and maleic anhydride used as a compatibilizer. The test materials were prepared by a series of filled i-PP composites with micro cellulose loading at 5 up to 20 phr (parts per hundred resin) and maleic anhydride grafted PP (MA-g-PP) loading was fixed at 10% wt/wt [6]. The effects of microcellulose contents and microwave heating on mechanical properties, thermal properties and morphological properties were studied via the fabricated trays using injection molding.

2. Materials and Methods

2.1 Materials

Isotactic polypropylene (i-PP, EL-Pro P702J; melt flow index (MFI) 12 g/10 min, density 0.910 g/cm^3) is a homopolymer served as a matrix material for the preparation of composites and suitable for injection molding. Maleic anhydride grafted polypropylene (MA-g-PP, Fusabond P613 anhydride modified polypropylene; MFI 120g/10 min, density 0.903 g/cm^3) was used as the compatibilizer. Microcellulose fibers (MC) were synthesized from microcellulose from cotton fabric waste (CFW). A 80 g of CFW was mixed with 1500 cm^3 of a 2M-hydrochloric acid (HCl) solution. The reaction was operated at 80^{o}C for 4 hr under mechanical stirring at 350 rpm. After that, filtration and neutralization to pH 6-7 with distilled

water was done. The resulting fibers were oven dried at 60°C for 24 hr before being ground to a fine powder using a general electric blender for 1 min and stored under controlled temperature and humidity.

2.2 Preparation of composite

The i-PP, MA-g-PP and MC were dried at 60°C for 48 hr before the preparation of composites. The i-PP composites reinforced with MC (varied from 5, 10 and 20 phr) were mixed with and without MA-g-PP (10%wt/wt. based on i-PP weight) [7, 8] and were prepared in a corotating twin screw extruder (Collin/T-20). The temperatures of the four zones of the extruder were controlled at 165, 165, 170 and 170°C for zones 1, 2, 3 and 4, respectively with screw speed at 40 rpm. The resulting composites pellets obtained by compounding were oven dried at 60°C for 24 hr before being molded. The test samples were prepared by injection molding to a rectangular-shaped tray (height 45 mm, thickness 0.67 mm, width at the top 50 mm, width at the bottom 30 mm, diameter at the top 50 mm, and diameter at the bottom 30 mm) as shown in Figure 1.

(a) (b)

Figure 1. The test samples were prepared by injection molding to a rectangular-shaped tray: (a) pure i-PP and (b) i-PP/MC 20 phr

2.3 Measurements

Specimens were heated by 2.45 GHz household microwave oven (Panasonic NE-1356) that operated at 1300 watt for 2.5, 5 and 10 min. Then, they were subjected to compression tests immediately after microwave heating. Mechanical properties were measured with an Instron Universal Testing Machine (Model 5965) at room temperature with a crosshead speed of 10 mm/min. All measurements were performed for three replicates of rectangular-shaped tray specimens and averaged to obtain the final results. Test samples were oven dried at 40°C for 24 hr before the measurement. The morphology of the composites were obtained by scanning electron microscope (SEM). The Bruker TENSOR-27 FT-IR spectrometer with a total of 32 scans and all spectra were scanned within the range 4000–500 cm^{-1}. The crystallization temperature and melting temperature were obtained by Mettler Toledo DSC1 STAR SYSTEMS differential scanning calorimeter (DSC) from approximately 10-mg samples. The temperature of each scan was maintained at 50°C and 230°C for 3 min, and cooling rate was fixed at 10 °C/min under a gaseous N_2.

3. Results and Discussion

3.1 Mechanical properties

The compressive strength and modulus of the composites varied with MC and MA-g-PP after microwave heating at 1300 watt for 2.5, 5 and 10 minutes were shown in Figures 2 and 3. This study focused on the effect of microwave heating at 1300 watt because that microwave heating at 340 and 650 watt, time spent using a microwave heating did not affect change in mechanical properties and generally, the most commonly used high microwave heating rate in order to take less time. At microwave heating for 2.5 min, the compressive strength and modulus of the i-PP/MC and i-PP/MA-g-PP/MC composites displayed higher when compared to 5 and 10 min.

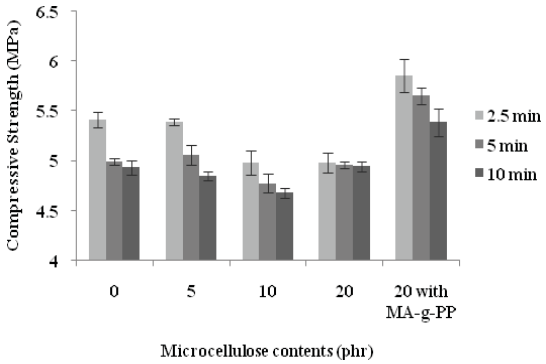

Figure 2. Compressive strength of pure i-PP and i-PP composites with MC and MA-g-PP contents after microwave heating at 1300 watt.

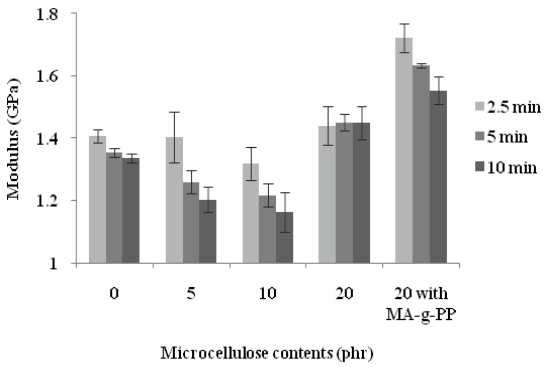

Figure 3. Modulus of pure i-PP and i-PP composites with MC and MA-g-PP contents after microwave heating at 1300 watt.

The effect of microwave radiation in the matter of time spent using a microwave heating can be explained by the high dielectric properties of i-PP. As time for microwave heating increases, i-PP matrix or high dielectric phase can be absorbed more microwave radiation and convert it to heat. The heat generated as a result of dipolar polarization of the molecules which are permanently polarized (chemical bonding), and they are realigned occurs a million times per second resulting in internal friction of molecules causing a volumetric heating of the i-PP [9]. Thus, the compressive strength and modulus of the composites after microwave heating at 1300 watt for 5 and 10 min displayed lower than 2.5 min, as would be expected.

With the addition of 10 phr microcellulose, the compressive strength and modulus decreases, but with the addition of 20 phr and 20 phr with MA-g-PP, it gradually increases. This behavior can be explained by the entanglement of the microcellulose fiber when its content is above 10 phr [2]. This entanglement was confirmed by the scanning electron micrographs that showed in Figure 4. The composites showed a similar trend of the compressive strength and modulus increase with the addition of MA-g-PP. It is worth noting that the addition the MA-g-PP compatibilizer in the composites for the i-PP/MA-g-PP/MC-20 phr yielded higher compressive strength and modulus than the i-PP/MC-20 phr that without MA-g-PP [2, 8, 10-13]. This action can be explained by the superior compatibility between MC and MA-g-PP than other composition without MA-g-PP because of the increased interaction between MC and i-PP matrix.

3.2 Morphological properties

The addition of MC and MA-g-PP influenced on the morphology of i-PP composites that can be shown in Figure 4. The morphology of the i-PP/MA-g-PP/MC composites (Figure 4(e)) displayed a strong interfacial

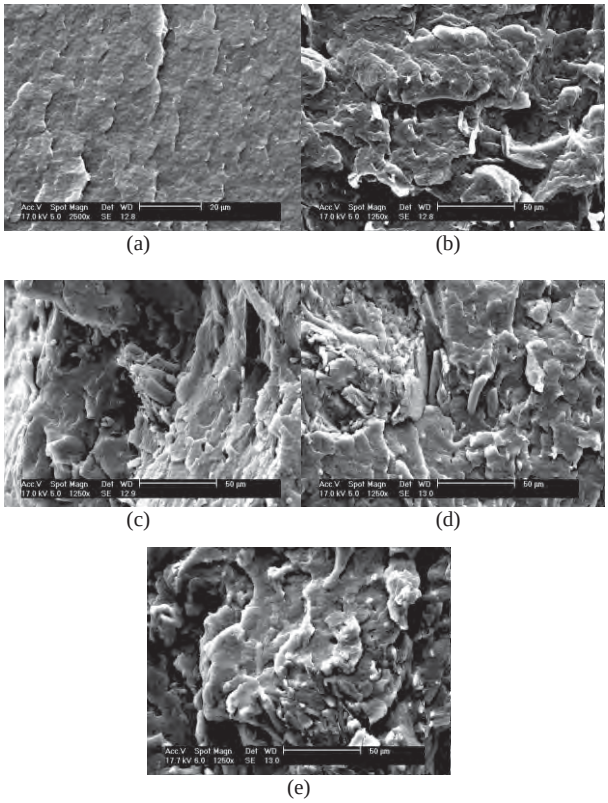

(a) (b) (c) (d) (e)

Figure 4. SEM micrographs of the i-PP/MC composites: (a) MC 0 phr, (b) MC 5 phr, (c) MC 10 phr, (d) MC 20 phr and (e) MC 20 phr with MA-g-PP

interaction between i-PP matrix phase and the MC reinforcement phase and also established smoother surfaces with less cavities and voids. This suggested that MA-g-PP is capable to improving the interfacial interaction between the polymer matrix and the cellulose fiber filler [2, 6, 8, 12, 14]. On the contrary, non-compatibilized composites (Figures 4 (b)-(d)) displayed an irregular surface appearance with large cavities and voids due to broken fibers and poor interfacial interaction with i-PP matrix [13, 15]. For the poor interfacial interaction easily led to complete debonding from the matrix in the compressive fracture surface and supported for lower mechanical properties of non-compatibilized composites.

3.3 Functional properties

FT-IR spectroscopy was used to observe the interaction between i-PP matrix, MC reinforcement and MA-g-PP compatibilizer, moreover to determine whether MA-g-PP would be efficiently used for the modification of the matrix or the surface of MC. The FTIR spectra can be shown in Figure 5.

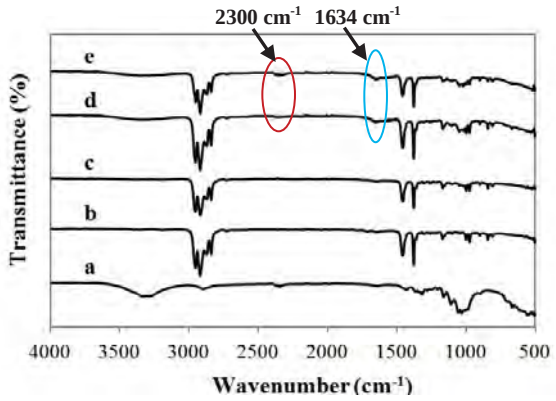

Figure 5. FT-IR spectra of (a) MC, (b) MA-g-PP, (c) pure i-PP, (d) i-PP/MC-20 phr and (e) i-PP/MA-g-PP/MC-20 phr.

The peak area at 3200-3400 cm^{-1} of (Figure 5 (d)) and (Figure 5 (e)) band has changed when compared to (Figure 5 (c)) band. This behavior might be the reason of the two different phases of the hydrophobic i-PP and hydrophilic MC that displayed higher peak area than (Figure 5 (c)) band. However, the peak shape and position of the composites with MA-g-PP as a compatibilizer are slightly changed as compared to the composites without MA-g-PP as a compatibilizer [16]. The peak at 1634 cm^{-1} of the composites indicated that the MA functional groups of MA-g-PP can be reacted with the hydroxyl groups of MC to produce covalent bonding that also can only be seen esterification reaction [16, 17]. Therefore, the ester bonding of MA-g-PP treated composites offer better dispersion which can thereby improve the mechanical and thermal properties of the final product [18]. The effect of microwave heating can be generated by vinyl group (CH_2-C=O) that can be seen in the peak area at 2300 cm^{-1} of (Figure 5 (d)) and (Figure 5 (e)) band. However, in the (Figure 5 (e)) band displayed higher peak area of vinyl group than (Figure 5 (d)) band. Therefore, the generation of vinyl group can be improved their mechanical properties such as the compressive strength and modulus. Ma-g-PP has the C=O and its can be exist in the i-PP. After heated by microwave, the pure i-PP showed the lower compressive strength than i-PP/MA-g-PP/MC-20 phr only (not lower compressive strength than other formulas) due to the improvement of interaction

adhesion between i-PP matrix and microcellulose reinforcement phase. For the prolonged microwave heating, all formulas exhibited similarly lower compressive strength because the high dielectric properties of the i-PP matrix phase can be absorbed high frequency electromagnetic energy (microwaves) and convert it to heat due to dipolar polarization of the molecules which are permanently polarized due to chemical bonding of the i-PP, and they are realigned in presence of high frequency electric field [19]. Because of high frequency, the realignment occurs a million times per second resulting in internal friction of molecules. Finally, the longer heated by microwave showed the lower compressive strength than shorter heated by microwave.

3.4 Thermal properties

The thermal parameters (crystallization temperature (T_c), melting temperature (T_m), heat of fusion (ΔH_f) and percentage of crystallinity (X_c)) determined and calculated from the differential scanning thermogrammes are summarized in Table 1. The composites with MA-g-PP show slightly lower T_m compared with the pure i-PP [20].

Table 1: Thermal properties of the i-PP composites

Sample	T_c (^oC)	T_m (^oC)	ΔH_f (J/g)	X_c (%)
i-PP	129	161	98	47
i-PP/MC-5 phr	128	156	90.5	43
i-PP/MC-10 phr	122.5	159	83	40
i-PP/MC-20 phr	121	159	84	40
i-PP/MA-g-PP/MC-20 phr	122	159	74	35.5

T_m decreased with MC content due to the addition of MC causing different crystallization in the matrix. This is because such nucleating agents changed the crystallization of the i-PP matrix phase around the MC reinforcement phase so the contact of i-PP and MC promoted a weak bond [20]. However, the results such as T_m and T_c were not significantly different from the pure i-PP. The temperature of operation of injection moulding is due to the crystallization temperature, so it was less effects from the blend of MA-g-PP. However, the heat load is slightly effect due to the decrease in percent crystallinity.

4. Conclusions

The optimum condition of i-PP/synthesized microcellulose was achieved at 20 phr of micro cellulose loading with the MA-g-PP as a compatibilizer at 10 %wt/wt. The compressive strength and modulus of i-PP/MA-g-PP/MC-20 phr showed higher results than those of i-PP/MC-20 phr without MA-g-PP. Especially, the effect of microwave heating gave the highest compressive strength and modulus because microwave heating can be generated by vinyl group. The morphological appearance of the composites displayed the improvement of interfacial interaction between the MC reinforcement and i-PP matrix, and also generated smoother surfaces when the addition of the MA-g-PP. The thermal properties of all composition composites were not significantly different from the pure i-PP so the composites can be used in the same temperature for i-PP thermoplastic. Finally, the synthesized microcellulose from cotton fabric waste has proven to be an appropriate reinforcing material in i-PP matrix for microwavable packaging and gave better properties than pure i-PP.

Acknowledgements

This work was partially supported by the Center for Advanced Studies for Agriculture and Food, Institute for Advanced Studies, Kasetsart University Under the Higher Education Research Promotion and National Research University Project of Thailand, Office of the Higher Education Commission, Ministry of Education, Thailand and the Graduate School Kasetsart University**.**

References

[1] X.L. Zhu, C.S. Wang, B. Wang and H.P. Wang, *Iran Polym J.* **17** (2008) 297-309.

[2] S.J. Kim, J.B. Moon, G.H. Kim and C.S. Ha, *Polym. Test*. **27** (2008) 801–806.

[3] A.K. Rana, A. Mandal, B.C. Mitra, R. Jacobson, R. Rowell and A.N. Banerjee, *Appl. Polym. Sci*. **69** (1998) 329-338.

[4] A. Amash and P. Zugenmaier, *Polymer*. **41** (2000) 1589–1596.

[5] U. Siripatrawan, G. Burgess and B. R. Harte, *Packag. Technol. Sci*. **13** (2000) 205-210.

[6] L.Y. Mwaikambo, E. Martuscelli and M. Avella, *Polym. Test.* **19** (2000) 905–918.

[7] S.H. Lee, S. Wang, G.M. Pharr and H. Xu, *Composites* **38** (2007) 1517–1524.

[8] S. Spoljaric, A. Genovese and R.A. Shanks, *Composites.* **40** (2009) 791–799.

[9] S. Chandrasekaran, S. Ramanathan, and T. Basak, *AIChE J*. **58** No. 2 (2012)

[10] W. Qiu, T. Endo and T. Hirotsu, *Eur. Polym. J*. **42** (2006) 1059–1068.

[11] A. Amash and P. Zugenmaier, *Polymer*. **41** (2000) 1589–1596.

[12] M. Bengtsson, M.L. Baillif and K. Oksman, *Composites*. **38** (2007) 1922–1931.

[13] A. Ashori and A. Nourbakhsh, *Composites*. **41** (2010) 578–581.

[14] C. Joly, R. Gauthief and B. Chabert, *Compos. Sci. Technol*. **56** (1996) 161-765.

[15] W. Qiu, T. Endo and T. Hirotsu, *Eur. Polym. J.* **42**, (2006) 1059–1068.

[16] D. Aht-Ong, D. Atong and C. Pechyen, *Mater. Sci Forum*. **695** (2011) 469-472.

[17] Mohanty S, Sushil KV, Sanjay KN, *Compos. Sci. Technol*. **66** (2006) 538–547.

[18] H.S. Kim, B.H. Lee, S.W. Choi, S. Kim and H.J. Kim, *Composites*. **38** (2007) 1473–1482.

[19] S. Chandrasekaran, S. Ramanathan, and T. Basak, AIChE Journal. **58** (2012).

[20] S.M. Luz, J. Del Tio, G.J.M. Rocha, A.R. Gonçalves and A.P. Del'Arco Jr, *Composites*. **39** (2008) 1362–1369.

PREDICTION OF THE OXIDATION STATE OF VANADIUM IN A VANADIUM REDOX FLOW BATTERY

Kittima Ngamsai[1], Amornchai Arpornwichanop[1,2*]

[1] Department of Chemical Engineering, Faculty of Engineering, Chulalongkorn University, Bangkok 10330, Thailand
[2] Computational Process Engineering, Chulalongkorn University, Bangkok, 10330 Thailand

[*] Author for correspondence; E-Mail: Amornchai.a@chula.ac.th, Tel. +66 2218 6878, Fax. +66 2218 6877

Abstract: Imbalance of vanadium ions in electrolyte and water diffusion across membrane degrades the efficiency of a vanadium redox flow battery system. To solve this problem, the electrolyte will be remixed or rebalanced to restore the cell capacity. In this study, a correlation of an open circuit voltage (OCV) and an oxidation state of vanadium in the electrolyte solution is investigated. Nernst equation is used to calculate the OCV from the vanadium oxidation state in each side of the electrolyte (positive and negative). The positive and negative OCVs are measured and compared with a reference electrolyte during the continuous charge-discharge cycling by using a constant current method. As a result, the vanadium oxidation state in the electrolyte is only a function of time and the charging time (or discharging time) can be then converted to vanadium oxidation state. The experimental results show that the prediction of cell voltage by Nernst equation agree reasonably with the experimental data at different oxidation states of vanadium. This information is beneficial to the prediction of cell performance (in term of capacity) from an available measurement of the modified OCV.

1. Introduction

Renewable energy has been presently received much attention as it can solve the problems of critical conventional energy sources. An inherent intermittency of renewable energy sources is the main problem which can be resolved by using energy storage technologies [1]. A vanadium redox flow battery (VRB) is one of the most promising energy storage technologies to alleviate an unpredictability of the supply of renewable energy sources [2]. VRB is a flexible system; its capacity and power rating can be independently designed. The capacity of VRB generally depends on volume and concentration of electrolyte solution, whereas the power rating depends on number and effective size of cells [3]. VRB is regarded as an electrochemical cell that energy is stored in an electrolyte solution (i.e., sulfuric acid with vanadium salt). Vanadium is a transition element and has four oxidation states, such as V^{2+}/V^{3+} and V^{4+}/V^{5+} represented by VO^{2+}/VO_2^{+} redox couples acted as the negative and positive electrolytes, respectively [4]. As the reduction and oxidation reactions (redox reactions) of vanadium occur, an electrical energy can be converted to chemical energy and stored into the VRB system. Because these reactions are reversible, electricity can be also discharged.

In normal operation, VRB faces a difficulty in the electrolyte imbalance that can cause a loss of capacity. Vanadium ions and water transfers across the membrane and side reactions, such as air oxidation of V^{2+} in the negative-half cell, are cause of the imbalance between the positive and negative electroactive species and a subsequent lose of its capacity [5]. To date, membranes have been developed to improve the transfer behavior of vanadium ion and water by several research groups [6]. Also, the periodic addition of chemical reactants to restore the electrolyte balance was studied [7].

In this study, a correlation of the open circuit voltage (OCV) and the oxidation state of vanadium in an electrolyte solution is investigated. The OCV will be an indicator of the electrolyte imbalance in each half cell and then proper action will be done to restore the cell capacity.

2. Materials and Methods

2.1 Correlation of OCV and oxidation state of vanadium in the electrolyte

Traditionally, an OCV cell is used to determine the overall state of charge (SOC). Data obtained can be correlated using Nernst equation when the electrolytes are balanced [5]. If the electrolytes become imbalanced, SOC in each half cell needs to be measured. Indeed, SOC represents the oxidation state of vanadium in electrolyte solution (e.g., 100% SOC or fully charged equals to 100% of V^{2+} and 100% of VO_2^{+} in negative and positive half cell, respectively; 0% SOC or fully discharged equals to 100% of V^{3+} and 100% of VO^{2+} in negative and positive half cell, respectively). There are two half cells in a conventional OCV cell: a half cell for the positive side and the other for the negative side. In this study, the OCV cell is modified to three half cells; an additional cell (the middle half cell) is used as a reference electrolyte (Figure 1).

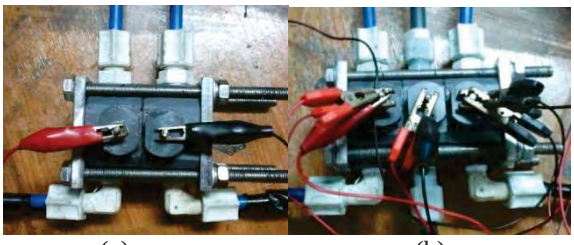

(a) (b)

Figure 1. (a) Conventional OCV cell and (b) modified OCV cell

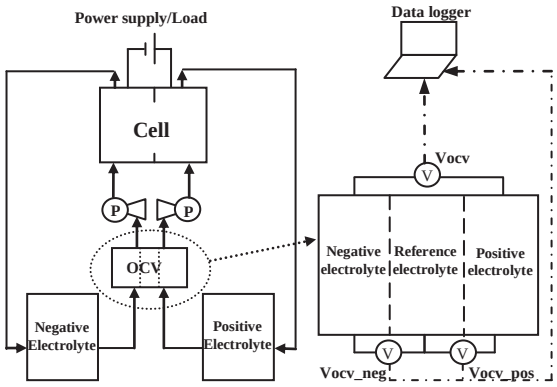

Figure 2. Schematic diagram of the VRB system

In order to determine a correlation of the OCV and the vanadium oxidation state, an experimental system was set up as shown in Figure 2. To prepare the initial electrolyte solutions, vanadium salt was dissolved in sulfuric acid solution at the concentration of 1.0 M, 1.5 M and 2.0 M and the same oxidation state of vanadium of +3.5 (including 50% V^{3+} and 50% VO^{2+}). This solution is used as positive, negative and reference electrolytes. The VRB single cell with effective area of 1 dm^2 and the modified OCV cell were employed. The electrolyte solutions were fed into the cell by two peristaltic pumps. A constant current was applied to charge and discharge for one cycle. Data logger was used to record OCVs for every 10 seconds. Three values of the OCVs are read: (1) OCV for positive side that is a measurement of the positive electrolyte compared to the reference electrolyte, (2) OCV for negative that is a measurement of the negative electrolyte compared to the reference electrolyte and (3) conventional OCV that is a measurement of the positive electrolyte compared to the negative electrolyte. The charging time (or discharging time) can be then converted to the vanadium oxidation state. In addition, to confirm the reliability of the used method, electrolyte solution samples were collected in different OCV values and were titrated to determine the oxidation state of vanadium using the potentiometric titration with potassium permanganate as a titrant.

2.2 Nernst equation for correlation of OCV and oxidation state of vanadium in the electrolyte

Nernst equation is used to describe the equilibrium potential of single redox electrode for an electrochemical system [8]. In the electrolyte system of VRB, the following reactions take place:

Oxidation of vanadium (from +2 to +3):

$$V^{2+} \Leftrightarrow V^{3+} + e^- \quad (1)$$

Oxidation of vanadium (from +3 to +4):

$$V^{3+} + H_2O \Leftrightarrow VO^{2+} + 2H^+ + e^- \quad (2)$$

Oxidation of vanadium (from +4 to +5):

$$VO^{2+} + H_2O \Leftrightarrow VO_2^+ + 2H^+ + e^- \quad (3)$$

Nernst equation can be applied to explain the correlation of OCV and oxidation state of vanadium, which is represented by a fraction of vanadium in different forms of the oxidation state as given in Equations (4) to (6). Actually, there are protons and sulphate ion in the electrolyte solution. These ions are called spectator ion because they are not an active part in the reaction [9]. The proton concentration $[H^+]$ in Equations (2) and (3) can be neglected because the variation of voltage is changed less than 7 mV from 0-100% SOC [10].

$$OCV_n = E_n^0 + \frac{RT}{nF}\ln\frac{[V^{2+}]}{[V^{3+}]} \quad (4)$$

$$OCV_m = E_m^0 + \frac{RT}{nF}\ln\frac{[V^{3+}]}{[VO^{2+}]} \quad (5)$$

$$OCV_p = E_p^0 + \frac{RT}{nF}\ln\frac{[VO_2^+]}{[VO^{2+}]} \quad (6)$$

where OCV_n, OCV_m, OCV_p are the OCV of the vanadium oxidation state from +2 to +3, +3 to +4 and +4 to +5, respectively, E_n^o, E_m^o, E_p^o are the potential that the reduced species equal to the oxidized species, in a range of vanadium oxidation state from +2 to +3, +3 to +4 and +4 to +5, respectively, R is the gas constant, T is the absolute temperature, n is the number of moles of electrons exchanged in a reaction, F is the Faraday's constant, $[VO_2^+]$ is the fraction of VO_2^+ in the electrolyte, $[VO^{2+}]$ is the fraction of VO^{2+} in the electrolyte, $[V^{3+}]$ is the fraction of V^{3+} in the electrolyte and $[V^{2+}]$ is the fraction of V^{2+} in the electrolyte.

3. Results and Discussion

3.1. Correlation of OCV and oxidation state of vanadium in the electrolyte

The OCVs were measured and recorded for every 10 seconds during charge/discharge cycles and the results are presented in Figure 3. According to Faraday's first law of electrolysis, the oxidation state of vanadium can be changed by charge transfer ($Q = \int Idt$) [9]. Since the constant current operation was applied, the oxidation state of vanadium is only a function of time.

As shown in Figure 3, the negative OCV and positive OCV are quite overlapped. It indicates that E_n^o equals to E_p^o. In general, the value of OCV measured includes the negative OCV and positive OCV. The same trend can be observed for the vanadium concentration of 1.0 M and 2.0 M, even the charging-discharging time changes. The charging and discharging times are converted to the oxidation state of vanadium as shown in Figures 4 and 5, respectively.

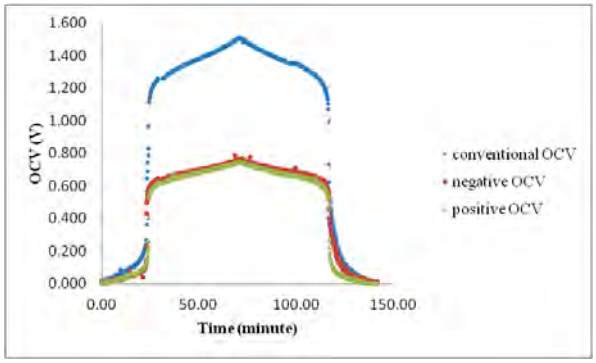

Figure 3. Correlation of time and OCVs at the vanadium concentration of 1.5 M

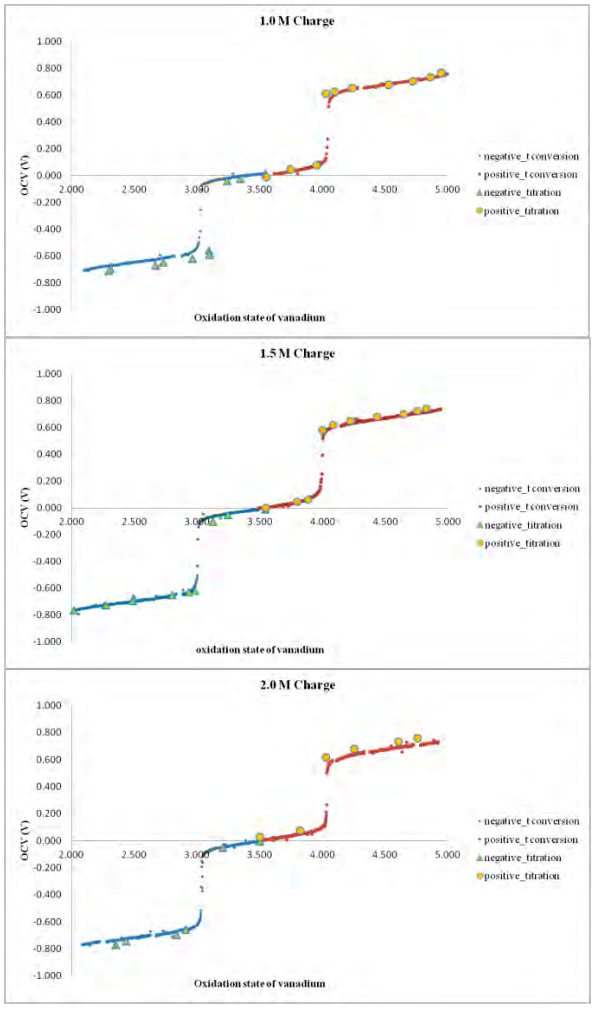

Figure 4. Correlation of OCV and oxidation state of vanadium at the vanadium concentration of 1.0 M, 1.5 M and 2.0 M (charging time conversion method and titration method)

Figure 4 shows the correlation of OCV and oxidation state of vanadium at the vanadium concentration of 1.0 M, 1.5 M and 2.0 M. The values of the oxidation state of vanadium obtained from the charging time conversion method agree with those obtained from the titration method; even though a difference is observed in cases of the vanadium concentration of 1.0 M and 2.0 M (oxidation state changed from V^{2+} to V^{3+}). Figure 5 shows the relationship between the oxidation state of vanadium and OCV at the vanadium concentration of 1.0 M, 1.5 M and 2.0 M, which is based on the discharging time conversion method and titration method. This confirms that the

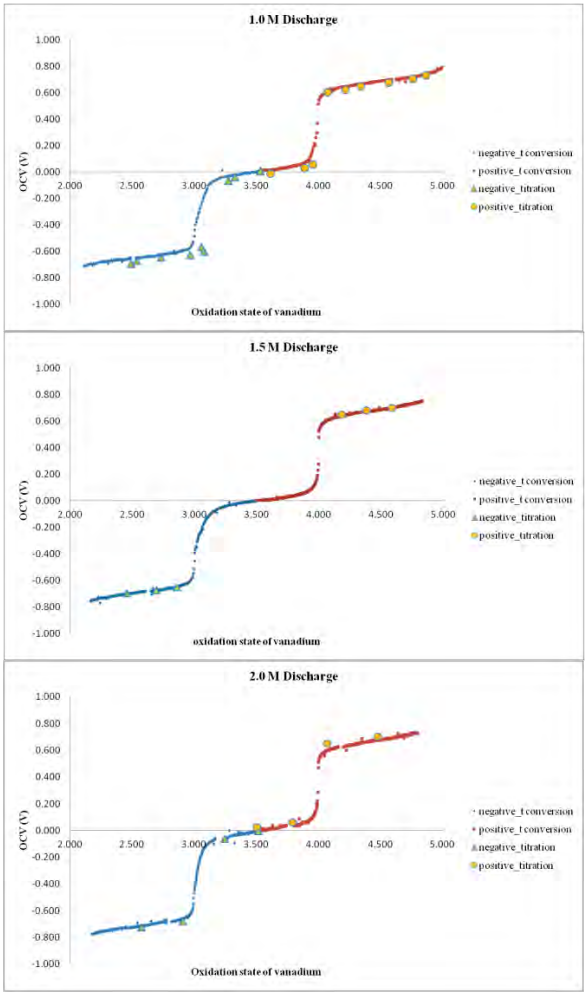

Figure 5. Correlation of OCV and oxidation state of vanadium at the vanadium concentration of 1.0 M, 1.5 M and 2.0 M (discharging time conversion method and titration method)

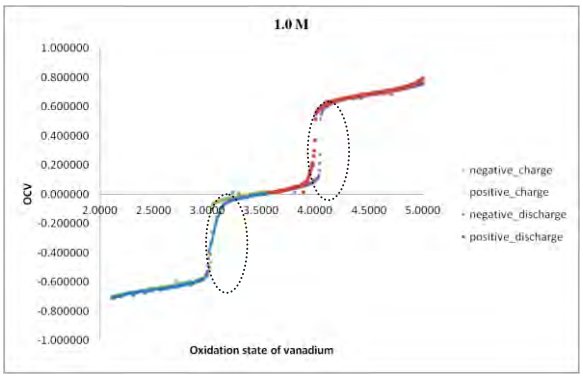

Figure 6. Comparison of the OCV and oxidation state of vanadium obtained from charging and discharging processes

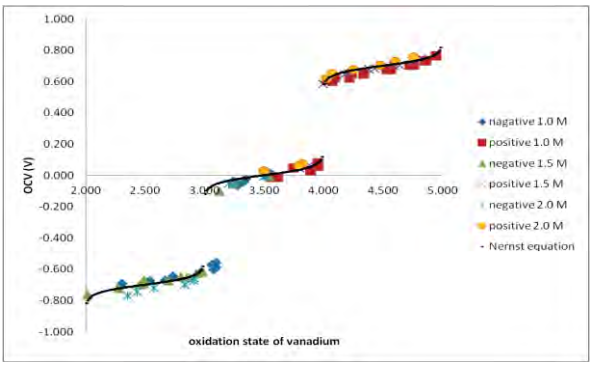

Figure 7. Comparison of OCV and oxidation state of vanadium at the vanadium concentration of 1.0 M, 1.5 M and 2.0 M (Nernst equation and titration method)

charging (or discharging) time conversion method can be used to estimate the oxidation state of vanadium instead of the titration method.

In both the charging and discharging processes, the difference of such a correlation is found in a range of the oxidation state change from +3.0 and +4.0, as shown in Figure 6.

3.2. Nernst equation

The experimental data is used to determine the values of E_n^o, E_m^o and E_p^o from Nernst equation (Equations (4) to (6)), respectively. Based on the oxidation state of vanadium of +3.5, as the reference electrolyte, it is found that the predicted values of E_n^o, E_m^o and E_p^o are -0.7, 0 and 0.7 V, respectively. Figure 7 compares the OCV predicted from Nernst equation and obtained from experimental results; the R^2 values are 0.9166, 0.9487 and 0.9989 for the vanadium concentration of 1.0 M, 1.5 M and 2.0 M, respectively. In an electrochemical cell, the standard potential of single cell is a combination of the standard reduction potential of the two half-cell [9]. Thus, the standard cell potential (E^0) in this study equals to 1.4 V, which is similar to that reported in the previous research [10]. Similarly, the OCV of the VRB can be calculated from a combination of the OCV of half-cell reduction and half-cell oxidation.

4. Conclusions

In this study, a correlation of the OCV and the oxidation state of vanadium is investigated. Nernst equation is used to describe this relationship. The standard potential of each half cell is obtained from experimental data. The results show that the prediction of cell voltage by Nernst equation agrees reasonably with the experimental data at different oxidation states of vanadium. Nernst equation with standard potential of each half cell from these experiments can be utilized to evaluate the oxidation state of vanadium in each side by measurement of the OCV at each half cell compared with the reference electrolyte. Electrolyte imbalance can thus be measured by modified OCV and Nernst equation. This information is beneficial to prediction of the system performance in term of capacity from an available measurement of the modified OCV.

Acknowledgements

Financial support from Cellennium (Thailand) Co., ltd., is gratefully acknowledged. The authors would also like to thank Dr. Suradit Holasut for his support and suggestions.

References

[1] P.J. Hall and E.J. Bain, *Energy Policy*. **36** (2008) 4352-4355.
[2] F. Xing, H. Zhang and X. Ma, *J. Power Sources* **196** (2011) 10753-10757.
[3] A. Tang, J. Bao and M. Skyllas-Kazacos, *J. Power Sources* **216** (2012) 489-501.
[4] D.S. Aaron, Q. Liu, Z. Tang, G.M. Grim, A.B. Papandrew, A. Turhan, T.A. Zawodzinski and M.M. Mench, *J. Power Sources* **206** (2012) 450-453.
[5] M. Skyllas-Kazacos and M. Kazacos, *J. Power Sources* **196** (2011) 8822-8827.
[6] D. You, H. Zhang, C. Sun and X. Ma, *J. Power Sources* **196** (2011) 1578-1585.
[7] M. Skyllas-Kazacos and L. Goh, *J. Membr. Sci. J.* **399-400** (2012) 43-48.
[8] K.W. Knehr and E.C. Kumbur, *Electrochem. Commun.* **13** (2011) 342-345.
[9] C. Blance, *Modeling of a vanadium redox flow battery electricity storage system*, Doctoral's Thesis, Polytechnic school Federal of Lausanne, (2009).
[10] T. Sukkar and M. Skyllas-Kazacos, *J. Membr. Sci. J.* **222** (2003) 235-247.

PURIFICATION PROCESS OF LANTHANUM AND NEODYMIUM FROM MIXED RARE EARTH

Dussadee Rattanaphra[1*], Orapun Leelanupat[2], Unchalee Suwanmanee[3]

[1] Research and Development Division, Thailand Institute of Nuclear Technology, Phathumtani, Thailand
[2] Nuclear Technology Service Center, Thailand Institute of Nuclear Technology, Nakhon Nayok, Thailand
[3] Department of Chemical Engineering, Srinakharinwirot University, Nakhon Nayok, Thailand

[*] Author for correspondence: E-Mail: drattanapra@yahoo.com, Tel. +66 2 4019889, Fax. +66 2 5772384

Abstract: The aim of this work is to study the purification process of lanthanum and neodymium from mixed rare earth by ion exchange technique. The products obtained from ion exchange process were precipitated with oxalic acid and finally calcinated at different temperatures. Effect of calcination temperatures (500, 600, 800 and 1000°C) on the purity of lanthanum and neodymium compounds was investigated. The purity of lanthanum and neodymium after ion exchange process were determined by ICP-AES. ED-XRF was used to measure the purity of both rare earth compounds. It was found that the purity of lanthanum and neodymium after ion exchange process were higher than 95% and 84% respectively. The calcination temperature (800-1000 °C) did not significantly affect the purity of both lanthanum and neodymium oxide. High purity lanthanum oxide of 98.68% and neodymium oxide of 94.92% were obtained after calcination at 800 °C.

1. Introduction

Recently, pure rare earth oxides play an important role in scientific and industrial applications. For example, their compounds are used in lasers, luminescence, magnets batteries and red phosphors. They are also used as catalyst and catalysts carrier in production of petroleum [1-3]. The minerals bastnasite, monazite, xenotime, loparite and fergusonite are the source of rare earth elements [1-2,4]. Lanthanum and neodymium are the most abundant of the rare earths after cerium. Lanthanum oxide is widely used in many fields such as a catalyst of oxidative coupling of methane, a catalyst support in the formation of gas conversion catalyst, optical glass, exhaust gas convertors, electrode materials and sensor [5-7]. Neodymium oxide has been extensively applied in various strategies. For example, it is used as components for advanced materials (e.g. ceramics and superconductors), as luminescent materials, as components of catalytic system (e.g. dehydration of alcohol and oxidative coupling of methane) or protective coatings [8-10].

It is extremely difficult to separate and purify lanthanum and neodymium from other rare earths due to their similar physical and chemical properties. The method for separation and purification of rare earth elements include fractional crystallization, fractional precipitation, solvent extraction and ion exchange methods [11]. The conventional method such as fractional crystallization and precipitation are laborious and inefficient [12]. Solvent extraction is reported to be an efficient method for separating and purifying rare earth elements. However, it has several limitations and disadvantages such as third phase formation, co-extraction, interference of different ions and use of high reagent concentration [13]. Ion exchange method has many advantages over separation and purification for the production of rare earths. It generates highly pure rare earths. This method requires little energy and the regenerated chemical are cheap. Moreover, it is a minimal organic solvent utilization, simple operation, compacted equipment and less waste accumulation [14-15]. However, it is time consuming process.

A survey of the literature reveals that not much research has been done on the purification of lanthanum and neodymium by ion exchange process. In this work, we attempt to purify both lanthanum and neodymium from mixed rare earth by ion exchange process. The effect of calcination temperature on the purity of both rare earth compounds was also study.

2. Materials and Methods

2.1 Purification of Lanthanum and Neodymium by Ion Exchange Process

Ion exchange process was conducted using seven glass columns, 10 cm in diameter and 100 cm long. Figure 1 shows the schematic diagram of ion exchange process for purification lanthanum and neodymium. Cation resin (Dowex™ HCR-S) with a particle size of 16-50 mesh was packed into the columns. The resin then was conditioned with 4% HCl solution. The column was washed with demineralized water to remove the excess acid. A 0.5 M of $CuSO_4$ was fed to the second to sixth column. The seventh column was loaded with 0.5 M of NH_4Cl solution. In this experiment, a sample solution was 0.15 M of mixed rare earth chloride. This solution was pumped through the first column. All columns were flushed with demineralized water until pH was 6-7. Then 0.015 M of EDTA at pH 8.2-8.4 was passed through the column with the flow rate of 1 L/h. The effluent from the column was collected in 240 ml fractions. The purity of lanthanum and neodymium in each fraction was analyzed by ICP-AES.

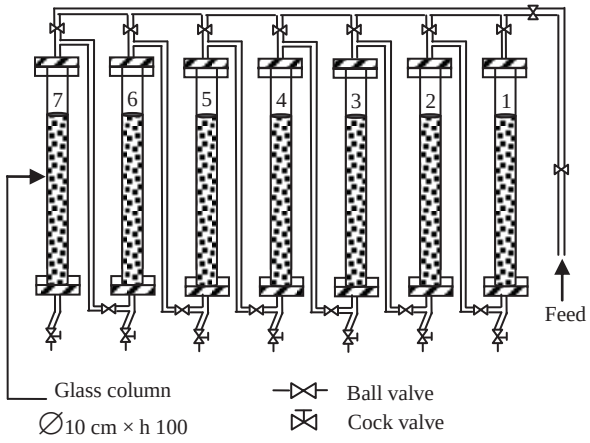

Figure 1. Schematic diagram of ion exchange process for purification lanthanum and neodymium.

After purification process by ion exchange column, the effluent which contained lanthanum was precipitated with 10 wt% of oxalic acid solution at pH 3-4. After that, the precipitate of lanthanum oxalate was filtrated in a vacuum Buchner filter and then dried at 110 ^{o}C for 12 h. The lanthanum was calcined at the different temperatures (500, 600, 800 and 1000 ^{o}C) for 3 h. The effluent which contained neodymium was precipitated as same as the precipitation method of lanthanum.

2.2 Analytical Methods

The composition of the feed solution (mixed rare earth chloride) and the purity of lanthanum as well as neodymium after ion exchange process were determined using ICP-AES (Optima 5300 DV, Perkin Elmer, USA). The operating parameters are shown in Table 1.

Table 1: ICP-AES operating parameters

Parameter	Setting
RF power	1300
Nebulizer gas flow rate	0.8 L min^{-1}
Auxiliary flow rate	0.2 L min^{-1}
Plasma gas flow rate	15 L min^{-1}
Wavelength	416.660 nm

The purity and composition of lanthanum and neodymium compounds calcined at different temperatures were measured by ED-XRF (Epsilon 5, PANalytiacl, Almelo, Netherland).

3. Results and Discussion

The composition of the feed solution is illustrated in Table 2. This solution was passed through the purification process using ion exchange column. This process took about 6 months. The 863 ml of effluent samples (240 ml of each) were collected to analyze the purity of lanthanum and neodymium.

Table 2: Composition of the feed solution (mixed rare earth chloride)

Element	%
Cerium (Ce)	69.79
Lanthanum (La)	5.90
Neodymium (Nd)	9.49
Samarium (Sm)	2.46
Gadolinium (Gd)	1.20
Praseodymium (Pr)	8.28
Yttrium (Y)	2.05
Europium (Eu)	0.01
Dysprosium (Dy)	0.79
Ytterbium (Yb)	0.07

Figure 2 presents the plot of the percentage purity of lanthanum and neodymium in the effluent from the ion exchange column against the effluent volume. It can be noted that the ion exchange process can efficiently improve the purity of both lanthanum and neodymium. The purity of lanthanum was increased from 5.90% to higher than 95%. In addition, the purity of neodymium was increased from 9.49% to greater than 84%.

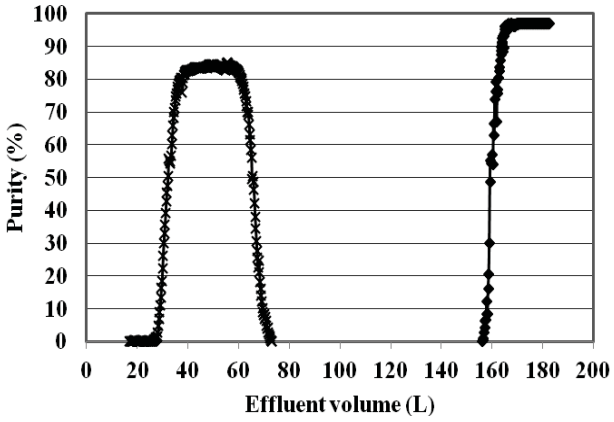

Figure 2. Percentage purity of lanthanum (—◆—) and neodymium (—×—) in the effluent from the ion exchange column

Tables 3 and 4 display the percentage purity of lanthanum and neodymium compound after precipitated and calcined at 500, 600, 800 and 1000 ^{o}C respectively. At calcination temperature 500-600 ^{o}C, both lanthanum and neodymium oxalate ($La_2(C_2O_4)_3$ and $Nd_2(C_2O_4)_3$) were decomposed into the dioxycarbonate form ($La_2O_2(CO_3)$ and $Nd_2O_2(CO_3)$) [16]. The purity of lanthanum and neodymium dioxycarbonate form did not obvious change when calcination temperature increased from 500 ^{o}C to 600 ^{o}C. The lanthanum and neodymium oxide (La_2O_3 and Nd_2O_3) were obtained when calcination temperature was in ranging of 800-1000 ^{o}C [16]. The increasing of calcination temperature from 800 to 1000 ^{o}C did not significantly affect the purity of both La_2O_3 and Nd_2O_3.

Table 3: Percentage purity of lanthanum compound after calcined at different temperatures

Calcination temperature (^oC)	Lanthanum compound*	Purity (%)
500	$La_2O_2(CO_3)$	98.76
600	$La_2O_2(CO_3)$	98.77
800	La_2O_3	98.68
1000	La_2O_3	98.69

Table 4: Percentage purity of neodymium compound after calcined at different temperatures

Calcination temperature (^oC)	Neodymium compound*	Purity (%)
500	$Nd_2O_2(CO_3)$	94.95
600	$Nd_2O_2(CO_3)$	95.09
800	Nd_2O_3	94.92
1000	Nd_2O_3	95.04

The chemical compositions of pure La_2O_3 and Nd_2O_3 calcined at 800 ^oC are shown in Table 5 and 6 reapectively.

Table 5: Composition of La_2O_3 calcined at 800 ^oC

Compounds	%
Al_2O_3	<0.01
SO_3	<0.01
Cl	0.01
CuO	0.01
La_2O_3	98.68
CeO_2	1.28
WO_3	0.01

Table 6: Composition of Nd_2O_3 calcined at 800 ^oC

Compounds	%
Cl	0.01
CuO	0.01
Y_2O_3	0.01
La_2O_3	0.14
CeO_2	0.05
Pr_6O_{11}	4.53
Nd_2O_3	94.92
Sm_2O_3	0.30
WO_3	0.01

4. Conclusions

The ion exchange process was developed to purified lanthanum and neodymium from mixed rare earth. The oxide form of both rare earths was prepared by the precipitation of effluents with oxalic acid and calcination at different temperatures (500-1000 ^oC). The results showed that the purity of lanthanum and neodymium after ion exchange process was increased to higher than 95% and 84% respectively. The calcinations temperature ranging from 800 to 1000 ^oC did not significantly affect the purity of lanthanum and neodymium oxide. At calcination temperature of 800 ^oC, high purity of lanthanum oxide of 98.68% and neodymium oxide of 94.92% were obtained.

Acknowledgements

Financial support from Thailand Institute of Nuclear Technology is gratefully acknowledged. The authors wish to acknowledge Mr. Chavalek Chayavadhanankur for the ideas and knowledge of rare earth purification.

References

[1] S. Radhika, B. Nagaphani Kumar, M. Lakshmi Kantam and B. Ramachandra Reddy, *Sep. Purif. Technol.* **75** (2010) 295–302.
[2] C.A. Morais and V.S.T.Ciminelli, Hydromethallurgy **73** (2004) 237–244.
[3] W. Yang, Y. Qi, Y. Ma, X. Li, X. Guo, J. Gao and M. Chen, *Mater. Chem. Phys*. **84** (2004) 52–57.
[4] S. Radhika, B. Nagaphani Kumar, M. Lakshmi Kantam and B. Ramachandra Reddy, *Hydrometallurgy* **110** (2011) 50–55.
[5] M. Salavati-Niasari, G. Hosseinzadeh and F. Davar, *J. Alloys Compd.* **509** (2011) 134–140.
[6] Z. Guang, Y. Jun-xia, X. Zhi-gao, Z. Fang and C. Ru-an, *Trans. Nonferrous Met. Soc. China* **22** (2012) 925–934.
[7] N.N. Soe, L.T. Shwe and K.T. Lwin, *World Academy of Science, Engneering and Technology 46* (2008) 142–145.
[8] M. Zawadzki and L. Ke piński, *J. Alloys Compd.* **380** (2004) 255–259.
[9] B.A.A. Balboul and A.Y.Z. Myhoub, *J. Anal. Appl. pyrolysis* **89** (2010) 95–101.
[10] M. Zawadzki, *J. Alloys Compd.* **451** (2008) 297–300.
[11] S. Jaffe and N.J. Plainfield, *Separation of rare earth values by means of a cation exchange resin*, Unitied States Patent, (1954).
[12] British Geological Survey, *Rare earth elements*, (2011).
[13] B.N. Kokare, A.M. Mandhare and M.A. Anuse, *J. Chil. Chem. Soc.* **55** (2010) 431–435.
[14] H. Hubicka and D. Kolodynska, *J. Rare earths* **26** (2008) 619–625.
[15] T. Arai, Y. Wei, M. Kumagai and K. Horiguchi, *J. Alloys Compd.* **408-412** (2006) 1008–1012.
[16] B.M.E. Russbueldt and W.F. Hoelderich, *J. Catal.* **271** (2010) 290–304.

CORROSION BEHAVIOR OF ELECTRODEPOSITED THIN FILM Co-Fe ALLOYS IN AERATED pH 4 SULFURIC ACID SOLUTION

Atittaya Chansena[1], Sutha Sutthiruangwong[2,*]

[1] College of Data Storage Innovation, King Mongkut's Institute of Technology Ladkrabang, Thailand
[2] Department of Chemistry, Faculty of Science, King Mongkut's Institute of Technology Ladkrabang, Thailand

[*] Author for correspondence; E-Mail: kssutha@kmitl.ac.th

Abstract: This work was separated into two parts, Co-Fe electrodeposition and corrosion study. According to electrodeposition, Co-Fe alloys were electrodeposited on copper substrate by cyclic galvanodynamic polarization technique. $CoCl_2 \cdot 6H_2O$ and $FeCl_2 \cdot 4H_2O$ were used as the source of cobalt and iron. The electrodeposition was studied in the field of effect of current range and electrodeposition time. The current range of 5 mA, total concentration of 0.1 M, and 5 hours of electrodeposition time are selected for this study. All the compositions of Co-Fe alloys were determined by X-ray fluorescence spectrometry (XRF) before corrosion measurement. The compositions of Co-Fe alloy can be controlled by adjusting Fe^{2+} and Co^{2+} concentration in the electrodeposition bath. The composition of Co-Fe alloy in deposit can be correlated with the Co and Fe concentration in solution. The corrosion behavior of Co-Fe alloys was studied in aerated pH 4 solution using potentiodynamic polarization technique. Corrosion current density was found to be increased with increasing Fe content.

1. Introduction

Soft magnetic materials are a central component of electromagnetic devices such as step motors, magnetic sensors, transformers and magnetic recording heads. In magnetic recording head technology, there are needs of higher areal density to increase storage capacity [1-3]. One of the common alloys for giant magneto resistive materials is Co, Ni, and Fe. Ferromagnetic materials Fe, Co and Ni can present instinctive magnetization as 1714, 1422 and 484 emu/cm^3 respectively. Co and Fe alloys are important materials in read/write head technology because they have the unique magnetic property to give high value of magnetization [4]. The parameters of electrodeposition such as the current density, electrolyte composition and bulk pH value on the deposited Co-Fe layer properties (morphology, structure, magnetic properties) have been investigated [5]. Magnetic alloy can be prepared by several techniques such as electrodeposition, DC sputtering, RF sputtering, chemical vapour deposition (CVD) and physical vapour deposition (PVD). Electrodeposition seems to be an interesting technique to prepare magnetic alloys because of high coating rate, easy to control alloys composition, be able to coat on curve or not flat surface, high density of metal alloy, good adhesion and low cost [6,7]. In previous research the electrodeposition was studied by several techniques such as cyclic voltammetry, pulse and pulse reverse plating [8-10]. Co-Fe electrodeposition can be controlled by adjusting Co^{2+} and Fe^{2+} in the solution [11]. XRD patterns of the precursor $CoFe_2O_4$ at different temperatures was found to be a spinel structure [12]. Corrosion is the major problem in chemical and many other industries. In general, corrosion is the result of water with a low pH. Acidic waters have lots of H^+ ions in the water to react with the electrons at the cathode, so corrosion is enhanced. Potentiodynamic polarization technique is the general technique to determine corrosion rate [13, 14]. The potentiodynamic polarization study of the addition of a small amount of Co on the corrosion properties of low alloy steel in a sulfuric acid solution was found that a higher Co content improves the active corrosion resistance [15].

In this study, the corrosion parameters were investigated in order to understand the corrosion behavior of Co-Fe alloy in aerated pH 4 solution by potentiodynamic polarization technique. It should be noted that there is small amount of research of corrosion issue on Co-Fe alloys fabricated using electrodeposition.

2. Materials and Methods

2.1 Co-Fe electrodeposition

Co-Fe alloy was deposited on copper substrate with diameter of 1.6 cm. Copper substrate was ground with 600 and 2000 grit SiC, respectively. Cleaning procedure was applied to remove lubricant and fingerprints on copper substrate. The copper substrate was cleaned with surfactant, rinsed with DI water, sonicated in isopropyl alcohol for 5 min and then dried with hot air. $CoCl_2 \cdot 6H_2O$ and $FeCl_2 \cdot 4H_2O$ were used as the source of cobalt and iron. The ratio of Co:Fe in the bath was specified as 20:80, 40:60, 60:40 and 80:20. The electrolyte was kept constant at pH 2 (adjusted by HCl). All solutions were prepared by using deionization water. The solution used for electrodeposition was purged with nitrogen gas for 30 min before deposition and during the experiment. The electrodeposition of Co-Fe alloy was done by Potensiostat/Galvanostat (PGSTAT 302N). The cyclic galvanodynamic polarization has been used for electrodeposition. Figure 1 shows the method of cyclic galvanodymanic polarization. The current was applied in cathodic region by starting from 0 mA for electrodeposition. The scan rate was kept constant at $1x10^{-4}$ A/s. The working electrode is copper substrate. Platinum and Ag/AgCl (3M KCl) were used as the counter and reference electrodes, respectively.

A lugging capillary was set at about 2 mm from copper substrate.

The electrodeposition was studied for the effect of current range, electrodeposition time and ion concentration in electrodeposition bath. The current range was varied as 4, 5, 6, 7.5, 10 and 15 mA to determine the optimal current range for deposition. The electrodeposition time was varied as 1, 3, 5 and 7 hours and the ion concentration in electrodeposition bath was varied as 0.01 and 0.1 M. The composition of Co-Fe deposits was measured by X-ray fluorescence spectrometry (XRF) and the crystal structure was determined by X-ray diffractrometer (XRD).

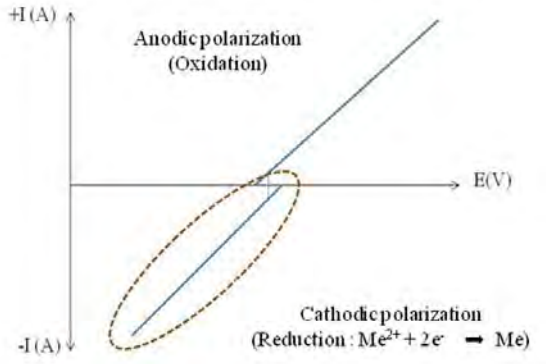

Figure 1. Cyclic galvanodynamic polarization for electrodeposition

2.2 Corrosion study

Potentiodynamic polarization test was applied to study the corrosion behavior of Co-Fe deposits in aerated pH 4 sulfuric acid solution at room temperature. The electrochemical measurement was measured by Potensiostat/Galvanostat (PGSTAT 302N) with a three-electrode cell. Platinum was used as a counter electrode. Ag/AgCl (3M KCl) was used as a reference electrode. A lugging capillary was set at about 2 mm from Co-Fe alloy substrate. The electrolyte used for measurement was purged with atmospheric air for 30 min before measuring and during the measurement to simulate the actual read/write head production environment and to ensure the oxygen saturation. The polarization was performed starting at -0.500 V from the open circuit potential (OCP). The scan rate was kept constant at 0.00028 V/sec (1000 mV/hour). The potential range of potentiodynamic polarization covered both cathodic and anodic region.

3. Results and Discussion

3.1 Co-Fe Electrodeposition

3.1.1 Effect of current range

The current range was varied as 4, 5, 6, 7.5, 10 and 15 mA to determine the proper current range for electrodeposition. The electrodeposition parameters were initially set as follows: 0.1 M total ion concentration, 3 hours of electrodeposition time, Co:Fe ratio of 60:40 and pH of the solution equals to 2. Figure 2 shows the surface morphology with current range of 4, 5, 6, 7.5, 10 and 15 mA respectively. Co-Fe alloys were fabricated by cyclic galvanodynamic polarization technique on copper substrate and currents were applied at the cathodic region starting from 0 mA. The surface morphology with current of 4, 5 and 6 mA shows no significant difference (see Figures 2a, 2b and 2c). The surfaces with current equal or higher than 7.5 mA show severe burn (see Figures 2d, 2e and 2f) due to higher current density per area. From the study current 4-6 mA is proposed as the proper current range for electrodeposition. For this work, 5 mA was used as a fixed current range for Co-Fe electrodeposition.

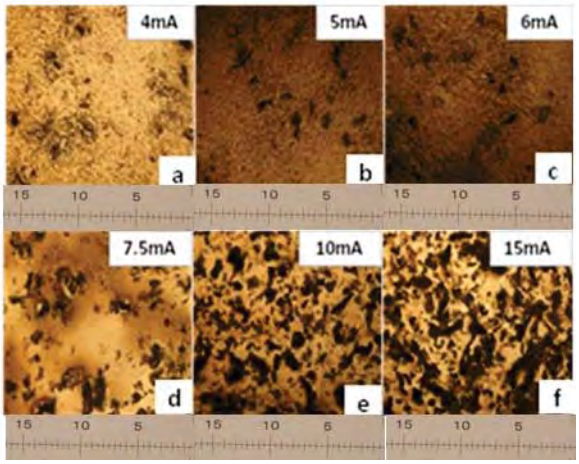

Figure 2. Surface morphology at different current range (milli inch)

3.1.2 Effect of electrodeposition time

The electrodeposition time was varied as 1, 3, 5 and 7 hours. The electrodeposition parameters were initially set as follows: 5 mA of current range, 0.1 M total ion concentration, Co:Fe ratio of 60:40 and pH 2. The composition of sample was determined by XRF. The XRF has been done for 2 points on the deposit. The data are shown in Table 1. Figure 3 shows the relationship between electrodeposition time and %Cu found from XRF. The %Cu was found to be decreased with increasing electrodeposition time. It means the deposition thickness was increased when the electrodeposition time was increased. Table 2 shows the average of Co and Fe contents in the deposit after normalization. The Co:Fe weight fraction in the deposit obtaining from XRF was similar to the ratio of Co:Fe in the solution. The difference between Co-Fe in deposit and Co-Fe in solution is about 1.33%.

Table 1: Composition of the Co-Fe deposit with different electrodeposition time

Time (hour)	2 points average			Stdev
	%Cu	%Co	%Fe	
1	93.6	3.77	2.63	0.05
3	79.8	12.18	8.06	0.03
5	48.1	30.75	21.14	0.27
7	27.6	44.32	28.07	0.62

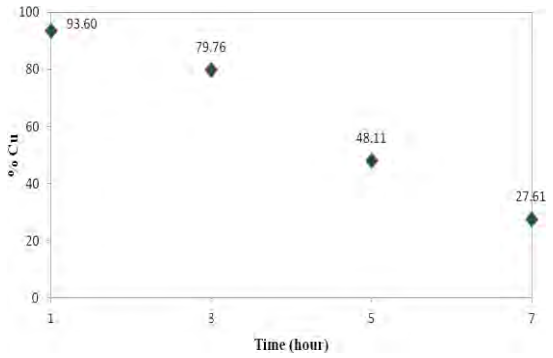

Figure 3. Relationship between electrodeposition time and %Cu from XRF

Table 2: Average Co and Fe content in the deposit

Time (hour)	Average		Stdev
	%Co	%Fe	
1	58.89	41.11	0.78
3	60.20	39.80	0.14
5	59.27	40.73	0.49
7	61.23	38.77	0.85

The crystal structure of sample was determined by XRD. The results of 1, 3, 5 and 7 hour electrodeposition time are shown in Figure 4. It can be confirmed that the structure of Co-Fe alloys are cubic structure for all electrodeposition time.

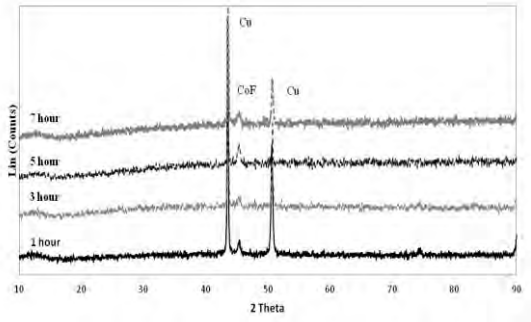

Figure 4. XRD pattern of Co-Fe alloys with different electrodeposition time

3.1.3 Effect of ion concentration

The ion concentration in electrodeposition bath was varied as 0.01 and 0.1 M. The electrodeposition parameters were initially set as follows: 5mA of current range, 5 hours of electrodeposition time, Co:Fe ratio of 60:40 and pH 2. Figure 5 shows the surfaces of deposited Co-Fe using 0.01 and 0.1 M ion concentration in electrodeposition bath. The surface obtained from 0.01 M shows incomplete deposition because of low ion concentration in electrodeposition bath. The surface obtained from 0.1 M shows complete deposition on copper substrate.

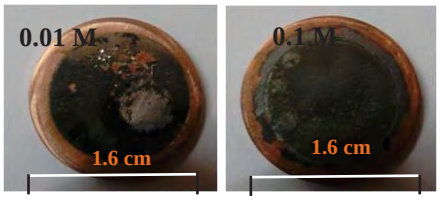

Figure 5. Surface deposit at 0.01 and 0.1 M ion concentration in electrodeposition bath

3.2 Corrosion behavior of Co-Fe deposits

For corrosion measurement, the Co-Fe alloys were prepared using 5 hour electrodeposition time, 0.1 M ion concentration and 5 mA current range with the ratio of Co:Fe as follows: 20:80, 40:60, 60:40 and 80:20. The Co-Fe composition was determined by XRF before corrosion testing. The relationship between Fe content in the deposit and Fe concentration in the solution is shown in Figure 6. Table 3 shows the average of Co and Fe contents in the deposition after normalization. The obtained composition can be controlled by adjusting the concentration composition of Co-Fe ion in solution.

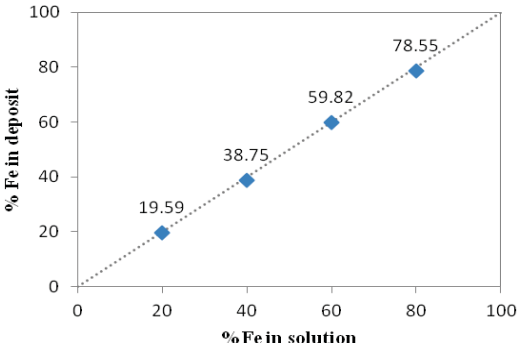

Figure 6. Relationship between %Fe in solution and %Fe in deposit

Table 3: Average Co and Fe contents in the deposit (for corrosion test)

Composition	Average		Stdev
	%Co	%Fe	
Co20Fe80	21.45	78.55	1.02
Co40Fe60	40.18	59.82	0.12
Co60Fe40	61.25	38.75	0.89
Co80Fe20	80.41	19.59	0.29

Figure 7 shows potentiodynamic polarization curves of Co-Fe alloys with Co:Fe ratio of 20:80, 40:60, 60:40 and 80:20 in aerated pH 4 solution. Tafel's extrapolation was used to determine corrosion potential (E_{corr}) and corrosion current density (i_{corr}). The E_{corr} of all samples maintain at around -0.310 V. The i_{corr} was found to be slightly increased with increasing Fe content. High Fe content alloy shows higher corrosion rate than that of low Fe content alloy. Fe is more active than Co because the standard

reduction potential value of Fe is lower than that of Co. The standard reduction potential of Fe is -0.440 V and the standard reduction potential of Co is -0.277 V. Therefore, the alloy with high Fe content was corroded in aerated pH 4 sulfuric acid solution faster than the alloy with high Co content. Corrosion parameters are listed in Table 4.

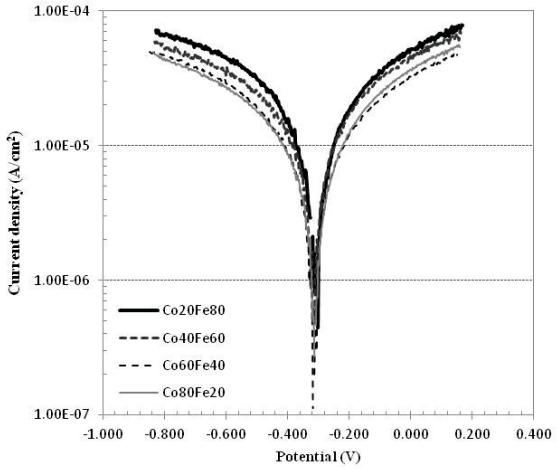

Figure 7. Potentiodynamic polarization curves of Co-Fe alloys with different weight fraction in aerated pH 4 solution

Table 4: Corrosion parameters for Co-Fe alloys in aerated pH 4 sulfuric acid solution

Compositions	i_{corr} (A/cm^2)	E_{corr} (V)
Co20Fe80	5.12×10^{-5}	-0.311
Co40Fe60	3.85×10^{-5}	-0.314
Co60Fe40	1.39×10^{-5}	-0.308
Co80Fe20	1.27×10^{-5}	-0.314

4. Conclusions

The Co-Fe alloys have been produced by using cyclic galvanodynamic polarization. The proper current range was 5 mA. Surface was burnt with high current. The composition of Co-Fe in electrodeposition bath can be related to Co-Fe content in deposit. The composition of the deposit can be controlled by adjusting Fe^{2+} and Co^{2+} in electrodeposition bath. According to XRD results, cubic crystal structure was obtained. The deposit thickness was increased when electrodeposition time was increased. Higher corrosion current density was obtained from the alloy with higher Fe content.

Acknowledgements

This work is supported by College of Data Storage Innovation, King Mongkut's Institute of Technology Ladkrabang (DSTAR, KMITL) and National Electronics and Computer Technology Center (NECTEC). Western Digital (Thailand) Company Limited is thankful for the equipment.

References

[1] Dennis E. Speliotis, *Magnetic recording beyond the Þrst 100 Years*, Journal of Magnetism and Magnetic Materials 193 (1999) 29-35.

[2] RogerWood, *Future hard disk drive systems*, Journal of Magnetism and Magnetic Materials 321 (2009) 555–561.

[3] LI Jing-feng, *Electrodeposition behavior of nanocrystalline CoNiFe soft magnetic thin film*, Trans. Nonferrous Met. SOC. China 16(2006) 659-665

[4] B.D. Cullity, C.D. Grahan, *Introduction to Magnetic Material*, IEEE Press 445 Hoes Lane,Piscataway, NJ 08854.

[5] E.I. Cooper, C. Bonhote, J. Heidmann, Y. Hsu, P. Kern, J.W. Lam, M. Ramasubramanian, N. Robertson, L.T. Romankiw, H. Xu, IBM J. Res. Dev. 49 (2005) 103.

[6] Pornpen Yaichareon, Pichet Limsuwan, Pongpan Chindaudom, *Research and Development of Thin Films Process by Ion Plating Method*, Department of Chemistry, Sience, KMUTT.

[7] Nasser Kanani, *Electroplating-Basic Principle, Process and Practice*, Atotech Deutschland GmbH, Berlin, Germany.

[8] Allen Bai, Chi-Chang Hu, *Effects of electroplating variables on the composition andmorphology of nickel-cobalt deposits plated through means of cyclic voltammetry*, Electrochimica Acta 47 (2002) 3447-3456.

[9] Allen Baib, Chi-Chang Hua, *Composition controlling of Co–Ni and Fe–Co alloys using pulse-reverse electroplating through means of experimental strategies*, Electrochimica Acta 50 (2005) 1335–1345.

[10] Penny Tsay, Chi-Chang Hu, Chun-Kuo Wang, *Compositional effects on the physical properties of iron–nickel deposits prepared by means of pulse-reverse electroplating*, Materials Chemistry and Physics 89 (2005) 275–282.

[11] Allen Bai a, Chi-Chang Hua, Ten-Chin Wen b, *Composition control of ternary Fe-Co-Ni deposits using cyclic voltammetry*, Electrochimica Acta 48 (2003) 2425-2434.

[12] Y.X.Gong, L.Zhen, J.T.Jiang, C.Y.Xu, W.Z.Shao. *Preparation of CoFe alloy nanoparticles with tunable electromagnetic wave absorption performance*, Journal of Magnetism and Magnetic Materials 321 (2009) 3702–3705.

[13] Amnuaysak Chianpairot, Gobboon Lothongkum, Christopher A. Schuh, Yuttanant Boonyongmaneerat, *Corrosion of nanocrystalline Ni–W alloys in alkaline and acidic 3.5 wt.% NaCl solutions*, Corrosion Science 53 (2011) 1066–1071.

[14] K.R. Sriraman, S. Ganesh Sundara Raman, S.K. Seshadri, *Corrosion behaviour of electrodeposited nanocrystalline Ni–W and Ni–Fe–W alloys*, Materials Science and Engineering A 460–461 (2007) 39–45.

[15] Keon Ha Kim, Seung Hwan Lee, Nguyen Dang Nam, Jung Gu Kim, *Effect of cobalt on the corrosion resistance of low alloy steel in sulfuric acid solution*, Corrosion Science 53 (2011) 3576–3587.

NANOENCAPSULATION OF EUGENOL BY β-CYCLODEXTRIN

Shunya Rodpothong, Thanya Ngamsantivong, Siriwimon Chutiwongsa,
Sitthiphol Puarattana-aroonkorn, Pisanu Toochinda*

Department of Bio-Chemical Engineering and Technology, Faculty of Engineering, Sirindhorn International Institute of Technology, Thammasat University, Pathum Thani,12121Thailand

*Email: pisanu@siit.tu.ac.th

Abstract: Eugenol compound is one of the major components that can be extracted from the clove of Thai sweet basil oil, *Ocimumbasilicum*. Eugenol has been used for antibacterial activity and dental application due to its properties of antiseptic and local anesthetic. The disadvantages of eugenol product in the market are strong odor and easy degradation by air and sunlight. According to its hydrophobicity, simulation result from molecular modeling indicated the formation of an inclusion complex with β-cyclodextrin (β-CD), water soluble cyclic oligomers of glucose, in order to encapsulate eugenol with 1:1 molar ratio. In this study, the formation of inclusion complex of β-CD and eugenol was carried out using three methods; normal grinding, cyclone and microwave. The encapsulation efficiency of eugenol in β-CD inclusion complex from different methods was determined by UV-visible spectroscopy and FT-IR. The experimental results show that, microwave is the best technique of the inclusion complex formation.

1. Introduction

Sweet basil oil (*Ocimum basilicum*) is extracted from sweet basil which is a spice used in Thai cuisine and commonly cultivated in Thailand. The major components in the oil are Linalool, Estragole, Methyl cinnamate and eugenol [1]. Among these components, eugenol plays an important role in many industries' utilization [2].

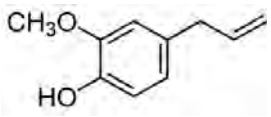

Figure 1: Structure of Eugenol

Eugenolis a phenolic compound as shown in Figure 1. Some of the most essential properties of eugenol are antibacterial and antifungal make it widely used in medical and dentistry fields [3]. However, eugenol is highly sensitive to light and air, which limits its application and bioavailability. Thus, the encapsulation techniques of eugenol are investigated for the benefit of shelf life extension and storage in several environmental conditions.

Cyclodextrins (CDs) are cyclic oligosaccharides that are composed of α-1, 4 linked glycopyranose with 6(α), 7(β) 8(γ) units [2]. They are produced from starch degradation by cyclodextrin glucanotransferase enzyme. Figure 2 shows the structure of beta-cyclodextrins (β-CD) which is the most accessible with the lowest price and water solubility of all cyclodextrins [4]. Due to its truncated-cone shape structure that possesses a hydrophobic cavity and hydrophilic at the outer surface, β-CD can effectively encapsulate hydrophobic molecules forming a host-guest complex [5]. The hydrophilicity of β-CD surface enhances the solubility in water of the host-guest complex therefore extending the range of application of the hydrophobic molecules [6]. Due to their ability to protect the guest molecules from oxidation, light-induced reaction and loss by evaporation, β-CD is widely used in pharmaceutical, food, and cosmetic applications [7]. There are studies that report the uses of β-CD for the encapsulation, for instance, cinnamon oil [8] and Carvedilol [9].

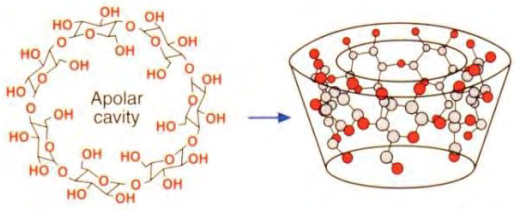

Figure 2: Structure of Cyclodextrin [10]

The present work describes a nanoencapsulation of eugenol (guest) using β-cyclodextrin (host) to form an inclusion complex using three different preparation methods; microwave, cyclone, and normal grindings. The goal of this study is to develop the preparation methods to encapsulate eugenol in form of inclusion complex β-CD which could enhance the stability of the guest molecule.

2. Materials and Methods

2.1 Materials

Eugenol (99%) and Ethanol (99%) were obtained from MERCK Ltd., and β-cyclodextrin (β-CD) was purchased from Sigma Aldrich, Inc.

2.2 Preparation of Eugenol and β-CD Inclusion Complex

The normal grinding, cyclone mixing and microwave technique were used to prepare the inclusion complex. 1 vol% and 10 vol% of ethanol in aqueous solutions were prepared to dissolve eugenol and β-CD respectively. The molar ratio of β-CD and

eugenol in all preparation methods were kept at 1:1 molar ratio. Both solutions were mixed in order to form inclusion complex.

In normal grinding technique, two mixtures were grinded using glass rod at 298 K for 1 minute continuously under closed container. The mixture was allowed to stay in the closed container in order to reach equilibrium for 5 minutes.

For cyclone mixing, the mixture was mixed using vortex mixer (vortex mixer –VELP-ZX3) at 15 rps for 10 seconds. The process was repeated for 6 times in order to achieve the total mixing time of 1 minute. The mixture was allowed to stay in the closed container in order to reach equilibrium for 5 minutes.

For microwave technique, the mixture was exposed to microwave radiation at 180 Watt for 3 seconds. In order to avoid the heat accumulation in the β-CD eugenol mixture, exposures were repeated every 15 seconds interval for 20 times. Total exposure time to the microwave radiation is 1 minute.

The preparation methods are all kept in 6 minutes in order to provide fairly evaluation of the effectiveness of each method. The complexes obtained from all preparation methods were filtered and then washed using 4°C of 30 wt% of ethanol aqueous solution three times to wash out non encapsulated eugenol. Finally, the inclusion complex powder were dried at room temperature

2.3 Characterization

2.3.1 UV-visible spectrophotometry

The UV-Visible spectrophotometer (Genesys 10uv scanning, Thermo Scientific) was used to determine the non encapsulated eugenol which remains in the filtrate. The known different concentrations of eugenol were dissolved into an ethanol aqueous mixture to prepare standard solutions. These standard solutions were scanned in the range from 200 to 350 nm to obtain the UV-visible absorption spectra. The calibration curve was constructed from the absorption spectra of 291 nm.

The efficiency of the encapsulation was determined by ultraviolet spectroscopy at 291 nm by the calibration curve.

2.3.2 Fourier transform-infrared spectroscopy (FT-IR)

The FT-IR spectra of eugenol/β-CD inclusion complex were collected between 500 and 4000 cm^{-1} by Smart Diffused Reflectance Infrared Fourier Transform Spectroscopy (DRIFTS) with the infrared spectrophotometer (Thermal Nicolet 6700). β-CD was used solely as a background then the inclusion complex was analyzed the existence of eugenol in the complex by subtracting with the pure β-CD background. From the study, the characteristic peaks of free eugenol are 1,610 cm^{-1} for aromatic bonding stretching [11]. While β-CD has characterized bonding of O-H stretching band at 3600-3200 cm^{-1} and alkene in plane bending at 1420 cm^{-1} [12].

3. Results and Discussion

3.1 UV-Vis Spectroscopy Analysis

The encapsulation efficiency for each method is analyzed by quantitatively measuring the concentration of non encapsulated eugenol which remains in the filtrate. The remaining concentration is calculated by using equation (1) that is obtained from the calibration curve of standard solutions at the wavelength of 291 nm.

$$\text{Absorbance} = 0.0149(C) + 2.7135 \qquad (1)$$

The percentage encapsulation efficiency of eugenol encapsulation is calculated from eugenol encapsulated concentration which is a subtraction of the initial concentration of eugenol with the concentration in the effluent after washing. The percentage of encapsulation of each method is calculated as following:

Table 1: Encapsulation efficiency of eugenol inclusion complex by 3 methods

Method	UV abs (at 291 nm)	**Remaining Concentration (µmol/L)**	**Encapsulation efficiency (%)**
Microwave	3.082	24.73	71.97
Cyclone	3.532	54.93	37.74
Normal Grinding	3.233	34.87	60.48

Table 1 shows the UV absorbance in relative to the remaining concentration of eugenol in the filtrates for 3 methods. The results demonstrate that Microwave is the most efficient method for encapsulation, which is almost 72% encapsulation efficiency. Microwave could gradually rotate eugenol molecule to boost the possibility of eugenol to enter into β-CD cavity and form the inclusion complex easily.

Surprisingly, the cyclone is the least efficient method for the encapsulation. The encapsulation efficiency is even lower than normal grinding which requires none of special process. The vigorous shake forces eugenol and water more soluble to each other. As a result, this method allows water molecules to form around eugenol and prevents Eugenol from forming an inclusion complex with β-CD.

3.2 Infrared spectrum of inclusion complex

In order to determine the eugenol presentation in the complex, the solid complexes were analyzed by using FT-IR technique. The result of FT-IR (Table 2) shows that the characteristic absorbances of eugenol complex as follows; carbon-carbon aromatic ring stretching (C=C) at wavenumber of 1613 cm^{-1} and 1654 cm^{-1} , the alkene stretching (C=C) at 1638 cm^{-1} and the carbon-hydrogen bond (C–H) on aromatic ring stretching at 3044 cm^{-1} and 3077 cm^{-1}. All of these

absorbances indicate the existence of eugenol in β-cyclodextrin inclusion complex powder.

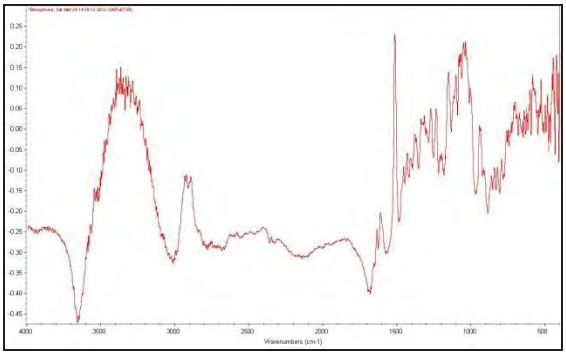

Figure 3: Infrared spectrum of eugenol β-CD inclusion complex

Table 2: Characteristic in FT-IR

Wavenumber (cm^{-1})	**Assignment**
1613, 1654	n(C=C, aromatic)
1638	n(C=C, alkene)
3077, 3044	n(C–H, sp^2)

4. Conclusions

Microwave is the most efficient method to form 1:1 molar ratio host-guest complex among other inclusion complex preparation methods in this study. Based on UV-visible spectroscopy analysis, microwave has the capability of encapsulating eugenol up to 72%. The FT-IR analysis confirmed the presence of aromatic carbon double bonds, alkene carbon, and carbon-hydrogen bonds of the aromatic ring which are the major parts of eugenol molecule structure in the inclusion complex. The results obtained from the study can be further applied globally in the preparation method of eugenol- β-CD inclusion complex.

Acknowledgements

This work was supported by the National Research University Project of Thailand Office of Higher Education Commission and Low Carbon Technology and Management Research Grant.

References

[1] S. J. Lee, K. Umano, T. Shibamoto, K.G.Lee. *Food Chemistry*, **91** (2005) 131-137.
[2] P. N. Ezhilarasi, P. Karthik, N. Chhanwal, C. Anandharamakrishnan, *Food Bioprocess Technology*, (2012) Publish Online: 12 August 2012
[3] Del Valle, E.M.M., Process Biochemistry, **39**(9) (2004) 1033-1046
[4] Ponce Cevallos, P.A., M.P. Buera, and B.E. Elizalde. Journal of Food Engineering, **99**(1) 2010 70-75
[5] Song, L.X., et al., Coordination Chemistry Reviews, **253**(9–10) (2009) 1276-1284**.**
[6] Szejtli, J., Chemical Reviews, **98**(5) (1998) 1743-1754.
[7] Hedges, A.R., Chem Rev, **98**(5) (1998) 2035-2044.
[8] Wen, X., et al., Journal of pharmaceutical and biomedical analysis,. **34**(3) 2004517-523.
[9] The university of Arizona- contaminant transport group.(2012) Characterization and Remediation of Hazardous Waste Sites (Internet) Available from: http://www.u.arizona.edu/~brusseau/research.htm Accessed date 14 Oct 2012
[10] Hao Zhan, Zi-Tao Jiang, Ying Wang**,** Eur Food Res Technol **227** (2008) 1507–1513
[11] Lai-Hao Wang, Wei-Chien Sung. Spectroscopy **26** (2011) 43–52
[12] A. Rukmani ,M. Sundrarajan. Journal of Industrial Textiles **42**(2) (2011) 132–144

PLANTWIDE CONTROL STRUCTURE DESIGN OF *TERT*-AMYL METHYL ETHER (TAME) PROCESS.

Thitima Tapaneeyapong[1], Montree Wongsri[1*]

[1]Department of Chemical Engineering, Faculty of Engineering, Chulalongkorn University, Pathumwam, Bankok, 10330 Thailand

*E-mail: montree.w@chula.ac.th

Abstract: The process of *tert*-amyl methyl ether (TAME) consists of a plug-flow reactor, one reactive distillation column, two conventional distillation column, two recycle streams and two fresh feed streams. That is a complex process. Therefore, the plantwide control structure is essential to the production process for reach the control objectives and effectively operating large disturbances (in production rate and fresh feed compositions). This paper presents the control structure of *tert*-amyl methyl ether that is designed by Wongsri's plantwide control structure design procedure (Wongsri's method). A material-balanced process plant is created by keeping the raw materials entered to the reactor fixed. Next, the flow of exit material streams is adjusted. Then, the quantifiers are located for the rest of the components to design the control loops to regulate their inventories. Finally, the disturbances are handled. The control structure is carried out using commercial process dynamic simulator.

1. Introduction

Plantwide process control has been an importance in the process industries because it concerns strategies required to control an entire chemical plant. Most industrial processes involve lots of unit operation, several recycle streams and energy integration connected the process. These make up the complex flowsheet structure. The recycle streams and energy integration caused a feedback of material and energy among the units up streams and down streams. These factors create a path of disturbances in the process; although, process economic can be improved by introducing recycle streams and energy integration into the process. Therefore, plantwide control is required to operate the entire process achieving design objective and plant safety.

tert-Amyl methyl ether (TAME) is used as a fuel oxygenate to increase the octane number in gasoline. Although production process of TAME consists of many operating units; however, a reactive distillation is the main focused in this study. The control of reactive distillation is different from a conventional distillation. One crucial important inherent advantage of reactive distillation is its feature of simultaneous production and its removal of products. For reversible chemical reactions, the removal product components drives reaction toward product side. Thus, the chemical equilibrium constraint on conversion can be overcome while high conversions can be achieved, even in many cases with small chemical equilibrium constrains. Of course, the reactive volatilities among reactants and products must be such that the products can be fairly easily removed from the region in column where reactions are occurring and reactants not lost from this region.

This research aimed to study the design procedure of the plantwide control structure by Wongsri and applied to *tert*-Amyl methyl ether (TAME) production process.

2. Materials and Methods

2.1 Plantwide control structure design procedure

The plantwide control structure of *tert*-Amyl methyl ether (TAME) production was designed using Wongsri procedure. The procedure consisted of eight steps of the plantwide control structure design which makes use of chemical engineering and process knowledge and heuristics. The design procedure was carried out in eight steps as follow:

Step1: Gather relevant plant information and control objective including constraints for control.

Step2: Plant Analysis.

2.1 List the manipulated variables (control degree of freedom, CDOF).

2.2 Heat pathways.

The first pathway is from inside the process and flows out to the environment heat generated by exothermic reactions and by degradation of mechanical work. A second pathway carries heat from utilities into the process and to the environment. The third pathway is internal to the process. The heat flow is circular and its magnitude depends upon the heating and cooling needs and the amount of heat integration implemented.

2.3 Material pathways.

The concept of material pathway is introduced here. The pathway is the flow path of a component from an entry point or an originated point to an exit point or an end point.

2.4 Locate quantifiers.

In order to regulate a component balance in a process plant, a location representing the amount of material in the plant must be identified to provide its handle. A material balance for each component must be satisfied. From the viewpoint of individual units, chemical component balancing is not a problem because exit streams from the unit automatically adjust their flows and compositions. However, when operating units are connected together with recycle streams, the entire system behaves almost like a pure

integrator in terms of the reactants. Luyben [1] gives a more complete discussion of this phenomenon. The features of material recycle and chemical component inventories mentioned above which have profound implications for a plant's control strategy [1] and can be handled quite readily by making use of quantifiers. By locating a quantifier, the quantity of a component quantified is regulated by using its handle.

Step 3: Establish fixture plant.

The principal idea of establishing a fixture plant is first to have an entire plant fluid-filled and a material-balanced. By establishing a fixture plant we mean creating a material-balanced process plant:

3.1 Keep the materials entered and reentered fixed.

3.2 Regulate the production rate.

3.2.1) Consume the limiting reactant.

3.2.2) Regulate the production rate. The product rate can be regulated through 3.2.1. If this is done and the production rate does not reach the objective or the production demand, the limiting reactant feed rate must be increased. The reaction information about the accumulation or depletion of the limiting reactant must be used to determine the control strategy. However the design constraint may limit this strategy concerning increasing the reactant feed rate.

3.3 Adjust the flow of exit material streams (products, by-products, and inert) according to their accumulations.

3.4 Regulate the rest of the components at their quantifiers, i.e. the indicators of the representative accumulation, for the rest of the components and design the control loops to regulate their inventories in the plant. The quantifier can be volume (mass), pressure, or flow rate.

Step4: Handling the disturbances

In this step, the disturbances are handled by configuring the control loops employing the principle of disturbances management:

4.1 Heat Disturbances.

4.1.1) Direct the thermal disturbances that are not directly related to quality to the environment via the next and nearest exit points, usually heaters or coolers, to keep the thermal conditions of process stream fixed. The thermal condition of process stream is changed along the process plant, usually by heater or cooler of process to process heat exchanger.

4.1.2) Manage the thermal disturbance that related to quality in order to maintain the product specification constraints.

4.2 Material disturbances.

The configuration of the control loops depend on the desired material pathways. The pathways can be obtained by analyzing the results of the material disturbance tests. The test is suggested to be done on the changing of compositions, total flows, and component flows.

Step5: Design the control loops for the remaining control variables and/or adding enhanced controls, i.e. cascade, feed forward controls.

Step6: Energy management via heat exchanger networks.

If potential heat exchanger networks or alternative heat integrated processes (HIPs) exist, Energy management via heat exchanger networks. List the additional control variables and manipulated variables.

Step7: Optimize economics and/or improve control performance.

Step8: Validate the designed control structures by rigorous dynamic simulation.

2.2 Process Description

The TAME train uses C5 fraction from a petroleum refinery and methanol as raw materials. TAME is produced by the catalytic etherification of isoamylenes [2-methyl-1-butene (2M1B) and 2-methyl-2-butene (2M2B)] with methanol. The three main reversible reactions in this process are the following:

$$2M1B + methanol \leftrightarrow TAME$$
$$2M2B + methanol \leftrightarrow TAME$$
$$2M1B \leftrightarrow 2M2B$$

The kinetics for reactions are given by Al-Arfaj and Luyben[2]. The process flowsheet is shown in Figure 1. The C5s fresh feed and methanols are fed to the prereactor, which contains 9544 kg of catalyst at catalyst bulk density is 900 kg/m^3. The reactor effluent and methanol stream are fed to the reactive distillation column (36-stages) at stage 28 and stage 23, respectively. The reactive zones are presented at stages 7-23. This column operates at a pressure of 4 bar. The reflux ratio is 4, which gives a bottoms purity of 99.2 mol% TAME. The distillate of reactive column is then fed to second column (the first of the two columns

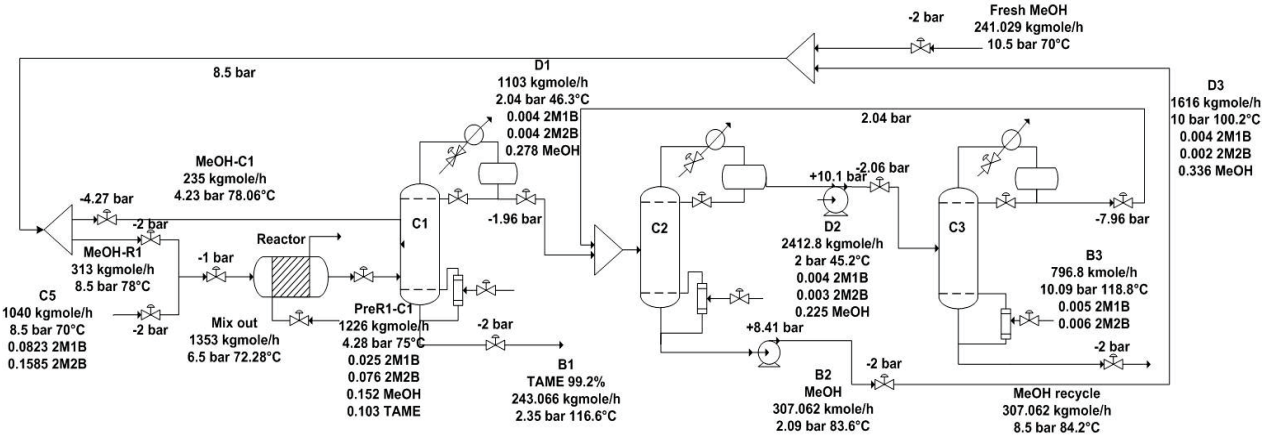

Figure1. TAME process flowsheet.

pressure-swing (10-stages)) at stage 5. Similarly, the distillate obtained from this column is fed to the third column (the second of the two columns pressure-swing (10-stages)) at stage 5. The operating pressures of the two columns pressure-swing are 2 and 10 bar, respectively. And the reflux ratios are 0.4 and 1. The bottoms purity of second column is 99.9 mol% methanol. This bottom is mixed with methanol fresh feed, and total is split between the methanol fed to reactor and methanol fed to reactive distillation column. Finally, the distillate of third column is recycled back to second column.

3. Results and Discussion

Here, the above plantwide control structure design procedure was applied to the tert-amyl methyl ether (TAME) production process. In Aspen dynamics program, a flowsheet with a tubular reactor would not operate properly. Thus, Al-Arfaj and Luyben [3] presented to a turbular reactor was replaced by two continuous stirred tank reactors in series.

Step1: Process information.

The process information given in section 2.2. The purity of the TAME product at 99.2 mol% with capacity of 217,408 tons/year was essentially required to meet process objectives.

Step2: Plant Analysis.

2.1 Control degree of freedom (CDOF).

The CDOFs for the TAME production process were presented in Table.1.

2.2 Locate quantifier.

The C5s quantifier was at the bottom of C3.

The Methanol quantifier was the flowrate stream of methanol fed to C1.

The TAME quantifier was at the bottom of C1.

Step 3: Establish fixture plant

3.1 Keep raw materials flow entered and reentered fixed. The raw materials were very important for demand production. In regulation, the C5s fresh feed to the first reactor by manipulating flow rate of C5s. Flow rate of methanol to reactor and reactive distillation column were controlled by adjusting methanol fresh feed.

3.2 Adjust flow of exit material streams according to their accumulations (products, by-products, and inert). The exit material stream in the process was at two end points, the bottom product of C1 and C3, respectively. The liquid levels in reflux drums were controlled by manipulating distillate flow rate.

Step 4: Handling the disturbances

4.1 Heat Disturbances

4.1.1) Direct heat disturbances which were not directly related to quality to the environmental via next and the nearest exit points, usually heaters of coolers, to keep thermal conditions of process stream constant.

4.1.2) Manage the heat disturbance which related to quality in order to maintain the product constraints. In this step the temperature was regulated in two reactors by adjusting cooling water. The tray temperature of C1, C2 and C3 were controlled by manipulating reboiler heat input. The trays were selected by location where temperature profile was sensitivity.

4.2 Material disturbances.

As the material disturbances entered process can be regulated by measuring the isoamylenes in PreR1-C1 stream and sent signal ratio with the methanol stream fed to C1 as shown in Figure 2.

Table.1 The control degree of freedom for the tert-amyl methyl ether production process.

Unit	Manipulated ariable	Quantity	DOF
Independent streams	Flow rate	3	3
Reactor	Outlet flow, Cooling flow	2	4
Distillation column	Distillate flow, Bottom flow, Reboiler heat remove, Condenser heat input	3	15
Total			22

Step5: Design control loops for the remaining control variables. All columns pressure were regulated the reaction in C1 and the separation in C1, C2 and C3. The reflux ratios in all columns were controlled by manipulating reflux rate.

Step6: Energy management via heat exchanger networks. In this process, temperatures of all streams were low temperature, therefore, heat exchanger network not necessary in this process.

Step7: Optimize economics and/or improve control performance. The flowsheet by Al-Arfaj and Luyben [1] has completed its economic optimization in previous work so this step was not taken into account.

Step8: Validate the designed control structures by rigorous dynamic simulation.

Figure 2 shows the new plantwide control structure of *tert*-amyl methyl ether process designed by Wongsri procedure. This control structure was examined by two kinds of disturbances. First is C5s feed rate disturbances. It is changed ±10% (±ΔF) at 0.5 hr. Figure 3 presents the responses to positive and negative 10% changes in the C5s feed rate. The procedure gives a positive result of dynamic control by effectively handling disturbance through process. The new control structure can be maintained TAME purity very close to its specification. The system reaches a new steady state in about 6 hr. The second is C5s feed composition disturbances. It is changed ±10% ((±ΔZ) of isoamylenes in the feed. The respones of design control structure shown in Figure 4. The control structure provides effective control of the process.

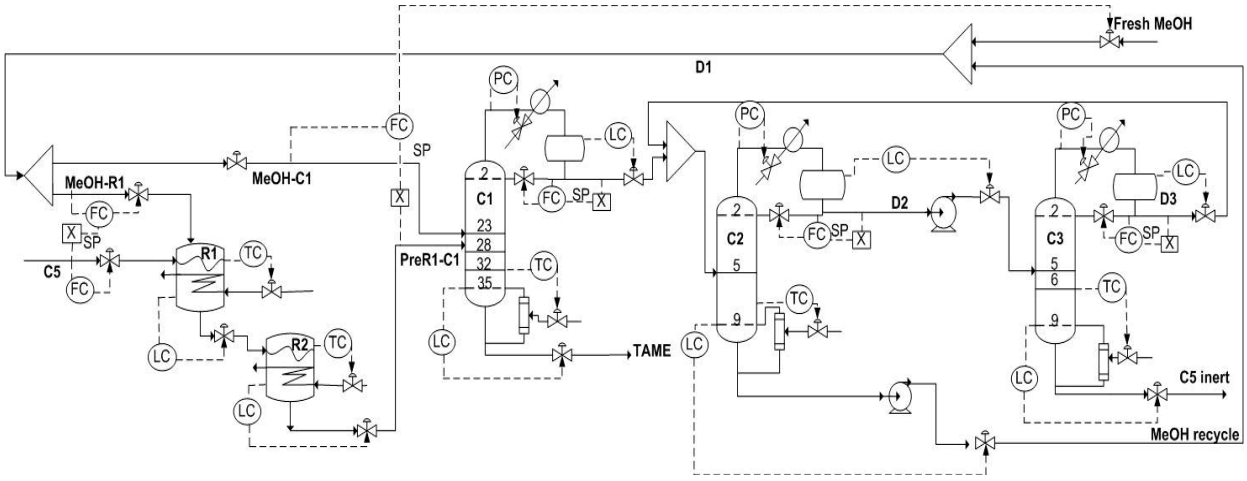

Figure 2. Designed control structure for TAME process.

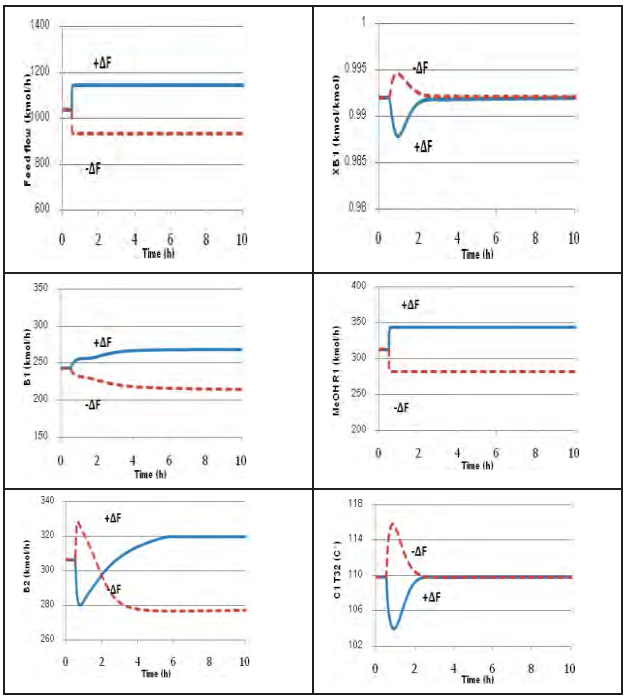

Figure 3. Dynamic responses of 10% fresh feed flow rate disturbances.

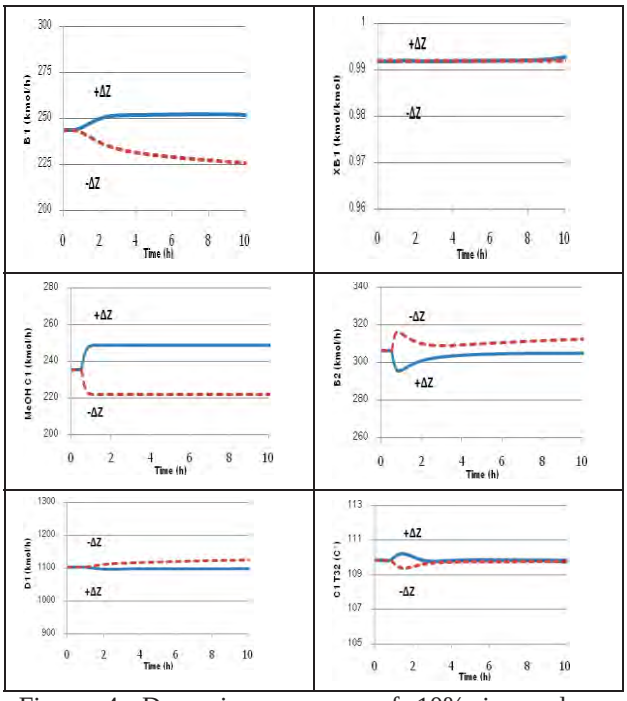

Figure 4. Dynamic responses of 10% isoamylenes compositions in the feed disturbances.

4. Conclusions

The new design procedure of Wongsri provides a simple methodology to design plantwide control structure. The design procedure is applied to tert-amyl methyl ether (TAME) production process. This control structure provides effective control of the process. That can be handled disturbances, which came across the process effectively. In practice, this designed control structure can be used in a real plant.

References

[1] W.L. Luyben and M.L. Luyben. *Essentials of Process Control*. McGraw-Hill, New York, 1997.

[2] M.A. Al-Arfaj, W.L. Luyben, *AIChE J.* **2004**, *50* (7), 1462.

[3] W.L. Luyben, *Ind.Eng.Chem.Res.* **2005**, 44, 5715-5725.

INVESTIGATION ON DEGRADATION AND STABILIZATION OF EPOXIDIZED PALM OIL

Thitimaporn Duangmanee[1*], Seng Yee Tan[2], Athip Achalanant[3], Boonyawan Yoosuk[1], Nuwong Chollacoop[1] and Suzana Yusuf[2]

[1]National Metal and Materials Technology Center (MTEC), Klong Luang, Pathumthani 12120, Thailand
[2] Universiti Teknologi PETRONAS,Bandar Seri Iskandar, 31750,Tronoh, Perak, Malaysia
[3]Department of Chemistry, Faculty of Science, Thammasat University, Klong Luang, Pathumthani, 12120 Thailand

*Author for correspondence: E-mail: thitimad@mtec.or.th. Tel. +66 25646500, Fax. +66 25646401

Abstract: Epoxidation of palm oil (PO) converts double bond in triglyceride structure of palm oil to epoxy functional group. Palm oil used in the present study has iodine value of 57 g/100g oil. Epoxidation of PO was achieved with peroxyacetic acid, which was generated in situ from 30% hydrogen peroxide and glacial acetic acid. The epoxidized palm oil (EPO) obtained from the epoxidation of PO was found to contain 2.04 percentage of oxirane oxygen (%OO). However, the opening of oxirane ring causes decreasing of %OO. Therefore degradation of EPO and the effects of opening oxirane ring were studied. Stabilization of EPO using an antioxidant was selected in this study. Three different types of antioxidants, which are butylated hydroxyanisole (BHA), tert-Butylhydroquinone (TBHQ) and propyl gallate (PG) were added at 2 %wt with respect to EPO and compared with EPO with no antioxidants. The properties of EPO, namely %OO, amount of glycol, acidity, water content and oxidative stability, were monitored continuously for twelve weeks.

Keywords: Epoxidation, Epoxidized Palm Oil, Bio-based Oil, Palm Oil.

1. Introduction

The depletion of petroleum-based material has become a concern for the future since it is non-renewable and will deplete if no other alternatives are used to substitute petroleum-based materials. Substitution of petroleum based-material by vegetable oil-based materials has caught attention widely as vegetable oils are renewable resources that are environmentally friendly, biodegradable, low cost and readily available. This application will help preserve the world environment by reducing the global warming affect with the utilization of environmental friendly and biodegradable materials. Application of vegetable oil-based materials in petroleum based-materials can be achieved via epoxidation process, which is a simple process that has been applied for karanja, mahua oil, soybean oil, jatropha oil, rapeseed oil, cottonseed oil, and canola oil nowadays. Epoxides with higher oxirane values and lower iodine values are considered to be of better quality [1, 2]. Such epoxides obtained can act as raw materials for a variety of chemicals such as alcohols, glycols, alkanolamines, carbonyl compounds, olefinic compounds and polymers such as polyesters, polyurethanes, and epoxy resins, which then help impart the stability of polymer aganist heat and UV radiation [3] and often used for both formation of thermosetting composites and coatings obtained by ultraviolet (UV) – initiated cross-linking [4].

Epoxidation is carried out using a peracid, formed in situ by reacting carboxylic acid, such as glacial acetic acid, with concentrated hydrogen peroxide with inorganic acid, such as sulfuric acid, as a catalyst. The epoxidation steps were suggested by Gan et al. [5] as shown in Figure 1. As the side reaction could lead to oxirane ring opening, as shown in Figure 2, it should be minimized to prevent the degradation of epoxidized oil caused from side reactions. There are many factors, such as water, hydrogen peroxide and acid, which lead to the opening of oxirane ring and formation of glycol [6]. The oxirane ring opening causes a decrease in yield; thus, synthesis of epoxidized palm oil and stabilization of the product were investigated in this study.

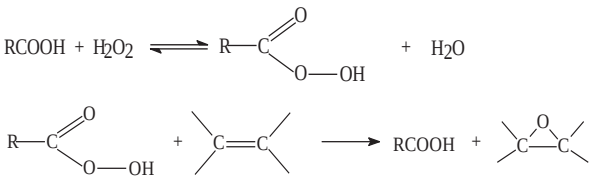

Figure 1. The main reactions of epoxidation process with peracids.

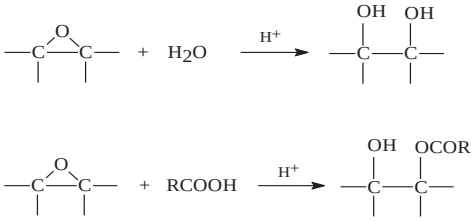

Figure 2 The side-reactions of epoxidation process.

Application of antioxidants, such as BHA, TBHQ and PG, has commonly been applied especially in food or cosmetic manufacturing industries.. Antioxidants act as chemical compounds, which are capable of delaying the initiation or slowing down the rate of lipid oxidation reaction in systems. Lipid oxidation occurs when the free alkyl radicals (R●) are formed in the initiation step or the free radical chains (RO●, ROO●) are propagated. Application of metal chelating agents, peroxide stabilizers and singlet oxygen inhibitors can inhibit the initiation of free radical

formation. Hydrogen atom from antioxidant (AH) will be donated to free radicals and thus produces antioxidant radical (A●). The produced antioxidants radicals do not lead to lipid oxidation due to its stability from delocalization, and can react with the free radicals to form stable complex compound, as shown in Figure 3. Propagation of free radical chain reactions is then minimized, which leads to reduction in lipid oxidation.

Three different types of antioxidants, which are Butylated hydroxyanisole (BHA), Tert-Butylhydroquinone (TBHQ) and Propyl gallate (PG), were added into EPO and compared with EPO without antioxidants.

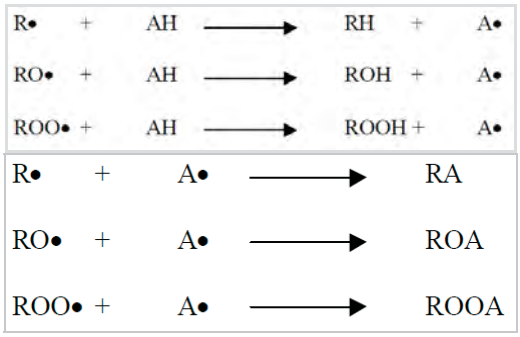

Figure 3 Mechanisms of Antioxidant

2. Experimental

2.1 Materials

Palm oil used to synthesize EPO in the present study was obtained from Siam Oil & Fat., Ltd. (Samut Sakhon, Thailand). The chemicals used in the study are glacial acetic acid (AA), 30 %wt aqueous hydrogen peroxide, 32 %wt hydrogen bromide in acetic acid, 0.1N sodium thiosulfate solution and sulfuric acid, which were obtained from Merck. Periodic acid (99+%) and benzyltrimethylammonium hydroxide 40 %wt solution in methanol were obtained from ACROS. Wijs solution was obtained from Sigma-Aldrich Co. Sodium sulphate anhydrous crystal and chloroform were obtained from Carlo Erba Reagenti SpA. HBr in acetic acid was diluted with acetic acid to prepare 0.1N HBr, and crystal violet solution was used in the titration method for determining the %OO.

2.2 Antioxidants

Three types of antioxidants were used in this study namely butylatedhydroxyanisole (BHA), tert-butylhydroquinone (TBHQ), and propyl gallate gallussäure-propylester (PG). They were blended into the EPO at 2 weight%. BHA (>98.5%), TBHQ (97%), PG (98%) were obtained from Sigma-Aldrich Co.

2.3 Preparation of EPO stock

Twelve batches of epoxidation reactions were carried out in a four round-bottom flask (500 mL capacity), equipped with a magnetic stirrer, a reflux condenser, and a thermometer. The flask was then placed in a water bath, where the temperature was controlled with a thermostat and monitored within ± 1°C of the desired temperatures. The 200 g of palm oil from each batch was poured into the round-bottom flask and heated up to the desired temperature. Calculated amount of glacial acetic acid and sulfuric acid catalyst was added into the flask, and the mixture was stirred for about half an hour. The 30% aqueous H_2O_2 solution was slightly added, and the reaction was completed in half an hour. The reaction was continued further for another half hour with controlled temperature and constant reaction stirrer speed of 1400 rpm. The mixture obtained was cooled down for reaction completion and separated for mixture phases. The sample was neutralized by water until pH of approximately 7 was reached. Remaining water was separated using oil test centrifuge and removed with sodium sulphate anhydrous crystal. All twelve batches of EPO were homogeneously.mixed together.

2.4 Analytical techniques

The iodine value was determined according to Wijs solution [7]. The alpha-glycol was determined by the method reported by May and Stenmark [8, 9] based on the oxidation of glycol with benzyltrime-thylammonium periodate in non-aqueous solution. The excess of periodate and iodic acid formed were reduced with potassium iodide, and the liberated iodine was titrated with sodium thiosulphate. The percentage oxirane oxygen (%OO) was determined by the direct method using hydrogen bromic acid solution in acetic acid solution following the official method AOCS Cd 9-57[10]. Furthermore, the samples were analyzed with 809 Titrando, Metrohm for acidity (ASTM D 664), 831 KF, Metrohm for water content (ISO 12937) and 743 Rancimat Metrohm for oxidative stability (EN 14112).

3. Results and Discussion

The homogeneous EPO was separated into four different groups with twelve bottles of each group for twelve weeks testing. The three antioxidants (BHA, TBHQ and PG) were added into three of those groups and one group was not added with any antioxidant for comparison.

3.1 Amount of glycol

Degradation of synthesized EPO leads to the production of glycol that has to be minimized in order to increase the yield of desired product. From the testing, the amount of glycol was observed, as shown in Figure 4, with some fluctuation. The trends of the glycol amount can be explained by the reaction of glycol with water, as shown in Figure 5. Glycol has a strong affinity towards water molecules due to the formation of weak electrostatic absorbing power known as H-bond by the electronegativity of the atoms [11]. Moreover, reaction of glycol with acetic acid forms ethylene glycol monoacetate and water, as shown in Figure 6 [12]. However, the reactions are

reversible and thus ethylene glycol can be formed again to reach equilibrium. This could explain the increasing and decreasing trend of glycol. Hence, the amount of glycol, acidity (shown in Figure 8) and water content (shown in Figure 9) are not consistent with some indication of interdependence among one another.

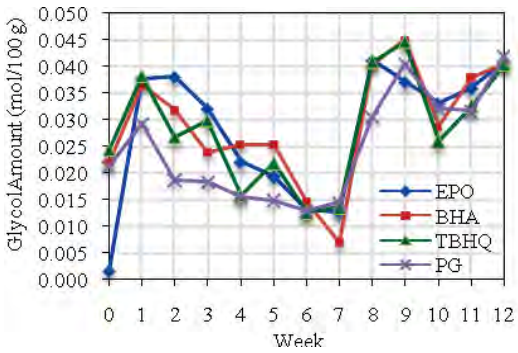

Figure 4 Glycol amounts of EPO both with and without antioxidant over the period of 12 weeks.

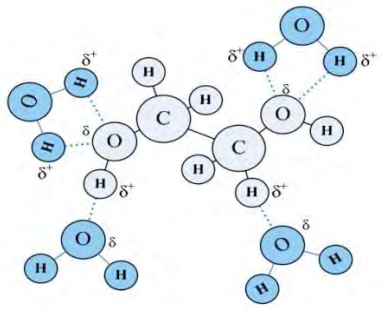

Figure 5 Hydrophilic properties of glycol [10].

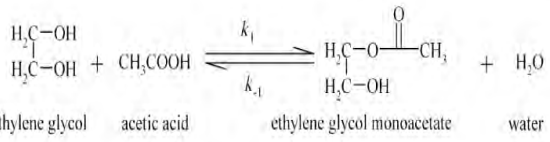

Figure 6 Reaction of glycol with acetic acid.

3.2 Percentage of Oxirane Oxygen (%OO)

The percentage oxirane oxygen is important property of interest in this study. The %OO of EPO, both with and without antioxidants, are shown in Figure 7. The %OO of all EPO has decreased over the 12-week period. EPO without antioxidant has the highest percentage oxirane oxygen, followed by EPO with BHA, EPO with PG and EPO with TBHQ, respectively. The study shows that the %OO of EPO without antioxidant decreases slower as compared to the EPO with antioxidants. Addition of antioxidants caused to a more rapid opening of oxirane ring and faster degradation of EPO due to the reaction between epoxides and antioxidants. Donation of hydrogen atom from antioxidants has led to a higher rate of acid hydrolysis on oxirane ring.

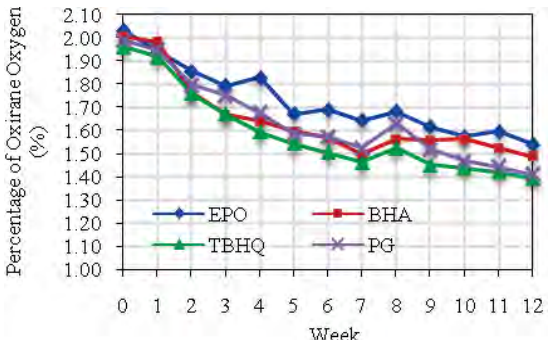

Figure 7 %Oxirane oxygen testing of EPO both with and without an antioxidant over the period of 12 weeks.

3.2 Acidity

The acidity of EPO with and without antioxidants including palm oil was measured for twelve weeks, as shown in Figure 8. The acidity of EPO with PG shows the highest value due to the chemical structure of PG (Figure 9), which can release proton and gives acid property to the solution; whereas, the acidity of EPO with TBHQ is the lowest value.

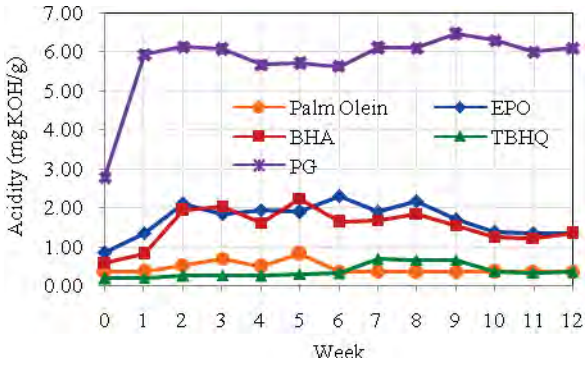

Figure 8 Acidity testing of EPO both with and without an antioxidant over the period of 12 weeks.

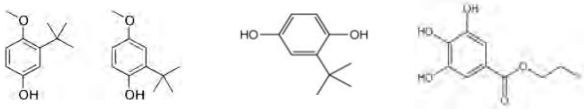

BHA TBHQ PG

Figure 9 The chemical structure of three antioxidant used in the present study.

3.3 Water content

From the testing, the water content of EPO both with and without antioxidants is higher than that of palm oil, as shown in Figure 10. The water in all of EPO samples can be produced from the reaction of glycol with remained acid in the EPO. The trend of water content has decreased from week0 to week12 continuously. The decrease of water content could come from the side reaction in epoxidation process, where epoxides group can react with the water.

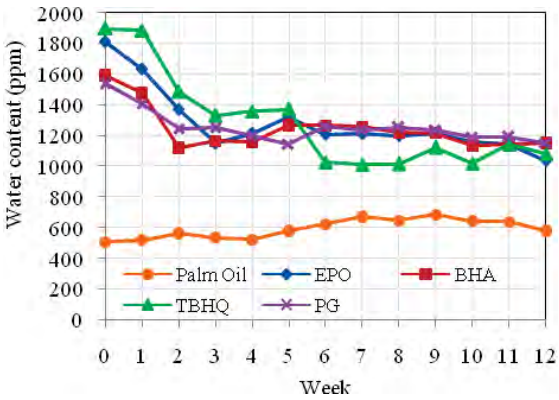

Figure 10 Water content of EPO both with and without an antioxidant over the period of 12 weeks.

3.4 Oxidative stability

The addition of antioxidants into EPO is to increase the oxidative stability. The antioxidants slow down the degradation of EPO in term of oxidative stabilization and maintain higher oxidative stability as compared to that of EPO without an antioxidant. From Figure 11, the oxidative stability of EPO added with BHA is the highest.

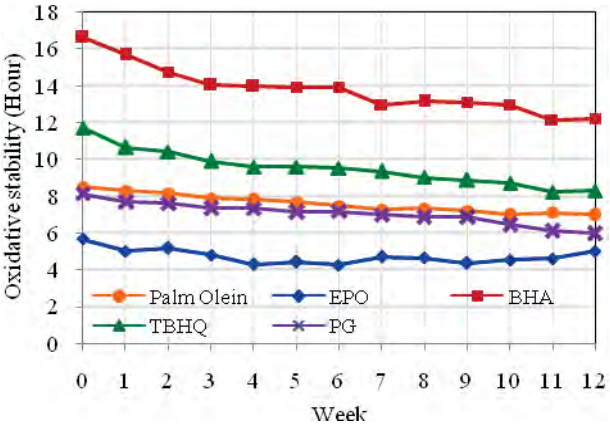

Figure 11 Oxidative stability of EPO both with and without an antioxidant over the period of 12 weeks.

4. Conclusions

The degradation and stabilization of epoxidized palm oil (EPO) had been studied. The addition of three types of antioxidants into the synthesized EPO affected the amount of glycol, acidity and water content. The antioxidant led to a decrease in percentage of oxirane oxygen due to donation of hydrogen atom from antioxidants to epoxide ring. However, the antioxidants improved the oxidative stability as compared to that of EPO without an antioxidant whereas the percentage of oxirane oxygen which is a main property indicated yield. Therefore, the use of an antioxidant for EPO stabilizing should concern about effect to all properties of EPO. This study is important data based for EPO synthesis and storage. The remaining some acid or water maybe decreases yield of EPO.

Acknowledgements

Greatest acknowledgement is given to National Metal and Material Technology Center (MTEC), Thailand for financial support.

References

[1] K.D. Carlson and S.P. Chan, *J. Amer. Oil Chem. Soc.* **62** (1985), 934-939

[2] X. Hang and H. Yang, *J. Amer. Oil Chem. Soc.* **76** (1999) 89-92.

[3] V.V.Goud et al., *J Am Oil Chem Soc.* **85** (2008) 887-896.

[4] E. Milchert and A. Smagowicz, *J. Am. Oil Chem. Soc.* **86** (2009) 1227-1233.

[5] L.H. Gan, S.H. Goh, and K.S. Ooi, *J. Am. Oil Chem. Soc.* **69** (1992) 347-351.

[6] A. Campanella, M.A. Baltanas, *Latin Am. Appl. Res.* **35** (2005) 205-210.

[7] C. Paquot, 1979. Standard method for the analysis of oils, fats and derivatives part I, 6th edn. Pergamon, Oxford. (1979) 66-70.

[8] C.A. May, Epoxy resins: chemistry and technology. Marcel Dekker, New York. (1973) 672-673.

[9] G.A. Stenmark, Determination of alpha glycol content of epoxy resins. Shell Development Co., Emeryville, California. 30 (1958) 381-383.

[10] AOCS Cd 9-57, Oxirane Oxygen, American Oil Chemists' Society, Champaing, IL. (1997) 1-2.

[11] M.J. Kao, D.C. Tien, C.S. Jwo, and T.T Tsung. The Study of Hydrophilic Charateristics of Ethylene Glycol, Institute of Physics Publishing. Journal of Physics: Conference Series 13 (2005) 442-225.

[12] V.P. Yadav, S.K. Maity, P. Biswas, and R.K. Singh, Chem Biochem. Eng. **25** (2011) 359-366.

DYNAMIC PERFORMANCE OF A PROTON EXCHANGE MEMBRANE FUEL CELL

Thanaphorn Hakhen[1], Suthida Authayanun[2], Amornchai Arpornwichanop[1,*]

[1]*Department of Chemical Engineering, Faculty of Engineering, Chulalongkorn University, Bangkok 10330, Thailand*
[2] *Department of Chemical Engineering, Faculty of Engineering, Srinakharinwirot University, Nakhon Nayok 26120, Thailand*

[*] Author for correspondence*: Amornchai.a@chula.ac.th*

Abstract: Due to its high current density and low-temperature operation, a proton exchange membrane fuel cell (PEMFC) is considered a promising candidate for transportation and stationary power generation. Understanding a dynamic behavior is essential to design a control scheme of PEMFC systems. This study focuses on the performance analysis of PEMFC under transient conditions. A dynamic model of PEMFC taking into account mass and energy conservations and electrochemical relations is used to predict its dynamic behaviors. Effect of load change on PEMFC performance in terms of cell voltage, stack temperature and partial pressures of H_2 and O_2 is presented and discussed. The simulation results show at high current load, more hydrogen and oxygen are consumed, resulting in a decrease in their partial pressure, whereas the stack temperature rapidly increases. It is found that the temperature of PEMFC is higher than 80 ^oC, which is a limited value for safe operation of PEMFC. Therefore, a control system is required to maintain the operating temperature at a desired condition when the electrical load is changed.

1. Introduction

A fuel cell is an attractive device for electricity generation. It can directly convert chemical energy in fuels into electrical energy and heat. In general, fuel cells can attain efficiency of 40-60% [1] and generate low levels of pollution. In case of hydrogen fuel cells, the primary products are electricity, heat and water. Among the various types of fuel cells, the proton exchange membrane fuel cell (PEMFC) has been received attention, especially for transportation applications and portable device, due to its high efficiency, low temperature operation, high power density, fast start-up and low pollution. In most stationary applications, PEMFC is used in conjunction with other power generation systems.

PEMFC is constructed by layering two electrodes on an electrolyte membrane. This combined entity is known as the membrane-electrode assembly (MEA). Figure 1 shows a simplified description of the PEMFC. The reactions occurred in PEMFC are given below:

$$Anode: 2H_2 \leftrightarrow 4H^+ + 4e^-$$

$$Cathode: O_2 + 4H^+ + 4e^- \leftrightarrow 2H_2O$$

$$Overall: 2H_2 + O_2 \leftrightarrow 2H_2O$$

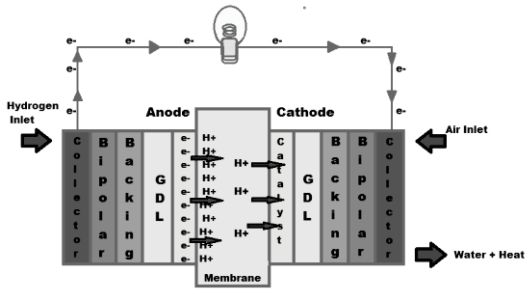

Figure 1: Schematic of a single typical PEMFC.

The reaction rates can be enhanced by adding a catalyst layer at the anode, cathode interfaces. At the anode side, hydrogen diffuses through a diffusion layer, and is converted at the active area of the anode to protons. Electrons released during this transformation are directed through an external electric circuit, where they are used to generate power, while protons are transferred to the cathode side. Protons recombine with electrons and oxygen to become water at the cathode.

In order to understand and improve the performance of PEMFC systems, several different mathematical models have been proposed. However, many previous studies were focused on design of PEMFC at steady state condition [2-4]. Understanding a dynamic behavior is essential to design a control scheme of PEMFC systems. Thus, the aim of this study is to perform a model-based analysis of PEMFC under dynamic condition. A dynamic model of PEMFC taking into account mass and energy conservations and electrochemical relations is used to predict its electrical characterize when power load is changed.

2. Mathematical model of a PEMFC

2.1 Electrochemical model

Electrical characteristics of PEMFC are described by a polarization curves. The thermodynamic potential of hydrogen/oxygen reaction is reduced by various overvoltage terms such as kinetic, ohmic and mass transport phenomena. In addition, a fuel cell is influenced by current, temperature and pressure. The output cell voltage can be defined as follows [5]:

$$V_{cell} = E_{Nernst} + \eta_{act} + \eta_{ohmic} \quad (1)$$

where E_{Nernst} is the reversible cell voltage and η_{act} and η_{ohmic} are the activation and ohmic voltage losses. It is noted that in other studies, a concentration loss has been used to explain the effects of mass transport. However, it has been shown that appropriate parameteric modelling with Eq. (1) can allow sufficient scope for exhibiting such phenomenon .

Equation (2) is used to compute the reversible cell voltage.

$$E_{Nernst} = 1.229 - 0.85e^{-3} \times (T - 298.15) + \frac{RT}{2F} \ln[P_{H_2} (P_{O_2})^{0.5}] \quad (2)$$

The activation overvoltage can be written as [5]:

$$\eta_{act} = -0.948 + \xi T + 7.6e^{-5} T \ln(C_{O_2}) - 1.93e^{-4} T \ln(i) \quad (3)$$

$$\xi = 2.86e^{-3} + 2e^{-4} \ln(A) + 4.3e^{-5} \ln(C_{H_2})$$

where i is the cell current (A), C_{H_2} is the hydrogen concentration at anode/membrane interface (mol/cm^3), C_{O_2} is the oxygen concentration at cathode/membrane interface (mol/cm^3) and A is the active area (cm^2).

The ohmic voltage loss is given as [6]:

$$\eta_{ohm} = -iR_{int} \quad (4)$$

$$R_{int} = \frac{r_M l_{mem}}{A}$$

$$r_M = \frac{181.6[1 + 0.03(i/A) + 0.062(T/303)^2 (i/A)^{2.5}]}{[\lambda - 0.634 - 3(i/A)] \exp[4.18(\frac{T - 303}{T})]} \quad (5)$$

where R_{int} is the internal resistance that protons pass the membrane (Ω), r_M is the specific resistivity for the flow of hydrated protons (Ωcm), l_{mem} is the membrane thickness (cm), and λ is the ratio of water for each sulfonic group in the membrane.

2.2 Reactant flow model

Fuel and oxidant gases go through the fuel and air channels at the anode and cathode side of PEMFC, respectively. The partial pressures of hydrogen and oxygen are changed as:

$$\frac{V_a}{RT} \frac{dP_{H_2}}{dt} = \dot{m}_{H_2,in} - k_a \left(P_{H_2} - P_{tannk} \right) - \frac{Ni}{2F} \quad (6)$$

$$\frac{V_c}{RT} \frac{dP_{O_2}}{dt} = \dot{m}_{O_2,in} - k_c \left(P_{O_2} - P_{BPR} \right) - \frac{Ni}{4F} \quad (7)$$

where V_a and V_c are the volume of fuel and air channels (cm^3), respectively, $\dot{m}_{H_2,in}$ and $\dot{m}_{O_2,in}$ are the inlet flow rate of hydrogen and oxygen (mol/cm^3), respectively.

2.3 Thermal model

A thermal model based on energy balance around PEMFC describes the dynamic of the fuel cell temperature as:

$$C_t \frac{dT}{dt} = P_{tot} - P_{elec} - \dot{Q}_{cool} - \dot{Q}_{loss} \quad (8)$$

The total power (P_{tot}) input to the stack is directly related to the amount of hydrogen consumption. The total power expression can be defined as:

$$P_{tot} = \frac{Ni}{2F} \Delta H \quad (9)$$

where ΔH is the enthalpy of combustion for hydrogen (385 kJ/mol), and $\dot{m}_{H_2,used}$ is the rate of hydrogen consumption (mol/s). The electrical power output (P_{elec}) is given by the volt-ampere relationship, as shown below:

$$P_{elec} = VI \quad (10)$$

A cooling system is used for removal of the excess heat and control of the fuel cell temperature at a desired value. The rate of removal of heat ($\dot{Q}_{cool}$) is expressed as:

$$\dot{Q}_{cool} = (h_{cond} + h_{conv} i) \frac{(T - T_{in}) - (T - T_{out})}{\ln[(T - T_{in})/(T - T_{out})]} \quad (11)$$

The heat loss ($\dot{Q}_{loss}$) to the environment that is proportional to both the fuel cell temperature and the ambient temperature is determined by:

$$\dot{Q}_{loss} = \frac{T - T_{amb}}{R_t} \quad (12)$$

where h_{cond} and h_{conv} are the parameters that characterize the conduction and convection properties, R_t is the thermal resistance of the stack ($^\circ C/W$) and T_{amb} is the ambient temperature ($^\circ C$).

3. Results and Discussion

The model of PEMFC including the fuel cell stack dynamic and anode and cathode channel dynamics is solved using Matlab. Simulation is performed to analyze effect of load change on the transient response of PEMFC in terms of cell voltage, stack temperature and anode and cathode channel pressures.

Figure 2 explains the change in current caused by the variation in power load. This operational policy is applied to PEMFC to investigate its dynamic behavior. It can be seen that at t = 3000 s, the current is increased from 10 to 50 A and kept constant until t = 7000 at which it goes down to 20 A. The voltage response of the PEMFC is shown in Figure 3. When the current load increases, the fuel cell voltage losses increase accordingly. This results in a drop of PEMFC voltage.

Figures 4 and 5 show responses of the partial pressures of hydrogen and oxygen at the anode and cathode sides of the PEMFC stack, respectively. At high current load operation (50 A), more hydrogen and oxygen are consumed so that their partial pressures

decreased. In addition, a quick response is observed for both the pressures of hydrogen and oxygen. On the contrary, when the current load decreases (20 A), the pressures of hydrogen and oxygen increase. In general, an increase in the current load is associated with a

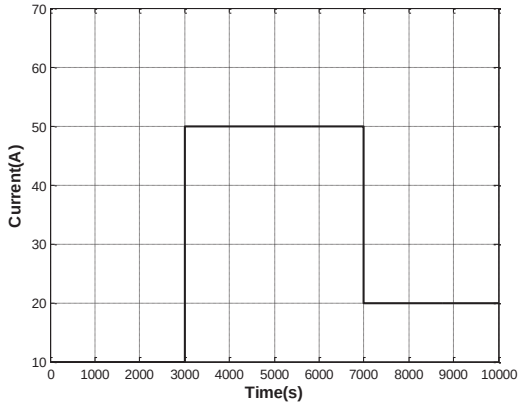

Figure 2: Variation in current due to load changes.

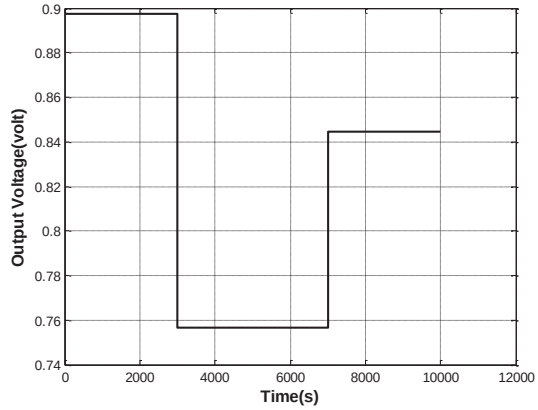

Figure 3: Response of output voltage.

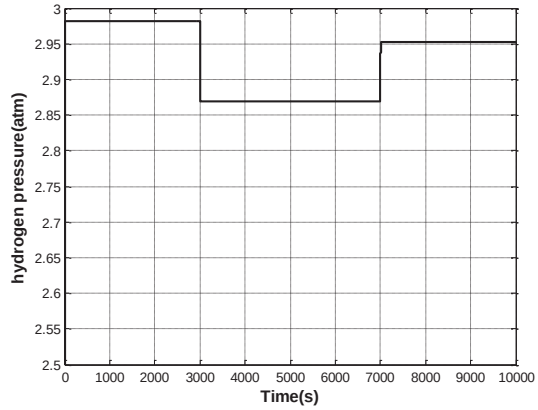

Figure 4: Profile of hydrogen partial pressure at the anode side.

higher fuel consumption, which will decrease the reactant pressures.

The PEMFC stack temperature is shown in Figure 6. At t = 3,000 s, the stack temperature slowly increases. This is due to an increase in the electrochemical reaction rate. In addition, heat generated by the electrochemical reaction is higher than heat loss due to the convection term. When the current load decreases at t = 7,000 s, the stack temperature decrease according to a decrease in the electrochemical reaction. In some cases, the PEMFC

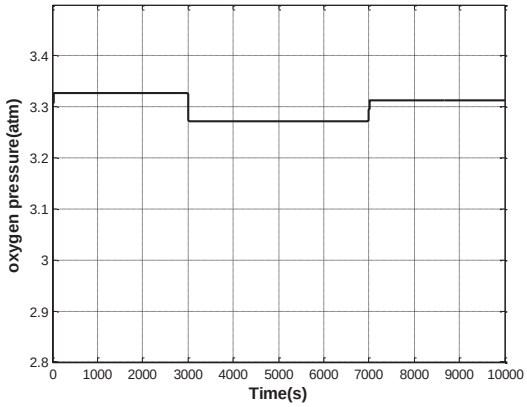

Figure 5: Profile of oxygen partial pressure at the cathode side.

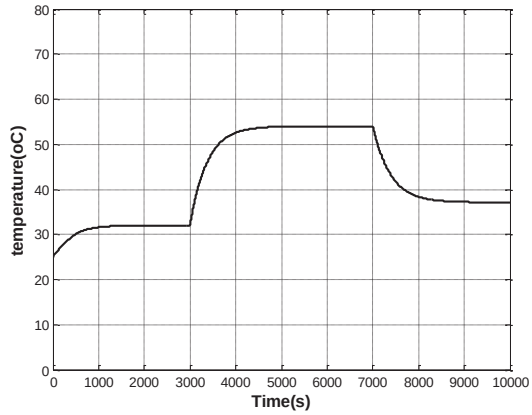

Figure 6: Profile of PEMFC temperatures.

temperature is higher than its desired operating conditions. Thus, a control system is required and this issue will be our future work.

4. Conclusions

A model-based analysis of PEMFC is performed in this study. The dynamic model of PEMFC is used to simulate its transient phenomena. The results show that a change in current load has an effect on a variation in the fuel cell voltage, pressure and temperature. This information is beneficial to a development of a control system for maintaining the PEMFC at desired conditions.

Acknowledgements

Support from the Thailand Research Fund and the Computational Process Engineering Research Group, Special Task Force for Activating Research (STAR), Chulalongkorn University Centenary Academic Development Project is also gratefully acknowledged**.**

References

[1] http://www.en.wikipedia.org/wiki/**Fuel_cell** (Retrieved December 2, 2012).
[2] J.J Baschuk, and L. Xianguo, *Power Sources* **86 (2000) 181-196**.
[3] M Ceraolo, C Miulli, and A. Pozio, *Power Sources* **108** (2002) 192-203.
[4] N.P. Siegel, M.W. Eillis, D.J. Nelson, and M.R. von Spakovsky, *Power Sources* **128** (2004) 173-184
[5] M. J. Khan, and M. T. Iqbal, *Fuel Cells* **05** (2005) 463-475
[6] S.M. Sharifi Asl, S. Rowshanzamir, and M.H.Eikani, *Energy* **35** (2010) 1633–1646.

INNOVATIVE ANTI-ACNE PRODUCT FROM NANOPARTICLES OF MANGOSTEEN

Atthakorn Wongsomboon[1]*, Porntip Pan-in[2], Chanpen Chanchao[3], Nuntaree Chaichanawongsaroj[4], Supason Wanichwecharungruang[5]

[1] Technopreneurship and Innovation Management Program, Graduate school, Chulalongkorn University, Bangkok 10330, Thailand
[2] Program in Biotechnology, Faculty of Science, Chulalongkorn University, Bangkok 10330, Thailand
[3] Department of Biology, Faculty of Science, Chulalongkorn University, Bangkok 10330, Thailand
[4] Innovation Center for Research and Development of Medical Diagnostic Technology Project, Department of Transfusion Medicine, Faculty of Allied Health Sciences, Chulalongkorn University, Bangkok 10330, Thailand
[5] Department of Chemistry, Faculty of Science, Chulalongkorn University, Bangkok 10330, Thailand

* Author for correspondence; E-Mail: bambie_flamer@hotmail.com, Tel. +66 85 8331726, Fax. +66 2 2541309

Abstract: Mangosteen extract has been used as an ingredient in various anti-acne products. The extract can inhibit the growth of *Propionibacterium acnes*, the bacteria that cause acne. However, mangosteen extract is poorly soluble in water. Here mangosteen extract was encapsulated into nanoparticles of methylcellulose (MC) and ethylcellulose (EC) blend and the obtained nanoparticles showed excellent inhibition on the growth of *P. acnes* with the MIC value of 15.625 µg/ml. The mangosteen extract-loaded nanoparticles were then incorporated into anti-acne lotion at the concentration of 0.5% w/v. Evaluation of the lotion revealed that the particles dispersed well in lotion and gave acceptable pale yellow color at pH value of 6. Stability test at 45 °C indicated that there was no physical change for 28 days.

1. Introduction

Acne is one of the skin diseases that can often be found on both male and female faces. This will affect the quality of life on emotional, psychological and social sides by causing loss of self-confidence, stress, anxiety and avoidance of social encounters. There are numerous causes of acne [1, 2]. One of the major causes of acne is *Propionibacterium acne*, a normal flora found in sebaceous glands on skin. This type of bacteria does not require oxygen for growth. It digests fat into fatty acids which causes irritation, inflammation and purulent.

In recent years, a variety of products have been developed for the reduction of bacteria that cause acne. However, most developed products use synthetic antibiotics, which may cause irritation to sensitive skin [3, 4]. In addition, long term usage has increased the risk of bacterial resistance [5].

These factors create the need to find alternative therapies. One alternative therapy is the use of herbal medicine. Mangosteen extract has been reported to possess various biological activities including antioxidant [6], antitumoral [7], antiallergic [8], anti-inflammatory [9], antibacterial [10], antifungal [11] and anti-acne [12, 13]. The compounds responsible for the anti-acne activity are xanthones [14]. However mangosteen extract, especially the xanthone rich extract is poorly soluble in water.

Here we showed that by encapsulating the mangosteen extract into polymeric nanocarriers, the water insolubility problem could be solved. In addition, the obtained mangosteen extract-loaded nanoparticles could be entrapped into the hair follicle shunt as demonstrated using the pig ear skin. *In vitro*, examination for anti-*Propionibacterium acnes* activity of mangosteen extract-loaded nanoparticles was also confirmed and the use of nanoparticles in anti-acne lotion was demonstrated.

2. Materials and Methods

2.1 Materials

Mangosteen extract (α-Mangostin 56%) was obtained from Tipco Foods PLC. (Prachuabhirikhan, Thailand). EC (MW 170000, ethoxy content 48%) and MC (Mn 40,000 with a degree of methoxy substitution of 1.60–1.90) were purchased from Sigma-Aldrich (St. Louis, MO, USA). Ethanol (absolute) was purchased from ACI Labscan Limited (Bangkok, Thaiand). Lotion used in formulation stability experiment was purchased from Johnson & Johnson (Thailand) Limited (Lat Krabang, Thailand).

2.2 Nanoencapsulation

The nanoparticles of mangosteen was prepared based on the method of N. Suwannateep [15], with a slight modification. The mangosteen extract-loaded dipolymeric carriers made from methylcellulose (MC) and ethylcellulose (EC) were fabricated at the ratio of mangosteen extract : MC : EC of 2 : 1 : 1 by weight. The procedure involved dissolving mangosteen extract (0.30 g) and EC (0.15 g) in ethanol (40 ml) and separately dissolving MC (0.15 g) in water (10 ml). The two solutions were mixed together and then transferred into the dialysis tube (76 mm flat width, 640 ml/ft volume capacity, Sigma-Aldrich, USA) and dialyzed against distilled water.

2.3 Determination of antibacterial activity of mangosteen extract-loaded nanoparticles

The test organisms used in this study was *Propionibacterium acnes* (ATCC 6919).

Antibacterial activity of mangosteen extract-loaded nanoparticles was compared with free mangosteen extract, metronidazole, DMSO 0.2% and unencapsulated polymeric nanoparticles. This experiment was performed by the broth microdilution technique [16]. *Propionibacterium acnes* were incubated in brain heart infusion agar at 37 °C for 48 h under anaerobic conditions. *P. acnes* were suspended in brain heart infusion broth and diluted to $1x10^8$ CFU/ml, by adjusting the turbidity to match the 0.5 McFarland standard. Mangosteen extract-loaded nanoparticles, free mangosteen extract and unencapsulated polymeric nanoparticles were dissolved and diluted with distilled water to give the concentrations of 500 µg/ml down to 0.24 µg/ml in well plates (serial 2-fold dilution). Free mangosteen extract and metronidazole were dissolved in DMSO and diluted with water to give the concentrations from 500 µg/ml down to 0.24 µg/ml in well plates (serial 2-fold dilution). The final concentration of DMSO was 0.2% v/v. Test solutions/suspensions were then mixed with *P. acnes* (1:1) to obtain the final concentrations of 250 µg/ml down to 0.12 µg/ml in well plates. The cultures were then incubated at 37 °C for 24 h under anaerobic conditions. The minimum inhibitory concentration (MIC) was defined as the lowest concentration of the compound to inhibit the growth of microorganisms and the minimum bactericidal concentration (MBC) was defined as the lowest concentration of the compound to kill the microorganisms.

2.4 Penetration of skin sample

The study was performed on pig ear skin. It is suggested as a good model due to its resemblance to human skin absorption in morphology, function and absorption rate [17, 18]. In addition, pig ear skin does not shrink due to its lining cartilage and thus the hair follicles remain the same for at least 6 h after execution. The mangosteen extract-loaded nanoparticles were applied to the pig ear skin to give the final coverage of 20 µg/cm^2, massaged for about 15 min and left for 2 h. The skin sample was analysed by confocal laser scanning microscopy.

2.5 Preparation of anti-acne lotion from nanoparticles of mangosteen

The lotion used in the experiment contained water, mineral oil, glycol stearate, glycerine, dimethicone, propylene glycol, polysorbate 20, hydroxypropyl methylcellulose, benzyl alcohol, carbomer, methylparaben, diethylhexyl sodium sulfosuccinate, propylparaben, sodium hydroxide and butylparaben. Mangosteen extract-loaded nanopaticles was dispersed into the lotion base at the concentrations of 0.1, 0.2, 0.3, 0.4, 0.5 and 0.6% w/v. Stability at the temperature of 45°C was evaluated by color, pH value, odor and stickiness.

3. Results and Discussion

3.1 Mangosteen extract-loaded nanoparticles

Mangosteen extract was successfully encapsulated into the dipolymeric nanoparticles made of MC and EC via solvent displacement method, with the spherical particles at a diameter of approximately 625.4 ± 19.6 nm. The obtained mangosteen extract-loaded nanoparticles dispersed well in water and could be entrapped into the hair follicle of the pig ear skin (Figure 1). This agreed well with the report by Patzelt *et al.* [19] which indicated that particles in the range of 400 to 700 nm penetrated deeply and efficiently into the hair follicles.

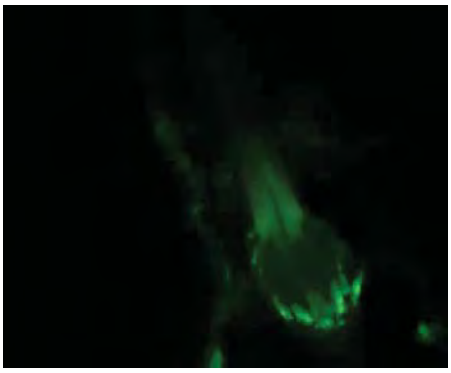

Figure 1. Entrapment of mangosteen extract-loaded nanoparticles (green) into the hair follicle of the pig ear skin (gray).

Table 1: The MIC and MBC values of all samples against *P. Acnes*.

Samples	MIC (µg/ml)	MBC (µg/ml)
GML-loaded nanoparticles	15.625	>250
Free GML in DMSO	15.625	15.625
Free GML in water	>250	>250
Metronidazole	>250	>250
Unencapsulated polymeric nanoparticles	>250	>250
DMSO 0.2%	-	-

GML = Mangosteen extract

3.2 Determination of antibacterial activity of mangosteen extract-loaded nanoparticles

Based on MIC value, the mangosteen extract-loaded nanoparticles (in water) showed good antimicrobial activity against *Propionibacterium acnes* (ATCC 6919) with the MIC value of 15.625 µg/ml (Table 1), which was equal to the value of the free mangosteen extract in DMSO. Interestingy, metronidazole, free mangosteen extract in water and unencapsulated polymeric nanoparticles gave MIC value of more than 250 µg/ml. However, only the extract in DMSO could kill this bacteria. The 0.2% DMSO in water (same concentration of DMSO used in the mangosteen extract in DMSO sample) gave no

detectable activity. This indicated that with nanoencapsulation the mangosteen extract could be used in water with good anti-acne activity.

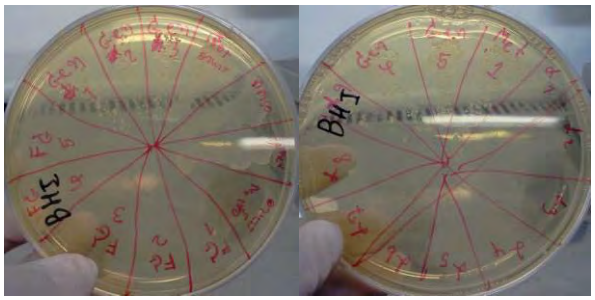

Figure 2. The MBC testing of GML-loaded nanoparticles, Free GML in DMSO, Metronidazole, Unencapsulated polymeric nanoparticles and 0.2% DMSO in water.

3.3 The development of anti-acne product containing nanoparticles of mangosteen.

The nanoparticles of mangosteen extract dispersed well in lotion base of pH 6. This was expected since water was a continuous phase and also a major component for this lotion and the particles dispersed well in water. There was no separation and precipitation of the product. The concentrations of 0.1, 0.2, 0.3, 0.4 and 0.5% w/v gave acceptable pale yellow color result while the concentration of 0.6% gave too strong yellow color appearance (Table 2).

Table 2: The physical value of anti-acne lotion from nanoparticle of mangosteen

Con. %w/v	Color	pH	Odor	Stickiness
0.1	Pale Yellow	6	No	Suitable
0.2	Pale Yellow	6	No	Suitable
0.3	Pale Yellow	6	No	Suitable
0.4	Pale Yellow	6	No	Suitable
0.5	Pale Yellow	6	No	Suitable
0.6	Yellow	6	No	Suitable

3.4 Stability test of anti-acne lotion from nanoparticles of mangosteen

After being kept at the temperature of 45°C for 28 days, no change in color, odor, stickiness was observed. This implied that anti-acne product from nanoparticles of mangosteen possessed good compatibility with lotion.

4. Conclusions

Nanoparticles of mangosteen i) showed good inhibition on the growth of *P. Acnes*, ii) could be entrapped into the hair follicle and iii) could help improving dispersion ability of mangosteen extract in water. The particles can be used in cosmetic lotion formulations easily. Here, the innovative anti-acne product from nanoparticles of mangosteen was successfully developed at concentration of 0.5% w/v as the best formula. The formulation possesses acceptable pale yellow color with good stability and suitably physical properties.

Acknowledgements

This research was funded by the Thailand Research Fund.

References

[1] D. S. Berson and A. R. Sharita, The treatment of acne: The role of combination therapies. *J Am Acad Dermatol* **32** (1995) 31-41.
[2] G. F. Webster, Topical tretinon in acne therapy. *J Am Acad Dermatol* **39** (1998) 38-44.
[3] J. I. Ross, A.M. Snelling, E. Carnegie, P. Coates, W.J. Cunliffe, V. Bettoli, et al., Antibiotic-resistant acne: lessons from Europe. *British Journal of Dermatology* **3** (2002) 467-478.
[4] J. J. Leyden, Topical treatment of acne vulgaris : Retinoids and cutaneous irritation. *J Am Acad Dermatol* **38** (1998) S1-S4.
[5] G. F. Webster, Topical tretinion in acne therapy. *J Am Acad Dermatol* **39** (1998) S38-S44
[6] L. Yu, M. Zhao, B. Yang, Q. Zhao and Y. Jiang, Pheonolics from hull of *Garcinia mangostana* fruit and their antioxidant activites. *Food Chem* **104** (2007) 176-181.
[7] Y.W. Chin, H.A. Jung, H. Chai, W.J. Keller and A.D. Kinghom, Xanthones with quinone reductase-inducing activity from the fruits of *Garcinia mangostana* (Mangosteen). *Phytochemistry* **69** (2008) 754-758.
[8] M. Sukma, M. Tohda, S. Suksamran, and B. Tantisira, γ -Mangostin increases serotonin$_{2A/2C}$, muscarinic, histamine and bradykinin receptor mRNA expression. *Journal of Ethnopharmacology* **135** (2011) 450-454.
[9] L. G. Chen, L. L. Yang and C. C. Wang, Anti-inflammatory activity of mangostins from *Garcinia mangostana*. *Food and Chemical Toxicology* **46** (2008) 688–693.
[10] J. Pedraza-Chaverri, N. Cardenas-Rodrigues, M. Orozco-lbarra, and J. M. Perez-Rojas, Medicinal propoties of mangosteen (Garcinia mangostana). *Food and Chemical Toxiccolony* **46** (2008) 3227-3239.
[11] G. Gopalakrishnan, B. Banumathi and G. Suresh, Evaluation of the antifungal activity of natural xanthones from the fruits of *Garcinia mangostana* and their synthetic derivatives. *J. Nat. Prod.* **60** (1997) 519-524.
[12] M. T. Chomnawang, S. Surassmo, V. S. Nukoolkarn and W. Gritsanapan, Antimicrobial effect of Thai medicinal plans against acne-inducting bacteria. *Ethnopharmacology* **101** (2005) 330-333.
[13] M. T. Chomnawang, S. Surassmo, V. S. Nukoolkarn and W. Gritsanapan, Effect of *Garcinia mangostana* on inflammation caused by *Propionibacterium acnes*. *Fitoterapia* **78** (2007) 401-408.
[14] W. Pothitirat, M.T. Chomnawang, R. Supabphol and W. Gritsanapan, Comparison of bioactive compounds content, free radical scavenging and anti-acne inducing activities of extracts from mangosteen fruit rind at two stages of maturity. *Fitoterapia* **80** (2009) 442-447.

[15] N. Suwannateep, W. Banlunara, S. P. Wanichwecharungruang, K. Chiablaem, K. Lirdprapamongkol and J. Svasti, Mucoadhesive curcumin nanospheres: Biological ajoctivity, adhesion to stomach mucosa and release of curcumin into the circulation. *Journal of Controlled Release* **151** (2011) 176-182.

[16] F. Sahin, I. Karaman, M. Gulluce, H. Ogutcu, M. Sengul, A. Adiguzel, S. Ozturk and R. Kotan, Evaluation of antimicrobial activities of *Satureja hortensis* L. *Journal of Ethnopharmacology* **87** (2003) 61-65.

[17] I.P. Dick and R.C. Scott, Pig ear skin as an in vitro model for human skin permeabillity. *J Pharm Pharmacol* **44** (1992) 640-645.

[18] M.J. Bartek, J.A. Labudde and H.I. Maibach, Skin permeability in vivo: Comparison in rat, rabbit, pig and man. *J In-esl Dermatol* **58** (1972) 114-123.

[19] A. Patzelt, H. Richter, F. Knorr, U. Schafer, C. Lehr, L. Dahne, W. Sterry and J. Lademann, Selective follicular targeting by modification of the particle sizes. *Journal of Controlled Release* **150** (2011) 45–48.

DEVELOPMENT OF Cu-Zn/Al_2O_3 CATALYST FOR HYDROGEN PRODUCTION FROM METHANOL-STEAM REFORMING

Chaichan Siriruang[1], Sumittra Charojrochkul[2] and Pisanu Toochinda[1*]

[1]Sirindhorn International Institute of Technology/School of Bio-Chemical Engineering and Technology, Thammasat University, P.O. Box 22, Pathumthani, 12121 Thailand
[2]National Metal and Materials Technology Center, 114 Thailand Science Park Paholyothin Rd., Klong 1, Klong Luang, Pathumthani, 12120 Thailand

[*] Author for correspondence; E-Mail: pisanu@siit.tu.ac.th Tel: +66 2 9869009 ext 2309

Abstract: Cu-Zn based catalysts are commonly used in hydrogen production from methanol-steam reforming. Most commercial co-precipitation Cu-Zn based catalysts suffer from high metal loading and sintering at high temperature. This study focuses on the Cu-Zn catalysts prepared by sol-gel method and incipient wetness impregnation over Al_2O_3 to overcome these problems. Sol-gel method provides a high dispersion of Cu-Zn metal over the Al_2O_3. The incipient wetness impregnation with urea provides homogeneity of metal salt solution, metal cluster size reduction, and better metal dispersion over Al_2O_3 support. The activities of these catalysts in methanol-steam reforming were determined by the hydrogen production in tubular reactor at the temperature range of 453-623 K in continuous mode. The hydrogen effluent gas was analyzed by gas chromatography (GC). Catalysts were characterized by XRD before and after reaction to identify the phases of metal on the catalyst. Metal cluster size and dispersion over the catalysts were identified by SEM-EDS. The results show that the impregnated catalyst could exhibit a higher activity than sol-gel catalyst at low temperature. Both catalysts exhibited the highest hydrogen production at 573 K. Catalysts from this study could provide an active catalyst for hydrogen production from methanol-steam reforming with lower metal loading than the commercial one. The detail comparison of catalytic activity, metal crystallinity and other physical properties of the catalysts prepared by sol-gel and impregnation methods will be discussed.

1. Introduction

Nowadays, the increasing of energy demands along with environmental changing are urgent problems of the world [1]. Researchers are trying to develop renewable energies that does not involve in the emission of greenhouse gases such as bio mass energy, solar energy, nuclear energy, and wind energy. Hydrogen fuel cells are considered as an interesting choice of renewable energy for the future. Hydrogen fuel cells provide electrical energy from electrochemical reaction of hydrogen with atmospheric oxygen. This reaction yields water, which is an environmental benign product. However, a major problem of a hydrogen fuel cell is the high amount of cost in hydrogen resources.

Hydrogen can be obtained by many methods such as hydrocarbon reforming process, pyrolysis, plasma reforming, biomass gasification, electrolysis and thermochemical water splitting [1-2]. Methanol-steam reforming reaction is an interesting process for the hydrogen production due to high hydrogen per carbon ratio and low operating temperature, which results in a lesser energy consumption than the reforming of other hydrocarbons [3]. The following equation shows the hydrogen production from methanol-steam reforming reaction.

Methanol-steam reforming reaction [4]:

$$CH_3OH + H_2O \rightarrow 3H_2 + CO_2 \qquad \Delta H_{Rxn} = 49.5 \text{ kJ mol}^{-1}$$

Active catalysts for methanol-steam reforming are Cu-Zn based catalysts. The commercial catalysts prepared by co-precipitation suffer from the requirement of high Cu and Zn metal contents up to 60-90 weight percent and the sintering of metal active site at high temperature [5]. These problems lead to high cost of the catalyst and the decreasing in catalytic activity. Incipient wetness impregnation and sol-gel techniques are introduced for the catalyst preparations in order to overcome these problems. Impregnation of metal over high surface area support provides an active catalyst with low metal loading [6]. The previous study shows that an additional of urea could enhance the homogeneity of metal salt solution. Hence, the impregnation with an additional of urea could provide the well dispersion of Cu-Zn metal over support. Sol gel method is widely used to synthesize nano particle catalysts and provide uniform metal thin film coating over support materials [7-8]. These methods could provide the benefit in preparation of active catalyst with low metal loading and well metal dispersion in low cost.

In this study, a low cost Cu-Zn based catalyst has been developed for methanol-steam reforming using incipient wetness impregnation with and without urea and sol-gel preparation. The activities of catalysts are evaluated and compared among each other and that of commercial catalysts as well.

2. Materials and Methods

2.1 Catalyst Preparations

Impregnated catalysts: Cu-Zn based catalysts over Al_2O_3 were prepared by incipient wetness impregnation methods. The catalysts were prepared by impregnating the aqueous solution of Cu $(NO_3)_2 \cdot 3H_2O$ (≥99%, Fluka) and Zn $(NO_3)_2 \cdot 6H_2O$ (≥99%, Fluka) with and without an addition of urea

(≥99%, Carlo) over Al_2O_3. The active metal loading is kept constant at 20 wt% and the molar ratio of Cu and Zn is fixed at 1:1. Impregnated samples were dried in air at 378 K for 6 h and then calcined at 573 K for 3 h.

Sol-gel catalysts: The sol-gel catalysts were prepared by mixing of Cu $(NO_3)_2 \cdot 3H_2O$ (≥99%, Fluka), Zn $(NO_3)_2 \cdot 6H_2O$ (≥99%, Fluka), citric acid ($C_6H_8O_7 \cdot H_2O$) (≥99%, Ajax Finechem) and DI water to form aqueous metal solution. The solution was heated to 343 K with constant stirring. After that, 25wt% ammonia in water was added to the solution to adjust the pH of 7. The alumina support was added into the solution. The mixture was stirred at a temperature of 343 K for 4 h to ensure the complete sol-gel formation [8]. The sol-gel catalyst was evaporated at 378 K for 4 h. Then the viscous gel was dried at 403 K for 6 h to remove ammonia and water. A dry gel was calcined at 573 K for 3 h. with a heating rate of 6 K/min.

2.2 Methanol-Steam Reforming in Tubular Reactor

The methanol steam reforming reaction for the hydrogen production was studied on the prepared catalysts in a stainless steel tubular reactor which has an inside diameter of 1 cm. Two grams of catalyst were packed between quartz wool in the reactor. The catalyst was reduced with 20 mL/min of 10% H_2: N_2 balanced at 453 K for 1 h. prior to the methanol reforming reaction test. The reactor was flushed with 20 mL/min N_2 flow at 453 K for 30 min to get rid of adsorbed hydrogen from the reduction process. The mixture of methanol and water solution was loaded into a saturator which was heated to 333 K. Compositions of methanol and water in the liquid phase are 0.125:0.875 molar ratios. The composition of solution was calculated by the Aspen Plus simulation program (Aspen Technology Inc., Burlington, Mass., USA) to ensure that the composition of the mixture in the vapor phase is a 1:1 molar ratio at the outlet from the saturator. The vapor of the mixture within the saturator was carried out at 20 mL/min N_2, and sent into the reactor at reaction temperature range 453-623 K in a continuous system. Therefore, the time spent in the packed bed reactor in continuous system was approximately 6 seconds. The product was collected and the production of hydrogen was determined via gas chromatograph (GC).

2.3 Analysis sections

A Perkin Elmer (Waltham, Mass., USA) Charus 500 gas chromatograph (GC) with Porapak Q column (Supleco, Bellefonte, PA, USA) coupled with a thermal conductivity detector (TCD) was used to determine the amount of hydrogen production.

Morphology of the catalysts was inspected by a scanning electron microscope (SEM, JEOL JSM-5410, Jeol Inc., Tokyo, Japan). The elemental composition of the catalyst surface was determined by energy dispersive spectrometry (EDS, Oxford, Oxford Instrument, Oxfordshire, United Kingdom) which the SEM was equipped with.

The catalysts were characterized by the X-ray diffraction technique (XRD, JEOL JDX-3530, Jeol Inc., Tokyo, Japan) using Cu Kα1 radiation, 30° - 41° 2-theta, 0.04° step size, 1 sec step time. JADE software (Jade Software Corporation Ltd., Christchurch, New Zealand) was used to determine the crystallize size of the CuO using the broadening of peak at 38.8° 2-theta. JADE software was also used to identify phases of the catalysts before and after calcination with the references of X-ray diffractogram database from the International Centre for Diffraction Data (Newtown Square, PA, USA).

3. Results and Discussion

3.1 Hydrogen production from Cu-Zn/Al_2O_3 catalyst prepared by impregnation with and without urea

The hydrogen productions from methanol-steam reforming over Cu-Zn/ Al_2O_3 with and without urea are listed on Table 1. Hydrogen yields were calculated using the following equation derived from stoichiometric coefficients of methanol and hydrogen from the balanced chemical reaction:

$$\%H_2\ yield = \frac{1}{3}\frac{mol\ of\ H_2}{mol\ of\ CH_3OH\ fed} \times 100$$

Table 1 shows that the impregnated Cu-Zn/Al_2O_3 with urea exhibits a higher hydrogen yield than impregnated Cu-Zn/Al_2O_3 without urea on both reaction temperatures. The impregnated Cu-Zn/Al_2O_3 with urea can increase hydrogen yield from 13.0% to 14.8% (13.8 % increment) at 453 K and 22.1% to 29.8% (34.8% increment) at 523 K.

Table 1: Hydrogen production from methanol-steam reforming over Cu-Zn/Al_2O_3 catalyst prepared by impregnation with and without urea

Temperature (K)	% Hydrogen Yield	
	Without urea	With urea
453	13.0±0.09	14.8±0.04
523	22.1±0.72	29.8±0.55

Figure 1 and 2 shows SEM images and EDS profiles of Cu-Zn/Al_2O_3 catalyst prepared by impregnation with and without urea. The SEM images show that the Cu and Zn are dispersed over Al_2O_3 support. The EDS profiles indicate that the small metal clusters are composed of Cu and Zn located on Al_2O_3 support.

The SEM image of the impregnated Cu-Zn/Al_2O_3 without urea (Fig 1.) shows the agglomeration of large Cu-Zn clusters (>5 μm) over Al_2O_3. Distributions of Cu-Zn clusters are inconsistent throughout Al_2O_3 support. The SEM image of impregnated Cu-Zn/Al_2O_3 with urea (Fig 2.) shows smaller Cu-Zn compounds clusters (≈ 0.2-1 μm) and better dispersion

of Cu-Zn clusters over Al_2O_3. These result exhibited that using urea in catalyst preparation method could provide a better metal dispersion over the support, which corresponded with hydrogen yield.

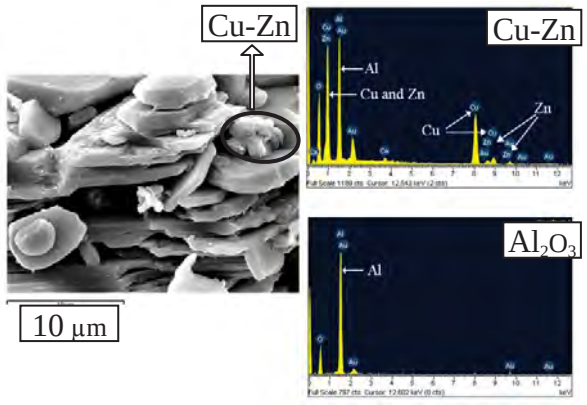

Figure 1. SEM image and EDS profiles of impregnated Cu-Zn/Al_2O_3 *without urea*

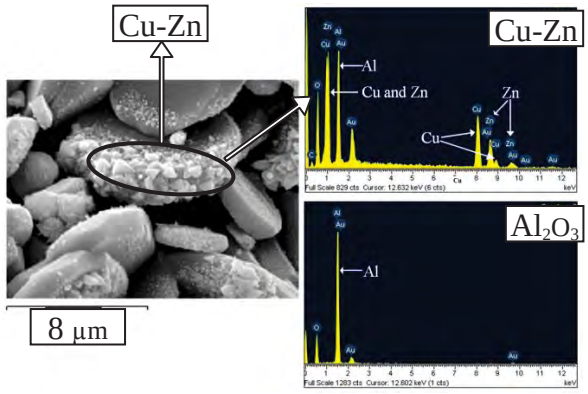

Figure 2. SEM image and EDS profiles of impregnated Cu-Zn/Al_2O_3 *with urea*

3.2 Hydrogen production over impregnated Cu-Zn/Al_2O_3 and sol-gel Cu-Zn/Al_2O_3

The aim of catalytic hydrogen production from this work is to feed hydrogen fuel cell in a continuous mode. Hydrogen production is presented in a hydrogen production rate (µmol/min) shown in Table 2.

Table 2: Hydrogen production from methanol-steam reforming over impregnated Cu-Zn/Al_2O_3 with urea and Sol-gel Cu-Zn/Al_2O_3

Temperature (K)	Hydrogen Production (µmol/min)	
	Impregnation	Sol-gel
453	107±5.0	83±2.0
523	274±0.5	204±3.0
573	307±3.0	304±3.0
623	293±0.5	292±2.0

The activity of impregnated catalyst is increased when reaction temperature is increased from 453 K to 573 K. The activity of catalyst is rapidly increased when the reaction temperature from 453 K to 523 K, the hydrogen production increased from 107 µmol H_2/min to 274 µmol H_2/min, respectively. The highest hydrogen production of 307 µmol H_2/min could be reached at the reaction temperature of 573 K. The hydrogen production is decreased at reaction temperature of 623 K. Literatures reported that the methanol steam reforming is a preferred reaction at the temperature lower than 573 K [4]. At the higher temperature, the methanol decomposition starts to dominate as shown in the following equation.

Methanol Decomposition reaction [9]:

$CH_3OH \rightarrow 2H_2 + CO \quad \Delta H_{Rxn} = 128\ kJmol^{-1}$

Methanol decomposition produces lower hydrogen than that of methanol steam reforming. In addition, the Cu-Zn based catalysts can be deactivated from sintering at the temperature higher than 573 K. [10-11]. Methanol decomposition and metal sintering could reduce the catalyst activity at high temperature.

The sol-gel catalyst can perform the same trend of hydrogen production as the impregnated catalyst. The hydrogen production is increased at the temperature range of 453-573 K. The highest hydrogen is 304 µmol H_2/min at reaction temperature of 573 K.

Hydrogen production of sol-gel Cu-Zn/Al_2O_3 catalyst is lower than the impregnated Cu-Zn/Al_2O_3 catalyst at the same reaction temperatures. Hydrogen production is decreased at the reaction temperature 623 K due to the fact that a sintering or the methanol decomposition is occurred same as the catalyst that is prepared by impregnation method.

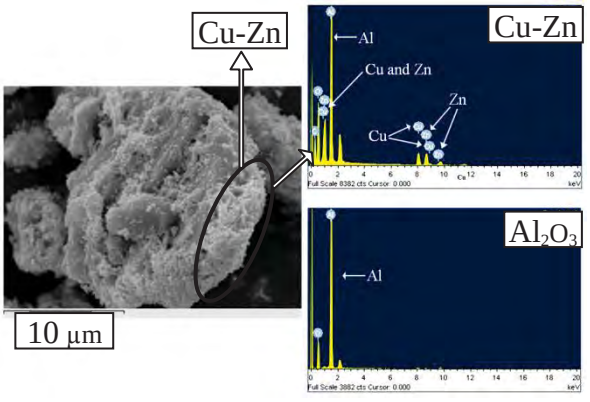

Figure 3. SEM image and EDS profiles of sol-gel Cu-Zn/Al_2O_3

Figure 3 shows SEM image and EDS profiles of Cu-Zn/Al_2O_3 catalyst prepared by sol-gel. The image shows that the Cu and Zn are deposited in a form of tiny clusters through out the Al_2O_3 support. The EDS

profiles indicate that the tiny clusters are composed of Cu and Zn located over Al_2O_3 support with well dispersion pattern.

Table 4: Estimated crystalline size of CuO in Cu-Zn/Al_2O_3

Cu-Zn/Al_2O_3 Catalysts	Estimated crystalline size of CuO* (nm)
Impregnated *without urea*	29
Impregnated *with urea*	14
Sol-gel	14

*determined by XRD using peak at 2-theta equal to 38.8 degree

Table 4 shows the estimated crystalline sizes of CuO determined by XRD band broadening. The data shows that the addition of urea in impregnated Cu-Zn/Al_2O_3 catalyst can reduce the CuO crystalline size from 29 nm to 14 nm. The CuO crystalline of the sol-gel Cu-Zn/Al_2O_3 also provide the same estimated CuO crystalline sizes as impregnated catalyst with urea (14 nm).

4. Conclusions

In this study, a low cost Cu-Zn based catalyst has been developed for methanol-steam reforming using impregnation with and without urea and sol-gel preparation. The results show that hydrogen production rate of impregnated Cu-Zn/Al_2O_3 with urea exhibits the highest activity among the catalysts in this study. The temperature that could yield the highest hydrogen production over this catalyst is 573 K. Hydrogen production is reduced at higher temperature due to the metal sintering and the methanol decomposition. The SEM-EDS images show that the use of urea can reduce the size of Cu-Zn metal clusters and provide better dispersion of Cu-Zn clusters throughout Al_2O_3 support. which results in a higher activity of hydrogen production. Urea addition can also reduce the crystallize size of CuO as well. The XRD exhibited that the addition of urea in impregnated Cu-Zn/Al_2O_3 catalyst can reduce the CuO crystalline size. The CuO crystalline of the sol-gel Cu-Zn/Al_2O_3 also provide the same estimated CuO crystalline sizes as impregnated catalyst with urea. The results of this study could lead to the development of the active catalyst, which is low cost and easy to be prepared, for hydrogen production from methanol-steam reforming.

Acknowledgements

This work was supported by National Research University Project of Thailand Office of Higher Education Commission and Low Carbon Technology and Management Research Grant.

References

[1] A. Tanksale, J. N. Beltramini, G. M. Lu, *Renewable and Sustainable Energy Reviews*. **14** (2010) 166–182.
[2] J. D. Holladay, J. Hu, D. L. King, Y. Wang, *Catalysis Today*. **139** (2009) 244–260.
[3] P. K. Cheekatamarla, C.M. Finnerty, *Journal of Power Sources*. **160** (2006) 490–499.
[4] M. Turco, G. Bagnasco, C. Cammarano, P. Senese, U. Costantino, M. Sisani, *Applied Catalysis B: Environmental*. **77** (2007) 46–57.
[5] S. Murcia-Mascarós, R. M. Navarro, L. Gómez-Sainero, U. Costantino, M. Nocchetti, J. L. G. Fierro, *Journal of Catalysis*. **198** (2001) 338–347.
[6] S. D. Jones, L. M. Neal, H. E. Hagelin-Weaver, *Catalysis B: Environmental*. **84** (2008) 631–642.
[7] S. Esposito, M. Turco, G. Bagnasco, C. Cammarano, P. Pernice, A. Aronne, *Applied Catalysis A: General*. **372** (2010) 48–57.
[8] K. H. Wu, Y. C. Chang, G. P. Wang, *Journal of Magnetism and Magnetic Materials*. **269** (2004) 150–155.
[9] J. Papavasiliou, G. Avgouropoulos, T. Ioannides, *Catalysis Communications*. **5** (2004) 231–235.
[10] S. D. Jones, H. E. Hagelin-Weaver, *Applied Catalysis B: Environmental*. **90** (2009) 195–204.
[11] S. D. Jones, L. M. Neal, M. L. Everett, G. B. Hoflund, H. E. Hagelin-Weaver, *Applied Surface Science*. **256** (2010) 7345–7353.

HYDROGEN PRODUCTION FROM AMMONIA DECOMPOSITION

Chaichan Siriruang, Phalotai Kuakpetoon, Kittipong Kulsiri, Julaluk Duangthong, and Pisanu Toochinda*

Sirindhorn International Institute of Technology /School of Bio-chemical Engineering and Technology, Thammasat University, P.O. BOX 22, Pathum Thani, 12121 Thailand

* Author for correspondence; E-Mail: pisanu@siit.tu.ac.th, Tel. +66 2 9869009 ext 2309

Abstract: Decomposition of ammonia is an interesting pathway for hydrogen production used in fuel cell applications. The decomposition of ammonia can produce hydrogen without CO_2 emission. Ni is one of the most active catalyst and low cost for this reaction. In this study, the Ni-based catalysts prepared by incipient wetness impregnation and sol-gel methods were investigated to determine the activity of hydrogen production and selectivity from the decomposition of ammonia. Catalytic decomposition was conducted at 773-873 K at 1 atm in continuous mode using packed bed reactor. The hydrogen yields from different Ni-based catalysts were analyzed by gas chromatography (GC). Catalysts were characterized by XRD and SEM-EDS before and after the decomposition reaction in order to determine the change of Ni metal size and the metal cluster. The active catalyst from this study could provide an effective hydrogen production process from catalytic ammonia decomposition. The hydrogen production activity of catalysts prepared by incipient wetness impregnation and sol-gel methods will be discussed. The achievement of this study is the feasibility of using nickel catalyst that exhibits the impressive yield of hydrogen to feed the hydrogen fuel cell without any CO_x emission which poisons the catalyst of the hydrogen fuel cell.

1. Introduction

Recently, clean energy production to replace energy from fossil fuel have become the most intentional subject in the world. One of the clean energies is hydrogen fuel cell, which takes more presence in many applications. A major problem of the fuel cell technology is the high cost and unclean process of the hydrogen production. The conventional production methods such as stream reforming, partial oxidation, autothermal reforming, water-gas shift, pyrolysis and co-pyrolysis of hydrocarbons, results in carbon dioxide emission, which causes the global warming [1-2]. Moreover, these methods also produce carbon monoxide which can poison the PEM fuel cell catalyst [1-3]. In the generation of clean hydrogen for fuel cells, motivation in catalytic ammonia decomposition is the recent intention.

Ammonia decomposition can produce hydrogen without CO and CO_2 emission [4-6]. Furthermore, hydrogen production via ammonia decomposition is more economically feasible than that via methanol reforming [4, 6]. According to all these considerations, ammonia decomposition becomes an outstanding alternative for hydrogen production.

Decomposition of ammonia is a reversible and endothermic reaction as shown in following equation [6-7]:

$2NH_3 \leftrightarrow N_2 + 3H_2 \qquad \Delta H_{rxn} = 46$ kJ/mol

The active catalysts for ammonia decomposition have been reported as group VIII metals (Ru, Ni, Ir, Fe, Co and Rh) [4, 6]. Ru is the most active metal among any others in exchange to its high cost and limited resources as the drawbacks [8]. Therefore, the Ni is reported as the substitution of Ru due to the high activity among non noble metal and its low cost [5, 7].

The objective of this study is to investigate the activity of Ni-based catalysts from two different preparation methods; incipient wetness impregnation [9] and sol-gel [10]. Catalyst properties, such as Ni metal site and metal dispersion, were investigated to support the activity of the catalyst in hydrogen production from ammonia. The result from this study may lead to the development of the novel active catalyst for ammonia decomposition.

2. Experimental

2.1 Catalyst Preparations

Impregnated catalysts: Ni-based catalysts over Al_2O_3 were prepared by incipient wetness impregnation method. The catalysts were prepared by impregnating the metal salt solution of nickel nitrate ($Ni(NO_3)_2 \cdot 6H_2O$) (≥97%, Ajax Finechem Pty Ltd) with urea (≥99%, Carlo Erba) over low and high surface area alumina powder, α-Al_2O_3 and γ-Al_2O_3. Catalysts were prepared with the variation of compositions; 10wt% Ni with urea and 20wt% Ni with urea. After impregnation, catalysts were heated at 378 K for 6 h and calcined at 873 K for 4 h.

Sol-gel catalysts: The sol-gel catalysts are prepared by mixing of nickel nitrate ($Ni(NO_3)_2 \cdot 6H_2O$) (≥97%, Ajax Finechem Pty Ltd), citric acid ($C_6H_8O_7 \cdot H_2O$) (≥99%, Ajax Finechem) and DI water to form aqueous metal solution. The solutions were heated constantly at 343 K. Ammonia (25wt%) was added into the solution to adjust pH to be 7. After pH was stable, alumina powder were added into solutions. Solutions were stirred and heated at 343 K for 4 h. They were evaporated at 343 K for 4 h, dried at 403 K for 6 h and calcined at 873 K for 4 h. All catalysts are shown in Table 1.

Table 1: Catalysts preparation

Catalysts	Active metal	Preparation Method
10Ni/α-Al_2O_3	10wt% Ni	Impregnation
20Ni/α-Al_2O_3	20wt% Ni	Impregnation
10Ni/α-Al_2O_3	10wt% Ni	Sol-gel
20Ni/α-Al_2O_3	20wt% Ni	Sol-gel
20Ni/γ-Al_2O_3	20wt% Ni	Sol-gel

* α-Al_2O_3 = Low surface area Al_2O_3;
γ-Al_2O_3 = High surface area Al_2O_3

2.2 Ammonia decomposition in tubular reactor

The ammonia decomposition reaction for the hydrogen production was studied on the prepared catalysts in a stainless steel tubular reactor which has an inside diameter of 1 cm. Two grams of catalyst were packed between quartz wool in the reactor. The catalyst was reduced with 25 ml/min of 10% H_2: N_2 balanced at 673 K for 1 h prior to the ammonia decomposition reaction test. The reactor was flushed with 20 ml/min N_2 flow at 673 K for 30 min to get rid of adsorbed hydrogen from the reduction process. The ammonia solution was loaded into a saturator which was heated to 308 K. Compositions of ammonia and water in the liquid phase is 0.1:0.9 molar ratios. The composition of solution was calculated by the Aspen Plus simulation program (Aspen Technology Inc., Burlington, Mass., USA). The vapor of the mixture within the saturator was carried out at 15 ml/min N_2, and sent into the reactor at reaction temperature range 773-873 K in a continuous system. The product was collected and the amount of hydrogen was determined via gas chromatograph (GC).

2.3 Analysis sections

A Perkin Elmer (Waltham, Mass., USA) Autosystem XL gas chromatograph (GC) with Porapak Q column (Supleco, Bellefonte, PA, USA) coupled with a thermal conductivity detector (TCD) was used to determine the amount of hydrogen production.

Metal clusters over support of the catalysts was inspected by a scanning electron microscope (SEM, JEOL JSM-5410, Jeol Inc., Tokyo, Japan) coupled with energy dispersive spectrometry (EDS, Oxford, Oxford Instrument, Oxfordshire, United Kingdom) to determine the elemental composition of the catalyst.

The catalysts were characterized by the X-ray diffraction technique (X'Pert PRO diffractometer, Panalytical, Almelo, The Netherlands) using Cu Kα1 radiation, 20° - 70° 2-theta, 0.02° step size, 1 sec step time.

3. Results and Discussion

3.1 Hydrogen production from ammonia decomposition production

Table 2 shows the hydrogen production rate (μmol/min) from ammonia decomposition over Ni on α-Al_2O_3 and γ-Al_2O_3. Ni-based catalysts prepared by impregnation and sol-gel methods exhibit the activity of hydrogen production from ammonia decomposition at the temperature range of 773-873 K in continuous mode. Blank run has been executed without the catalyst. A trace amount of hydrogen was found in the negligible amount that should be mention.

Table 2: Activities of catalysts

Catalysts	Temperature (K)	Hydrogen rate (μmol/min)
Impregnation		
10Ni/α-Al_2O_3	773	167.9
	873	250.4
20Ni/α-Al_2O_3	773	181.1
	873	219.5
Sol-gel		
10Ni/α-Al_2O_3	773	134.3
	873	220.6
20Ni/α-Al_2O_3	773	134.3
	873	241.8
20Ni/γ-Al_2O_3	773	176.0
	873	251.2

For impregnated catalysts, the hydrogen rate is increased relatively to the increasing of the operating temperature. At 773 K, 20wt% Ni catalyst exhibit reaction activity higher than 10wt% Ni catalyst. However, at 873 K, 10wt% Ni catalyst surprisingly exhibited higher hydrogen production rate than that of 20wt% Ni catalyst. The reason can be described by the calculation of metal occupied area and surface area of the support over a gram of catalyst basis shown in Table 3.

Table 3: The surface area ratio of metal and support.

Catalyst	Area/g catalyst		%Ni occupied area over support
	Ni (m^2)	γ-Al_2O_3* (m^2)	
10wt% Ni	71.51	198.00	36.00 %
20wt% Ni	143.02	176.00	81.30 %

Ni atomic radius (r) = 149 pm [11];
Occupied Ni area = πr^2
*γ-Al_2O_3 surface area is 220 m^2/g [12].

The result shows that 10wt% Ni catalyst has 36.00% Ni occupied area over the support surface while that of 20wt% Ni catalyst is 81.30%. Thus, for 20wt% Ni catalyst, high Ni metal loading may lead to the deposition of Ni atom on the top of each others. Therefore, impregnated 20wt% Ni catalyst might suffer from the sintering of Ni metal cluster at high temperature easier than 10wt% Ni catalyst. Moreover, the method of impregnation uses metal salt aqueous solution to be dropped on the support randomly, the metal may not well distribute on the Al_2O_3 support. These matters could lead to the low activity in 20wt% Ni catalyst at high temperature.

For sol-gel catalysts, 10wt% Ni and 20wt% Ni catalysts on α-Al_2O_3 show the same result of hydrogen rate at temperature of 773 K, which is 241.8 μmol/min. This phenomenon might happen because

the support (α-Al_2O_3) has limited surface area and it is already fully occupied by Ni atoms. Therefore, the hydrogen rate does not increased when the metal loading is increased.

Thus, high surface area support, γ-Al_2O_3, is introduced to be use as support for 20wt% Ni catalyst in order to investigate the efficiency enhancement of high metal loading over high surface area support. According to the result, it is clearly shown that 20wt% Ni catalyst on γ-Al_2O_3 catalyst provides a higher hydrogen production rate than 20wt% Ni catalyst on α-Al_2O_3 by 4%. Therefore, it can be concluded that the higher surface area increases the efficiency of 20wt% Ni catalyst.

At the temperature of 873 K, 20wt% Ni loading on both α-Al_2O_3 and γ-Al_2O_3 yield the higher hydrogen production rate than that of the 10wt% Ni catalyst which is opposite from the results in the impregnated catalysts. The high activity of 20wt% Ni catalyst may cause from the sol gel preparation method. In contrast of impregnation method, the support (Al_2O_3) were introduced during the sol-gel matrix has been built. Thus, the well distribution via sol-gel method might be able to boost the dispersion of the metal on the support better than impregnation. Therefore, it can be summarized that the sol-gel method may improve the distribution of the metal cluster and reduce the sintering of the metal cluster.

Based from the results compared between impregnation and sol-gel preparation methods, it is undoubtedly shown that the dispersion of metal in a catalyst made by sol-gel is better than the one made by impregnation at 10-20wt% of metal loading. Nevertheless, the Ni-based catalysts exhibit the impressive hydrogen production rate relative to hydrocarbon reforming [13]. Ammonia decomposition provides no CO and CO_2 contaminants in the hydrogen product stream which can lower the hydrogen purification process for requirement in fuel cell applications [14]. The activity enhancement of Ni-based catalyst could be done by adding the promoter or co-active metals which are under investigation.

3.2 Catalysts characterization

3.2.1 Scanning Electron Microscope (SEM)

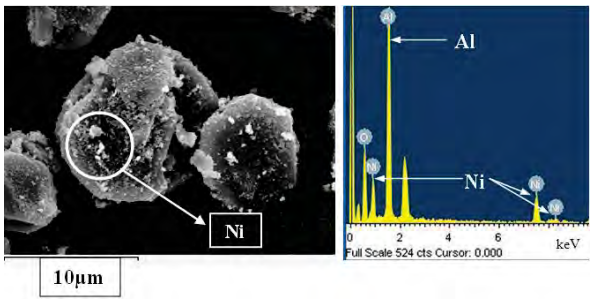

Figure 1. SEM image and EDS profile of 20Ni/α-Al_2O_3 impregnation method.

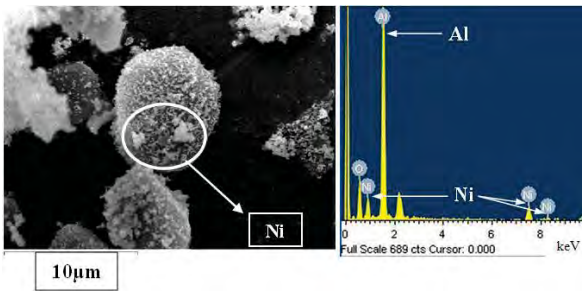

Figure 2. SEM image and EDS profile of 20Ni/α-Al_2O_3 sol-gel method.

Figures 1 and 2 show the SEM image and EDS profile of 20Ni/α-Al_2O_3 prepared by impregnation and sol-gel method respectively. As shown in the result, both impregnation and sol-gel preparation technique could provide a good dispersion of the Ni cluster.

3.2.2 X-ray Diffractogram of catalysts

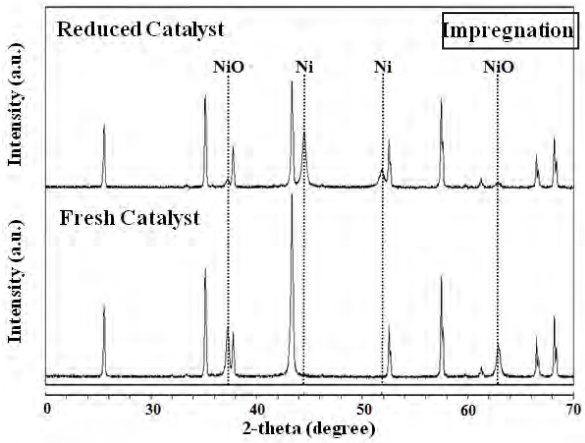

Figure 3. XRD of impregnated 20Ni/α-Al_2O_3 catalyst before and after reduced.

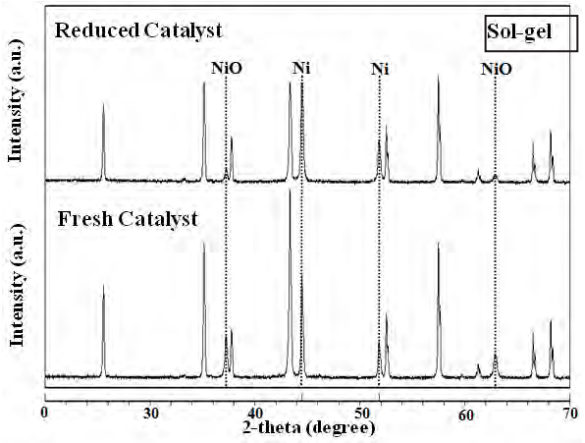

Figure 4. XRD of sol-gel 20Ni/α-Al_2O_3 catalyst before and after reduced.

Figures 3 and 4 show the XRD of 20Ni/α-Al_2O_3 catalyst (before and after reduction) prepared by impregnation and sol-gel method respectively. For sol-gel catalyst, Ni^0 is presented even before the reduction process while none have been observed in the impregnated catalyst. Sol-gel matrix might encapsulate

Ni^0 and prevent the oxidation reaction of Ni to occur. Sol-gel catalyst, after reduction, also shows higher Ni^0 composition than the impregnated catalyst.

The result shows the same Ni phase (Ni(111)) represented over both impregnated and sol-gel catalysts after reduction, which are evidenced by the peak at 2-theta of 45 °. Thus, the reaction mechanism of the catalysts prepared by two methods in this study might be the same.

4. Conclusions

The results of this study show the feasibility of hydrogen production from catalytic ammonia decomposition without CO and CO_2 emission. The ammonia decomposition reaction can occur with impressive hydrogen yield over catalysts prepared by impregnation and sol-gel methods at the operating temperature range of 773-873 K. The hydrogen rate of the sol-gel catalyst provides a better result than the impregnated catalyst. The highest hydrogen production rate of 251.2 μmol/min could be obtained from 20wt%Ni/γ-Al_2O_3 sol-gel catalyst at 873 K. Characterizations of the catalysts from XRD and SEM also show that catalysts prepared by these two methods provide a good dispersion of the Ni cluster. In addition, the Ni active site over the impregnation and sol gel catalysts from this study are the same Ni (111) metal site which be able to utilize the same reaction mechanism.

Benefits of both methods provide the possibility for the enhancement of the catalyst. The result of this study may lead to the development of the novel Ni-based catalysts for hydrogen production from ammonia decomposition.

Acknowledgements

This work was supported by the National Research University Project of Thailand Office of Higher Education Commission and Low Carbon Technology and Management Research Grant.

References

[1] H. Song, U. S. Ozkan, *International journal of hydrogen energy.* **35** (2010) 127–134.
[2] A. Miltner, W. Wukovits, T. Proll, A. Friedl, *Journal of Cleaner Production.* **18** (2010) S51–S62.
[3] A.J. Vizcaíno, A. Carrero, J.A. Calles, *International Journal of Hydrogen Energy.* **32** (2007) 1450–1461.
[4] T.V. Choudary, C. Sivadiinarayana, D.W. Goodman, *Catal. Lett.* **72** (2001) 197.
[5] X.-K. Li, W.-Ji. Ji, J. Zhao, S.-J. Wang, C.-T. Au, *Journal of Catalysis.* **236** (2005) 181–189.
[6] S.F. Yin, B.Q. Xu, X.P. Zhou, C.T. Au, *Applied Catalysis A: General.* **277** (2004) 1–9.
[7] H. Muroyama, C. Saburi, T. Matsui, K. Eguchi, *Applied Catalysis A: General.* **443–444** (2012) 119–124.
[8] J. Zhang, H.Y. Xu, X.L. Jin, Q.J. Ge, W.Z. Li, *Applied Catalysis A: General.* **290** (2005), 87–96.
[9] R. A. Koppel, C. Stocker, A. Baiker, *Journal of Catalyst.* **179** (1998) 515–527.
[10] T. Lopez, M. Alvarez, R. Gomez, D. H. Aguilar, P. Quintana, *Journal of Sol-Gel Science and Technology.* **33** (2005) 93–97.
[11] http://www.alfa.com/ (Retrieved September 24, 2012)
[12] http://www.webelements.com/ (Retrieved 2012)
[13] C. Siriruang, P. Vacharapong, S. Ajavakom, T. Sumonsart, P. Toochinda, *Role of Urea and Zirconia in Cu-Zn/Al_2O_3 for Methanol-stream Reforming,* Proceeding of Pure and Applied Chemistry International Conference (PACCON 2010), Ubon Ratchathani, Thailand, (2010), pp. 251–254.
[14] C. Liu, Z. Noda, K. Sasaki, K. Hayashi, *International Journal of Hydrogen Energy.* **37** (2012) 13529–13535.

STUDY OF HEAT AND MASS TRANSFER DURING FALLING RATE PERIOD OF SPRAY DRYING OF A SLURRY DROPLET WITH NANOPARTICLES

Wittaya Julklang, Boris Golman*

School of Chemical Engineering, Institute of Engineering, Suranaree University of Technology,Nakhon Ratchasima, Thailand

* Author for correspondence; E-Mail: golman@sut.ac.th, Tel. +66 44224325, Fax. +66 44 224609

Abstract: The agglomerates of nanoparticles produced by spray drying of slurry feed are used as high-value functional materials in various industries. The mathematical model has been developed for simulation of time variation of temperature and vapor concentration distributions in the radial direction of a slurry droplet during the falling rate period of spray drying. The effects of drying gas temperature and flow rate, and the porosity of agglomerated product were analyzed on the heat and mass transfer in a droplet. The simulation demonstrated that both heat and mass transfer in the falling rate period significantly effect on the drying rate of a slurry droplet involving nanoparticles.

1. Introduction

The agglomerates of nanoparticles produced by spray drying of a slurry feed are used as high-value functional materials in various industries such as chemical, pharmaceutical, food and agriculture [1]. The superior physical and chemical properties of agglomerate of various morphologies prepared by spray drying of nanometer to submicron particles were described by Nansiyanto et al. [2] .

Spray drying is a complex process involving the heat, mass and momentum transfer between the droplet and the drying gas [3]. The kinetics of drying process is often determined by rates of external heat and mass transfer from the bulk gas to the droplet surface and internal heat and mass transfer through a solid layer formed around the core containing slurry of nanoparticles during drying in the falling rate period. The knowledge of the drying kinetics is important for design and optimization of spray drying process.

The experimental measurements and mathematical modeling were reported by Nesic et al. [4] on the drying of a slurry droplet. The model was applied for both constant and falling rate periods with simplified representation of heat and mass transfer resistances in the falling rate period. However, their model did not account for distributions of temperature and vapor concentration in the droplet.

Dalmaz et al. [5] derived the drying model which includes heat and mass transfer resistances in the droplet during the falling rate period. Though, an extreme value of the porosity of agglomerated product was used in the model calculations.

The temperature distributions in the slurry droplet during the falling rate were calculated by Golman [6] using the model which takes into account the external and internal heat and mass transfer resistances. However, the vapor concentration distributions inside the droplet were not reported as well as the number and the range of operational parameters under investigation were limited.

Therefore, the mathematical model of spray drying of the slurry droplet involving both external and internal mass and heat transfer resistances was developed in the present study. This model was used to elucidate the influence of mass and heat transfer phenomena on the drying in the falling rate period.

2. Materials and Methods

The spray drying process is commonly divided into two periods corresponding to the constant and falling drying rates. The mathematical model of drying of the slurry droplet in the falling rate period is derived separately for two parts, the wet core and the dry crust, as illustrated in Figure 1.

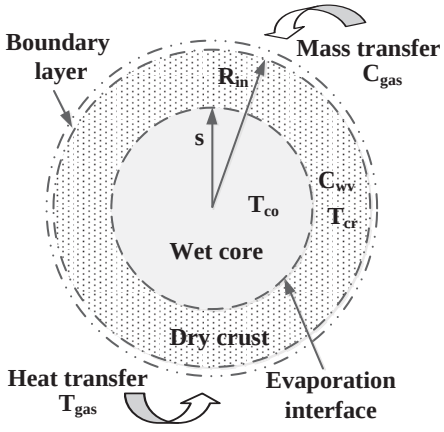

Figure 1. Illustraition of drying model of the slurry droplet in the falling rate period.

The temperature distribution in the radial direction of wet core, T_{co}, is calculated by the following heat balance equation

$$\frac{\varepsilon\rho_w Cp_w + (1-\varepsilon)\rho_s Cp_s}{k_{co}} \frac{\partial T_{co}}{\partial t} = \frac{\partial^2 T_{co}}{\partial r^2} + \frac{2}{r}\frac{\partial T_{co}}{\partial r} \qquad (1)$$

where t is the drying time, r is the radial position, ε is the porosity of agglomerated product, k_{co} is the heat

conductivity of wet core, Cp_w and ρ_w are the heat capacity and the density of water, and Cp_s and ρ_s are the heat capacity and the density of solid particle, respectively.

The continuity boundary condition at the evaporation interface is expressed as

$$T_{co} = T_{cr} \tag{2}$$

The distributions of temperature and water vapor concentration in the dry crust are described as

$$\frac{(1-\varepsilon)\rho_s Cp_s}{k_{cr}}\frac{\partial T_{cr}}{\partial t} = \frac{\partial^2 T_{cr}}{\partial r^2} + \frac{2}{r}\frac{\partial T_{cr}}{\partial r} \tag{3}$$

$$\frac{\varepsilon}{D_{cr}}\frac{\partial C_{wv}}{\partial t} = \frac{\partial^2 C_{wv}}{\partial r^2} + \frac{2}{r}\frac{\partial C_{wv}}{\partial r} \tag{4}$$

where C_{wv} is the concentration of water vapor, and k_{cr} and D_{cr} are the heat conductivity and the effective diffusivity of dry crust, respectively.

The heat and mass balances at the evaporation interface are derived as

$$\varepsilon\rho_w\lambda_w\frac{ds}{dt} = -k_{cr}\frac{\partial T_{cr}}{\partial r} + k_{co}\frac{\partial T_{co}}{\partial r} \tag{5}$$

$$\varepsilon\rho_w\frac{ds}{dt} = D_{cr}Mw\frac{\partial C_{wv}}{\partial r} \tag{6}$$

where s is the radial postion of the evaporation interface, λ_w is the latent heat of water evaporation and Mw is the molecular weight of water.

The mass and heat transfer from the surface of agglomerate at R_{in} to the drying air are expressed as

$$-D_{cr}\frac{dC_{wv}}{dt} = k_m\left(C_{wv} - C_{gas}\right) \tag{7}$$

$$-k_{cr}\frac{dT_{cr}}{dr} = h\left(T_{cr} - T_{gas}\right) \tag{8}$$

where k_m and h are the convective mass and heat transfer coefficients, and C_{gas} and T_{gas} are the vapor concentration and the temperature of bulk air, respectively.

The effective diffusivity and the heat conductivity of the dry crust are defined as [5]

$$D_{cr} = \frac{2\varepsilon D_{wv}}{3-\varepsilon} \tag{9}$$

$$k_{cr} = \varepsilon k_{mx} + (1-\varepsilon)k_s \tag{10}$$

where D_{wv} is the diffusivity of water vapor, k_{mx} and k_s are the heat conductivities of air-water mixture and solid, respectively.

The diffusivity of water vapor as a function of temperature T' is given as [5]

$$D_{wv} = 0.220\times10^{-4}\left(\frac{T'}{273.15}\right)^{1.75} \tag{11}$$

The convective heat and mass transfer coefficients are calculated by utilizing Ranz and Marshall correlations [7] as

$$Nu = \frac{h2R_{in}}{k_g} = 2 + 0.65\,\mathrm{Re}^{0.5}\,\mathrm{Pr}^{0.33} \tag{12}$$

$$Sh = \frac{k_m 2R_{in}}{D_{wv}} = 2 + 0.65\,\mathrm{Re}^{0.5}\,Sc^{0.33} \tag{13}$$

where Nu, Sh, Re, Pr and Sc are the Nusselt, Sherwood, Reynolds, Prandtl and Schmidt numbers for drying air, respectively. These dimensionless numbers are defined as $\mathrm{Re} = 2R_{in}v_g\rho_g/\mu_g$, $\mathrm{Pr} = Cp_g\mu_g/k_g$, $Sc = \mu_g/\rho_g D_{wv}$, where v_g is the gas velocity, and Cp_g, k_g, ρ_g and μ_g are the heat capacity, the heat conductivity, the density and the viscosity of drying gas, respectively.

During the falling rate period, the agglomerate weight is calculated as

$$W_{ag} = \frac{4}{3}\pi\left[\rho_w\varepsilon s^3 + \rho_s(1-\varepsilon)R_{in}^3\right] \tag{14}$$

The system of partial and ordinary differential equations of heat and mass balances was solved by a finite difference method with the utilization of a fully implicit numerical scheme.

The validity of the present model was confirmed by comparison of calculated results with experimental data [4] for drying of colloidal silica at 101°C with primary particles of 16 nm in diameter, as shown in Figure 2.

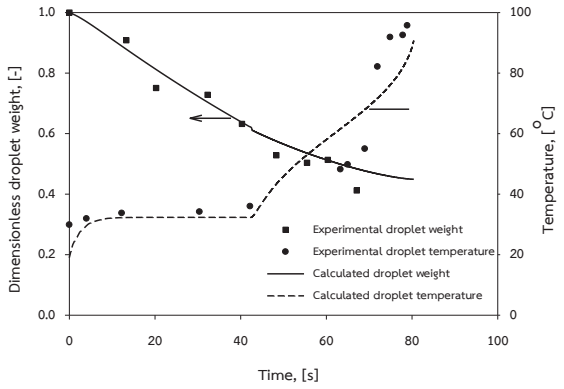

Figure 2. Comparison of model calculation and experimental data for drying of colloidal silica.

The effects of heat and mass transfer resistances inside the agglomerate were studied by varying the porosity of agglomerated product from 0.3 to 0.5, and the heat and mass transfer resistances outside agglomerated particle by changing the air flow rate from 1.0 to 2.0 m/s and the air temperature from 101 to 200°C. The crust layer formed by nanoparticles is assumed to be of constant porosity equal to the porosity of dried product agglomerate. The drying time was measured from the beginning of the falling rate period.

3. Results and Discussion

Figure 3 illustrates the movement of the air-liquid interface, where the evaporation is taking place, with drying time. The rate of interface movement is constant during the constant drying rate period as this interface coincides with the outer droplet surface.

During the falling rate period, the interface located inside the agglomerate moves inward with increasing speed as the small amount of water is left in the shrinking wet core, even the drying rate is significantly lower in comparison with one in the constant rate period by virtue of heat and mass transfer resistances in the crust region of agglomerate.

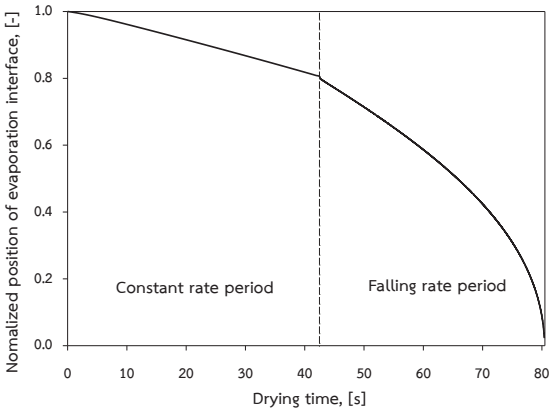

Figure 3. The movement of the evaporation interface with drying time.

Figure 4 displays the temperature profiles in the agglomerate for various flow rates of drying air at drying times corresponding to dry crusts of uniform thicknesses of 0.00025 and 0.0005 m. The surface temperature increases at high flow rate due to the enhancement of convective heat transfer from the bulk air to the agglomerate surface. The temperature distributions in the agglomerate show a similar trend because the internal heat transfer resistances are constant for dry crust layers of the same thickness. The temperature of the wet core also increases following the rise of dry crust temperature.

At the same air flow rate, the difference in temperature between the agglomerate surface and the wet core rises with drying time as the growing crust layer causes the additional resistance to the heat transfer inside the agglomerate.

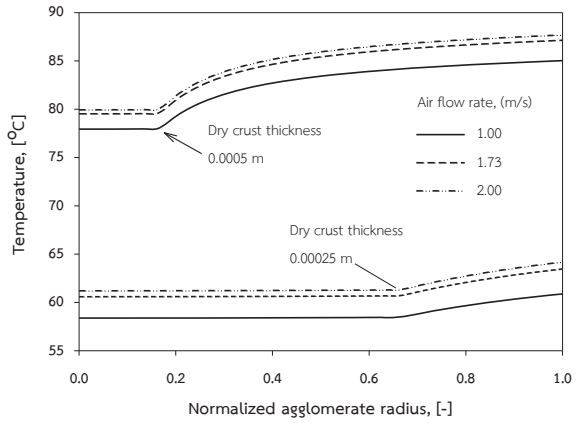

Figure 4. Temperature profiles inside the agglomerate at different air flow rates.

The concentration of water vapor in the crust layer of agglomerate slightly increases at high air flow rate for the same thickness of dry crust as the larger amount of heat supplied from the surface results in the acceleration of the drying rate at the evaporation interface, as shown in Figure 5. However, no difference is observed in the concentration of water vapor at the agglomerate surface. The reduction in vapor concentration in this region at high air flow rate can be explained by enhancements of the rate of mass transfer from agglomerate surface to the bulk air as well as the rate of mass transfer in the crust layer close to the agglomerate surface due to the large value of diffusivity of water vapor at high temperature.

Figure 5 also illustrates that the large amount of water vapor is accumulated close to the evaporation interface of thick crust layer due to the enlarging mass transfer resistance.The comparison of water vapor concentration profiles at the same air flow rate reveals that the vapor concentration at specified position in the dry crust is low in the agglomerate dried for long time corresponding to the thick crust layer owing to the enhancement of vapor diffusivity at high temperature.

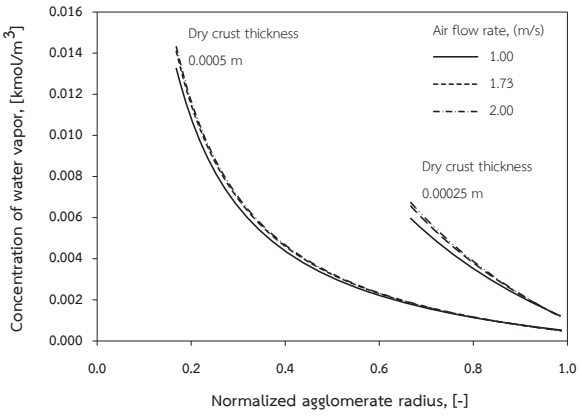

Figure 5. Concentration of water vapor inside the agglomerate at different air flow rates.

Figure 6 confirms that the drying of agglomerated nanoparticles in the falling rate period occurs more quickly at high air flow rate as a result of the intensification of convective heat transfer from the bulk air to the agglomerate surface and mass transfer in the opposite direction.

Figure 7 shows the variation of dimensionless droplet weight with respect to drying time for various drying air temperatures. The result confirms that the droplet weight reduces more rapidly at higher air temperature because of the higher drying rate at those conditions. Thus, the higher flow rate and temperature of the drying air result in the acceleration of external heat and mass transfer which in turn entails enhancement of mass and heat transfer inside the agglomerate.

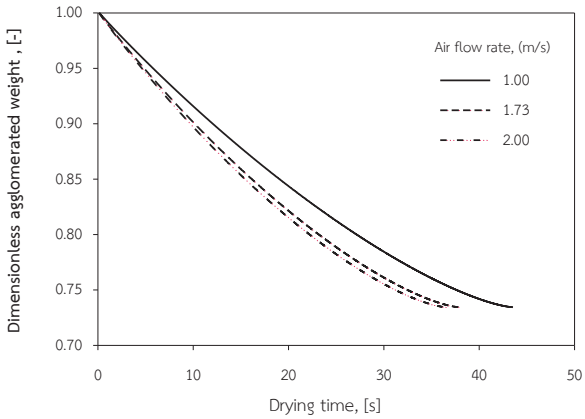

Figure 6. Dimensionless weight of the agglomerate dried at various air flow rates.

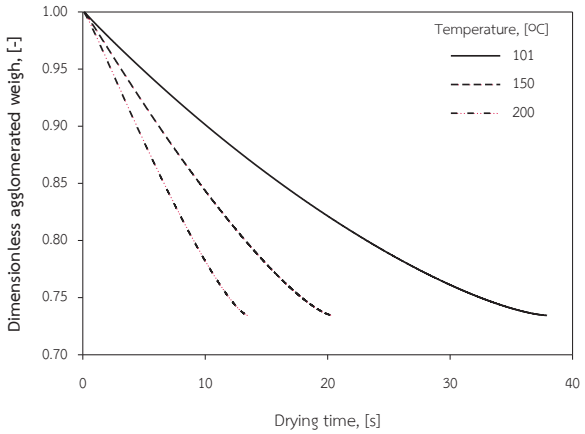

Figure 7. Dimensionless weight of the agglomerate dried at various air temperatures.

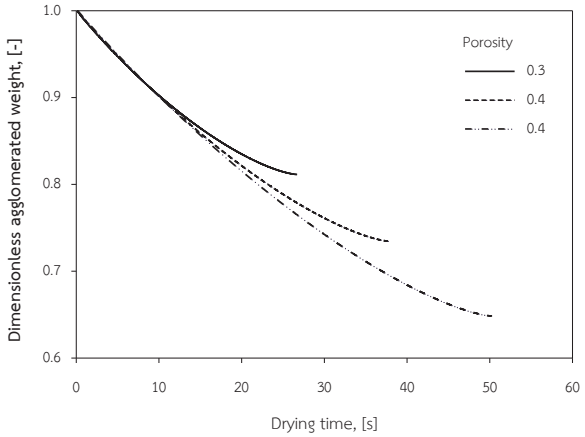

Figure 8. Dimensionless weight of the agglomerate of various porosities.

In this study, the agglomerated particles of different porosities were obtained by spray drying of the slurry of constant concentration. Hence, the amount of solid in the droplet was kept constant. Thus, the loose agglomerates were of larger sizes than the ones of lower porosities.

The rate of external heat and mass transfer is high in the case of the tight agglomerate of small size. The heat transfer in the crust layer of this agglomerate is also high due to the high value of solid heat conductivity. However, the rate of internal mass transfer is balanced by the larger value of the effective diffusivity in loose agglomerate by Eq. (9) and the larger value of water vapour diffusivity at high temperature for tight agglomerates by Eq. (11). As a result, the drying time of the agglomerate of lower porosity is shorter in the falling rate period in comparison with loose agglomerate, as indicated in Fig. 8.

4. Conclusions

The mathematical model of spray drying of the slurry droplet of nanoparticles was derived taking into account the external and internal mass and heat transfer resistances. The developed model was used for simulation of time variation of temperature and vapor concentration profiles in the radial direction of the agglomerated particles during the falling rate period.

The agglomerate surface, dry crust and wet core temperatures increased with drying time during the falling rate period due to the accumulation of heat in the dry crust. The difference in temperature between the agglomerate surface and the wet core rised with time as a result of heat transfer resistance of the growing crust layer. The accumulation of water vapor in the crust also increased with drying time owing to the enlarging mass transfer resistance. The rate of mass transfer enhanced at the same position in the crust layer at higher crust temperature.

The drying rate in the falling rate period is governed by the heat and mass transfer resistances both inside and outside the agglomerate.

Acknowledgements

The authors would like to thank the National Research Council of Thailand for their funding of this research.

References

[1] F. Iskandar, Advanced Powder Technology, **20** (2009) 283–292.
[2] A.B.D. Nandiyanto and K. Okuyama, *Advanced Powder Technology*, **22** (2011) 1-19.
[3] K. Masters, Spray drying handbook, Longman Scientific and Technical, Harlow, England (1985).
[4] S. Nesic and J. Vodnik, *Chemical Engineering Science*, **46** (1991) 527-537.
[5] N. Dalmaz, H.O. Ozbelge, A.N. Eraslan and Y.Uludag, *Drying Technology*, **25** (2007) 391-400.
[6] B. Golman, *AJCHE*, **11** (2011) 1-7.
[7] W.E. Ranz and W.R. Marshall, *Chemical Engineering Progress*, **48** (1952) 141-146.